AgCu and AgPd Single-atom Alloys: Electronic Structure, Surface Dynamics and Chemical Properties

Dissertation

Zur Erlangung des akademischen Grades eines Doktors der Naturwissenschaften
- Dr. rer. nat. -

vorgelegt von

Caroline Hvolmgaard Hartwig

geboren in Hamburg

Fakultät für Chemie
der
Universität Duisburg-Essen

2021

DOI: 10.17185/duepublico/74898
URN: urn:nbn:de:hbz:464-20211020-094224-5

“Science is not done alone.

It is through talking with others and sharing that progress is made.”

Carol W. Greider

Acknowledgments

I want to thank all people, who supported me during my PhD time at the MPI CEC.

First of all, I want to thank my group leader Dr. Mark Greiner, who accepted me as PhD in his group, although I did not have much background knowledge in surface science and solid-state physics before I started. I always especially enjoyed the very inspiring and motivating scientific discussions I had with him. Mark is a very good teacher and I learned extremely much under his supervision. For instance, through his expertise and up-to-date mindset, I learned a lot about programming and data management. Besides, I want to thank him for his dedication to optimize the daily working routines of our working group by providing and developing a data content management system. I am also very thankful for the scientific freedom and the trust he gave me.

A big thank you is for my Professor Dr. Robert Schlögl for the employment and the scientific as well as financial support. Through latter I could do exciting experiments at the ETH in Zurich and at synchrotron facilities in Italy as well as in Berlin. Additionally, I was able to participate at international conferences to present and discuss scientific results.

I thank Prof. Dr. Malte Behrens for being my second supervisor for the doctoral examination.

A special thank is for Gudrun Klihm and her support regarding all questions in the XPS lab.

I want to thank the whole Schlögl group for the pleasant, helpful and respectful working environment. I highly enjoyed to work in an international working group with colleagues from different scientific fields. The diverse ways of thinking led to new ideas and the exciting cultural and personal insights enriched me very much.

I also want to thank my colleagues and collaboration partners at MPI for iron research and at the FHI in Berlin for the support in sample synthesis, beamtimes and scientific discussions. Additionally, I am thankful for the collaboration I had with the group of Prof. Stephan Barcikowski at the University Duisburg-Essen. Without this collaboration I would not have met my boyfriend. This leads me to the point where I want to thank by boyfriend, my former flatmates and all my other good friends, who mentally supported me and made me feel home in the Ruhr area. Finally, I want to thank my family, who has always been there for me.

Without all the people I mentioned here I would not have been able to become the person I am today and to gain my PhD degree, and for this I will thank them forever.

Caroline Hartwig

Die vorliegende Arbeit wurde im Zeitraum von Oktober 2017 bis Mai 2021 im Arbeitskreis von Prof. Dr. Robert Schlögl am Max-Planck-Institut für Chemische Energiekonversion durchgeführt. Die mündliche Prüfung fand am 20.09.2021 statt.

Gutachter:

Prof. Dr. Robert Schlögl
Max-Planck-Institut für Chemische Energiekonversion

Prof. Dr. Malte Behrens
Christian-Albrechts-Universität zu Kiel

Prüfungsvorsitzender:

Prof. Dr. Jochen Niemeyer
Universität Duisburg-Essen

Table of contents

3. Results 37

List of abbreviations

AE	Auger electron
BElChem	Berlin joint laboratory for electrochemical Interfaces
BEP	Brønsted-Evans-Polanyi
BESSY	Berlin electron storage ring society for synchrotron radiation
BF	Bright field
BSE	Backscattered electrons
CENIDE	Center for nano integration Duisburg-Essen
CLS	Core level shift
CPS	Counts per second
DF	Dark field
DFT	Density functional theory
DOS	Density of states
DS	Doniach-Sunjic
EAL	Elastic attenuation length
EDX	Energy dispersive X-ray spectroscopy
EELS	Electron energy loss spectroscopy
EM	Electron microscopy
ESCA	Electron Spectroscopy for Chemical Analysis
ESEM	Environmental scanning electron microscopy
EPD	Electrophoretic deposition
FHI	Fritz Haber Institute
FID	Flame ionization detector
FWHM	Full with half maximum
GC	Gas chromatography
HAADF	High-angle annular dark-field
IMFP	Inelastic mean free path
MFC	Mass flow controller
MPI	Max Planck Institute

MS	Mass spectrometry
NAP	Near ambient pressure
OODT	Onset oxide decomposition temperature
OOT	Onset oxidation temperature
PC	Principal component
PCA	Principal component analysis
PDOS	Projected density of states
PES	Photoemission signal
PLAL	Pulsed laser ablation in liquids
QMS	Quadrupole mass spectrometry
RGA	Residual gas analyzer
SAA	Single-atom alloy
SAC	Single-atom catalyst
SE	Secondary electrons
SEM	Scanning electron microscopy
SI	Supporting or supplementary information
STEM	Scanning transmission electron microscopy
STM	Scanning tunneling microscopy
TCD	Thermal conductivity detector
TEM	Transmission electron microcopy
TU	Technical University
UHV	Ultra-high vacuum
UPS	UV-Vis photoemission spectroscopy
XPS	X-ray photoemission spectroscopy

Motivation

To address challenges of heterogenous catalysts, such as insufficient selectivity or catalyst deactivation, rational catalyst design is desirable to identify structure-function correlations. However, this task is very challenging because of the high structural and compositional complexity of heterogeneous catalysts.[1] One way to reduce the catalyst complexity is to reduce the amount of active sites to well-defined, isolated metal sites (Pt, Pd, Rh) in a host metal matrix (Cu, Ag, Au), and thereby forming a so-called single-atom alloy (SAA).[2] In a bifunctional SAA the dissociation and reaction sites are decoupled, hence, SAAs have the potential to escape from linear scaling relationships that limit the performance of conventional catalysts.[1]

A couple of years ago our group discovered that the $Ag_{0.995}Cu_{0.005}$ alloy, where Cu atoms are isolated in the Ag host, has a unique electronic structure, where the d-valence states of Cu and Ag are well separated from each other.[3] Thereby the Cu3d state is so narrow that it is more similar to the electronic state of a Cu atom in gas phase than to bulk Cu. Such a free-atom-like electronic structure of the minority element has the potential to combine the advantages of homogeneous- and heterogeneous catalysis.[3] Building upon this work, the present thesis aims to investigate which effect this unique electronic structure has on catalysis and adsorbate bonding. Therefore, it is studied, how an AgCu SAA with high specific surface area can be synthesized, to be able to measure its structure-function correlation in *operando* conditions by near ambient pressure X-ray photoemission spectroscopy (NAP-XPS). *Operando* studies are crucial for rational catalyst design to obtain insights into the catalyst transformation under reaction conditions (e.g. surface segregation), and they help to close the pressure gap between surface science studies in UHV and high-pressure experiments under industrially relevant conditions.

Additionally, AgPd SAA foils, which also exhibit a free-atom-like electronic structure are synthesized. The foils suffer from surface area, but have the advantage that they are less complex (e.g. metal-support interactions can be avoided). The structure-performance relationship of AgPd SAAs in the semi-hydrogenation of acetylene are investigated and discussed.

Furthermore, the transformation of AgPd SAA in oxidative environments is studied using NAP-XPS to compare the oxidative behavior of Pd in the SAA with bulk Pd. This comparison helps to better understand the catalytic behavior of Pd in oxidative reactions. For such XPS studies, the application of statistical analysis methods is of great benefit and are discussed in this work.

Summary

During the past decade, single-atom alloys (SAAs) have been a lively topic of heterogeneous catalysis research. SAAs are bimetallic systems, where the atoms of the more active metal are present as isolated sites at the surface of a host metal at very low concentrations. The active solute atoms are thereby thermodynamically more stable when surrounded by the host metal. SAAs have the advantage that only small amounts of the expensive active metal are needed. Within this thesis the AgPd single-atom alloy system, where Ag is the host, has been intensively investigated. To study potential novel catalytic properties of such systems it is important to recognize experimental evidence of characteristic features in their electronic structure. Using X-ray photoemission spectroscopy (XPS) and computational chemistry, it was found that $Ag_{0.98}Pd_{0.02}$ SAA exhibits a free-atom-like electronic structure. Such unique electronic structure has been previously reported for AgCu SAAs by *Schlögl* and coworkers. Free-atom-like electronic structures are characterized by narrow d-valence states of the solute metal (Pd, Cu), that are separated (either spatially or energetically) from the d-states of the host metal. The measured photoemission spectra were compared with the calculated photoemission signal (PES) of a free Pd atom in the gas phase, with very good agreement, suggesting the Pd4d states in the alloy exhibit very weak hybridization with their surroundings, and are therefore electronically isolated. This thesis aims to investigate structure-function correlations, meaning, it aims to determine what impact the unique electronic structure has on adsorbate bonding and catalysis. Specifically, the chemical properties of $Ag_{0.98}Pd_{0.02}$ SAA model catalysts were investigated.

AgPd alloys are known for their superior performance in the industrially relevant semi-hydrogenation of acetylene, thus it was investigated whether it is worthwhile to drive the dilution of Pd in the inert Ag host to the single-atom level. The results reveal, that, in the case of an unsupported $Ag_{0.98}Pd_{0.02}$ model catalyst, the site-isolation of Pd and the associated electronic structure changes lead to a catalyst deactivation. From this observation it was concluded, that the active, isolated Pd atoms need the coordinating atoms to participate in the reaction to enable the reaction of activated H_2 with acetylene.

Besides the unique properties of Pd in reductive (e.g. hydrogenation) reactions, Pd has also the highest catalytic activity of all metals in oxidative reactions. In this work it was investigated how the chemical reactivity of AgPd SAA differ from its constituent Pd in oxidative atmospheres. For this purpose, electronic structure changes of an $Ag_{0.98}Pd_{0.02}$ SAA foil in 1 mbar of O_2 were studied by *in situ* XPS and compared with the electronic structure of a Pd foil under the same conditions. Pd in $Ag_{0.98}Pd_{0.02}$ partially oxidizes, and forms a unique meta-stable PdO_x surface oxide. By using a peak area modelling procedure, it could be predicted that PdO_x on $Ag_{0.98}Pd_{0.02}$ is present as thin, possibly monolayer thick, PdO_x islands. In comparison to the PdO formed on Pd foil, the PdO_x formed on AgPd is substantially less thermodynamically stable. Such behavior is an interesting property of oxides formed on dilute alloys, which could potentially be utilized in oxidative catalytic reactions such as methane oxidation.

To understand the dynamic processes taking place at the sample's surface in reactive atmospheres, e.g. of the oxidation study of Pd and AgPd, a sufficient temperature resolution, time resolution, energy resolution and signal quality are required. This can be achieved by measuring all relevant high-resolution XPS spectra repeatedly in rapid succession, whereby the temperature is increased at a slow, constant rate. This procedure generates large datasets, with good temperature resolution, which is beneficial to identify correlations between e.g. metal oxide species and the corresponding O1s species. Peak fitting models needed to be internally consistent across thousands of spectra. Thus, data analysis strategies were developed to process those large and often challenging datasets in appropriate time with high reliability of the peak fitting model. Within this PhD project different statistical data analysis methods like principal component analysis, Pearson correlations and correlograms are applied to find correlations in temperature series *in situ* XPS datasets, as well as to iteratively adapt the peak-fitting model. The methods are applied and discussed in this work using the example of Pd in oxidative environment.

Furthermore, this thesis deals with the question, which requirements a sample needs to fulfil, whose structure-function correlations should be measured by *operando* XPS. *Operando* means that gas phase changes are detected simultaneously with the electronic structure. For this purpose, a so called "Sniffer QMS" (quadrupole mass spectrometer) was developed and installed to the XPS setup. The gas detection of products requires catalysts with a high active surface area. AgCu SAAs with high surface area were synthesized by depositing AgCu nanoparticles, made by pulsed laser ablation in liquids, onto a porous silver support. During the subsequent *operando* analysis, in epoxidation conditions, the total oxidation product CO_2 could be measured, which verifies the successful operation of the self-developed "Sniffer QMS".

Zusammenfassung

Während des letzten Jahrzehnts waren Einzelatomlegierungen (SAAs) ein lebhaftes Thema der heterogenen Katalyseforschung. SAAs sind bimetallische Systeme, bei denen die Atome des aktiveren Metalls als isolierte Stellen an der Oberfläche eines Wirtsmetalls in sehr geringen Konzentrationen vorhanden sind. Die aktiven, gelösten Atome sind dabei thermodynamisch stabiler, wenn sie von dem Wirtsmetall umgeben sind. SAAs haben den Vorteil, dass nur geringe Mengen des teuren, aktiven Metalls benötigt werden. Im Rahmen dieser Arbeit wurde das AgPd-Einzelatom-Legierungssystem, bei dem Ag das Wirtsmetall ist, intensiv untersucht. Um mögliche neuartige katalytische Eigenschaften solcher Systeme zu untersuchen, ist es wichtig, experimentelle Hinweise auf charakteristische Merkmale in ihrer elektronischen Struktur zu erkennen. Mit Hilfe von Röntgen-Photoemissionsspektroskopie (XPS) und computergestützter Chemie wurde herausgefunden, dass $Ag_{0,98}Pd_{0,02}$ SAA eine Elektronenstruktur ähnlich zu einem freien Atom aufweist. Eine solche einzigartige elektronische Struktur wurde zuvor von *Schlögl* und Mitarbeitern für AgCu SAAs berichtet. Freie atomähnliche elektronische Strukturen sind gekennzeichnet durch schmale d-Valenzzustände des gelösten Metalls (Pd, Cu), die (entweder räumlich oder energetisch) von den d-Zuständen des Wirtsmetalls getrennt sind. Die gemessenen Photoemissionsspektren wurden mit dem berechneten Photoemissionssignal (PES) eines freien Pd-Atoms in der Gasphase verglichen, mit sehr guter Übereinstimmung, was darauf hindeutet, dass die Pd4d-Zustände in der Legierung eine sehr schwache Hybridisierung mit ihrer Umgebung aufweisen und daher elektronisch isoliert sind. In dieser Arbeit sollen Struktur-Funktions-Korrelationen untersucht werden, d.h. es soll festgestellt werden, welchen Einfluss die einzigartige elektronische Struktur auf die Adsorbat-Bindung und die Katalyse hat. Konkret wurden die chemischen Eigenschaften von $Ag_{0,98}Pd_{0,02}$ SAA-Modellkatalysatoren untersucht.

AgPd-Legierungen sind für ihre überlegene Performance bei der industriell relevanten Semi-Hydrierung von Acetylen bekannt. Daher wurde untersucht, ob es sich lohnt, die Verdünnung von Pd im inerten Ag-Wirt auf das Einzelatom-Niveau zu treiben. Die Ergebnisse zeigen, dass im Falle eines ungeträgerten $Ag_{0,98}Pd_{0,02}$-Modellkatalysators die Platzisolierung von Pd und die damit verbundenen elektronischen Strukturänderungen zu einer Katalysatordeaktivierung führen. Aus dieser Beobachtung wurde gefolgert, dass die aktiven,

isolierten Pd-Atome die koordinierenden Atome zur Teilnahme an der Reaktion benötigen, um die Reaktion von aktiviertem H_2 mit Acetylen zu ermöglichen.

Neben den einzigartigen Eigenschaften von Pd bei reduktiven Reaktionen (z.B. Hydrierungen), hat Pd auch die höchste katalytische Aktivität aller Metalle bei oxidativen Reaktionen. In dieser Arbeit wurde untersucht, wie sich die chemische Reaktivität von AgPd SAA in oxidativen Atmosphären von der seines Bestandteils Pd unterscheidet. Zu diesem Zweck wurden elektronische Strukturänderungen einer $Ag_{0,98}Pd_{0,02}$ SAA-Folie in 1 mbar O_2 mittels *in situ* XPS untersucht und mit der elektronischen Struktur einer Pd-Folie unter den gleichen Bedingungen verglichen. Pd in $Ag_{0,98}Pd_{0,02}$ oxidiert teilweise und bildet ein einzigartiges, metastabiles PdO_x-Oberflächenoxid. Mit Hilfe eines Peakflächen-Modellierungsverfahrens konnte vorhergesagt werden, dass PdO_x auf $Ag_{0,98}Pd_{0,02}$ als dünne, möglicherweise einschichtige, PdO_x-Inseln vorliegt. Im Vergleich zu dem auf Pd-Folie gebildeten PdO ist das auf AgPd gebildete PdO_x thermodynamisch wesentlich instabiler. Dieses Verhalten ist eine interessante Eigenschaft von Oxiden, welche sich auf verdünnten Legierungen bilden, und möglicherweise in oxidativen katalytischen Reaktionen wie der Methanoxidation genutzt werden könnten.

Zum Verständnis der dynamischen Vorgänge an der Probenoberfläche in reaktiven Atmosphären, z. B. bei der Oxidationsstudie von Pd und AgPd, ist eine ausreichende Temperaturauflösung, Zeitauflösung, Energieauflösung und Signalqualität erforderlich. Dies kann erreicht werden, indem alle relevanten, hochaufgelösten XPS-Spektren wiederholt in schneller Folge gemessen werden, wobei die Temperatur mit einer langsamen, konstanten Rate erhöht wird. Dieses Verfahren erzeugt große Datensätze mit guter Temperaturauflösung, was vorteilhaft ist, um Korrelationen zwischen z. B. Metalloxid-Spezies und den entsprechenden O1s-Spezies zu identifizieren. Die Peak-Fitting-Modelle mussten über Tausende von Spektren hinweg intern konsistent sein. Daher wurden Datenanalysestrategien entwickelt, um diese großen und oft schwierigen Datensätze in angemessener Zeit mit hoher Zuverlässigkeit des Peak-Fitting-Modells zu bearbeiten. Im Rahmen dieses Promotionsprojekts wurden verschiedene statistische Datenanalysemethoden wie Hauptkomponentenanalyse, Pearson-Korrelationen und Korrelogramme angewandt, um Korrelationen in Temperaturreihen von *in situ* XPS-Datensätzen zu finden und um das Peak-Fitting-Modell iterativ anzupassen. Die Methoden werden in dieser Arbeit am Beispiel von Pd in oxidativer Umgebung angewendet und diskutiert.

Weiterhin beschäftigt sich diese Arbeit mit der Frage, welche Anforderungen an eine Probe gestellt werden, deren Struktur-Funktions-Korrelationen mittels *operando* XPS gemessen werden sollen. *Operando* bedeutet, dass Gasphasenänderungen gleichzeitig mit der elektronischen Struktur detektiert werden. Zu diesem Zweck wurde ein sogenannter "Sniffer QMS" (Quadrupol-Massenspektrometer) entwickelt und in das XPS-Setup eingebaut. Die Gasdetektion der Produkte erfordert Katalysatoren mit einer hohen aktiven Oberfläche. AgCu SAAs mit hoher Oberfläche wurden durch Abscheidung von AgCu-Nanopartikeln, die durch gepulste Laserablation in Flüssigkeiten hergestellt wurden, auf einen porösen Silberträger synthetisiert. Bei der anschließenden *operando*-Analyse konnte unter Epoxidations-Bedingungen das Totaloxidationsprodukt CO_2 gemessen werden, was den erfolgreichen Betrieb der selbst entwickelten "Sniffer QMS" verifiziert.

1. Introduction

Industrial production without heterogeneous catalyst is unimaginable, but there are still many challenges associated with their use, like insufficient selectivity towards the desired products, or catalyst deactivation due to poisoning or coking.[2] To address those challenges, and in the spirit of Max Planck's famous quote: "The application must be preceded by recognition", rational catalyst design is preferred over the traditional "trial and error" path to identify structure-function correlations.[4] However, this task is difficult, due to the high structural and compositional complexity, and the enormous parameter space in reaction conditions.

In computational chemistry the complexity is reduced by finding key descriptors, such as the adsorption energy, to predict the catalytic properties of a range of possible elements and compositions. Finding the right descriptor leads to the concepts of Brønsted-Evans-Polanyi relations and scaling relationships. Brønsted-Evans-Polanyi relations are linear correlations between the activation energy and reaction energy.[5,6] On the one hand, such scaling relations are very helpful in finding trends, and when there is just one main descriptor one can arrive to a simple volcano plot, where the maximum refers to the optimum catalyst. The optimum catalyst binds to the adsorbates with an intermediate bond strength, which is not too weak in order to activate the reactants, yet not too strong so that the products can desorb without the formation of undesired byproducts.[7] On the other hand, scaling relations limit the performance of conventional catalysts, since one cannot have both a weak binding energy to intermediates and a low activation barrier.

Experimentally, the catalyst complexity can be decreased by reducing the number of active sites to well-defined, isolated metal sites in a host metal matrix. Thereby a so-called single-atom alloy (SAA) is formed.[2] Besides reducing the complexity, this approach has the advantage that less of the expensive active metal (Pt, Pd, Rh) is needed. Those highly active elements have positive aggregation energies with group 10 (Cu, Ag, Au) elements, whereby the dilute metal prefers to be bound to the host metal and is therefore present as isolated atoms.[4] SAAs are reported to have several promising properties, such as the prevention of coking,[8,9] the spillover of adsorbates to different active sites,[10] and improved catalytic selectivity compared to the bulk active metal.[2] Those properties might have their origin in the potential of SAA to escape from the above mentioned linear scaling relationships, because different reaction steps may occur at different sites in a bifunctional SAA.[2] An example for bifunctionality is the PdCu SAA in the hydrogenation of acetylene, where the Pd sites are responsible for the H_2 dissociation, after which the H atoms spill over to the Cu host.[11,12] Other synergistic effects (ensemble, ligand and strain effects) do also affect the catalytic performance of SAAs. In general, ligand and strain effects alter the electronic structure of the active sites (e.g. due to alloying or doping), whereas ensemble effects refer to changes in the geometric structure (e.g. surface segregation or different surface facets).[13] The synergistic effects are closely related to each other, since changes in the geometry also influence the electronic structure. Electronic structure changes can be detected by surface sensitive spectroscopy such as XPS.

A couple of years ago our group discovered that the $Ag_{0.995}Cu_{0.005}$ alloy, where Cu atoms are isolated in the Ag host, has a unique electronic structure, where the d-valence states of Cu and Ag are well separated from each other.[3] Thereby the Cu3d state is so narrow that it is more similar to the electronic state of a Cu atom in gas phase than to bulk Cu. Hence, this alloy deviates from the mean-field behavior of transition metal alloys, where there is typically just a shift in the d-band center of the broad, hybridized d-states. Such free-atom-like electronic structure of the minority element (here Cu) has the potential to combine the advantages of homogeneous- and heterogeneous catalysis.[3] A DFT-based study of free-atom-like SAA, revealed that there is no linear correlation between the H_2 dissociation energy, which is the rate determining step in hydrogenation reactions and the valence d-band center.[14] This is a promising result, since it suggest, that free-atom-like SAA are capable to break linear scaling relationships. The d-band center is a common descriptor for the activity of transition metals according to the d-band model of Hammer and Nørskov (see chapter 1.1.1).[15]

Such theoretical screening studies are very helpful, since they can expose some interesting catalytic materials, but generally they do not provide complete information about the stability of the material (e.g. alloy), and catalyst deactivation processes under reactive conditions. To understand the transformation processes of the catalyst under reaction conditions, *operando* and *in situ* surface science techniques are crucial.[4] XPS, which is conventionally a UHV technique, has been further developed in recent years to be able to operate under near ambient pressure (NAP) conditions (mbar range). NAP-XPS enables one to detect electronic structure changes (e.g. oxidation state, surface segregation, charge transfer) of heterogeneous catalyst under reaction atmospheres (see chapter 2.1). *Operando* compared to *in situ* means, that changes in the gas phase are detected simultaneously with the spectroscopic signal from XPS, for instance, by using gas chromatography (GC) or mass spectrometry (MS).[4] *Operando* XPS is therefore very powerful in measuring structure-function correlations, and was applied in this work. By using this method, the structure-function correlation of AgCu SAA was studied. To reach this goal, high surface area AgCu SAA needed to be developed, and our *in situ* XPS needed to be adapted to be able to detect gas phase changes (chapter 3.1).

AgPd SAAs have also been predicted to exhibit a free-atom-like electronic structure, and are the main systems to be investigated in this thesis. Therefore, polycrystalline AgPd SAAs were synthesized, and their electronic structure was investigated in detail by XPS, before the performance in selective acetylene hydrogenation was studied (chapter 3.2). Additionally, surface structure changes of AgPd SAA in an oxidative environment were studied, whereby the catalytic properties of Pd in the SAA with pure Pd (chapter 3.3) were compared. During those studies it was searched for ways to improve the peak fitting model and data analysis procedure of the large datasets, which were generated when measuring electronic structure changes by temperature/time-series *in situ* XPS. For this approach, statistical analysis methods were applied to analyze correlations of e.g. metal core-level species and their corresponding oxide species. In chapter 3.4 those statistical methods are explained and applied on the example of Pd in oxidative environment.

1.1 Rational catalyst design

The properties of a heterogeneous catalyst surface depend on its structure and composition on the atomic scale.[16,17] Therefore, the key goal of catalyst characterization is to investigate the surface structure, ideally atom by atom under operative conditions. Figure 1-1 represents how complex supported catalyst surfaces are, and how many aspects play a role in the investigation of catalytic processes.[18]

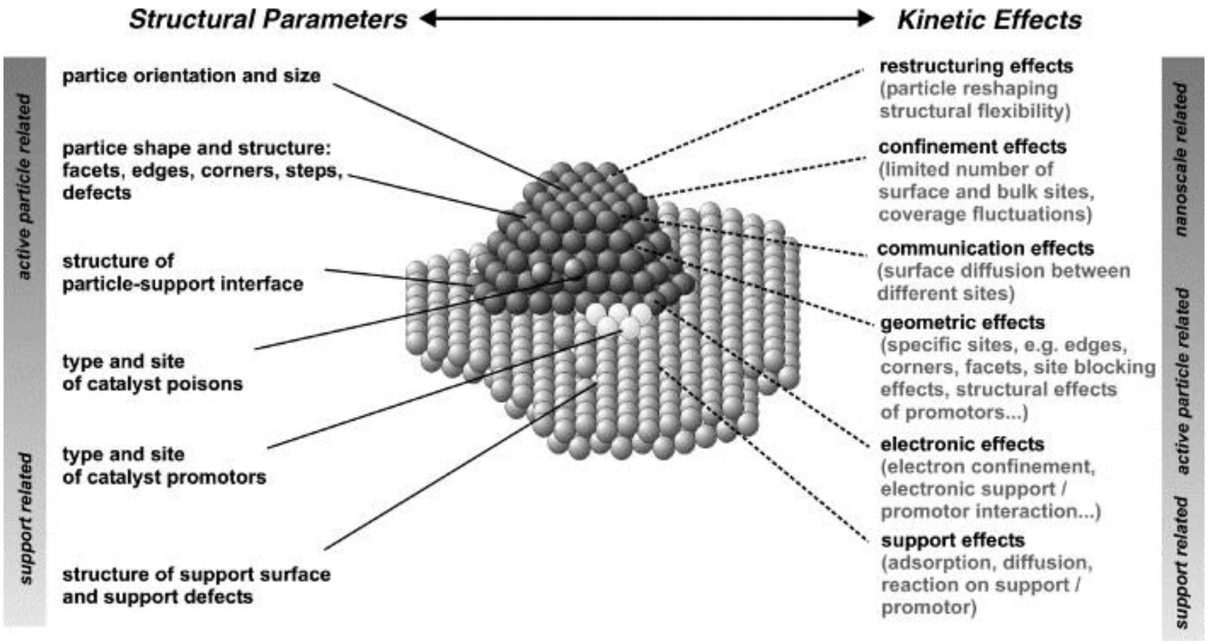

Figure 1-1: Scheme representing the many different aspects which needs to be considered and studied to understand the catalytic properties of a supported catalyst.[18] Copyright © 2005 Elsevier B.V.

As real industrial catalysts are extremely complex systems, theory, surface science and catalysis research under “real” catalytic conditions have to work hand-in-hand to achieve the goal of rational catalyst design.

1.1.1 The theory approach

Theoretical- and computational chemists have developed descriptor-type approaches to screen the catalytic properties of groups of elements and alloys. This approach is based on the Brønsted-Evans-Polanyi (BEP) relationships, which identifies linear correlations between the activation energy and the reaction energy in a chemical process.[5,6,19] The reaction energy can be related to the adsorption energy of key intermediates on the catalyst surface by scaling relationships.[20] Additionally, Nørskov and coworkers showed with their d-band model, that the adsorption energy is correlated to the d-band center of the catalyst.[7,15,21–23] Hence many catalytic processes of transition metals can be broken down to one key descriptor; the d-band center. In the following paragraphs, the theory behind the d-band model is explained in more detail.

When an adsorbate moves closer to a transition metal surface, the adsorbate’s valence electrons interact with those of the transition metal. These interactions can be considered in two steps (Figure 1-2).[15] First, the interaction with the extended metal s-states, which always result in attractive interactions and can be considered as constant for different transition metals. Consequently, the strength of the bond mainly depends on the second interaction – the adsorbates bonding states with the narrow metal d-states. This coupling results in a splitting into bonding and antibonding states (Figure 1-2). The bond strength depends on the degree of filling of the antibonding states. If the antibonding states are empty the bond is stronger, and this again depends on the d-band center (ε_d) of the catalyst relative to the Fermi level.[7,15,21–23]

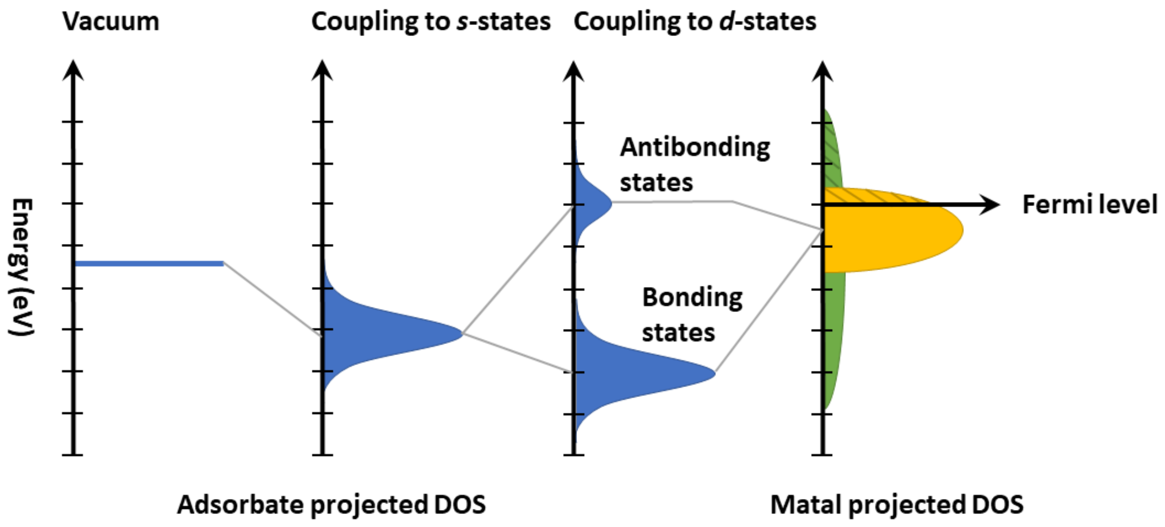

Figure 1-2: Projected DOS for the bond formation of an adsorbate at a transition metal surface. In the first step the sharp atomic states of the vacuum level couple with the s-states of the transition metal resulting in a down-shift and bond broadening. In the second step the bonding states interact with the narrow d-band of the transition metal, forming covalent bonding and antibonding states. As emptier the antibonding states are, which depends on the d-band center of the transition metal and accordingly higher in energy relative to the Fermi level, as stronger is the adsorbate-surface bond.

When going to the right in the periodic table, the metals' d-bands becomes more filled and therefore the d-band is positioned below the Fermi level (see values in Figure 1-3). Upon binding of the adsorbate with low-lying d-states, the resulting antibonding states will be occupied and below the Fermi level, hence the interaction is repulsive. The opposite is true when going to the left in the periodic table, where the antibonding states are empty and above the Fermi level. As a result, the metal-adsorbate interactions are attractive. When going down in the periodic table from the 3d to the 5d elements the bond strength also decreases (Figure 1-3). This has to do with the increasing Pauli repulsion, and consequently increasing adsorbate-metal d-coupling matrix element V_{ad}^2. When the adsorbate approaches the surface the electronic states overlap, the Pauli principle forces them to be perpendicular to each other, which costs energy and leads to so-called Pauli repulsion or orthogonalization energy. The 5d metals have more extended d-states as the 3d metals therefore the 5d metals have a larger V_{ad}^2.[15,21]

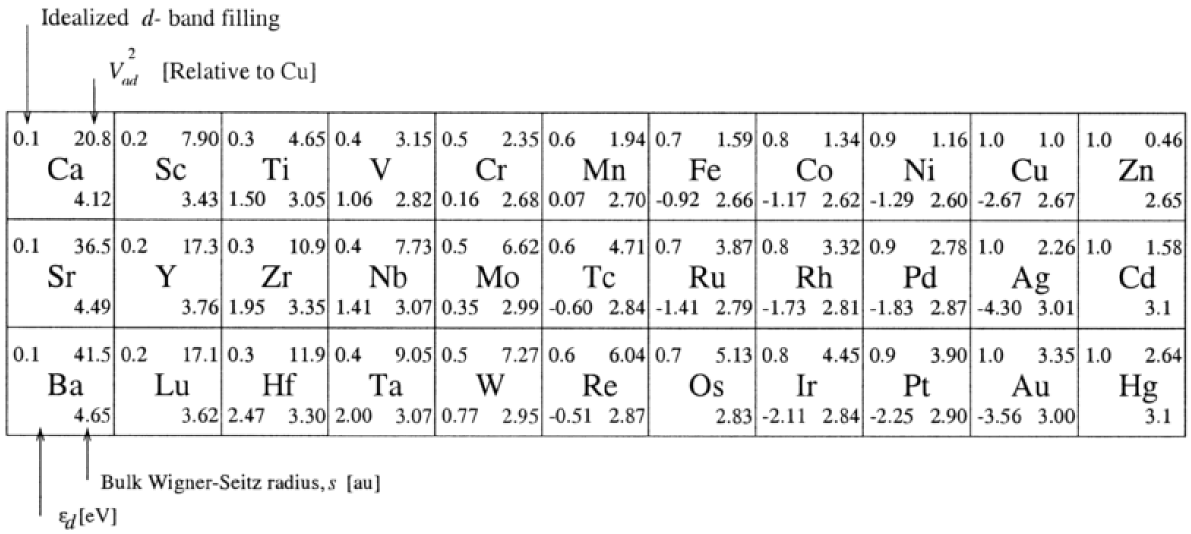

0.1 20.8 Ca 4.12	0.2 7.90 Sc 3.43	0.3 4.65 Ti 1.50 3.05	0.4 3.15 V 1.06 2.82	0.5 2.35 Cr 0.16 2.68	0.6 1.94 Mn 0.07 2.70	0.7 1.59 Fe -0.92 2.66	0.8 1.34 Co -1.17 2.62	0.9 1.16 Ni -1.29 2.60	1.0 1.0 Cu -2.67 2.67	1.0 0.46 Zn 2.65
0.1 36.5 Sr 4.49	0.2 17.3 Y 3.76	0.3 10.9 Zr 1.95 3.35	0.4 7.73 Nb 1.41 3.07	0.5 6.62 Mo 0.35 2.99	0.6 4.71 Tc -0.60 2.84	0.7 3.87 Ru -1.41 2.79	0.8 3.32 Rh -1.73 2.81	0.9 2.78 Pd -1.83 2.87	1.0 2.26 Ag -4.30 3.01	1.0 1.58 Cd 3.1
0.1 41.5 Ba 4.65	0.2 17.1 Lu 3.62	0.3 11.9 Hf 2.47 3.30	0.4 9.05 Ta 2.00 3.07	0.5 7.27 W 0.77 2.95	0.6 6.04 Re -0.51 2.87	0.7 5.13 Os 2.83	0.8 4.45 Ir -2.11 2.84	0.9 3.90 Pt -2.25 2.90	1.0 3.35 Au -3.56 3.00	1.0 2.64 Hg 3.1

Figure 1-3: Extract of the periodic table showing the 3d, 4d, and 5d transition metals. In the upper left corner, the idealized d-band fillings are shown. In the upper right corner there is the adsorbate-metal d-coupling matrix element V_{ad}^2 relative to Cu. V_{ad}^2 increases when going down in the periodic table and decreases when going to the right because of the increasing nuclear charge. In the lower left corner the d-band position relative to the Fermi level is shown and in the lower right corner the Bulk Wigner-Seitz radius.[21] Copyright © 2000 Published by Elsevier Inc.

The here-mentioned descriptor-based methods are based on DFT studies, and enable one to estimate bond strength and apply the Sabatier principle from 1920.[24] The Sabatier principle expresses the catalytic performance in so called volcano plots, where the maximum determines the optimum catalyst, which binds to the adsorbates with an intermediate bond strength, which is not too weak to activate the reactants, yet not so strong that the products become trapped on the surface or form undesired byproducts.

Such DFT-based studies are useful in identifying reactivity-trends and promising catalyst candidates, which should, in subsequent research, be investigated by experimentalists. The scaling relations also illustrate limitations in catalyst performance, since, due to the mean field behavior of surfaces, an active site cannot have both low activation energies and weak binding strength of adsorbates at the same time.[19] Hence, researchers are searching for catalysts, which are able to escape from linear scaling relationships of pure transition metals. One class of promising candidates are single-atom alloys (see chapter 3.4).[25]

1.1.2 The surface science approach

Model catalysts are often used to reduce complexity of real catalysts in order to study individual fundamental properties of active surfaces. This surface science approach towards rational catalyst design has numerous techniques available for examining active surfaces. Those techniques include various microscopic, spectroscopic and diffraction methods. Each of these techniques can only provide a few pieces of the total desired information, and a combination of different methods is necessary to obtain a complete picture of an active material. The physical restrictions of the various methods often require that a sample's physical form be adapted to the method.

A general difficulty with many surface-sensitive methods is that they require low-energy electrons to measure the desired properties. Since electrons have a small mean free path at elevated pressures, such experiments need to be performed in high vacuum conditions. This restriction means that it is, in many cases, not yet possible to measure the desired properties of a catalyst in its “real” operating conditions. Instead “model” conditions are used where the catalyst is brought as close as possible to the real operating conditions, and the influences of the conditions are characterized. However, when changing from model to realistic conditions, mostly significant changes to the sample morphology and chemistry occur.[26]

Hence, one of the goals towards rational catalyst design is to “bridge” the gap between ultra-high vacuum and high-pressure conditions (“pressure gap”), together with the gap between investigating single crystal model catalyst and real catalyst (“material gap”). Those gaps can be minimized by *operando* surface science techniques.

1.1.3 *Operando* surface science

In order to bridge the pressure gap, extensive effort has been invested into the design of new instruments, and into the development of existing techniques to be able to analyze catalysts under industrially relevant conditions, which means elevated temperatures and (near) atmospheric pressures.[4] Such *in situ* techniques can be further developed to *operando* methods, if functional properties (such as product formation) is detected at the same time (by GC or MS).

There are various approaches to develop conventional surface science techniques into *in situ* techniques. One approach is to separate the high-pressure region from the high-vacuum region by a differential pumping system. This is e.g. applied for TEM, low-energy ion scattering, and XPS (see chapter 2.1), which enables them to operate in the mbar regime.[4] Another approach is to build micro- or nanoreactors, where the small high pressure volume is separated from the high vacuum region by a ultrathin, inert material. Examples for this approach are X-ray microscopy (e.g. ESCAmicroscopy beamline at Elettra-Sincrotrone) and *in situ* TEM.[4]

By a combination of (i) different *in situ* and *operando* surface science techniques, (ii) the testing of real catalysts in reactors and (iii) a previous theoretical screening of promising catalyst candidates, great progress towards rational catalyst design is already- and will be achieved in future.

1.2 Definitions of different kinds of alloy catalysts

Alloying is a very common tool to tune the chemical properties of metal surfaces, since alloys can have catalytic properties which are significantly different from those of the constituent elements.[27,28] The general definition is that alloys are metallic systems containing two or more components.

But what is exactly meant when taking about solid solutions, intermetallics or surface alloys? V. Ponec differentiated between them based on the sign and size of the mixing enthalpy.[28] A mixing energy around zero results in an statistical alloy, where the atoms of the constituents are randomly distributed. When the enthalpy is small and negative, mixing is favored, and one obtains a solid solution. They are characterized by consisting of a single phase, and metallic bonds between the constituents, whereby they do not change their crystal structure. If the enthalpy of mixing is large and negative, an intermetallic compound is obtained. Intermetallics exhibit covalent bonds, thereby forming an ordered crystal structure different from the crystal structure of the constituents. They are often highly stable, and no phase segregation occurs under reactive atmosphere. When the mixing enthalpy is small and positive, the alloy can either exist as single-phase or multiple phases, depending on the conditions (atmosphere, temperature), they often tend to form clusters, have metallics bonds and keep the crystal structure of the constituents. Finally, in the case of surface alloys, the mixing enthalpy is highly positive, leading to limited solubility. As a consequence, only the surface of the matrix element (primary metal) can be alloyed.

1.3 Single-atom alloys (SAA)

Sykes and coworkers first introduced the term single-atom alloy (SAA) in 2012, and defined them by two key characteristics:[29] Firstly, the more active metal in the bimetallic system is present at the surface of the host metal at very low concentrations. Second, the dilute active metal is thermodynamically more stable when surrounded by the host metal. Consequently, *in a SAA, small amounts of one metal are atomically dispersed in the surface of a different metal, revealing a bimetallic single-site heterogeneous catalyst*.[2] The isolated, reactive dopant is thereby a group 8,9 or 10 metal (most often (Pt, Pd, Rh)) in a host metal matrix of group 11 elements (Cu, Ag, Au). It is important to mention, that alloys with small amounts of transition metal dopants were not novel in 2012, and were already intensively investigated in the 1960's to 1980's, where the influence of the impurity/dopant metal on the valence-band structure was intensively analyzed.[30–32] However, the interest of such impurity alloys in catalysis application gained first considerable attention during the last decade (Figure 1-4).[2]

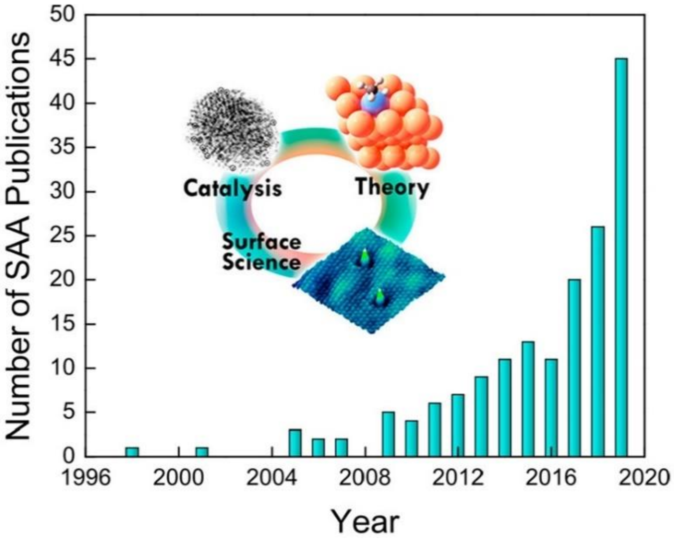

Figure 1-4: Increase of publications in the SAA field during the last decade. The circle symbolizes the synergy between surface science, theory and catalysis in investigating SAA catalysts.[2] Copyright © 2020 American Chemical Society.

Single-atom alloys are not to be confused with single-atom catalysts (SACs). SAC is more the collective title for heterogeneous catalyst's following the "active-site isolation" approach. In this approach, the advantages of homogeneous catalysis, where only one type of active metal exists, and heterogeneous catalysis are combined. SAAs, as well as supported single atoms and intermetallics, are hence subgroups of SACs (Figure 1-5). In comparison to SAAs, intermetallics consist of far more "active" metal atoms in order to form a single-phase ordered structure (e.g. GaPd, $GaPd_2$) and have covalent bonds between the atoms.[33,34]

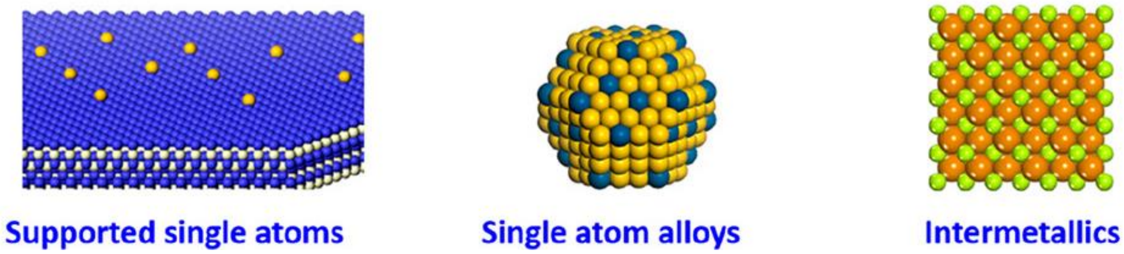

Figure 1-5: Illustration of different kinds of single atom catalysts (SACs).[125] Copyright © 2020 American Chemical Society.

SAAs fall in the above-mentioned alloy category of solid solutions, since slightly negative mixing enthalpies are required to avoid cluster formation of the solute metal. However, there are many more factors influencing the stability of single-atom alloys.

1.3.1 Structural stability of single-atom alloys

There are several key contributions influencing the stability and phase segregation of alloys, which are the cohesive energy, the surface energy, and the Wigner-Seitz radius.[35] In general, metals with a low cohesive energy have also a low surface energy, and stay therefore preferred at the surface. Especially in nanoparticles, the Wigner-Seitz radius has considerable impact, and the larger constituent stays preferred at the surface, which can give rise to core-shell nanoparticles.[35] Ruban at al. calculated surface segregation energies of transition metal impurities in another transition metal host.[36] The more negative the surface segregation energy is, the more likely it is that the solute/dopant stays at the surface. For most of the SAAs, the surface segregation energy of the solute is positive because of the lower surface energy of the host. Hence the solute is preferred in the bulk, which would make them inaccessible for the adsorbates in the catalytic reaction. However, depending on the reactants, adsorbate-induced surface segregation might occur, especially CO binds strongly to the active, isolated sites, and hence, keep them at the surface or even support reverse segregation.[9,37] The aggregation energy describes the stability of the dopant as isolated atoms vs cluster formation, whereby a negative aggregation energy supports cluster formation. Stamatakis and coworkers published an extensive computational study about the stability of platinum group metals (Pd, Pt, Rh, Ir and Ni) in the metal host (Cu, Ag, Au) in vacuum as well as in CO atmosphere.[9] The results show, among other things, that even if the alloy has initially a positive aggregation energy (isolated-atoms), the dopant might aggregate to clusters or islands depending on the alloy composition and CO-coverage.[9] This study demonstrates the importance of *in situ* studies, to analyze the stability of SAAs is reactive atmospheres, as the multitude of factors involved make *in situ* structures very difficult to predict, and there is not yet a general-purpose theoretical approach to predict the structure of a catalyst under reactive conditions.

1.3.2 Free-atom-like electronic structure

A couple of years ago our group (Greiner *et al.*) examined experimentally and theoretically AgCu alloys which are dilute in Cu.[3] These alloys have a unique free-atom-like electronic structure, due to very small orbital overlap between the Cu3d and Ag4d states. Figure 1-6a,b show the valence band spectrum of Ag$_{0.997}$Cu$_{0.003}$ with the unique narrow d-band of Cu between 2-3 eV. It is worth mentioning, that the spectra are measured with a photon energy of 150 eV, at this energy the sensitivity to Cu3d states is about 20 times higher than for Ag4d states, due to the Cooper minimum of Ag4d.[3] Comparing the valence band of AgCu with pure Ag (Figure 1-6a), it is obvious that the Ag4d band is almost unchanged, because there is no wave function mixing and no hybridization between the Ag4d and Cu3d states. Due to the low amount of Cu atoms in the alloy, Cu is only surrounded by Ag atoms, and on average, no Cu-Cu interactions exist. This is also a reason, why the Cu3d band is so narrow with a full-with-half-maximum (FWHW) value of 0.5 eV, whereas the Cu3d states in bulk Cu has a FWHW of 2.5 eV (Figure 1-6b). Hence, the Cu3d states are more similar to a free Cu atom in the gas phase, as to Cu metal and are therefore called free-atom-like d-states. The narrow d-band of the Cu3d states agrees with the calculated pDOS spectrum of Ag$_{31}$Cu$_{1}$ (Figure 1-6c). It can be seen that the Cu e_g and t_{2g} states are degenerate and overlap (Figure 1-6c), whereby they split in bulk Cu (Figure 1-6d). The splitting is caused by strong interactions of the Cu atoms with their coordination environment as it occurs in all metal bulk materials and therefore results in a broad d-band.

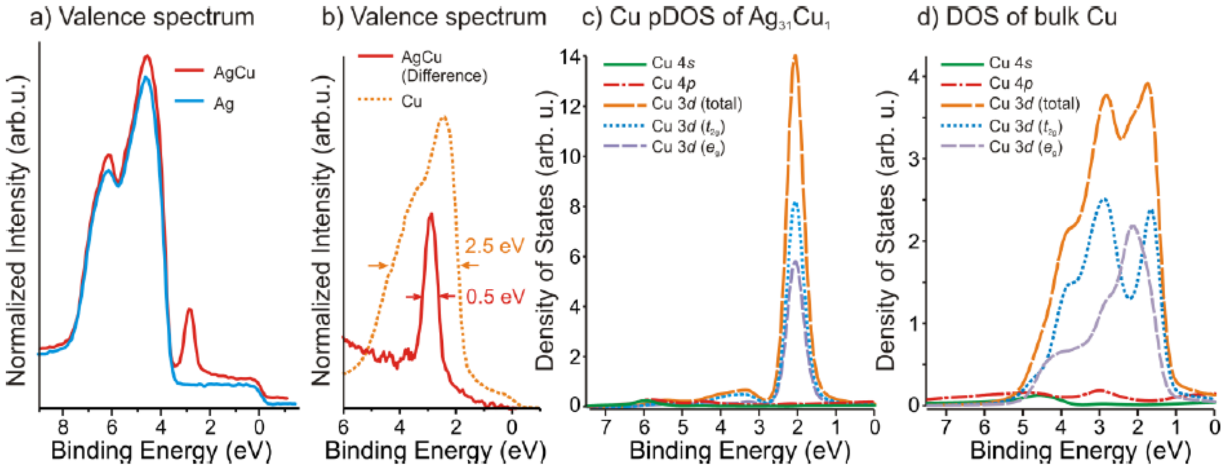

Figure 1-6: a) Photoemission valance band spectrum (hυ=150eV) of AgCu0.3% (red) and metallic Ag (blue); b) comparison of Cu bulk valence band spectrum (yellow) and the difference spectrum of AgCu and Ag (red); c) calculated Cu-based spectrum of Ag$_{31}$Cu$_{1}$ and d) calculated DOS spectrum of bulk Cu.[3] Copyright © 2018, The Author(s).

Since Cu and Ag are both coinage (group 11) metals, it is not a SAA by the definition of Sykes (see above).[2]

By theoretical screening of many different transition metals (Au, Ni, Sc, Y, Ti, Zr, Hf, V, Nb, Ta, Cr, Mo, Fe, W, Mn, Re, Co, Rh, Ir, Pd, Cd, Zn, Pt and Os) in a Ag host, the authors found that only four compositions are expected to have a similar free-atom-like electronic structures, namely AgNi, AgPd, AgMn and AgCr.[3] For this PhD project, it was decided to focus on AgPd, which is an SAA. Already in the 1960's to 1980's the valence band structure of Pd impurities (Pd concentration ≤ 5%) in a Ag host was studied by UPS, XPS and optical methods.[30–32,38,39] It was found, that the Ag4d and Pd4d states are well separated from each other, and the localized impurity states were described by the Friedel-Anderson virtual bound state model.[30,40,41] Whereas back then, fundamental understanding of the valence band structures and the magnetic properties of transition metal impurities in a Cu, Ag or Au host were the research focus, the main interest in SAAs in present days is the catalytic properties. In our group, we are especially interested in which effects the free-atom-like electronic structure of AgCu and AgPd have on adsorbate bonding and catalysis, and hence to study their structure-function correlation (Figure 1-7).

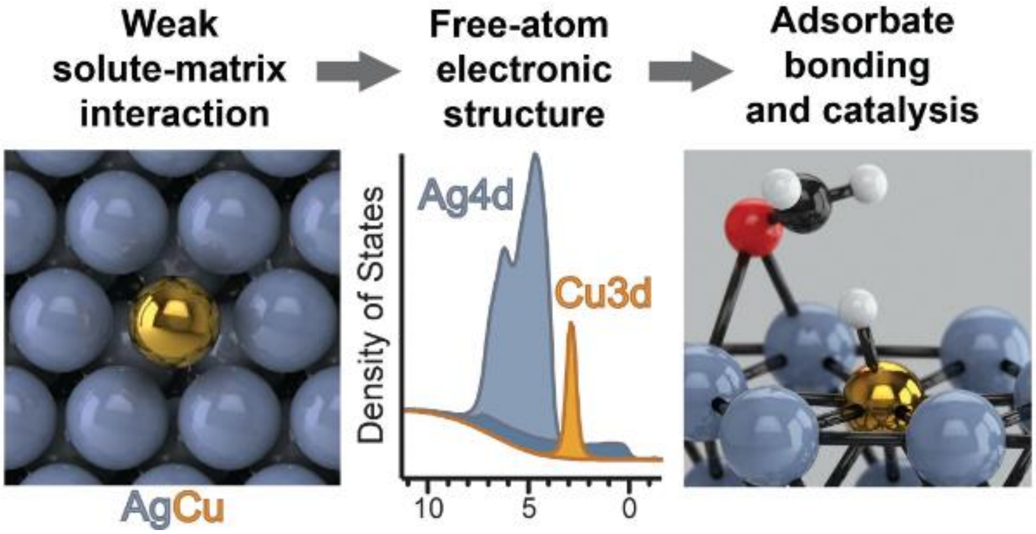

Figure 1-7: Scheme explaining the observation and motivation behind the $Ag_{0.997}Cu_{0.003}$ research. There are isolated Cu sites in an Ag matrix and because of the weak solute-matrix interactions of the two metals, their valence states are well separated from each other and the Cu states are more similar to a free Cu atom in vacuum than to the Cu metal (free-atom-like electronic structure). The next step is then to study its structure-function correlation, meaning: which effect does this unique electronic structure has on adsorbate bonding and catalysis.[3] Copyright © 2018, The Author(s).

1.3.3 Properties of single-atom alloys

The goal in new catalyst design is to overcome limitations of catalytic properties such as mean-field behaviors and scaling relationships (see chapter 1.1). Therefore, materials need to be found that exhibit unusual electronic structures – the free-atom-like electronic structure of some SAAs can make them promising candidates. The idea thereby is that the narrow, free-atom-like d-band can circumvent scaling relationships, regarding the sharpness of the d-states, small changes in the energetic position of adsorbate are imaginable to strongly influence the bonding strength. In that way, an adsorbed state of one of the intermediates or transition state could be stabilized without stabilizing others.

Thirumalai *et al.* screened the pDOS of 15 different SAAs and found that many of those compositions exhibit also a sharp, free-atom-like electronic structure of the solute near the Fermi edge.[14] Additionally they found computationally, that the d-band center of the solute is not a good descriptor for the binding strength in the dissociation of H_2. Also the work of Darby *et al*. showed, that the SAAs do not follow Brønsted-Evans-Polanyi (BEP) relationships in the H_2 dissociation (Figure 1-8).[42] The transition state adsorbed on the atop side of the Pd atoms is stronger stabilized than the final H atoms which is bound in the hollow sites between dopant and the host atoms (Figure 1-8). Those two studies give evidence that SAAs can escape from the linear scaling relationships.

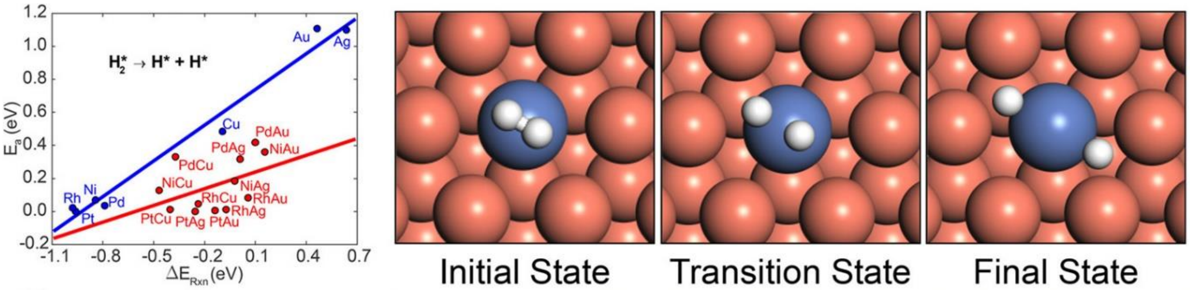

Figure 1-8: BEP relationships: activation energy as a function of reaction energy in the dissociation of H_2 for the pure metals and different SAAs. Right figures show the initial-, transition- and final state configuration of H_2 on NiCu(111).[2,42] Copyright © 2020, American Chemical Society.

For SAAs such as CuPd and CuPt, the activated H atoms can, in a subsequent step, be spilled over to the Cu host, which allows a high hydrogen uptake for hydrogenation reactions, such as the selective hydrogenation of acetylene towards ethylene (Figure 1-9).[11,25,29,43] This bifunctionality, meaning that different reactions steps occur at different sites, provide another way by which SAAs can deviate from linear scaling relations.[25,44]

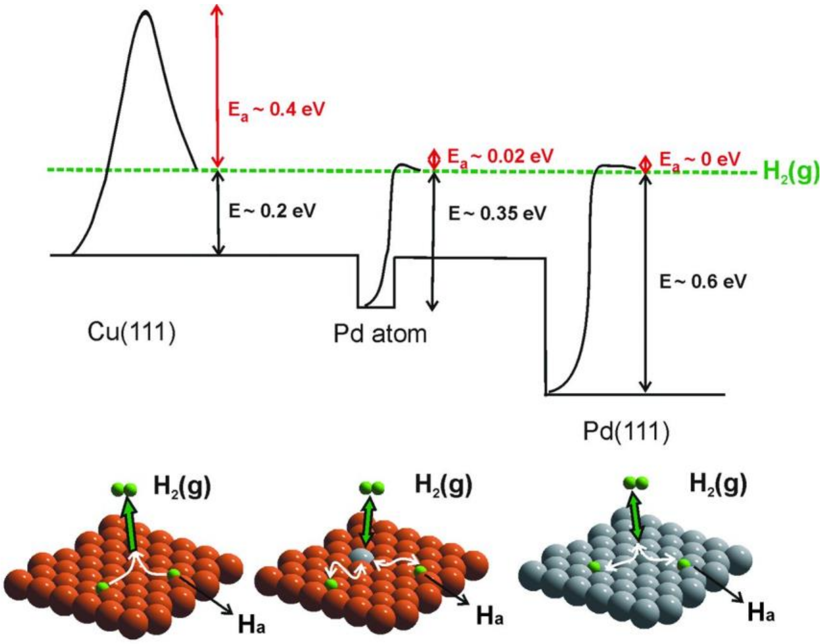

Figure 1-9: Potential energy diagram and schemes of the processes taken place at the surface. On Cu(111) the dissociation of H_2 is a highly activated process, whereas it has no barrier on a Pd(111) surface, but the H atoms are bound strongly. On a CuPd SAA H_2 activation is also almost barrierless, but the bond is less strong than for Pd(111), hence the H atoms can spillover towards Cu.[29] Copyright © 2012, American Association for the Advancement of Science.

The pure active metals Pt, Pd, Ni, Rh, Ru often suffer from low selectivity, catalyst deactivation and poisoning. Those metals, exhibit strong bonds towards carbon, and hence, promote C-C bond activation, which leads to unwanted side products, coking and poisoning by CO. The alloying with often selective host metals Cu, Ag, Au to the single-atom limit lead to ligand, ensemble and strain effects, which influences the properties of the active metal. For most SAAs the site-isolation leads to weaker bonding of the adsorbates, that could e.g. be shown by lower CO desorption temperatures.[45] As a consequence, SAAs are more resistant against coke formation,[46] and products can desorb easier, which hinders the formation of subsequent reactions to unwanted side-products. Therefore, SAAs often exhibit a higher selectivity compared to their monometallic counterparts.

2. Methods

2.1 (Near ambient pressure) XPS

XPS is extensively used in catalysis research, because it provides information about the elemental composition and the electronic structure of a solid surface.[17] This spectroscopic technique is based on the photoelectric effect.[47] An atom adsorbs an incident photon whereby a photoelectron is emitted.[17] The kinetic energy of the photoelectron is determined, from which the binding energy can be calculated. Since the binding energy for every electron of every element is specific, conclusions about the chemical composition and the electronic structure can be made. Usually XPS requires ultrahigh vacuum conditions (UHV), since the emitted photoelectrons have a short inelastic mean free path when travelling through gases at atmospheric pressure. In order to enable the electrons to reach the detector before being scattered by other gas molecules, and thereby losing energy, conventional XPS is performed in UHV.[16] This issue was solved for *in situ* NAP-XPS by a differential pumping system. Here, the first aperture (nozzle), through which the photoelectrons need to travel to reach the detector, is located directly above the sample. The short distance between sample and nozzle is the reason why some electrons can still reach the detector without being inelastically scattered. This new NAP-XPS technique offers the possibility to characterize surfaces under reaction conditions, and to determine correlations between the electronic structure and the catalytic activity of a surface by simultaneously investigating the gas phase products.[26] Since (NAP)-XPS is the main technique used during this work, the physics and the instrumental arrangement behind this method are explained in more detail in the next sections.

2.1.1 Photoelectron spectroscopy

As mentioned above, XPS as well as UPS (ultraviolet photoelectron spectroscopy) are based on the photoelectric effect. Thereby a photon of energy $h\upsilon$ is adsorbed by an atom, whereby a core level or valence electron with a specific binding energy (E_B) is emitted with kinetic energy (E_K). E_K depends on the excitation energy $h\upsilon$, E_B and the work function Φ:

$$E_K = h\upsilon - E_B - \Phi \tag{2-1}$$

The work function Φ is defined as the minimum energy required to take an electron from the Fermi level E_F to the vacuum level just outside the surface of a solid. In an XPS setup the sample and the spectrometer are both grounded, and therefore in electrical contact, so that their Fermi levels are lined up.[16]

Usually either a MgK_α (1253.6 eV) or an AlK_α (1486.6 eV) X-ray source is used. Our XPS device uses AlK_α irradiation and a monochromator, which further reduces the spectral line width to 0.3 eV, cuts out background radiation and unwanted satellites.

In XPS the photoelectron intensity is measured as a function of E_K but usually plotted versus E_B, which can be calculated using equation (2-1). On the left in Figure 2-1 the photoemission process of copper is shown, and compares the kinetic energy of photoelectrons ejected from 2p and 3p states. When a 2p electron, which has a high binding energy E_B, is ejected by the incident photon beam hυ, more energy is adsorbed by the copper atom, resulting in a lower kinetic energy E_K. Less energy is necessary to eject a 3p electron, which is why the photoelectron has a higher E_K. The right side of Figure 2-1 represents the corresponding copper XPS spectrum. Except for the s levels, all signals appear as doublets, due to spin-orbit splitting. This is especially obvious for the 2p peaks in Figure 2-1. Photoelectron signals are labelled according to the quantum numbers of the states they originate from in form of nl_j. Thereby n is the main quantum number – the shell from where the electron is ejected (n=1, 2, 3..), l is the orbital momentum (0, 1, 2, 3… indicated as s, p, d, f) and j=l+s, where s is the spin momentum ($s=\pm\frac{1}{2}$). Consequently, the two 2p peaks are labelled $2p_{1/2}$ and $2p_{3/2}$. The intensity ratio of the spin-orbit doublets can be calculated by 2j+1. Hence, the ratio for the $2p_{3/2}$ to $2p_{1/2}$ peak is 2:1.

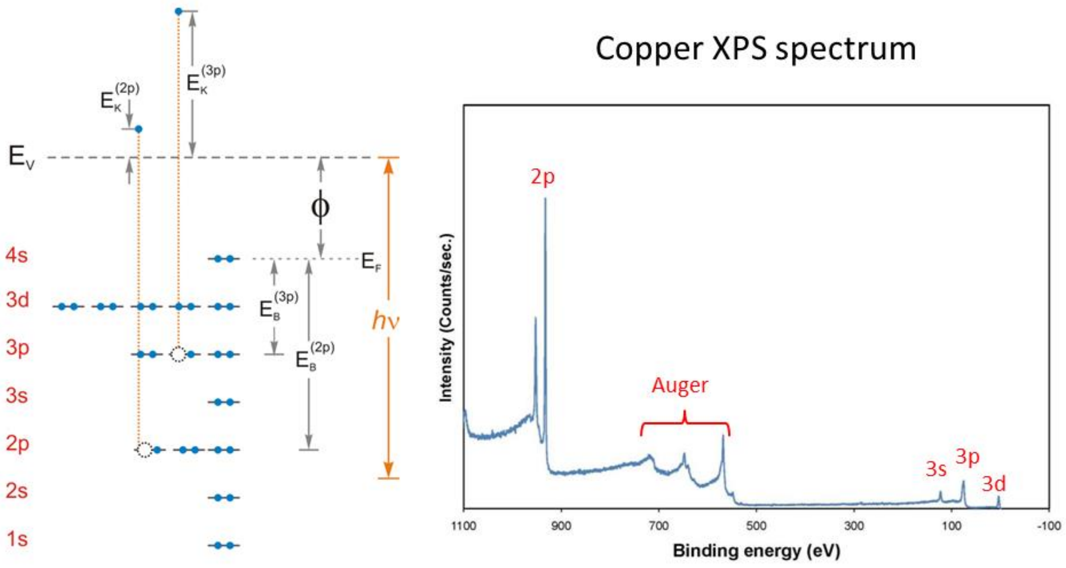

Figure 2-1: Left) photoemission process visualized using the electron configuration of copper; right) XPS survey spectrum of copper.[48] © Copyright by Mark Greiner 2012.

In addition, to the XPS signals there are Auger peaks visible in the XPS spectrum of copper. Auger electrons are a consequence of the core-hole relaxation. When a core electron is ejected by the X-ray beam, an electron from a higher state fills the hole in the core level. The energy released by this transition is adsorbed by another electron, the Auger electron, which is emitted with an element specific kinetic energy. Since the kinetic energy of the electrons is independent of the incident photon energy, equation (2-1) cannot be applied, therefore their position on the binding energy scale depends on the photon energy used for the measurement.

Setup and experimental aspects of XPS

In an XPS instrument electrons are accelerated onto an anode material (Al or Mg) whereby X-rays are released from the K-shell. A monochromator focuses the X-rays with a small energy width onto the sample. Through the photoelectric effect, photoelectrons are emitted. These electrons pass through a hemispherical analyzer and finally reach the electron multiplier or multi-channel plate detector (Figure 2-2).

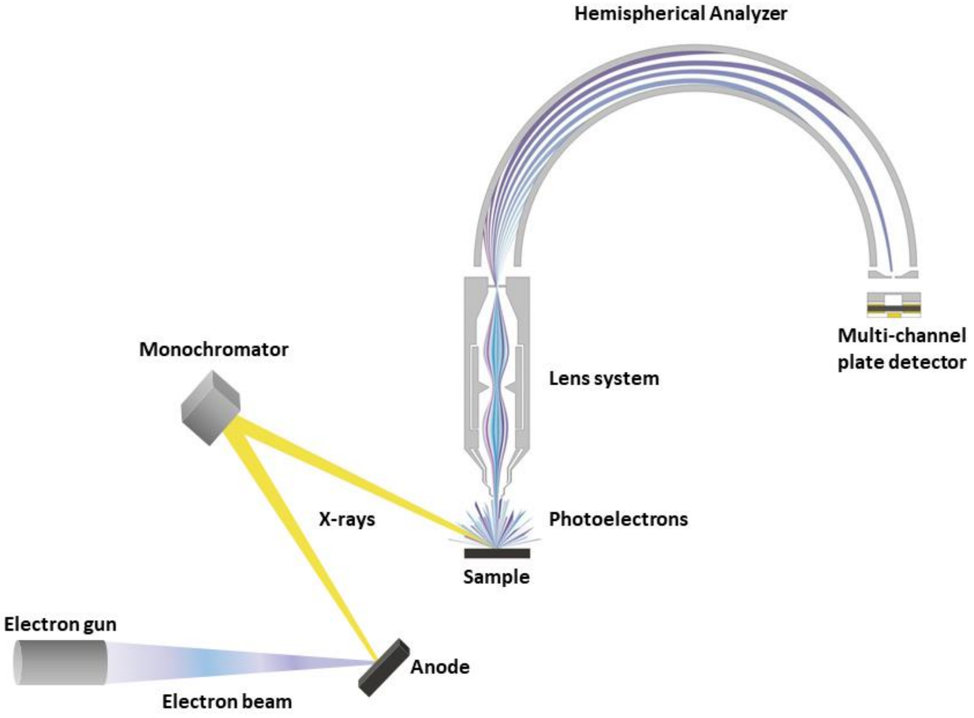

Figure 2-2: Scheme of the main components of an XPS spectrometer.

At the entrance tube of the hemispherical analyzer the electrons are retarded or accelerated to a velocity called the “pass energy” with which they travel through the analyzer. The higher the pass energy, the higher the number of electrons that reaches the detector resulting in a high intensity but also in peak broadening.

There are three factors contributing to the energy resolution (ΔE) of XPS: the line width of the X-ray source ΔE_X, broadening caused by the pass energy of the analyzer ΔE_{an} and the natural line width of the electron state, ΔE_{nat} (2-2). The line width ΔE is measured at full width at half maximum (FWHM) of the peak.

$$(\Delta E)^2 = (\Delta E_X)^2 + (\Delta E_{an})^2 + (\Delta E_{nat})^2 \qquad (2\text{-}2)$$

The monochromatized X-ray line width is about 0.3 eV. The broadening due to the analyzer does not only depend on the pass energy but also on the width of the slits between the energy filter and the actual detector, the instrumental broadening is in general Gaussian shaped, and the broadening becomes negligible with small pass energies, at the cost of intensity. The Heisenberg’s uncertainty relationship is responsible for the natural line width, and implies that states with a longer life time have narrower peaks, and a Lorentzian shape.

XPS binding energies and chemical shifts

From the binding energy of an XPS peak, chemical information, such as the oxidation state, can be obtained, because the energy level of the core electrons depends on the chemical state of the atom. A general rule-of-thumb is that the binding energy increases with increasing oxidation state, or for a fixed oxidation state with the electronegativity of the neighboring atoms. Also, charge transfer between neighboring atoms can be interpreted through the chemical shift; however, this statement is only a rule-of-thumb, and there are many situations where this trend is not observed, due to surface core-level shifts and final-state effects. To understand XPS data it is also important to consider that the data represent a state from which an electron had just left, creating a core-hole. Hence the sum of charges of the nucleus (positive) and of the core electrons (negative) is imbalanced. Consequently, relaxation and rearrangement of the remaining electrons occur, which is called core-hole screening (final state effect). The screening efficiency depends, to a great extent, on the density of states around the Fermi edge, and their kind of orbitals. For instance, when the photoionized atom (e.g. Pd) has electronegative neighbors (e.g. O) attracting the valence electrons, then the metal’s valence electrons are less efficient in screening the core-hole. As a result, the leaving photoelectron experiences stronger coulomb attraction, resulting in the electron having a lower kinetic energy and a chemical shift towards higher binding energy compared to a bulk metal (Pd) sample. Consequently, a peak position contains always both information about the initial state (prior to photoemission) and the final state. Strong final state effects lead to additional signals in the XPS spectra, called satellites.

A very important aspect in photoemission spectroscopy is that the sample has to be conductive. Nonconductive samples will become charged, since electrons leave the sample constantly, thereby creating electron-holes. Charging leads to peak shifts towards higher binding energies, since the remaining electrons are more strongly bound. Additionally, inhomogeneous charging leads to peak broadening and a lower signal-to-noise ratio. This requirement for the sample constitutes a problem in investigating real catalysts, because they usually have a nonconductive Al_2O_3 or SiO_2 support. Hence, some XPS devices have a charge neutralization system inside their XPS analysis chamber.

Surface sensitivity and peak quantification

XPS is a surface sensitive characterization method. The sampling depth is the depth from where 95% of the photoelectrons reach the detector, corresponding to 3λ. λ is the inelastic mean free path (IMFP), and depends on the kinetic energy of the photoelectrons and the specific material.[49] For an AlK_α X-ray source the sampling depth x is between 3-9 nm, and can be calculated by the following equation:

$$I = I_0 e^{-\frac{x}{\lambda cos\theta}} \tag{2-3}$$

The signal intensity I decays exponentially with the sampling depth x (when elastic scattering can be neglected). θ is hereby the take-off angle, which is the angle between the aperture of the energy analyzer and the surface normal.[50] The measured intensity of a core-level peak depends highly on the photoionization cross-section that a specific core-level species has at a distinct excitation energy. Figure 3-2 show the photoionization cross-section of copper. It can be observed that with a photon energy of 1486.6 eV (AlK_α), the Cu2p peak is most intense, whereas at energies below 400 eV the Cu3d state becomes the most intense signal.

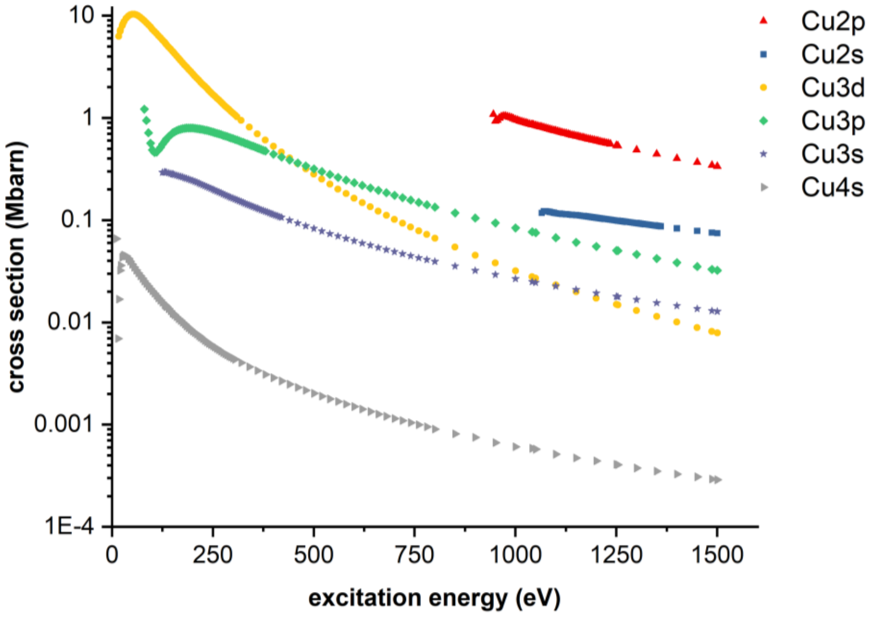

Figure 2-3: Photoionization cross-sections of copper. The data points are exported from reference tables.[51]

Quantitative analysis of XPS spectra is crucial to evaluate the elemental composition of the sample. For a homogeneous sample equation (2-4) can be applied:

$$x_i = \frac{A_i/s_i}{\sum_{j=1}^{n}(A_i/s_i)} \tag{2-4}$$

A_i is the area under the core-level peak of interest and s_i the relative sensitivity factor (RSF). The RSF is an empirical value and includes the photoionization cross-section and the IMFP for the specific element, but also spectrometer dependent factors such as the transmission function of the analyzer. Therefore, the RSF values should ideally be determined for each spectrometer and combination (anode power, pass energy etc.) individually. Since this is challenging and time consuming, reference values exist, but one needs to be aware of the fact that this approach leads to substantial errors in quantification.

Another source of error in the quantification of XPS data is the background analysis. The purpose of background algorithms is to remove all the inelastically (extrinsically) scattered photoelectrons from the data. Thereby it is often difficult to distinguish energy losses caused by final state effects or inelastic scattering. For instance, plasmon loss features, which are quantized excitations of the conduction electrons, and depend on the density of the electron gas. Those plasmons can either appear through the core-hole from the photoemission process (final-state effect) or during the transport of the photoelectrons through the solid, which is an inelastic scattering effect. Energy loss events through interactions with the valence electrons of metals with a high DOS at the Fermi edge lead to tails at the high binding energy side of the core-level signal, such asymmetric line shape can be described by the so-called Doniach-Sunjic (DS) line shape, and is characteristic for Pd. There are different standard background algorithms e.g. linear, Tougaard and Shirley, which are all approximations, and their accuracies depend on the kind of sample and the region chosen to determine the peak area.[52,53] The region can, for example, differ extremely if it was decided to analyze the entire Pd3d signal or just the Pd3d$_{5/2}$ peak, and there are no clear guidelines for what is correct and what not.[50]

It is very important to keep in mind, that the above-described quantification is only valid, when the sample is homogeneous over the entire region of interest. Figure 2-4 shows how different Cu concentrations with different nanostructures in an Au matrix lead to the same Cu2p intensities and how the signal intensity of Au4d changes when the same Au thin film thickness is located at different depths.

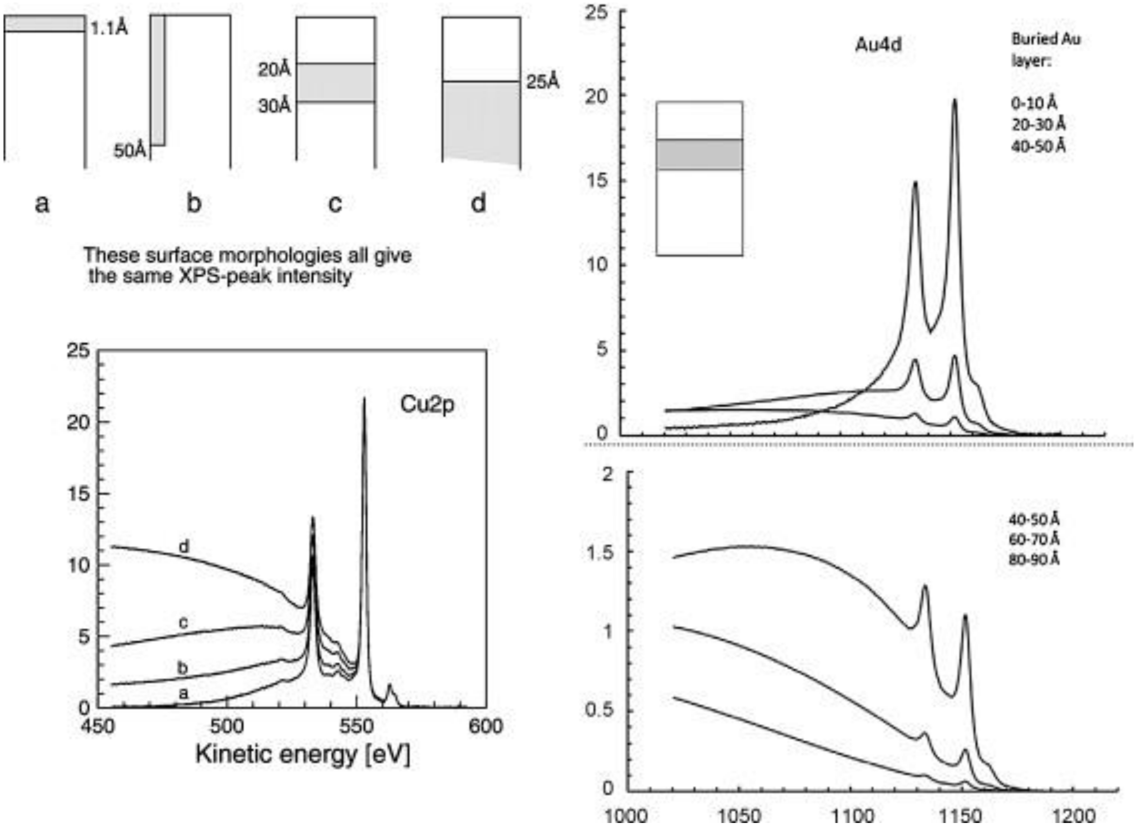

Figure 2-4: left) Different nanostructures and concentrations of Cu in an Au matrix give rise to the same Cu2p peak intensity. Right) Different Au4d intensities where a 1nm thick layer of Au is located at different depth in a material, which has a IMFP od 13.5 Å.[54] Copyright © 2009 Elsevier B.V.

Tougaard developed an advanced formalism, how the layered structures can be quantified by considering the peak area and the inelastically scattered background.[54] In chapter 3.3 it is explained in more detail how thin film XPS data can be quantified.

2.1.2 *In situ* photoelectron spectroscopy (NAP-XPS)

For several reasons XPS is conventionally performed under UHV conditions: to remove adsorbed gases from the sample, to prevent adsorption of contaminants on the sample, to avoid discharges and high voltage breakdown, and most important to increase the inelastic mean free path for photons and electrons. Unfortunately, it is impossible to study heterogeneous catalytic reactions under UHV conditions, since no high adsorbate coverage can be achieved. This problem is known as the “pressure gap”. In the 1960’s the first XPS experiment at near ambient pressures (NAP-XPS) was designed.[55] The biggest problem to overcome during the development of NAP-XPS was the short mean free path of the photoelectrons at high gas pressures. This problem was solved by separating the analysis chamber, which contains the sample, from the X-ray source and the electron analyzer, where high vacuum is required. A differentially pumped electronic lens system was developed, whereby the photoelectrons feel a high pressure for a short path before they enter the first aperture, though which the electrons travel to the analyzer.[56] The dimension of the entrance aperture, also called nozzle, has to be as close as possible to the mean free path of the photoelectrons. The optimum distance between the aperture and the sample is usually around two times the diameter of the aperture.[26] The smaller the nozzle diameter, the higher are the pressures feasible in the analysis chamber, with the cost of losing intensity. Typical nozzle diameters are between 300 µm and 1 mm.

The first NAP-XPS setups were built at synchrotron facilities, where a high intensity radiation and free choice of photon energies are available. Recently, NAP-XPS instruments were also developed for laboratory X-ray sources.[57]

Our laboratory at the Max Planck Institute for chemical energy conversion is equipped with such a NAP-XPS system. Figure 2-5a shows a picture of our NAP-XPS including the analysis chamber and the analyzer and a cut-out illustration of our Phoibos NAP-150 hemispherical analyzer from SPECS GmbH (Figure 2-5b) as well as a picture from inside of the analysis chamber during an *operando* measurement (Figure 2-5c).

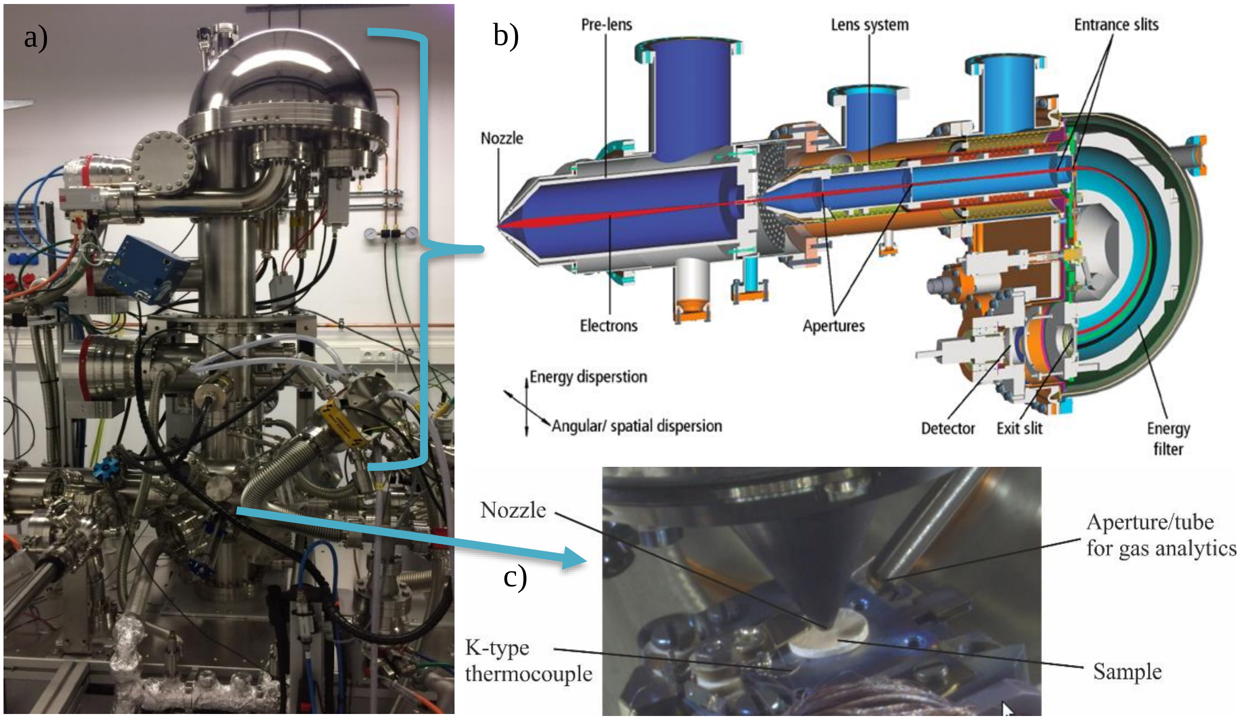

Figure 2-5: a) Picture of our NAP-XPS instrument; b) Cross-section of our Phoibos NAP hemispherical electron analyzer (Copyright © SPECS GmbH); c) Picture from the inside of the analysis chamber during an *operando* experiment.

Using a nozzle with 800 µm aperture, the electronic structure of samples under *in situ* conditions around 1-5 mbar can be investigated. Additionally, the samples can be heated by an IR laser from the rear. With the aid of mass flow controllers (MFC), the pressure of up to four reactive gases can be controlled simultaneously including liquid vapors such as methanol. During this work, gas analytics for our XPS were developed, to be able to make *operando* studies (see chapter 3.1.2). Some XPS measurement within this thesis were performed using tunable synchrotron radiation, those measurements were performed at BESSY II (UE56-2_PGM1 beamline), which is also equipped with a hemispherical analyzer from SPECS GmbH.

2.1.3 Routine XPS analysis procedures

The experimental and data analysis workflow for many datasets, collected during this PhD project, was as follows: (i) A sample was exposed to a reactive atmosphere at either constant temperature, or a varying temperature, increasing or decreasing at a constant rate. During these treatments, XPS spectra were measured. Due to the dynamic nature of the samples in reactive environments, the spectra changed with time. In order to obtain reasonable time resolution, the spectra were measured repeatedly in rapid succession. Consequently, an individual spectrum can have low signal-to-noise ratios. To improve the spectrum quality while retaining time resolution, the datasets were processed using principal component analysis (PCA). This processing routine provided 1) noise reduction and 2) an indication of how many significant changes take place in the dataset.

After noise reduction, the XPS spectra are fitted using a combination of reference spectra, as well as synthetic compounds for species of which no reference spectrum was available. The next sections deal in more detail with principal component analysis on XPS spectra and the peak fitting procedure.

2.1.3.1 Principal component analysis, for noise reduction in XPS datasets

PCA is generally applied to express the variability of a dataset in the fewest possible dimensions, so-called principal components (PC), which is done by a coordinate transformation procedure.[58–60] Hence, each PC is a linear combination of the original dimensions. In an XPS dataset, the dimensions are n variables, which are the data points (each at a certain binding energy) and m different spectra collected at different times or temperatures. The spectral information can be expressed in a matrix $X_{m\times n}$.

The main intention of using PCA in this work is to reduce the noise in the spectra, by which the acquisition time to collect the spectra can be highly reduced and therefore enables a particularly good time or temperature resolution. Thus, PCA is used for pre-processing the data prior to the peak fitting procedure. To receive good understanding of the PCA procedure, an example dataset of the sample $Ag_{0.98}Pd_{0.02}$ is evaluated. The sample was heated in oxygen from 70°C-400°C with a heating ramp of 0.3°C/min. During the heating procedure the spectra of the main component Ag3d, Pd3d, O1s but also of impurities such as S2p, Si2s, Cu2p and C1s were measured repeatedly to identify spectral correlations between the different chemical species. In total, each spectrum was measured 242 times. Figure 2-6a shows the measured spectra of Pd3d at selected temperatures. Each spectrum is measured with a step size of 0.1 eV and has therefore 140 data points. Consequently, the data matrix of Pd3d has the size $X_{242\times 140}$.

The matrix X can be remodeled by:[61]

$$X_{m\times n} = T_{m\times r} \cdot P^{T}_{r\times n} + E = \hat{X} + E \qquad (2\text{-}5)$$

The rank (r) is hereby the number of PCs necessary to explain the variability in the XPS dataset, and is also the number of linearly independent spectral features in the dataset.[60] T represents the matrix of scores, which could be expressed as a plot of the intensity vs. temperature for the relevant

PCs. P is the orthogonal loading matrix, where the rows express the weights/contribution of each datapoint to a principal component. The rows can also be called abstract factors, and bear some resemblance to spectra, except that they often contain negative values. PC1 or r_1 has thereby the highest variance, which means that it explains the original dataset in the best possible way and can be seen as the average spectrum. Due to the orthogonality of P, the r components are linearly independent. Figure 2-7 shows the first six abstract factors of the Pd3d dataset. The first abstract factor (AF1) represents the average spectrum of the 242 Pd3d spectra. AF2 is orthogonal to AF1 and has a much lower significance than AF1, which can be seen in the CPS scale. For each succeeding AF (or PC), the significance decreases until it appears to represent only Poisson noise, which could be removed from the original data. In order to analyze how many AFs are needed to express the original data in the most accurate way, without losing chemical information, the matrix product TP^T is calculated. The resulting matrix has the same shape as X and is therefore indicated as $\hat{X}$ (in equation (2-5)). Figure 2-6b,-c represent the remodeled data using two and three PCs respectively, and Figure 2-6d,-e shows the residuals E, which are obtained by subtracting the remodeled spectra form the raw data. It can be seen that the reconstructed data, when using three PCs (Figure 2-6c) is slightly noisier than the spectra when only the first two principal components are applied (Figure 2-6b). The corresponding residuals contain no chemically relevant information, and only represent noise. Hence, two principal components are sufficient to describe the raw data for this example. This means that only two linearly independent events are taken place in the Pd3d spectrum upon heating the $Ag_{0.98}Pd_{0.02}$ sample in oxygen. The remodeled data (Figure 2-6b) is further used for the peak fitting procedure.

Note, when all 242 abstract factors are used to reconstruct the raw spectra, the original data is obtained.

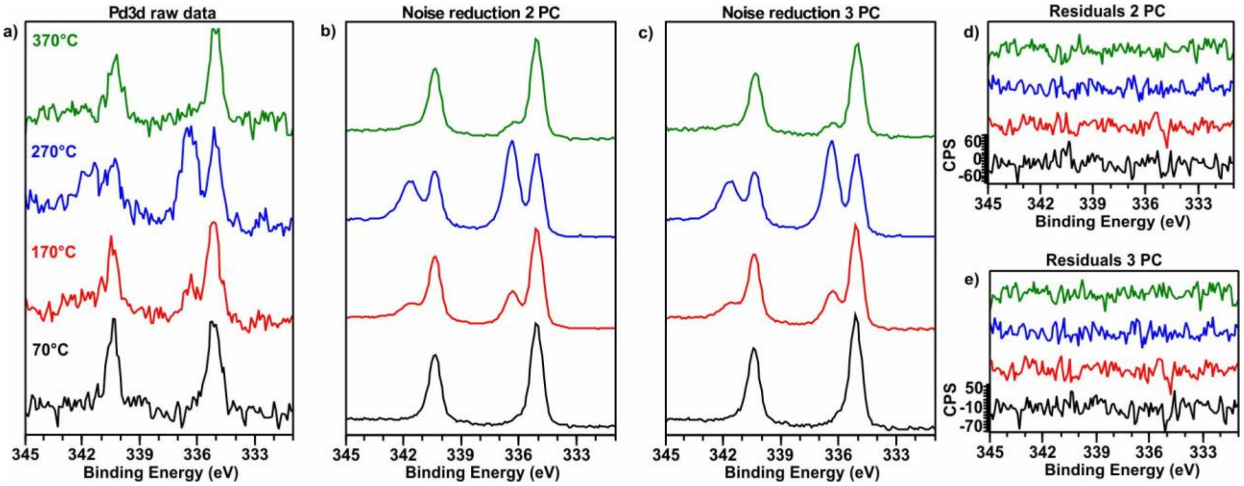

Figure 2-6: a) Raw data of Pd3d at selected temperatures, collected by heating a $Ag_{0.98}Pd_{0.02}$ sample from 70°C to 400°C in 1 mbar O_2; b) remodeled data by applying two PCs for PCA noise reduction; c) remodeled data by applying three PCs for PCA noise reduction; d) residuals E by subtracting the spectra remodeled spectra (b) from the raw data (a); e) residuals E by subtracting the spectra remodeled spectra (c) from the raw data (a).

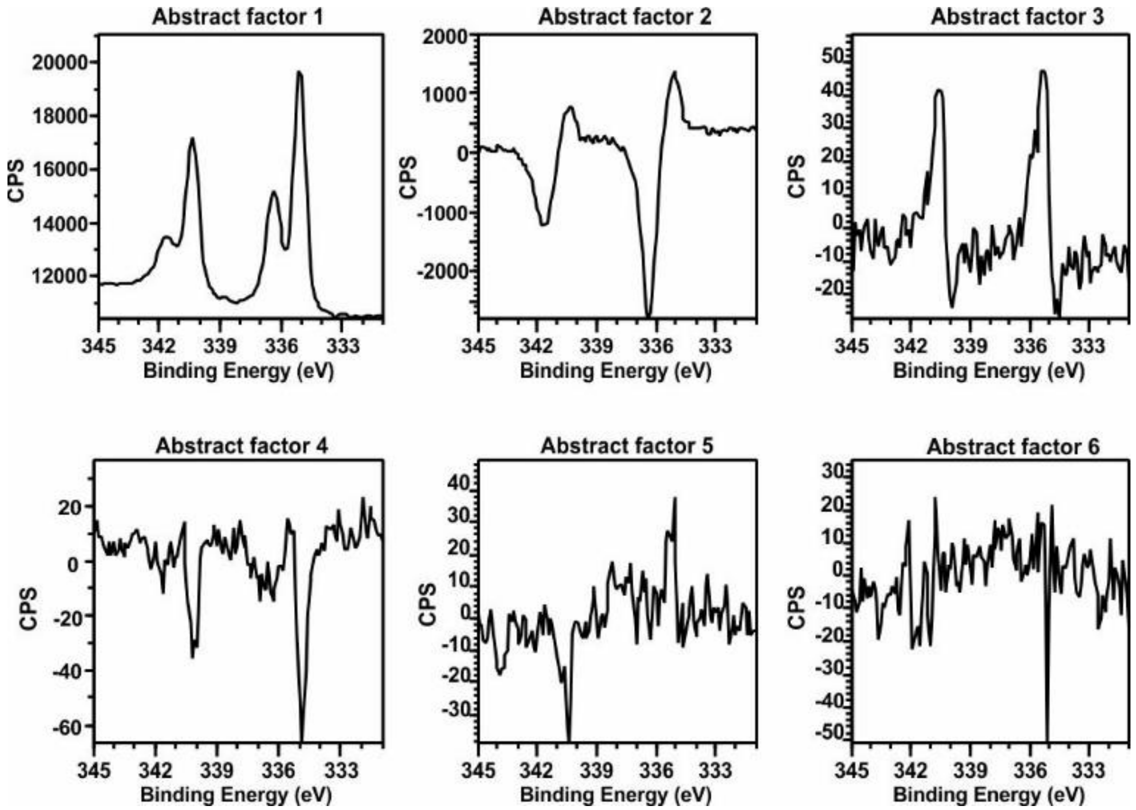

Figure 2-7: The first 6 abstract factors of P (loading matrix) when PCA is applied on the raw data. The abstract factor 1 describes the original data in the best possible way, and is the average spectrum of the original data. As higher the abstract factor, as likelier it resembles the noise in the data.

So far, the graphical results of applying PCA on XPS spectral series for noise reduction is discussed. In the following, the mathematics behind this procedure are considered in more detail and lead to the understanding of eigenvalue, eigenvector and eigenvalue decomposition.
The general eigenvalue equation is:[61]

$$Az = \lambda z \tag{2-6}$$

Where A is a squared matrix, z the eigenvector and λ the eigenvalue.
The full eigen-decomposition of the symmetric matrix A is:[61]

$$A = Z\Lambda Z^T \tag{2-7}$$

Z is thereby an orthogonal matrix and Λ a nonzero diagonal matrix.
In the example above the squared matrix is the covariance matrix C, which can be expressed as $X^T X$ (2-8):

$$C = \frac{1}{n-1}(X-\bar{X})^T(X-\bar{X}) = X^T X \tag{2-8}$$

Equation (2-7) describes the eigen-decomposition of the covariance matrix. Instead of eigen-decomposition, singular value decomposition is typically used in PCA, since it is computationally more effective (2-9).[61]

$$X_{m\times n} = U_{m\times n} \times S_{n\times n} \times V_{n\times n}^T \tag{2-9}$$

Herein, U is the score and V the loading matrix. The rows of V contain the eigenvectors (abstract factors) of the principal components as shown in Figure 2-7. S is a diagonal matrix with the non-zero singular values on its diagonal, and represent the variation of the particular principal component.
Let us now consider the covariance matrix $X^T X$ and combine equation (2-7) and (2-9) to show the relationship between the eigenvalues and the singular values. The covariance matrix is decomposed into orthogonal datasets (V), from which the maximum variation in the dataset is expressed by the abstract factors (rows in the loading matrix V) with the largest eigenvalue (S^2). Since U is an orthogonal matrix $U^T U = I$ (I=identity matrix), it can be eliminated in equation (2-10).[61]

$$X^T X = VS^T U^T USV^T = VS^2V^T = Z\Lambda Z^T \tag{2-10}$$

From this equation it can be concluded that the singular value is the square root of the eigenvalue.

PCA noise reduction is routinely applied to spectromicroscopy datasets,[62,63] where each pixel contains a noisy spectrum, hence PCA has already been implemented in the CasaXPS software.

Nevertheless, it is not yet used as standard procedure to process XPS data, although there are strong advantages of this procedure. Those advantages are a shorter data acquisition time and hence a better time or temperature resolution as well as an idea of how many linearly independent chemical processes take place at the surface. As a consequence, PCA noise reduction is particularly helpful, when the electronic structure changes during the data acquisition time, e.g. *in situ* XPS datasets, or when analyzing beam damage.

2.1.3.1.1 Peak fitting procedure

The peak fitting procedure of XPS spectra is not straightforward, which leads to erroneous application of peak fitting in parts of the literature.[64] Before starting the peak/curve fit, the binding energy calibration should be controlled. This is done by regularly instrument calibration sessions, where the peak positions, line shapes and FWHM of $Cu2p_{3/2}$, $Ag3d_{5/2}$ and $Au4f_{7/2}$ reference samples are controlled and adjusted if necessary.

After the above-described noise reduction by PCA, the XPS spectra are fitted using a combination of reference spectra, as well as synthetic compounds for species for which no reference spectra are available. In the following, an example of the peak fitting procedure of a high-resolution Pd3d spectra is shown. The Pd sample was oxidized *in situ* in 1 mbar O_2 using a temperature ramp of 1.5°C/min. The peak fitting procedure was exclusively performed using the CasaXPS software (version 2.3.23).

The Pd3d spectrum in its clean metallic state was applied as reference spectrum for the Pd metal species. For the Pd^{2+} (PdO) species the reference spectrum was conducted at 560°C in 1 mbar O_2, since at those conditions Pd^0 in fully oxidized to Pd^{2+}. The same Tougaard background algorithm was applied to both reference spectra (Figure 2-8a). Afterwards the background was subtracted and a processed copy of the data was saved. Additionally, the processed copy is assigned to a special block ID (Figure 2-8b). The line shape of the reference signal can afterwards be applied as a synthetic line shape during the peak fitting procedure.

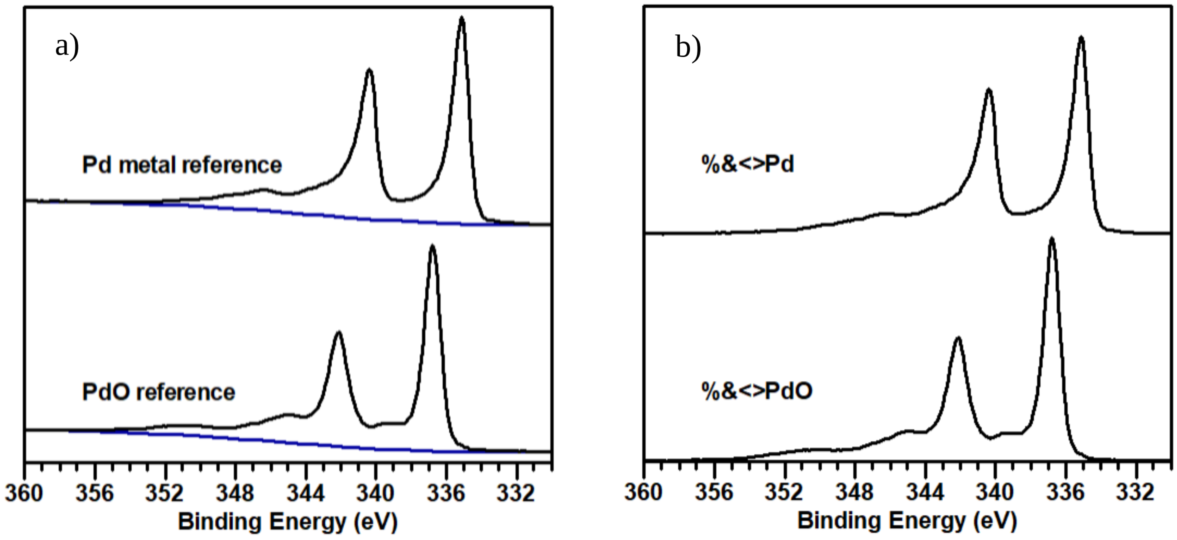

Figure 2-8: a) Pd metal and PdO reference spectra of a polycrystalline Pd foil with a U2 Tougaard background algorithm; b) The processed copy of the reference spectra after background subtraction. Those signals can be used as line shapes for the peak fitting procedure.

Figure 2-9a shows the curve fit of selected Pd3d spectra measured during the *in situ* heating of Pd in 1 mbar O_2. The same background algorithm as for the reference spectra has to be chosen in order to apply the line shape of the reference spectra. The spectra at 654°C and 374°C can be fitted by using a combination of the two reference spectra. The Pd3d spectrum at 183°C was not entirely matching with the Pd metal line shape. Hence, additional Pd3d species are supposed to be present. In order to identify additional species, the literature was screened. For the example of Pd oxidation, a Pd_5O_4 precursor species might be present, which has two Pd components Pdox(I) and Pdox(II) with a ratio of 4:1.[65–67] The two components were added using the line shape of PdO. The resulting area ratio of Pdox(I) and Pdox(II), 18800 : 5150 , was close to 4:1, and it was concluded that the Pd_5O_4 precursor is indeed present. Figure 2-9b shows the different parameters during the fitting process of a component. In this case it presents the parameters of the Pd3d signal at 183°C in 1 mbar O_2. In the row ‘line shape’, the line shapes of the reference spectra were inserted.

a)

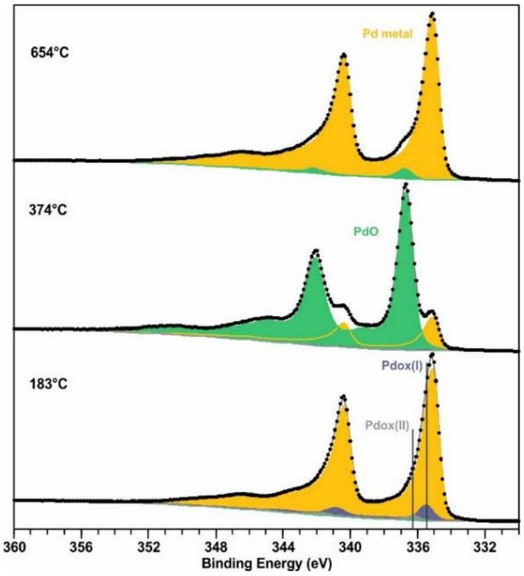

b)

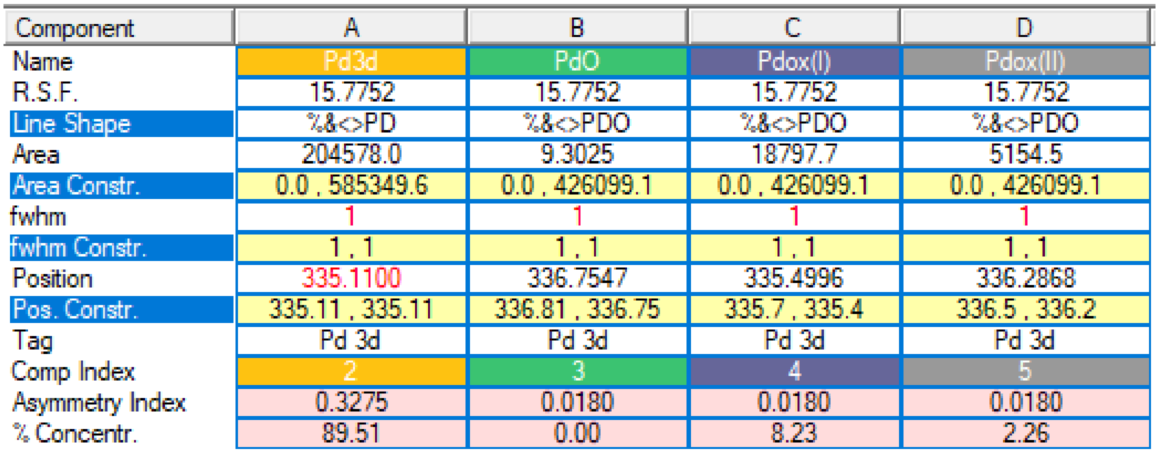

Component	A	B	C	D
Name	Pd3d	PdO	Pdox(I)	Pdox(II)
R.S.F.	15.7752	15.7752	15.7752	15.7752
Line Shape	%&<>PD	%&<>PDO	%&<>PDO	%&<>PDO
Area	204578.0	9.3025	18797.7	5154.5
Area Constr.	0.0 , 585349.6	0.0 , 426099.1	0.0 , 426099.1	0.0 , 426099.1
fwhm	1	1	1	1
fwhm Constr.	1 , 1	1 , 1	1 , 1	1 , 1
Position	335.1100	336.7547	335.4996	336.2868
Pos. Constr.	335.11 , 335.11	336.81 , 336.75	335.7 , 335.4	336.5 , 336.2
Tag	Pd 3d	Pd 3d	Pd 3d	Pd 3d
Comp Index	2	3	4	5
Asymmetry Index	0.3275	0.0180	0.0180	0.0180
% Concentr.	89.51	0.00	8.23	2.26

Figure 2-9: a) Peak fit of the Pd3d spectrum measured at different temperatures in 1 mbar O_2. Thereby the line shape of Pd metal and PdO reference spectra are used; b) The different parameters for the peak fitting procedure of a component in CasaXPS. Here for the example of Pd3d at 183°C in O_2.

The advantage of the peak fitting using the line shapes of reference spectra, which were measured under the same spectrometer settings, is that little care has to be taken of other intrinsic signals such as plasmons or satellites since they are already included. However, such reference spectra are often not available. For instance, when a reference FeO sample is loaded, it might be that the oxidation state of Fe changes under the conditions in the spectrometer, or that only the bulk consist of FeO and that different oxide species are present at the surface. As a consequence, it is uncertain what is exactly measured, and the sample becomes inappropriate as a reference. Another example are the O1s spectra, because the O1s surface species are often intermediates, that are only present at certain conditions and their chemical or physical nature is not always clear.

When no reference spectra are available, synthetic components are added. Thereby it is important to start the peak fitting with a chemically and physically meaningful picture. For this approach, the addition of constraints is helpful. The constraints can be added for the peak area, the FWHM, the peak position and the line shape (see Figure 2-9b). For instance, for a 3d signal, the constraint should be set such that the $3d_{3/2}$ and $3d_{5/2}$ peak areas have a 2:3 ratio. Many transition metals have asymmetric line shapes due to the interaction with the valence band d-electrons at the Fermi edge. On the other hand, the line shapes of O1s and C1s components are symmetric and have a Voigt shape which is a convolution of Gaussian and Lorentzian line shapes. For more detailed information about the complex peak fitting procedure the reader is referred to the literature.[64,68]

2.2 Gas analytics

In order to perform *operando* NAP-XPS studies, the gas phase in the analysis chamber, which contains the educts and products, needs to be analyzed. One big difficulty to overcome hereby is that most of the gas molecules pass through the analysis/reaction chamber without contact to the sample. Hence, the conversion is very low and the gas analyzer needs to have a high sensitivity. Gas analytics applied in this work are quadrupole mass spectrometry (QMS) and gas chromatography (GC), which both have their advantages and disadvantages.

2.2.1 Quadrupole mass spectrometry (QMS)

A mass spectrometer consists of three main components, (i) the ion source, which produces ions from the analyte, (ii) the analyzer, analyzing the ions with respect to their mass to charge (m/z) ratio and (iii) the detector.[69] For different MS applications there are many different methods for the ion source, the analyzer and the detector available. In a QMS the molecules in the gas phase are ionized by electron ionization. Hereby, the molecules are bombarded with electrons from a cathode material (filament) leading to positively charged ions, e.g. the molecular charged ion $M^{+\bullet}$, and fragments of this molecule. Each molecule has a typical fragmentation pattern which can be found in MS libraries.[69] The ions then pass the quadrupole analyzer (mass filter), which consists of four hyperbolic section rods, where a potential of type $U \pm Vcos(\omega t)$ is applied. U is the direct current potential and $Vcos(\omega t)$ the alternating radio frequency. By changing the electric field and scanning both U and V, the ions can be detected selectively, since for each pair of U and V only a certain mass to charge ratio can pass through the analyzer, whereas others will discharge at the wall of the rods.[69] The ions are detected by an electron multiplier or a Faraday-cup. The latter is a conductive metal cup, which catches the ions, thereby the ions become neutralized. The resulting current is measured and used to determine the number of ions hitting the cup.[70] In an electron multiplier detector, the incident charges (ions) become multiplied. This is done by bombarding a secondary-emissive material with the ions, which induces a secondary emission of roughly 1 to 3 electrons, which will be again multiplied and so forth. At the end the large amounts of secondary electrons will be detected by an anode metal. The electron multiplier is much more sensitive than the Faraday-cup, but the Faraday-cup can operate at higher gas phase pressures. When qualifying QMS signals, it is important to keep in mind, that different ions and fragments can have the same mass to charge ratio e.g. $N_2^{+\bullet}$ and $CO^{+\bullet}$ (both 28 amu), latter can be the molecular ion of CO or a fragment of CO_2. Overlapping signals are a big disadvantage of QMS, and knowledge about the gas phase components is crucial for correct signal assignment. Compared to GC, QMS has a better time resolution, since the gas phase can be detected continuously and the scanning through the different U and V values is relatively fast.

The QMS used for *operando* experiments with our laboratory NAP-XPS is an e-Vision 2 General Purpose Residual Gas Analyzer (RGA) from the company MKS Instruments. This device has a tungsten coated iridium filament and a maximum operating pressure of $1.3e^{-4}$ mbar. The RGA-QMS, is a relatively simple QMS with the main purpose being the detection of leaks and contaminations, which are more qualitative applications. Hence, its software is not appropriate to perform quantitative investigations. As a consequence, this RGA-QMS was mostly used for qualitative research questions, e.g. can any gas phase products be detected under certain reaction conditions? A detailed description of how the QMS was assembled on our NAP-XPS, to achieve maximum sensitivity can be found in chapter 3.1.2.

2.2.2 Gas chromatography (GC)

A chromatographic separation process always involves a “mobile-” and a “stationary” phase. In GC the mobile phase is an inert gas such as helium or nitrogen, which carries the analyte molecules through the separation column. The column is filled with the stationary phase, which is either a solid adsorbent or a liquid on an inert support. The analyte molecules interact with differing strength with the stationary phase. Hence, they elute from the column at different times, the so-called retention time, and can therefore be separated. The qualitative analysis of the components is ensued by either a thermal conductivity detector (TCD) and/or a flame ionization detector (FID).

Whereas the TCD is sensitive to all species, with the requirement that their thermal conductivities are different from the carrier gas, the FID is specialized to detect hydrocarbons, with a higher selectivity than a TCD. The TRACE 1310 GC from Thermo Scientific, which is used within this work is equipped with TCDs and FID detectors as well as a methanizer. The methanizer consists of a hydrogenating reactor which converts hydrocarbons as well as CO and CO_2 to methane, which can then afterwards be detected by an FID. In the resulting chromatogram, which is measured and analyzed by the Chromeleon^{TM} software, the peak area of the signals is proportional to the carbon number of a molecule in the analyte, which makes quantitative analysis straightforward. For GC analysis a small portion of the gas phase is injected with the carrier gas, then the molecules will be separated by the column and afterwards detected, During the separation process, the column is heated up and afterwards cooled down again to be ready for the next injection. In the experiments performed in this work each run took 15-20 min, hence the time resolution of GC is much lower than for QMS. However, the big advantage of the TRACE GC used in this work is the high selectivity of the FID, which can extend to the ppm level depending on the gas.

2.3 Electron microscopy

The goal of rational catalyst design is to analyze the structure and composition of the catalyst on the atomic scale and preferable under operating conditions. Electron microscopy (EM) and especially the recently developed *in situ* EM techniques facilitate a big contribution towards this goal. Hence, the principles behind the EM techniques will be briefly described in this chapter.

Electron microscopy is based on the interaction of the primary electron beam with the sample, which results in different detectable signals (Figure 2-10). All those signals contain valuable information about the sample and depending on the microscope the operator can chose which signals to capture. Auger electrons (AE) are the result of relaxation processes after an electron is emitted from the sample, due to their low kinetic energy, only AEs emerging from the surface can be detected. Secondary electrons (SE) and backscattered electrons (BSE) can be detected by scanning electron microscopes. For very thin samples a part of the primary electrons passes through the sample. Those transmitted electrons as well as the diffracted electrons can be detected by transmission electron microscopes (TEM). TEM has a higher spatial resolution than SEM, and advanced TEM instruments are even able to detect the energy loss of inelastically scattered electrons by electron energy loss spectroscopy (EELS).

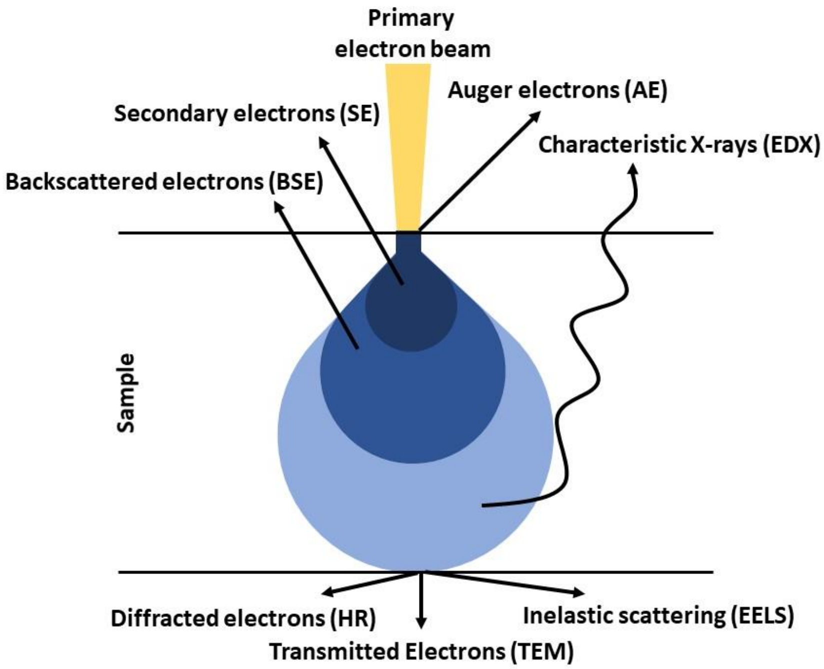

Figure 2-10: The interaction of the primary electron beam with the sample leads to several signals detectable by electron microscopy.

To identify the elemental composition, energy dispersive X-ray detectors (EDX) are often included in a SEM as well as TEM microscope. The characteristic X-rays emerge from the relaxation process. For example, when an electron is emitted from the K shell of an atom, an electron from a higher shell, e.g. L-shell, is filling the hole in the K-shell and thereby releases its excess energy as X-rays, in this case as K_α radiation. Due to the high energy of the X-rays, EDX is a bulk sensitive and not a surface sensitive method.

2.3.1 SEM

In SEM the narrow primary electron beam with an acceleration voltage between 5-30 kV is scanned over the surface and either the SE or BSE yield is detected as a function of the position of the incident electron beam. The contrast is caused by the morphology and orientation of the sample, parts of the surface which are facing the detector are brighter as parts pointing away from the detector. SEs give more surface sensitive information, because they have low kinetic energies and originate from the surface region. BSEs on the other hand originate from deeper parts of the sample and contain information about the composition. Since heavier elements scatter the electrons better than lighter elements, parts with heavier elements appear brighter.[16] SEM instruments can have maximum spatial resolutions of about 2-10 nm. Within this work, several SEM setups were used to characterize the high surface area samples (see chapter 3.1) and the foil samples (see chapter 3.2 & 3.3). In the beginning of my work there was no SEM available, hence I conducted measurements at the MPI for Iron Research and at the MPI for Carbon Research (Hitachi S-5500 in-lens field emission SEM). With the help of my dedication we got a table top SEM for our institute (Phenom Pharos Desktop SEM from Thermo Fisher), which is equipped with an SE, BSE and EDX detector.

2.3.1.1 *In situ* environmental SEM (ESEM)

In SEM there is already a solution to overcome the "pressure gap" – the so-called environmental SEM (ESEM). In this technology, secondary electrons emitted by the sample ionize the surrounding gas molecules, thereby creating a cascade of additional secondary electrons, which are then collected by the detector.[16] ESEM is widely applied for vacuum sensitive and none conductive organic samples, and only a few research groups expanded this method to do *in situ* experiments, which means that the instrument is equipped with a sample heating station, a gas supply system and eventually also with a mass spectrometer (for *operando* experiments). With this method, it is possible to monitor dynamic changes at the surface of a sample in reactive atmospheres.[71] Hence, the samples can be investigated at very similar conditions to those applied for the NAP-XPS studies. By a combination of those two techniques, electronic structure changes observed by NAP-XPS (with a poor spatial resolution) can be assigned to surface transformation processes or the other way around and thereby reveal, whether the structure changes occur locally (e.g. at specific grains) or homogeneously over the entire sample. In this work ESEM measurements in oxidative conditions of a Pd sample and the AgPd SAA sample were performed using a modified commercial ESEM (FEI Quanta 200F) at ETH in Zurich in the group of Marc Willinger. For the heat treatment, the thermocouple is spot welded on the samples with the aid of a Pt wire.

2.3.2 TEM

TEM requires thin samples (<200 nm), since the electron beam with acceleration voltages typically between 100-200 kV should penetrate through the sample. The detected electrons, which are transmitted without any scattering, produce the bright-field (BF) image. In a BF image thicker parts or particles and elements with a high atomic number appear dark, since they scatter the electrons, whereas thin parts or light elements (e.g. support material) appear bright. This is the opposite for the dark-field (DF) image, where the diffracted electrons are detected, since the heavier elements scatter the electrons stronger. Many TEM instruments can operate in the scanning (STEM) mode, which is a combination of SEM and TEM as shown in (Figure 2-11). Whereas in TEM a parallel electron beam is produced by the condenser lenses, the beam is converged to a focal point in STEM, which scans the specimen.

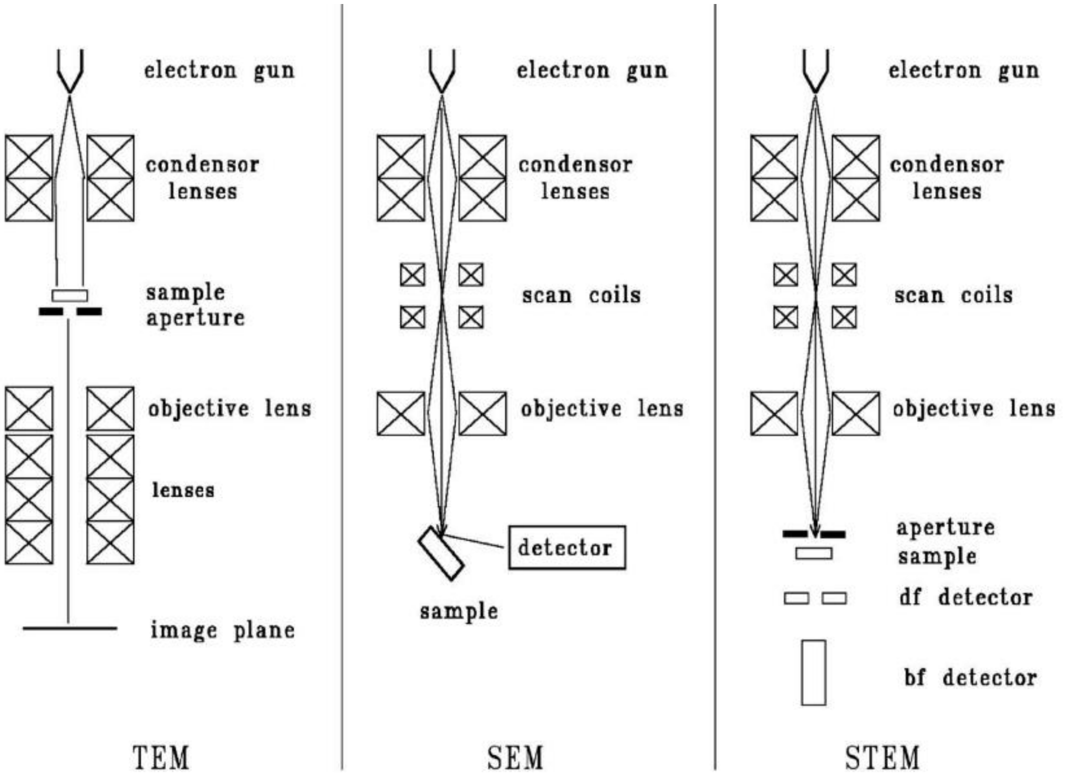

Figure 2-11: Lens configuration and set-up of TEM, SEM and STEM microscopes.[72] **Copyright © 1996 Springer Berlin Heidelberg.**

High-resolution (HR) TEM/STEM instruments enable resolution in the sub nanometer region or even atomic resolution.

Within this PhD project the particle size and composition of the AgCu nanoparticles generated by PLAL (see chapter 3.1.1) were characterized by a Hitachi HD-2700 CS-corrected STEM equipped with an EDX detector (MPI carbon research). To determine the homogeneous distribution of Pd inside the AgPd SAA, STEM measurements were performed with a Thermo Fisher Talos F200X, also equipped with an EDX detector (see chapter 3.2).

3. Results

The result part is divided into four sections. The content of chapter 3.2 and 3.3 has been published in the Journal of Chemical Physics (volume 154, 2021)[73,74] and reprinted with permission of AIP publishing. Besides, the chapters contain some additional information and studies, which are not present in the published versions. Chapter 3.1 and 3.4 contain unpublished results of the PhD project and are written close to publication style. This means that each section contains an introduction, methods, result and discussion and conclusion part (although those parts are sometimes named differently).

Since the same references are often cited in each chapter, all references are together listed at the end of this thesis.

3.1 Developing high surface area model catalyst and gas analytics for *operando* testing by NAP-XPS

The initial goal of this thesis was to develop high surface area SAA catalysts to study their structure-function correlations. This goal should be realized by measuring simultaneously in a NAP-XPS setup the electronic structure and the gas phase composition by QMS. The development of the gas analytics is discussed in more detail in chapter 3.1.2, whereas the focus in the next section is the synthesis of the high surface area catalysts.

3.1.1 Developing high surface are model catalyst

A high specific surface area of the sample is required, in order to form enough product, such that products can be detected by the gas analytic system. There are many requirements for the samples to make a structure-function correlation study feasible. (i) The avoidance of support material such as SiO_2 or Al_2O_3, since these materials are non-conductive, and therefore, charge during the photoemission process, leading to a shift and/or broadening of the XPS signals, and consequently, an electronic structure analysis would be infeasible. Additionally, a support can cause different metal-support interactions, and therefore strongly increases the complexity of the catalyst. Since it is attempted to understand fundamentally, the role of the solute’s electronic structure on the catalytic processes, e.g. the influence of the minority element in the SAA on the selectivity, it is aimed to keep the sample as simple as possible. (ii) The synthesis method should reveal a homogeneous SAA with (iii) a very high purity. The high purity is required, to ensure that changes in the catalytic performance can be referred back to the metal composition in the alloy, and since the solute (X) in the AgX alloy has a concentration of max. 2at%, the amount of impurities should be far below that concentration. Finally (iv), the synthesis should be applicable to a range of different alloy compositions e.g. AgCu, AgPd with different compositions, to be able to compare the structure-function correlation of different samples.

During this work, two different approaches for sample preparation were focused on: (1) Laser induced surface roughening in collaboration with TU Clausthal, and (2) the deposition of alloy nanoparticles on a silver support. The second approach was realized within a master thesis project (Master student: Orhun Altundas) through the collaboration with CENIDE (Chemical engineering group of Prof. Stephan Barcikowski, University Duisburg Essen). The two synthesis approaches will be discussed in more detail in the following sections.

3.1.1.1 Deposition of alloy nanoparticles on a silver support

The nanoparticles were created by pulsed laser ablation in liquids (PLAL) and subsequently deposited onto a porous silver pellet by electrophoretic deposition.

PLAL has the advantage over conventional wet-chemistry methods, that no surfactants are needed.[75–77] Surfactants, which are often hard to remove quantitatively, can alter the catalytic properties in many different ways, such as undesired chemical reactions with the educts, and should therefore be avoided when possible.[78] In short, a PLAL setup consist of a pulsed laser, focusing optics, a laser scanner and the ablation chamber, where the metal target (sample) is located within a solvent (Figure 3-1a).[79] The nanoparticles are formed by the condensation of a plasma plume which is generated, by the absorption of the photons of the incoming pulsed photon beam (laser ablation) by a bulk metal plate inside a liquid solution.[5] The particle size as well as the ablation rate thereby depends on many different parameters, such as the pulse duration, pulse energy, the focal distance, laser fluence, the pump flow rate and the solvent.[79,6] In this work a pump-through laser ablation setup was used, where the metal-target was an $Ag_{0.98}Cu_{0.02}$ foil and isopropanol was the solvent. The laser ablation parameters were chosen in a way to receive high ablation rates. Isopropanol was chosen as solvent, since Ag nanoparticles are not stable in H_2O and additional stabilizer such as sodium citrate should be avoided.[81] Due to the extreme conditions during the laser ablation process, the organic solvent (isopropanol) decomposes and forms a carbon shell around the nanoparticles, which leads to increased stabilization.[82] The formation of a graphitic-like carbon shell around the AgCu particles could be verified by Raman spectroscopy.[83] Porous silver powder pellets (Figure 3-2a) were chosen as support material for the laser ablated AgCu nanoparticles, since silver is conductive, and will therefore not charge during the XPS measurement. Additionally, silver will not strongly alter the chemical behavior of the sample, since the majority of the AgCu SAA is silver as well. The pellets are produced by filling silver powder into a pressing tool, afterwards the powder was compacted with very little weight (387 g), to retain the porosity of the very soft silver powder. The stability of the pellet is achieved by subsequent sintering in argon atmosphere.

In order to evaluate, if a performed deposition procedure of AgCu nanoparticles on the Ag support was successful, it needed to be specified, how the ideal sample should look like. Ideally the nanoparticles should be homogenously distributed on top and inside the pores of the Ag pellet. Since it was not aimed to study the catalytic performance of the Ag support, as much of the $Ag_{0.98}Cu_{0.02}$ nanoparticles as possible should be deposited. Thereby larger nanoparticles are even desired over smaller nanoparticles, which is why the AgCu colloid dispersion was centrifuged after the laser ablation process, revealing AgCu particles with a mass-based mean diameter of 135.6 nm. The particles were then re-dispersed in isopropanol, and used for the electrophoretic deposition (EPD) process.[84] The electrophoretic-deposition was performed in a self-designed (by M.Sc. Orhun Altundas) EPD chamber consisting of a vessel, where the positively charged working electrode consist of the support (Ag pellet) and the counter electrode of a silver foil. The AgCu colloid dispersion was filled inside the vessel and pumped in a circuit (Figure 3-1b). By applying a voltage between the electrodes, the negatively charged AgCu nanoparticles deposit on the support.

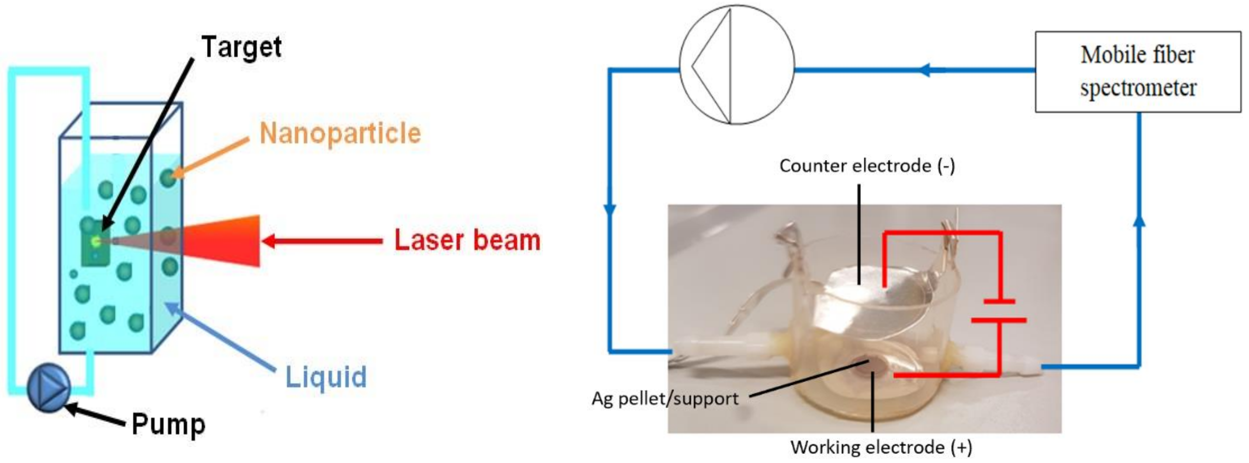

Figure 3-1: a) Setup of a flow-through laser ablation process[79] Copyright © 2017, American Chemical Society; b) Self designed EPD chamber consisting of the working electrode on which the Ag pellet is positioned, the counter electrode made out of silver and a pump, which pumps the colloid dispersion in a closed circuit. Additionally, a mobile fiber UV/Vis spectrometer is attached, which detects the changes in the colloid concentration to monitor the deposition process.

In Figure 3-2b it can be observed that the whole Ag pellet is densely covered with the AgCu particles, from which the sample received a black color. At 30000 times magnification it can be obtained that the AgCu nanoparticles agglomerated to form larger particles (Figure 3-2c). The optimization of the EPD process was time-consuming, as parameters such as the deposition time, the electric field strength, the pumping speed, and the particle concentration, as well as particle size, needed to be optimized.[84] Nonetheless the process remains sensitive to minor process-parameter changes making sample reproduction challenging. The sample described here is later studied in ethylene oxidation conditions in the NAP-XPS (see section 3.1.3.2).

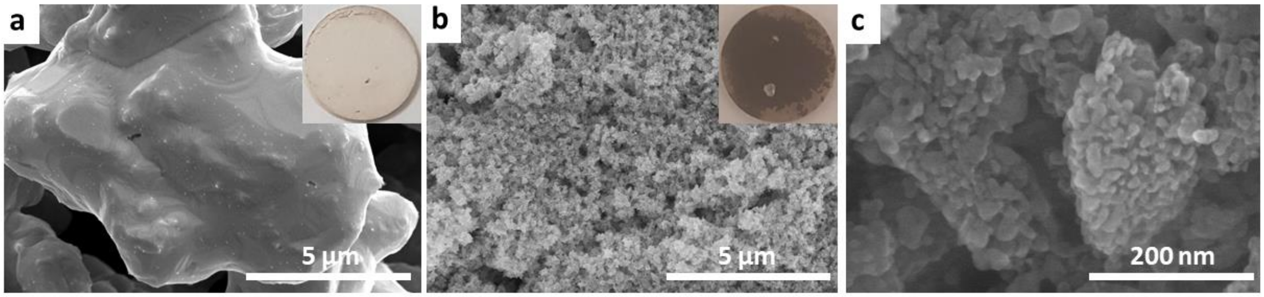

Figure 3-2: Optical microscope and SEM images (magnification 20000x) of a) the Ag substrate pellet; b) the Ag substrate completely covered with $Ag_{0.98}Cu_{0.02}$ particles, which rendered the surface black; c) SEM image at 30000x magnification, which shows small particles at the surface of larger AgCu particles. The sample has a diameter of 8 mm.

3.1.1.1.1 Experimental parameters

The $Ag_{0.98}Cu_{0.02}$ (Princeton Scientific, 99.999% purity) colloid was produced by PLAL (for 30 min) in 17 mL isopropanol using a flow-through chamber. The Nd:YAG laser from the company Ekspla had a wavelength of 1064 nm, a repetition rate of 100 kHz and a pulse duration of 10 ps. The working distance between sample and laser scanner was 111.7 mm and the laser power at scanner output 8.6 W. The pulse energy is consequently 0.086 mJ. The solvent was pumped with a flow rate of 0.405 mL/s. The pulsed laser beam scanned the target in a spiral, to avoid strong ablation at just one point on the sample.

The Ag-pellets were produced by filling 100 mg of silver powder (Merck, 99.99% purity, average particles size 700 nm) into an 8 mm pressing tool, afterwards the powder was compacted with very little weight (387 g), to retain the porosity of the very soft silver powder. The stability of the pellet was achieved by subsequent sintering at 575°C for 170 min under argon.

The colloid dispersion used for the EPD process, was compiled from different laser ablation batches and afterwards centrifuged to receive larger particles. The centrifugation led to agglomeration of the AgCu particles. The agglomerated AgCu particles (mass-based mean: 135.6 nm) were then re-dispersed in isopropanol revealing a concentration of (41-46 µg/mL). This colloid dispersion was used for the EPD, thereby an electric field strength of 30 V/cm was applied for 1 h, and the colloid was continuously pumped in a closed circuit (Figure 3-1).

3.1.1.2 Laser-induced surface roughening

The process behind laser-induced surface roughening is in principle the same as for the laser ablation (see section 3.1.1.1), but this time the specimen is the metal target itself, and not the nanoparticles, which are formed through removal of material by laser ablation.

For the laser induced surface roughening an ultrashort-pulse (femtosecond) laser is required, which scans, with parameters individually set for each material, over the samples, thereby material is removed, revealing a high surface area sample. More detailed information about the process can be found in the publication of Gabler *et. al.*,[85] the same group also roughened the surface of an Ag foil for us. After the roughening it is possible to achieve an alloy material such as AgPd, AgCu SAAs by sputter coating.[85]

Figure 3-3 represents how the surface of Ag looks like after the laser roughening performed in air. The surface of Ag became oxidized, which can be recognized by the brown color of the specimen (Figure 3-3a). Additionally, it can be observed that the laser pulse scanned in lines over the sample

(Figure 3-3b). On the µm scale laser induced periodic surface structures in terms of a wave-like structures, as well as small Ag particles can be observed. Consequently, the surface area could definitely be increased by the ultrashort-pulse laser structuring procedure. Nevertheless, the surface area increase for Ag is much less than for example for Ti,[85] due to soft nature of Ag.

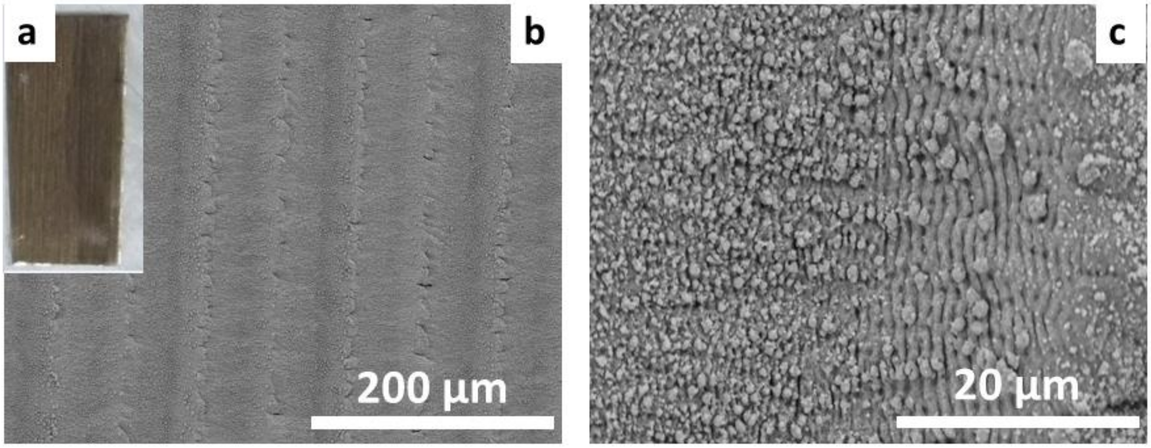

Figure 3-3: a) Macroscopic picture of the Ag foil, which has a brown color after the laser roughening procedure in air, due to oxide formation; b) SEM image (magnification x500) of the Ag foil, the line structure of the laser beam can be observed; c) SEM image (magnification x5000), there is a wave-like fine structure, as well as small particles (down to nm size) of silver at the surface.

3.1.1.2.1 Experimental parameters for the laser induced surface roughening

An Ag foil with a thickness of 0.5 mm (size: 1×1 cm) and a purity of 99.99% (from Aldrich), was used for the laser structuring.

The laser structuring was performed in air (950 mbar) as process gas by using an amplified Ti:Sa femtosecond laser system.[85]

The laser power after gray wedge P_{GW} was 2.54. The focus length was 519 mm and the spot diameter equaled to 100 µm. The distance between the different scanned lines was 60 µm and the laser polarization was parallel to the scan direction, each spot was exposed to 800 pulses.

3.1.2 Development of the gas analytics “Sniffer QMS”

To analyze structure-function correlations, the structure of the catalyst during reaction (in the NAP-XPS) has to be analyzed simultaneously to its function, which are the catalytic properties. The catalytic properties can be investigated by detecting changes in the gas phase composition (e.g. product formation), this can be done by a quadrupole mass spectrometer (QMS). The main issue to overcome is that our XPS analysis chamber has a volume of 22 L, hence the gas phase of the chamber mainly contains the educts, and the amount of product, which can be generated by the small 1 cm² sample, is very low and diluted in the gas phase of the whole chamber. As a consequence, changes in the gas phase cannot be detected when analyzing the volume of the whole chamber. To counteract this problem, the so-called Sniffer QMS was developed. The Sniffer QMS collects the gas phase directly above the sample (the distance can be adjusted by a manipulator), through a tube with a very small opening of 75 µm. Within this setup (Figure 3-4), the pumping power of the turbo pump can be adjusted by a butterfly valve, which enables operation of the QMS at its optimum pressure (1E-4 mbar). This arrangement makes the gas analysis much more sensitive towards the detection of products.

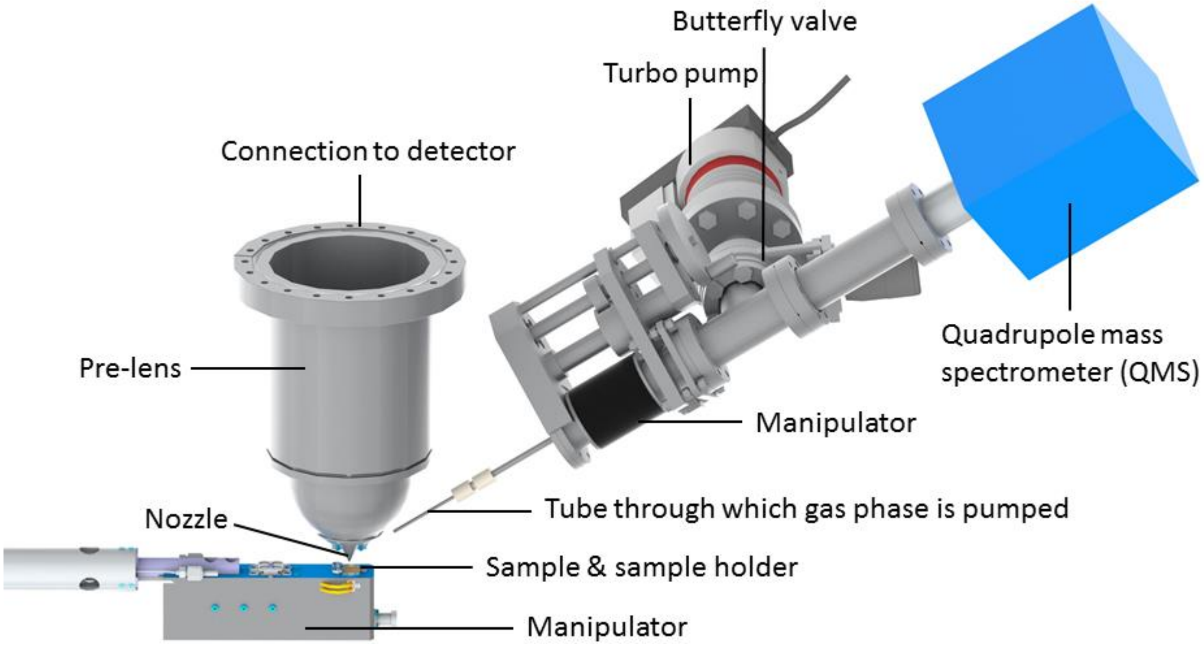

Figure 3-4: Sniffer QMS setup in the analysis chamber of the NAP-XPS.

It has to be mentioned that the Sniffer QMS, which main function from the manufacturer is qualitative residual gas analysis (see chapter 2.2.1), is not calibrated in its present state, for this reason only qualitative analysis and comparison of the catalyst performance was possible and discussed in this chapter.

3.1.3 Ethylene oxidation to test the performance of the high surface area samples and the Sniffer QMS

After designing and assembling the Sniffer QMS, its performance in catalytic reactions using the high surface area samples should be tested.

When deciding for a test reaction, many aspects needed to be considered: Firstly, many reductive reactions, such as methanol reforming, would result in activity from the sample holder, since the sample holder was composed of stainless-steel parts, whereas stainless-steel should be inactive in oxidative conditions. The benchmark oxidative reaction – CO oxidation – was also not suitable, because CO forms with nickel unwanted and poisoning carbonyls, which pollute the sample. Nickel is inside the K-type thermocouple used to control the temperature and additionally the whole inner-wall of the analysis chamber is coated with µ-metal, which consist of ~80% Ni. Therefore, experiments using CO were avoided in our NAP-XPS. Finally, it was decided to use epoxidation reaction conditions, to test the function of the Sniffer QMS and the silver as well as AgCu samples. This reaction is well suited for several reasons: first, silver is industrially used as catalyst in epoxidation,[86] so that high conversion is expected. Additionally, a lot of research has already been done to analyze the electronic structure of silver during that reaction.[87,88] Furthermore, there exists already some results about the electronic structure of $Ag_{0.995}Cu_{0.005}$ in epoxidation conditions,[89] but so far no catalytic conversion could be measured, because the specific surface area was too small.

In epoxidation conditions there are two competing reactions, the ethylene epoxidation (3-1) and the total oxidation reaction (3-2):

$$\frac{1}{2}O_2 + C_2H_4 \rightarrow C_2H_4O \tag{3-1}$$

$$3O_2 + C_2H_4 \rightarrow 2CO_2 + 2H_2O \tag{3-2}$$

3.1.3.1 Experimental procedure

The reaction was performed in an excess of oxygen (C_2H_4: O_2: 2:5) the reaction temperature was 300°C and the pressure 1 mbar. Prior to the reaction conditions, some activation steps were performed. 1) The samples were annealed in oxygen to max. 400°C to remove the carbon contamination from air and the carbon shell from laser ablation in the case of AgCu nanoparticles. 2) For the copper containing samples the copper was reduced to Cu metal by annealing in hydrogen at max. 500°C. 3) The chlorine atoms at the surface, which poison the catalyst were removed by burning them off in ethylene at 500°C (without that step no activity could be measured).

Then the reaction gases ethylene and oxygen were introduced at room temperature and maintained until a stable base pressure was reached, followed by raising the temperature to 300°C. When the gas phase pressure was stabilized, the reaction was stopped by removing the temperature, followed by waiting again for a stable gas pressure. During the whole procedure, the gas phase was detected with the Sniffer QMS. The product of both competing reactions (3-1) C_2H_4O and (3-2) CO_2 have the same mass of 44, therefore they cannot be distinguished by analyzing only the mass 44 signal. If water, with mass 18, is formed simultaneously it is a hint, that the total oxidation reaction (3-2) takes place, whereas the epoxide would have a fragmentation signal at mass 29. Additionally, the masses of the educts, 32 for oxygen, 28 for ethylene (which could also be from CO or N_2) and 27 a fragment of ethylene are detected.

When the temperature is raised to 300°C the gases expand, which leads to an increase in gas pressure. But the butterfly valve, used to maintain constant pressure in the analysis chamber, always adjusts the total pressure to 1 mbar, therefore the analysis chamber contains less gas phase molecules, and consequently a decrease in signal is detected by the QMS.

Following samples were investigated under epoxidation conditions:

1) Pressed and sintered Ag pellet (support)
2) The support (like in 1) with laser-ablated AgCu nanoparticles on the top, deposited by EPD
3) The rough Ag foil made by laser induced surface roughening

In the following the samples will be compared regarding their catalytic properties (characterized using the QMS signals) and their electronic structure, measured by XPS. Additionally, changes in the surface morphology arising through the treatment in the XPS chamber will be discussed by comparing microscopy images.

3.1.3.2 Results

The changes in the gas phase composition during ethylene oxidation conditions are studied, therefor the pressure in mbar of each mass detected by the QMS is plotted in a logarithmic scale as a function of scan number, which corresponds to time.

From the QMS data it can be observed that the Ag pellet, with and without AgCu nanoparticles, form water and most likely CO_2 under reaction conditions (Figure 3-5). Since there is no increase in the epoxide fragment with mass 29, it is assumed that mainly the total oxidation reaction takes place. Although this experiment does not show the more desired product ethylene epoxide, it is still a success, since it demonstrates that the self-designed Sniffer QMS is sensitive enough to detect product formation.

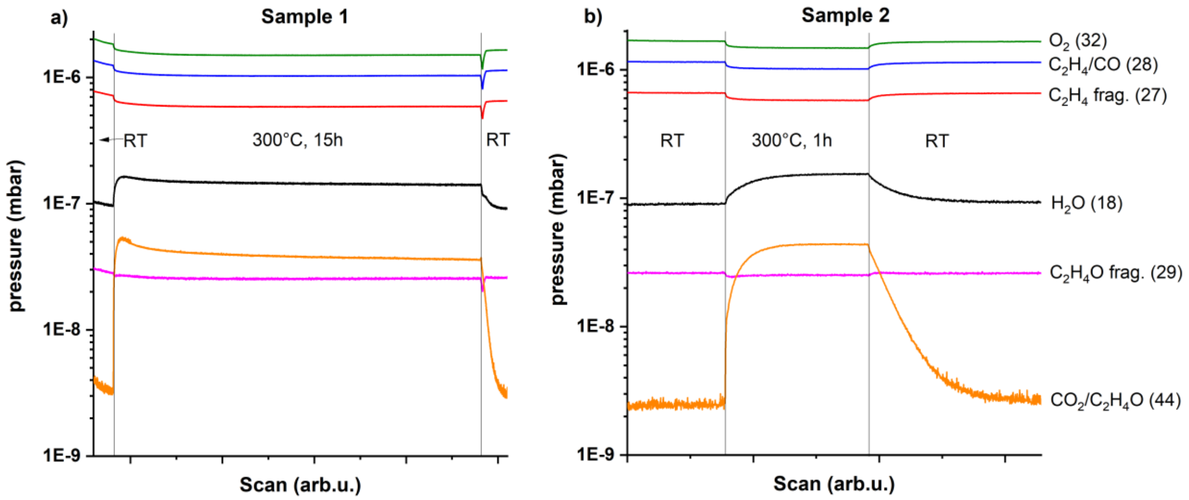

Figure 3-5: Gas phase pressure changes for a) the silver pellet and b) for Ag pellet with AgCu nanoparticles on the surface in epoxidation conditions. Mass signal 18 and 44 is increased during reaction. At the end of the reaction in a) there is a short decrease followed by again an increase in the educt signals. This is because the gas supply was accidentally switched off and then turned on again. In b) the sample was exposed to reaction conditions for only one hour, because the product pressure of mass 18 and 44 looked already stable after that time.

Instead, for the laser roughened Ag sample, no product formation could be observed, which implies that the surface area of that sample is still too low for observing gas phase changes using this QMS system.

It is of great interest to analyze, if the additional copper in the sample has a positive effect on the catalytic activity, but the differences in product formation of both samples in Figure 3-5 are too low to draw any conclusions. Additionally, the following effects can have an influence on the QMS signal intensity: 1) The surface area of both samples is not identical, since sample 2 has additional AgCu particles at the surface. Additionally, the surface area might change during the treatment. 2) The reaction temperature could be slightly different for both samples, due to issues with the temperature control when the experiment was performed; 3) Not exactly the same values can be compared since the two samples had different reaction times.

Furthermore, the sensitivity of the QMS was low towards changes in the product signals. Consequently, the sensitivity was improved for later experiments by increasing the Sniffer QMS nozzle size, so that the total pressure at the QMS reaches a value around 1E-4 mbar (here 5E-6 mbar) which is an increase of almost two orders of magnitude. Additionally, the temperature control was improved later on.

The surface morphology and composition of the Ag pellet did not change during ethylene oxidation conditions in the NAP-XPS, whereas changes of Ag rough (sample 3) and the Ag pellet with deposited AgCu particles (sample 2) could be observed (Figure 3-6). In both cases the sample changes its color from brown in the case of Ag rough (compare with Figure 3-3) and from black in the case of sample 2 (compare with Figure 3-2) towards "white" – the color of silver, as soon as the samples was heated (in oxygen). Ag_2O, which might have formed during the laser structuring procedure, decomposes at elevated temperatures, which explains the change in the color. Despite that, the sample morphology had not changed much during the treatment in the NAP-XPS chamber, since the wave-like structure and the small Ag particles at the surface are retained (Figure 3-6a).

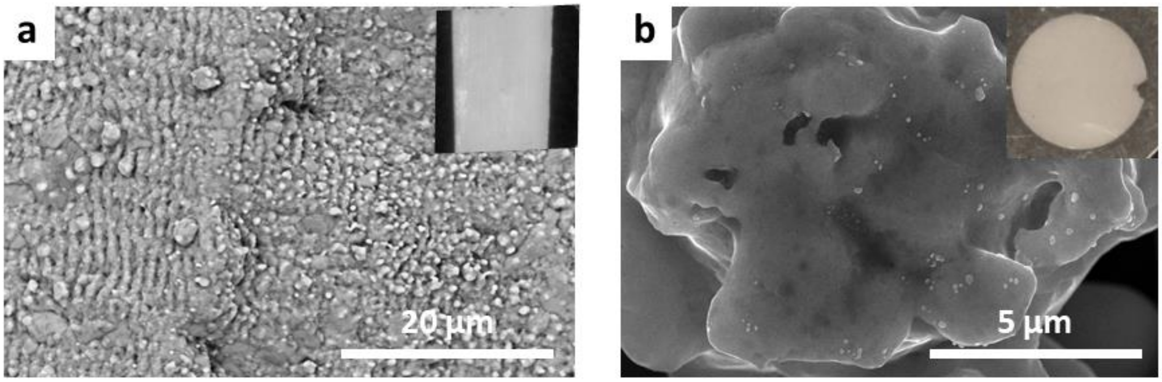

Figure 3-6: SEM and optical microscope image of a) Ag rough (sample 3) and Ag pellet with deposited AgCu particles after treatment in the NAP-XPS (oxidation, reduction, ethylene oxidation).

For the Ag pellet with deposited AgCu particles, the black color was immediately gone after the sample was heated in oxygen. A possible explanation is that the carbon shell, which surrounds the particles after laser ablation, is burned off during the oxidation treatments, and therefore the sample gains the color of Ag. This explanation could be verified by XPS, through the decrease of the C1s signal. In Figure 3-6b it can be observed that after the whole XPS study (described in 3.1.3.1), only very few particles are visible at the surface. Consequently, it was assumed that the $Ag_{0.98}Cu_{0.02}$ particles are sintered together at elevated temperatures (compare to Figure 3-2). As a consequence, the AgCu fuse with the Ag support, so that they can be barely distinguished. The sintering effect has undoubtedly a major effect on the surface area, and the Ag:Cu composition at the surface. The poor controllability of the surface area and the surface composition makes the deposition of AgX SAA nanoparticles on a silver support procedure inappropriate for structure-function correlation studies. Furthermore, the Cu2p signal intensity of sample 2 is too low to observe any electronic structure changes, since Cu has just a concentration of 2% in the AgCu particles and becomes then even more diluted by the Ag support.

3.1.4 Conclusion and outlook

There are very high requirements for an AgX (X=Pd, Cu) SAA sample, where the structure-function correlation should be studied by NAP-XPS. Those requirements are a high surface area, a high purity, the avoidance of a support and the applicability of the synthesis route to a range of compositions in order to make them comparable. It was tried to fulfill those requirements by applying two different synthesis routes. First, the deposition of $Ag_{0.98}Cu_{0.02}$ particles on an Ag support pellet, which is done by pulsed laser ablation in liquids (PLAL) and subsequent deposition of the (nano)particles on the Ag pellet by electrophoretic deposition (EPD). The second synthesis route was laser induced surface roughening. The samples of both routes were then tested in ethylene oxidation conditions in the NAP-XPS chamber, whereby the goal of that study was less to study the structure-function correlation but more to test, if the new designed Sniffer QMS is sensitive enough to detect product formation. The catalytic testing revealed that in the case of the Ag pellet, with and without deposited AgCu SAA particles, the total oxidation reaction of ethylene took place, because CO_2 and H_2O formation could be detected by the QMS. This was a highly positive result, since it showed that the new developed Sniffer QMS is sensitive enough to measure reaction products. In the case of the laser structured Ag foil, no products could be detected, from which it was concluded that the surface area of the laser-structured sample was still too low. Due to the insufficient surface area, and because there was, at that moment, no working sputter coater available to promote the Ag surface with Cu or Pd atoms to form a SAA, it was decided to stop this laser structuring project. The study of the Ag pellet with deposited AgCu SAA particles by SEM revealed, that the surface had changed drastically when the sample was exposed to heat and reactive atmospheres in the NAP-XPS. Thereby the AgCu particles sintered together and united with the Ag support, this had the disadvantage that the high surface area was lost and that the composition of Ag:Cu changed. Those two observations did not only lead to an incomparability of different samples but also to an impossible detection of electronic structure changes of the Cu atoms during reaction. Latter is because Cu became increasingly diluted by Ag and at a certain point Cu could not be detected anymore by our NAP-XPS. As a consequence, without being able to detect electronic structure changes, the study of structure-function correlations becomes impossible. Therefore, it was decided to change the focus of this project to study less complex AgPd SAA foils by NAP-XPS. Before understanding the catalytic performance of AgPd SAAs it is crucial to first investigate their electronic structure, especially of the valence band states (see chapter 3.2). Afterwards, changes in the electronic structure and surface segregation in oxidizing and reducing atmosphere were studied. Followed by testing its catalytic performance in a dehydrogenation reaction (reducing environment) and in methane oxidation (oxidizing environment) (see chapter 3.2 and 3.3). During those studies, different ways to improve the data analysis of the large datasets obtained when studying electronic structure changes in temperature/time-series *in situ* XPS data, were found and applied (see chapter 3.4).

3.2 Isolated Pd Atoms in a silver matrix: Spectroscopic and chemical properties

Caroline Hartwig[*], Kevin Schweinar[#], Travis E. Jones[§], Sebastian Beeg[*], Franz-Philipp Schmidt[*§], Robert Schlögl[*§], Mark Greiner[*]

[*] Max Planck Institute for Chemical Energy Conversion, Mülheim an der Ruhr, Germany.

[#] Max-Planck-Institut für Eisenforschung GmbH, Düsseldorf, Germany.

[§] Fritz Haber Institute of the Max Planck Society, Berlin, Germany.

3.2.1 Abstract

Over the past decade, single-atom alloys (SAAs) have been a lively topic of research due to their potential for achieving novel catalytic properties and circumventing some known limitations of heterogeneous catalysts, such as scaling relationships. In researching SAAs, it is important to recognize experimental evidence of peculiarities in their electronic structure. When an isolated atom is embedded in a matrix of foreign atoms, it exhibits spectroscopic signatures that reflect its surrounding chemical environment. In the present work, using photoemission spectroscopy and computational chemistry, we discuss the experimental evidence from $Ag_{0.98}Pd_{0.02}$ SAAs that show free-atom-like characteristics in its electronic structure. In particular, the broad Pd4d valence band states of bulk Pd-metal become a narrow band in the alloy. The measured photoemission spectra were compared with the calculated photoemission signal (PES) of a free Pd atom in the gas phase, with very good agreement, suggesting the Pd4d states in the alloy exhibit very weak hybridization with their surroundings and are therefore electronically isolated. Since AgPd alloys are known for their superior performance in the industrially relevant semi-hydrogenation of acetylene, we considered whether it is worthwhile to drive the dilution of Pd in the inert Ag host to the single-atom level. We conclude that, although site isolation provides beneficial electronic structure changes to the Pd centers, due to the difficulty in activating H_2 on Ag, utilizing such SAAs in acetylene semi-hydrogenation would require, either a higher Pd concentration to bring isolated sites sufficiently close together or an H_2-activating support.

3.2.2 Introduction

During the last decade single-atom alloys (SAA) have gained considerable attention in heterogeneous catalysis research,[2] especially in selective hydrogenation reactions.[14,90–96] Usually, in a SAA, a dilute active metal of group 10 (Ni, Pd, Pt) is substituted in a noble metal host of group 11 (Cu, Ag, Au).[1-11] By this approach only small amounts of the expensive active metal are used.[1]

For selective hydrogenation reactions, the ability of SAAs to dissociate H_2,[10,11,97] and the spillover of hydrides from the active single sites to host metal atoms[10,29,98] are often discussed, which both influence the catalytic selectivity compared to the bulk active metal. One selective hydrogenation reaction of considerable interest is the semi-hydrogenation of acetylene towards ethylene. Ethylene, the monomer for the large-scale industrial product polyethylene, is mainly produced by thermal cracking of hydrocarbons such as naphtha. During this process, small amounts (0.5%-2%) of acetylene are produced. Acetylene has to be diminished to ppm level, since it poisons the catalyst in the following ethylene polymerization reaction.[99] Bimetallic AgPd alloys are industrially applied in this reaction[100–102] since they show increased selectivity towards ethylene compared to monometallic Pd catalysts, which also forms side products, such as fully hydrogenated ethane and polymers, known as green oil, which poisons the catalyst.[103–105] The superior performance of AgPd alloys in the semi-hydrogenation of acetylene can be referred to their electronic structure and the questions arises how the catalytic properties of AgPd changes, when the dilution is pushed to the Pd site-isolation limit in a SAA.

The changes to catalytic properties upon alloying are generally classified as ensemble or ligand effects. Ensemble effects refer to the change in coordination environment that occurs upon alloying, while ligand effects refers to the change of the electronic structure of metals, when they are alloyed together.[106] Since ligand effects alter a metal atom's electronic structure, they can in principle be observed using electronic-structure sensitive spectroscopies, such as photoemission spectroscopy. In many alloys, differences in electro-negativity between the constituent elements give rise to a partial charge transfer.[107,108] Charge transfer can, in some cases, be observed by shifts in core-level XPS peaks (as long as the shift is not counter-acted by some other process, such as final-state effects).[109,110] Additionally, the electronic structure of the surrounding matrix can alter the screening properties of the photoemission process, giving rise to additional binding energy shifts[111] and possible changes in peak line shape.[54] Changes to the electronic structure might also be observed in the valence band spectra, which to a first approximation, represent the cross section weighted valence projected density of states (PDOS) of the alloy, and has an impact on the line shape and the core level shifts (CLS).[109]

In some SAAs, the solute exhibits a very weak interaction with the matrix element, resulting in an electronically isolated metal site, where the solute's valence states resemble a free-atom state. This behavior can be seen in the d-band of the solute. While most transition metals in their pure form, have d-bands that are several eV in width, in certain alloys the solute's d-bands become very narrow.[14] This phenomenon has been shown recently for $Ag_{0.995}Cu_{0.005}$[3] and can also be found in older literature about transition metals containing impurities of another transition metal.[30,31,38]

In the present work, we demonstrate the spectroscopic characteristics of an $Ag_{0.98}Pd_{0.02}$ SAA, and discuss how they are a consequence of its electronic structure and coordination environment, by comparing with the computed photoemission signal (PES) of a free Pd atom. We also discuss, whether the geometric and electronic site-isolation of Pd in the $Ag_{0.98}Pd_{0.02}$ model catalyst can manifest themselves in the catalytic behavior in the semi-hydrogenation of acetylene. This discussion contributes to an improved understanding of the nature of active sites in SAAs and single-atom catalysts (SACs).

3.2.3 Experimental section

3.2.3.1 Synthesis of the $Ag_{0.98}Pd_{0.02}$ alloy

Quantitative amounts of the Ag (slugs 3×3mm, 99.99%) and Pd (granules <7mm, 99.95%) purchased from EvoChem were melted in a light oven, with a four times re-melting process for homogenization. Afterwards the alloy was cold-rolled to a 1.6 mm thick foil and then annealed for 6h at 800°C to promote grain growth. The foil was cut into smaller pieces and mechanically polished step by step until a roughness of 1 µm was archived by using a diamond suspension as an abrasive. Subsequent annealing in 0.5 mbar O_2 at 500°C led to the surface segregation of impurities such as Cu, K, S, Si, Cl, which could then be removed by Ar^+ sputtering. This procedure was repeated several times to clean the sample surface. The last step was heating in UHV at 500°C for recrystallization. Additionally, an $Ag_{0.95}Pd_{0.05}$ alloy was prepared using the same procedure.

3.2.3.2 Polycrystalline Pd and Ag foil

The 0.1 mm thick Pd foil was purchased from Alfa Aesar (99.9%), the Ag foil from Sigma Aldrich (99.99%) is 0.5 mm thick. Both samples were cleaned by several Ar^+ sputtering and annealing cycles (in O_2, H_2 and vacuum).

3.2.3.3 XPS experiments

For the XPS measurements, two different near ambient pressure (NAP) XPS setups were used; (i) a lab source (NAP) XPS using monochromatic Al Kα (1487 eV) radiation and a Phoibos NAP-150 hemispherical analyzer from SPECS GmbH, and (ii) the (NAP) XPS setup at the UE56-2_PGM1 beamline at Bessy II, which is also equipped with a hemispherical analyzer from SPECS GmbH. For the experiments performed in this work they were both operated in UHV.

Before performing XPS measurements the samples were Ar^+ sputter cleaned for 15 min. All spectra of the $Ag_{0.98}Pd_{0.02}$ alloy (except of Figure 3-9c,-d) were measured using synchrotron radiation, thereby excitation energies of 520 eV for Ag3d, 485 eV for Pd3d and 200 eV for the valence band spectra were used. Reference spectra of the polycrystalline Pd and Ag foil were collected using the laboratory XPS (with Al Kα excitation). All peaks were analyzed using the CasaXPS software and fitted using a U2 Tougaard background.

3.2.3.4 STEM-EDX measurements

Scanning transmission electron microscopy (STEM) in combination with energy-dispersive X-ray spectroscopy (EDX) was performed using a Thermo Fisher Talos F200X at 200 kV. The focused electron beam was raster scanned across the region of interest - 222 x 620 nm large - and EDX spectra were collected by a 4-quadrant detector (Super-X detection system, Thermo Fisher) from each scanning point (696 x 1940 spectra).

The scanning step size was 320 pm and the acquisition time was 10 µs per pixel. 70 frames were acquired and the collected EDX spectra of each frame were summed up, resulting in an improved signal-to-noise ratio. A beam current of 3.2 nA was used to resolve the low Pd signal within the sample. For quantification, background subtracted Pd-K and Ag-K lines were considered (using an empirical power law fitting). The peak areas were weighted by Brown-Powell ionization cross sections, as given within the analysis software (Velox 2.13, Thermo Fisher Scientific).

3.2.3.5 Calculations

The 4d PES spectra of the free Pd atom were computed using Quanty using Slater integrals and the spin orbit coupling parameter computed for the neutral free atom at the Hartree-Fock level and empirical spectral broadening.[112] Density functional theory calculations of the solids were performed using the Quantum ESPRESSO package version 6.4.1[113] at the PBE level using pseudopotentials from the PSlibrary[114] with a kinetic energy (charge density) cutoff of 60 Ry (600

Ry) for scalar relativistic and fully relativistic simulations. AgPd SAAs were computed by substituting a single Ag atom with a Pd atom in (2×2×2), and (3×3×3) crystallographic supercells of fcc Ag and relaxing all atom positions and lattice vectors until forces dropped below 10^{-3} a.u., the cell-pressure dropped below 0.5 kbar, and the change in total energy was below 10^{-4} Ry at the scalar relativistic level. Fixed geometry calculations were performed including spin-orbit coupling for Pd. The PDOS was generated with a broadening of 0.17 eV. Core level shifts were computed using the ΔSCF method.

3.2.4 Results and discussion

3.2.4.1 Homogeneity and electronic structure of $Ag_{0.98}Pd_{0.02}$ SAA in comparison with its plain constituents

Before going into the details of the valence states of the $Ag_{0.98}Pd_{0.02}$ alloy, it is necessary to verify that the Pd atoms are indeed present as geometrically isolated single sites in the Ag host. This is a challenging, but inevitable part of all SAA studies. For the case of AgPd alloys it is especially difficult, since the constituents are neighboring atoms in the periodic table, and therefore it is not possible to distinguish them by their contrast using HAADF-STEM. However, it is reasonable to expect that in low concentrations, Pd is present statistically as isolated atoms, since the AgPd phase diagram shows them to be completely miscible, and that the heat of formation is always negative, indicating an attraction between Ag and Pd.[115] Additionally, DFT calculations reveal a positive aggregation energy for the formation of Pd dimers and trimers in an Ag host. From these studies, it can be concluded that Pd atoms prefer to be isolated.[25]

Further evidence for the Pd atom isolation was found in studies on AgPd alloys using a variety of methods including STM,[116] CO adsorption[91] and a simulation method based on machine learning.[117]

To confirm these previous findings, we have used EDX mapping in a TEM on a thin piece of the alloy. Figure 1a shows a dark field (DF) image of the analyzed sample position. The simultaneously collected EDX signal results in Ag and Pd maps as given in Figure 1b. The uniform distribution of the Pd signal in the EDX map indicates that the Pd is homogeneously distributed. The low Pd signal and therefore high signal-to-noise ratio hinders a clear interpretation on the very local scale (for a more detailed discussion on the homogeneity of Pd see Figure S1 in the supplementary information). However, integrating the EDX signal over the whole region shown in panels a and b, gives a clear Pd peak (yellow arrows in Figure 1c), which is identified by 2±0.5 at% (see experimental section for details on the quantification).

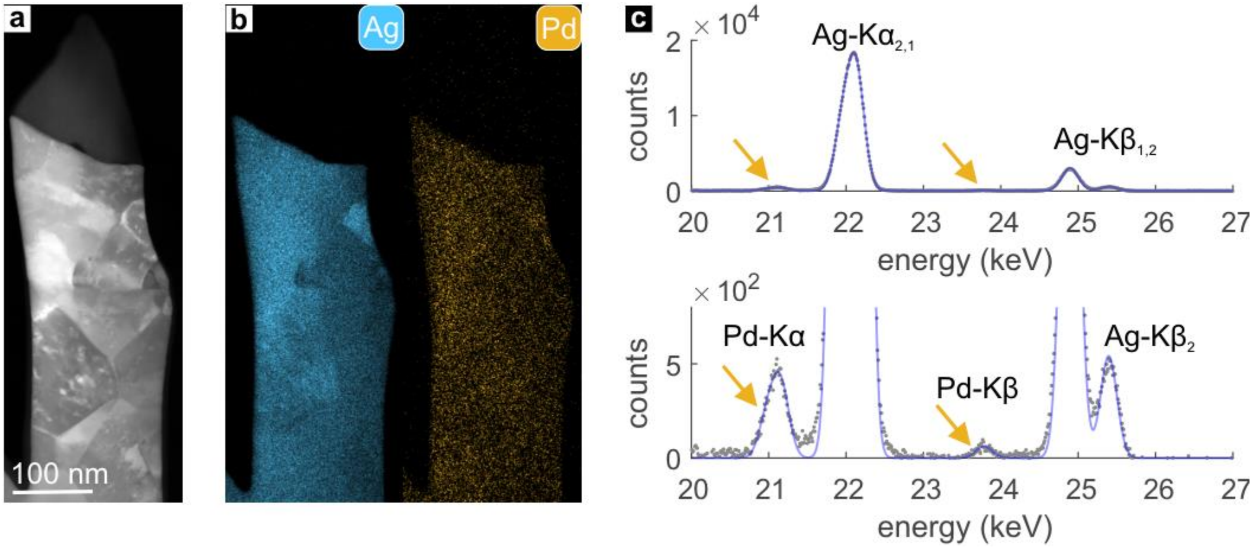

Figure 3-7: STEM-EDX analysis: a) Dark field image of the Ag/Pd sample. b) EDX maps showing the elemental distribution of Ag (left) and Pd (right) over the sample position as shown in a). The color-coded signal corresponds to the net counts of the corresponding EDX signal (i.e. after background subtraction). c) EDX spectrum extracted from the whole region shown in a) and b) (top). The Ag-K peaks are clearly resolved, while the Pd signal is hardly visible (yellow arrows), due to its low content of approximately 2 at% relative to the Ag signal. Therefore, a magnified view of the same spectrum is shown in the lower panel, now clearly displaying the Pd-Kα but also Pd-Kβ peak. The blue lines are gaussian fits to the experimental data (gray dots).

Stronger evidence of the isolated nature of the Pd atoms can be seen in the XPS core level and valence band spectra, as explained here, with a discussion of the differences in the electronic structure of the Pd3d core level, and the valence band states of the $Ag_{0.98}Pd_{0.02}$ alloy and pure Pd. Figure 3-8a shows the Pd3d spectrum of bulk metallic Pd. The peaks are asymmetric (asymmetry factor at 10% peak height is 0.4), with a tail extending to the high binding energy side of the main peak. The asymmetry is a result of intrinsic energy losses caused by interactions of the core-level electrons with the valence band electrons.[54,118] The degree of asymmetry depends on the local DOS at the Fermi level.[119] The DOS at the Fermi edge for bulk Pd is very high (Figure 3-8b), because the Pd4d states are not completely filled, having an electron configuration of $4d^{9.5}$ $5s^{0.5}$.[119,120]

In contrast, the Pd3d line shape in the $Ag_{0.98}Pd_{0.02}$ alloy is quite symmetric (asymmetry factor of 0.95). The reason for the more symmetric shape is the low DOS around the Fermi level in the alloy. In the alloy, the Pd4d band becomes filled, so that the states around the Fermi level in AgPd are primarily Ag5s (Figure 3-8b). Thus few valence excitations are available to cause the energy loss that gives rise to peak asymmetry.

Additionally, it can be seen in the valence band spectra, that the Pd4d valence states are well separated from the Ag4d states (Figure 3-8b), which can be explained by weak wave-function mixing of the metal 4d states, as was previously also shown for a $Ag_{0.995}Cu_{0.005}$ SAA,[3] and by DFT calculations of the DOS of multiple SAA combinations.[14] The weak wave-function mixing results from the fact, that the filled Ag4d valence states are located below the Fermi level. For this reason almost no hybridization of the Pd4d and Ag4d states is possible, hence the Pd electrons are located at the Pd atom forming a narrow, electronically isolated virtual bound state.[109]

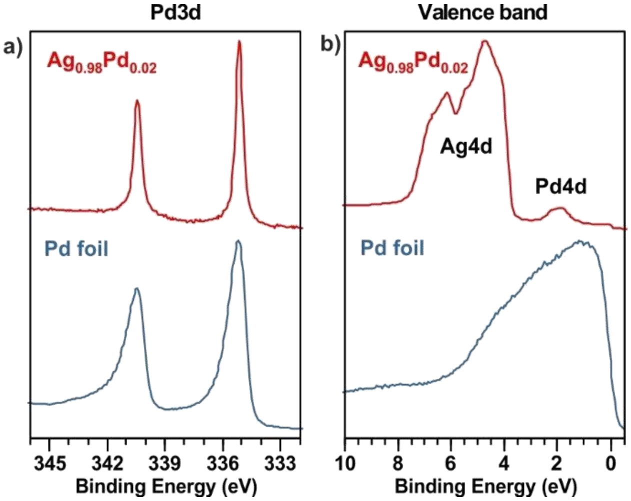

Figure 3-8: Comparison of (a) the Pd3d and (b) the valence states of the $Ag_{0.98}Pd_{0.02}$ alloy with the polycrystalline Pd foil.

Spectroscopic evidence of the homogeneity of the AgPd SAA can be found in the XPS line shape of the $Ag3d_{5/2}$ and the $Pd3d_{5/2}$ signals. As mentioned above, the line shape depends on the DOS at the Fermi level. In a homogeneous alloy the components share the same DOS, therefore they are expected to have similar line shapes (in the absence of satellites on the solute atom). Figure 3-9a,-b shows a comparison of the line shape of Pd3d in $Ag_{0.98}Pd_{0.02}$ with that of Ag3d. Here we fit the $Ag3d_{5/2}$ signal using generalized Voigt line-shape (LF in CasaXPS 2.3.23) on a Tougaard background. The exact same line-shape was then used to fit the $Pd3d_{5/2}$ signal. As one can see in Figure 3-9a,-b, an identical line-shape can be used to fit both signals reasonably well, suggesting that they share a similar electronic structure, both in terms of initial-state and final-state.

Further indication for successful alloying is the core level shift (CLS) of the $Ag3d_{5/2}$ peak from 368.20 eV for pure Ag to 368.18 eV for $Ag_{0.98}Pd_{0.02}$ and 368.10 eV in the case of an $Ag_{0.95}Pd_{0.05}$

alloy. The peak shift goes hand-in-hand with an increase in the FWHM of Ag3d$_{5/2}$ from 0.70 eV for the Ag reference sample to 0.78 eV for the Ag$_{0.95}$Pd$_{0.05}$ sample (Figure 3-9c). Calculations of the CLS of Ag, as a function of the Pd neighbors, revealed a linear correlation towards lower binding energies of Ag.[109,121] The CLS of Ag3d towards lower binding energies, as the concentration of Pd increases, can be explained by charge transfer of Ag5s states to Pd4d states, as it can also be observed for the metal-to-oxygen charge transfer in oxidized Ag.[122] This negative shift is attributed to final state effects, where the screening charge has bonding 5s character.[122] The impact of charge transfer is very weak for the highly diluted Ag$_{0.98}$Pd$_{0.02}$ alloy, where the CLS accounts only to 0.02 eV. As the concentration of Pd in Ag increases additional hybridization effects lead also to a more negative shift of the Ag3d states.[109] The broadening of the Ag core level signal suggests that there are distinct CLS for Ag atoms adjacent to Pd atoms, and Ag atoms not in the direct neighborhood of Pd atoms.[121]

Additionally, slight differences in the binding energy of the Pd3d$_{5/2}$ core level could be observed from 335.04 eV for the pure Pd metal, 335.12 eV for Ag$_{0.98}$Pd$_{0.02}$ to 335.06 eV for Ag$_{0.95}$Pd$_{0.05}$ (Figure 3-9d). It should be mentioned that the CLS does not show a linear trend in the case of Pd, and it is important to distinguish between initial- and final-state effects. Due to the higher density of states near the Fermi level in bulk Pd metal, compared to Ag$_{0.98}$Pd$_{0.02}$, Doniach-Sunjic core-hole screening,[118] which leads to asymmetry, plays a more dominant role in Pd metal than in Ag$_{0.98}$Pd$_{0.02}$, where there is almost no screening charge at the Fermi level. Since bulk Pd and Pd in the AgPd SAA have very different DOS, it is not straight forward to directly compare and discuss the Pd3d peak positions of Pd metal and Ag$_{0.98}$Pd$_{0.02}$.

In contrast, Ag$_{0.98}$Pd$_{0.02}$ and Ag$_{0.95}$Pd$_{0.05}$ have very similar valence electronic structures, and the Pd3d peak positions can be more directly compared. In this case, we see that the peak position shifts slightly toward lower binding energy, as the Pd concentration increases.

As mentioned above, the Pd4d virtual bound state in AgPd SAA shifts below the Fermi level, and becomes very narrow, due to the localization of the Pd electrons around the atom, because of the weak wave function mixing of the Ag4d and Pd4d states. One would expect that this effect would lead to a decrease in the binding energy for the Pd3d core levels in the initial state, since the Pd4d band becomes more populated and more negatively charged, due to the charge transfer of Ag5s states towards Pd4d states. However, in an AgPd SAA the screening charge at the Fermi level changes its character from 4d orbitals with a high DOS in pure Pd to sp character from the neighboring Ag atoms with low DOS at the Fermi level. The low DOS at the Fermi edge, leads to very little core-hole relaxation, and hence, to a pronounced final-state effect. As a consequence, the shift towards higher binding energies becomes more pronounced as the Pd concentration decreases towards infinite dilution, due to the reduction in screening charge.[109] Therefore, the positive shift is higher for $Ag_{0.98}Pd_{0.02}$ than for $Ag_{0.95}Pd_{0.05}$. In order to validate the measured CLS, the CLS of AgPd SAAs in comparison to Pd bulk was computed by substituting a single Ag atom with a Pd atom in (2×2×2) and (3×3×3) crystallographic super-cells of fcc Ag, revealing $Ag_{31}Pd_1$ ($Ag_{0.97}Pd_{0.03}$) and $Ag_{107}Pd_1$ ($Ag_{0.99}Pd_{0.01}$) respectively. For both supercells the computed $Pd3d_{5/2}$ CLS is 0.08 eV, which is precisely the shift we measured for the $Ag_{0.98}Pd_{0.02}$ alloy (Figure 3-9d). This result demonstrates that no further CLS and electronic structure changes are expected when diluting Pd below 3 at% in Ag.

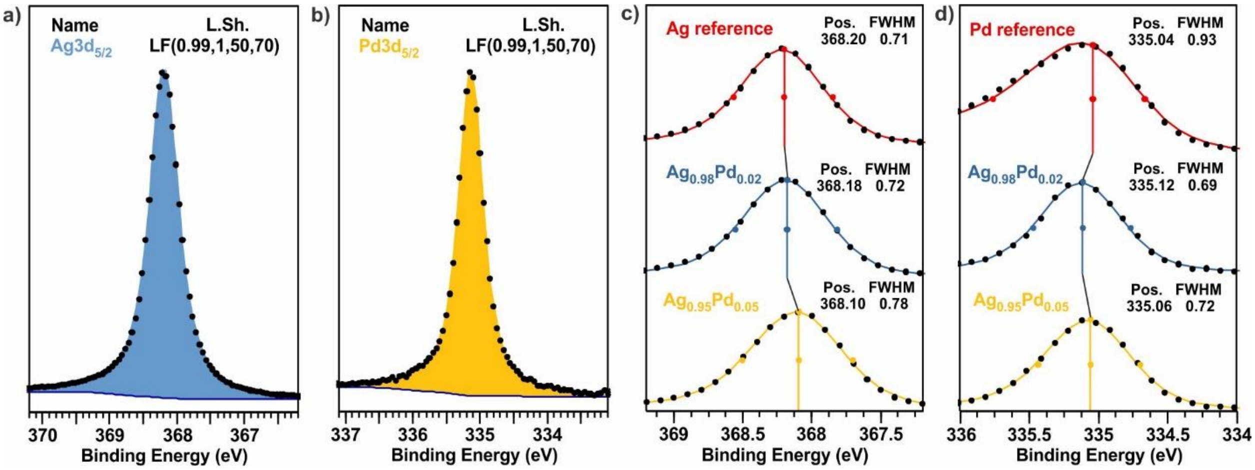

Figure 3-9: Fitting of the $Ag3d_{5/2}$ (a) and $Pd3d_{5/2}$ (b) signal of $Ag_{0.98}Pd_{0.02}$ using the same line-shape. An identical line-shape is a sign for a homogeneous alloy, because it means that the constituents share the same DOS. CLS and peak broadening of $Ag3d_{5/2}$ (c) and $Pd3d_{5/2}$ (d) due to alloying in an $Ag_{0.98}Pd_{0.02}$ and $AgPd_{0.58}Pd_{0.05}$ alloy compared to pure Ag and Pd. The colored points represent the FWHM.

It should be noted that the discussed CLS for Ag- and $Pd3d_{5/2}$ states are very small, but previous researchers performed experimental and theoretical calculations of the CLS in Ag-Pd alloys over the whole concentration range.[109,123] Thereby they found that the effect of inter-atomic d-electron charge transfer, which is often discussed as origin for CLS's, is negligible for Ag-Pd alloys.[109]

3.2.4.2 $Ag_{0.98}Pd_{0.02}$ valence band

In this section, we analyze in more detail, the valence band of $Ag_{0.98}Pd_{0.02}$ measured with synchrotron radiation, and discuss the findings by considering the literature from the 1960's to 1980's, where electronic structure changes induced by transition metal impurities in another transition metal were intensively studied.[30,31,38] The materials previously studied are in principle the same as the materials now referred to as SAAs. As shown in Figure 3-8b, the Pd4d states are well separated from the Ag4d states, but the FWHM of the Pd4d virtual bound states is 0.85 eV broader than it was for the $Ag_{0.995}Cu_{0.005}$ SAA (0.5 eV).[3] This observation opens the question: which parameters have an impact on the width of the valence states? Parameters giving rise to broadening are crystal field (d-d)-, s-d- and spin-orbit coupling. In general, the d-band width increases along a row of the periodic table and reaches its maximum in group 5, then it decreases again as the d-band becomes filled. Along the column from 3d to 5d elements, the d-band width increases due to more interacting electrons.[124] Consequently, the fact that Pd is a 4d and Cu a 3d element, and that Pd is in group 10 whereas Cu in group 11 leads to broader Pd valence states.

Norris and Meyers claimed already in 1971 that even at infinite dilution there is broadening of the Pd4d bound states, due to the spin-orbit splitting and the s-d coupling. The d-d interactions (crystal field effects) can be neglected in the case of transition metal impurities in the host metal.[30] In 1985 van der Marel et al. investigated experimentally (UPS) and theoretically Pd and Pt induced changes in noble-metal density of states.[3] From the UPS results of a $Ag_{0.97}Pd_{0.03}$ alloy it became clear that spin-orbit splitting plays a role for the broadening of the Pd4d valence states. Consequently, we fitted the Pd4d states of the $Ag_{98}Pd_{0.02}$ sample using two signals with the typical area ratio for 4d states of 2:3. In Figure 3-10a it can be seen that this approach results in a good fit for the Pd4d signal shape. The $Pd4d_{5/2}$ and the $Pd4d_{3/2}$ peak in the fit are centered at a binding energy of 1.8 eV and 2.2 eV. The positions are identical with the one observed in the literature for the $Ag_{0.97}Pd_{0.03}$ alloy.[3] In that publication, the authors found an identical FWHM of 0.8 ± 0.1 eV for the entire Pd4d signal. Furthermore, they theoretically calculated the valence band using a spin-orbit coupling and a s-d coupling parameter, but no crystal field coupling parameter. This agrees with the predictions of Norris and Meyers, that only spin-orbit coupling and s-d interactions have an influence on the broadening.[38]

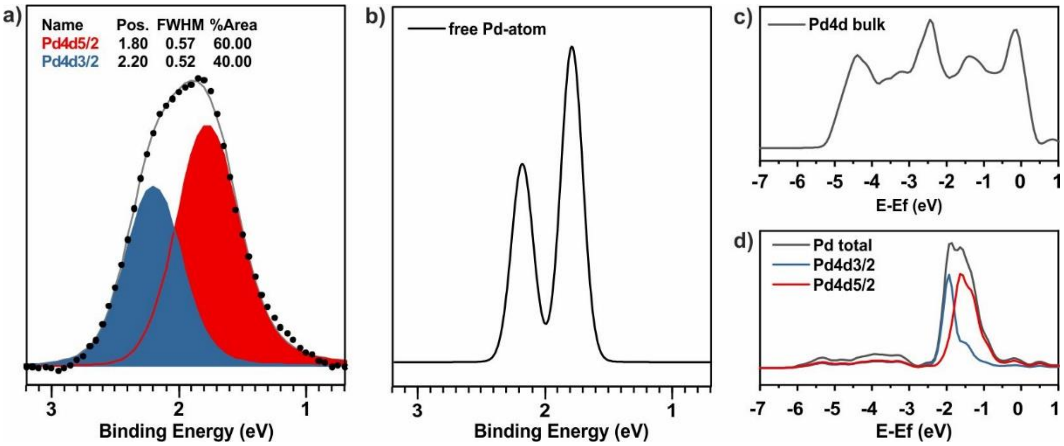

Figure 3-10: a) The Pd4d valence states are fitted using two peaks due to spin-orbit splitting, thereby the typical area ratio of 2: 3 is used. b) calculated PES of a free Pd-atom with spin-orbit splitting. The energy scale is adjusted to the XPS experiment. The calculated splitting is 0.4 eV, closely matching the splitting in the measured signal. c) PDOS of bulk Pd; d) Pd4d PDOS of $Ag_{31}Pd_1$ including the spin-orbit splitting of $Pd4d_{3/2}$ and $Pd4d_{5/2}$.

To estimate, if the Pd atoms in the $Ag_{0.98}Pd_{0.02}$ alloy really behave like electronically isolated free-atoms sites, as it was predicted for the free-atom-like $Ag_{0.995}Cu_{0.005}$ SAA,[3] one can compare the impurity valence d-states of the alloy with the calculated states of a single metal atom in the gas phase. The result of the calculations of the photoemission signal (PES) of such an isolated gas phase atom is shown in Figure 3-10b which demonstrates that spin-orbit splitting plays a significant role in the valence states of a free Pd atom. The calculated splitting is 0.4 eV, and is very close to the result obtained by fitting the Pd4d valence states in the XPS spectra (Figure 3-10a). Since spin-orbit splitting can account for the Pd4d band width, there might be very little hybridization between the Pd and Ag valence d-states, and therefore a free-atom-like behavior of Pd.[125–127] To verify this proposition, the Pd4d PDOS of $Ag_{31}Pd_1$ was computed by fully relativistic DFT and a broadening of 0.17 eV (Figure 3-10d). It can be observed that there is also a weak Pd4d electron density between -6 and -3 eV, the range of the Ag4d states and consequently there is a small degree of hybridization between Ag and Pd. For comparison, the PDOS of bulk Pd is also plotted (Figure 3-10c), which shows the width and the high DOS at the Fermi edge of Pd4d.

Our $Ag_{0.98}Pd_{0.02}$ SAA provides a reference for the often-discussed phenomenon of site-isolation, whereby in this case geometric site-isolation is accompanied by electronic site-isolation. In the next section, we will discuss the effect of the geometric and electronic site-isolation on the catalytic performance of AgPd SAAs in the selective hydrogenation of acetylene.

3.2.4.3 Discussion of the catalytic properties of AgPd SAA in selective acetylene hydrogenation

Previous work has shown that bimetallic AgPd alloys can exhibit increased selectivity towards ethylene, compared to monometallic Pd catalysts, which also forms side products, due to its high activity.[103,104,128,129] Those side products are fully hydrogenated ethane and polymers, known as green oil, which poisons the catalyst.[103–105] It is believed that alloying Pd with Ag increases ethylene selectivity for two reasons: (i) It hinders the formation of sub-surface hydrogen, which is responsible for the full hydrogenation pathway towards ethane;[104,129,130] (ii) It weakens the binding strengths towards all surface intermediates, leading to increased desorption of the desired product ethylene.[131–133] The latter effect is because the d-band of Pd becomes filled due to alloying,[109,134,135] which weakens the adsorption of π-electron donors such as acetylene and ethylene, since they can donate fewer electrons into the Pd d-band.[103] In the present work, the valence band spectra (Figure 3-10) indicate a full d-band for Pd, strongly supporting this model. Due to the filled d-band, the ethylene desorption barrier becomes lower than the hydrogenation barrier,[131] and also C-C coupling, which leads to the formation of green oil, is unlikely to occur.[136]

On the other hand, one can say that Ag is inactive in acetylene hydrogenation, since (defect free) Ag ensembles can neither adsorb acetylene,[137,138] nor activate H_2.[139] Therefore, although the selectivity increases when Pd is alloyed with Ag, the overall activity of the selective hydrogenation reaction decreases with increasing Ag content. Consequently, the question arises, which Ag:Pd ratio is ideal to catalyze the reaction. Freund and coworkers thoroughly summarized the requirements of an ideal AgPd catalyst:[104] "*the Pd-Ag system should have, on the one hand, the Pd-rich surface to dissociate hydrogen and catalyze reaction with acetylene and, on the other hand, an Ag-rich core to prevent hydrogen migration into the particle*." In their work, they showed that an AgPd model catalyst became inactive at very high Ag surface coverages. In essence, if H_2 is activated at Pd sites, and if acetylene adsorbs at Pd sites, then in the case of site-isolation, the adsorbates must be able to diffuse to each other for the reaction to occur.

Sykes and coworkers demonstrated theoretically[11] and by STM experiments[98] that H_2 dissociation can occur on isolated Pd sites of CuPd and AuPd SAAs, however, they found that only for CuPd SAAs a subsequent spillover of hydrides to the host atoms (Cu) was possible.[10,29,98] Previous DFT calculations of the formation energy of adsorbed H atoms by Darby *et al*. revealed formation energies of 0.16 eV for a Ag(111) surface and -0.12 eV for a Pd-doped Ag(111) surface, whereas the energies for a Pd doped Cu(111) and plain Cu(111) surface were -0.27 eV and -0.26 eV respectively.[42] These values verify why spillover of H atoms is likely to occur on CuPd SAAs but not on AgPd. Thus, we expect that without H spillover, isolated Pd sites in AgPd SAAs must be sufficiently close to one another for semi-hydrogenation to occur.

The work of Armbrüster and coworkers on Ga-Pd intermetallics demonstrated such an effect.[33,34,140] In that example, Pd and Ga are covalently bonded in a ordered crystal structure different from their constituents. Pd atoms are isolated in that no neighboring Pd atoms are present in the first coordination sphere.[34] The isolation of Pd sites hinders the formation of bulk hydrides, and therefore avoids the formation of fully hydrogenated ethane,[140] while the close proximity of neighboring Pd atoms allows for adsorbates to encounter one another. The experiments show that $GaPd_2$ compared to GaPd has a 30-fold higher activity, but the same selectivity (75%). The reason for the lower activity of GaPd is explained by the differences in the valence band structure. GaPd has a lower DOS at the Fermi edge (0.2 states eV^{-1} $atom^{-1}$), a lower lying d-band center (0.4 eV) and a narrower d-band width (0.9 eV) than $GaPd_2$,[33,34] similar effects were observed for the Pd valence structure of AgPd in the present work. As mentioned above for the AgPd alloys, this electronic effect (i.e. filling of the d-states) enhances the selectivity towards ethylene. In the case of AgPd, site-isolation could in principle still be obtained at Pd concentrations as high as 7 atomic percent–that is, one Pd atom for every 12 Ag atoms–such that, in the FCC unit cell, the 12 atoms in the coordination sphere of a Pd atom are all Ag.

While close proximity of isolated sites can enable the semi-hydrogenation reaction to occur, the hydrogen uptake can also be increased by the support. In a previous study by Pei *et al.*, it was found that nanoparticle-sized, SiO_2 supported AgPd SAA catalysts were efficient and highly selective in the hydrogenation of acetylene in an excess of ethylene.[91] In their study, H_2 activation was likely enhanced by the presence of the support. Claus and coworkers' work on H-D exchange experiments on Ag/SiO_2, investigated by FTIR spectroscopy, revealed that even the bare SiO_2 support is able to activate H_2.[141,142] Other groups found that the H_2 dissociation on such non-reducible supports can be attributed to defect sites in the support.[143,144] It was experimentally shown, that the H_2 activation increases for Ag nanoparticles on the SiO_2 support,[141,142] which could be explained by H-H exchange at the metal-support interface, where a H atom on the metal exchanges with a proton of the OH (silanol) group on the SiO_2 support.[144,145] Thereby residual water molecules accelerate the H-H exchange.[144,146] Such metal-support interactions are possible for the supported AgPd/SiO_2 SAA catalysts, but not for the unsupported AgPd SAA foil examined in the present work. Besides, the AgPd nanoparticles in AgPd/SiO_2 might contain additional electron-deficient sites (defect sites, step and corner atoms), which lead to valence d-band vacancies and the facilitation of metal-H bond formation. Hence, Ag atoms in nanoparticles might be able to activate H_2.[142,147]

In summary, a hydrogenation reaction requires two initial steps, the dissociation of hydrogen and the adsorption of the hydrocarbon (here acetylene). The alloying of Pd with another metal such as Ga or Ag hinders the formation of sub-surface hydrogen and also weakens the binding towards the desired product ethylene due to d-band filling, both effects increase the selectivity.[51,52,140] The dissociation of hydrogen is possible at the single-atom Pd sites in SAAs, for CuPd SAAs a subsequent spillover of H atoms to the Cu host occurs, increasing the hydrogen uptake.[29,98] Additionally, the spillover enables the reaction of the hydrides with acetylene, which is adsorbed on the Pd sites. AuPd and AgPd SAAs are not expected to exhibit H_2 spillover to the host, due to weak binding between H atoms and Ag or Au.[10,11,42,98] Hence, the H atoms cannot approach and react with acetylene, when the isolated Pd sites are far away from each other. In intermetallics such as GaPd, the Pd sites are also geometrically isolated, but close enough for the adsorbates (H and acetylene) to react with each other.[33,140] In supported SAA catalysts, such as AgPd/SiO_2, H_2 can be activated at the defect sites of the support, and also electron-deficient Ag sites might activate H_2.[142] Those two effects increase the H_2 uptake and enable the reaction of H_2 and acetylene.

3.2.5 Conclusion

Here we have investigated an unsupported AgPd single-atom alloy foil using electron spectroscopy and computational chemistry. This $Ag_{0.98}Pd_{0.02}$ alloy is one of the few documented cases of electronic site-isolation in heterogeneous catalysis, and we demonstrate and discuss the ways in which its unusual free-atom-like electronic structure is manifested in the measured spectra.

In particular, a comparison of the core level Pd3d line-shapes of $Ag_{0.98}Pd_{0.02}$ and bulk Pd revealed a symmetric line-shape for Pd3d in AgPd. The change in the line-shape can be referred to the change in the local density of states at the Fermi level. Bulk Pd has very high density of states due to unfilled Pd4d states, which lead to asymmetric core-level line-shapes. In contrast, the Pd4d states in the AgPd single-atom alloy are very narrow and filled and are hence shifted below the Fermi level. Furthermore, it was found that the Ag3d and Pd3d core-level states can be fitted using exactly the same line-shape, which indicates, that both metals share the same density of states and that the Pd atoms are homogeneously distributed in the alloy. Additionally, the Pd4d valence states in $Ag_{0.98}Pd_{0.02}$ are well separated from the Ag4d valence states. A comparison of the Pd4d valence states in the single-atom alloy with a calculated photoemission signal of a free Pd atom in gas phase showed good agreement. Consequently, there is a weak wave-function mixing of the Pd4d states with their surroundings, which verifies the electronic site-isolation of the Pd atoms.

We also discussed the effect of the site-isolation on the catalytic activity in acetylene hydrogenation. From the discussion we concluded, that the geometric and electronic Pd site-isolation in the inert Ag host should reduce the catalytic performance of the Pd atoms, as adsorbates (H_2 and acetylene) on isolated Pd sites of the $Ag_{0.98}Pd_{0.02}$ alloy would be too far away from each other to react. This issue can be avoided when the host material participates in the reaction, e.g. in CuPd SAAs, H_2 will be dissociated by the Pd sites followed by spillover to the Cu host.[29] Besides, defect sites in the support are able to activate H_2 and hence increase the H_2 uptake and the catalytic performance.[91,142,144]

Data Availability Statement

The XPS data that support the findings of this study are openly available in Zenodo at https://doi.org/10.5281/zenodo.4481984, https://doi.org/10.5281/zenodo.4482000 and https://doi.org/10.5281/zenodo.4482138.

3.2.6 Supplementary information

3.2.6.1 STEM-EDX analysis

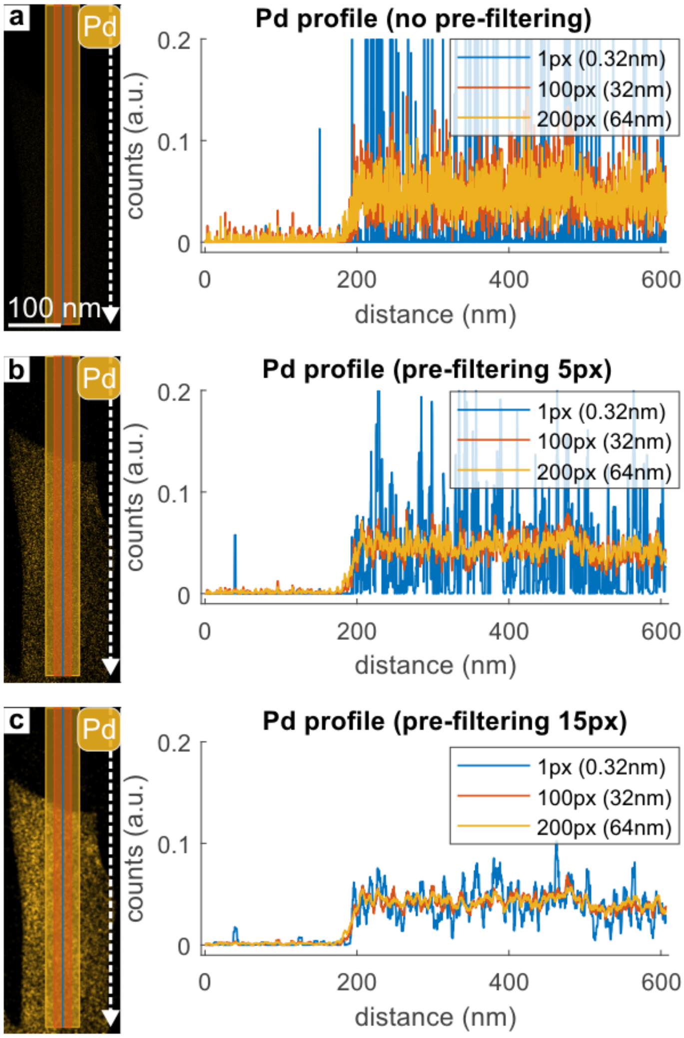

Figure S 1: Homogeneity of Pd: Pd line profiles across the sample position discussed in Figure 1 of the main manuscript using no pre-filtering (a), pre-filtering averaging over 5px (b) and pre-filtering averaging over 15px (c). Pre-filtering means, that each spectrum of the spectrum image data set is averaged (arithmetic mean) by its next neighbor spectra BEFORE the Pd-map is extracted from spectrum image. Averaging over 3px includes the next neighbors only, averaging over 5px also includes the next neighbors to next neighbors and so on. Therefore, the signal-to-noise-ration is stepwise improved going from no-prefiltering (a), over pre-filtering averaging over 5px (b) to pre-filtering averaging over 15px (c). This can be clearly seen in the Pd-maps (left, enhanced Pd signal) and in the according Pd-profiles (right, less noise contribution). In addition, Pd line profiles are compared for different integration widths in horizontal direction: The blue profiles are not integrated along the horizontal direction (1px), the red profiles are integrated over 32nm (100px) and the blue profiles are integrated over 64nm (200px), as indicated by the blue, red, and yellow areas in the Pd-maps, respectively. Both, pre-filtering and integrating improves the signal-to-noise ratio, while losing spatial resolution at the same time. We observed no significant (further) improvement of the signal-to-noise ratio above an integration width of approximately 15-20 nm, while gaining a constant Pd value within 20-30% variation, which is close to the quantification error of 25% (2±0.5at%). Note that possible thickness variations may alter the Pd signal. We therefore conclude from the EDX data a homogeneous Pd distribution (within ±25%) above a size range of approximately 15-20 nm. The low Pd signal prohibits a statement on the more local scale.

3.2.6.2 Catalytic investigation

In chapter 3.2.4.3 it was discussed, that the geometric and electronic Pd site-isolation in the inert Ag host are expected to reduce the catalytic performance of the Pd atoms in the semi-hydrogenation of acetylene. This conclusion was also tried to verify experimentally. Since it was not possible to quantitatively analyze the catalytic performance of the AgPd SAA foil with the experimental method described below, the supporting experimental results of the catalytic investigation are discussed here in supplementary information section.

3.2.6.2.1 Experimental procedure

The catalytic testing was performed to compare the catalytic properties of the Pd foil and $Ag_{0.98}Pd_{0.02}$ in selective acetylene hydrogenation. The tests were carried out in a NAP-XPS test station, (i.e. the same setup used to perform NAP-XPS experiments using synchrotron radiation), but without the attachment of the electron energy analyzer. This configuration enabled to reach higher gas pressures, up to 100 mbar. Previous experiments of our group, in a NAP-XPS setup, revealed that an increased pressure led to higher conversion in the acetylene hydrogenation reaction (see the section 3.2.6.2.3). The reaction chamber, which has a volume of 4 L was pumped continuously, and the gas phase was detected with a gas chromatograph (GC) (TRACE 1310, thermo scientific). The samples (of the size 8×8 mm) were cleaning by means of Ar^+ sputtering before loading into the reaction chamber.

After loading the sample the reaction mixture C_2H_2:H_2:N_2 1:10:0.67, with a total flow rate of 35ml/min was introduced until a pressure of 100 mbar was reached. The pressure was automatically controlled by a throttle valve. The samples were then heated to 100°C, which is the temperature leading to the highest conversion, as our previous experiments in the NAP-XPS setup revealed. The gas phase was measured at 100°C until steady-state conditions were reached. Additionally, the background gas flow was measured using the same gas flow at room temperature without any sample. N_2 in the reaction chamber was introduced as an internal standard.

3.2.6.2.2 Catalytic results by using the NAP-XPS test station

The AgPd SAA foil, the Pd foil and the plain stainless-steel sample holder (blank) were investigated in acetylene hydrogenation conditions (Figure S 2). The blank measurement was performed to identify, if the AgPd SAA show at all any catalytic performance. Since the calculated conversion of the blank sample and the AgPd SAA foil are in the same region (0.1%), it can be concluded, that there is no measurable catalytic activity originating from the AgPd SAA foil. Since ~0.1% conversion seems to be the detection limit of the GC, it is still possible that there is some activity of the $Ag_{0.98}Pd_{0.02}$ foil, which is too low to be measurable with the here applied setup. On the other hand, the results show, that the experimental setup is sensitive enough to measure the catalytic performance of foil samples, since for the Pd foil a conversion of 26.5% and a selectivity of 75% could be measured (Figure S 2).

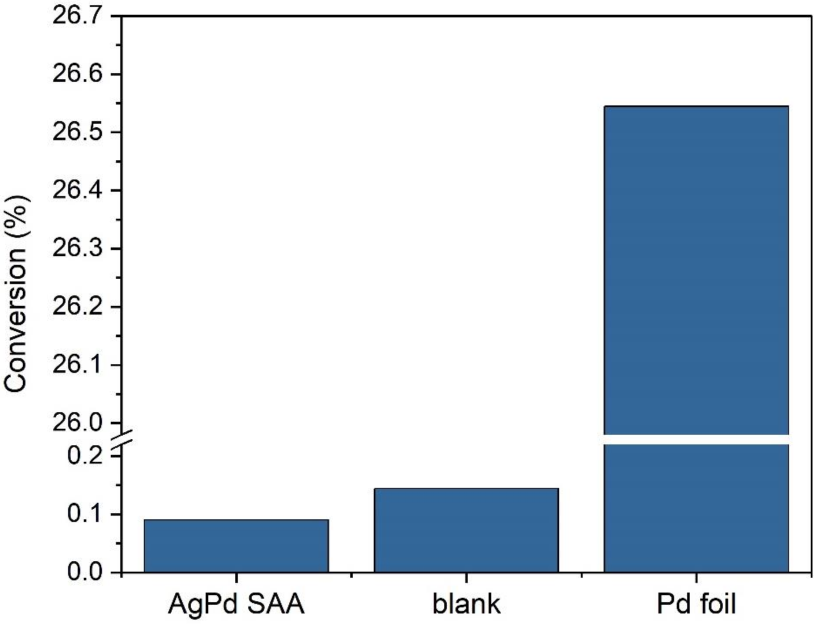

Figure S 2: Comparison of the conversion of the Pd foil with the $Ag_{0.98}Pd_{0.02}$ SAA and the plain stainless-steel sample holder (blank). All samples are exposed to the same conditions C_2H_2: H_2 (1:10), 100°C, 100 mbar in a reaction chamber having a volume of 4 L. The sample foils have a size of 8×8 mm. For the AgPd SAA and the blank measurement almost a similar conversion of ~0.1% was measured, revealing that the SAA sample is not active in the selective hydrogenation reaction, or that its activity is below the detection limit of the GC. (The selectivity values are not shown here, because they can't be measured, when the conversion is below the detection limit. The selectivity of the Pd foil was 75%.)

To evaluate the catalytic results, it needs to be clarified is, if the Pd atoms were accessible at the surface for the reactants. It is well known that Ag has a lower surface free energy under UHV conditions compared to Pd and is therefore expected to be at the surface. As a consequence, Pd migrates into the Ag bulk at elevated temperatures.[35,117,148] From previous surface sensitive XPS experiments we know that the Ag:Pd composition after an Ar^+ sputter cleaning step, which is the only pre-treatment step we performed prior to the reaction, is with 97 at% to 3 at% even a bit higher than the bulk sample composition (98 at% to 2 at%) (see Figure S 5 in section 3.2.6.3). Consequently, Pd atoms should be accessible to the reactants. The question remains, however, if the number of active sites on the surface, i.e. isolated Pd atoms, is high enough to yield measurable catalytic activity. Ag and Pd atoms have a similar covalent diameter (~0.3 nm),[35] therefore it is assumed that there are similarly many surface atoms on the Pd foil and the AgPd SAA foil (both foils have a size of 8×8 mm). The AgPd SAA foil contains only 2 at% of Pd, hence a conversion below $0.02\times26.5\% \approx 0.5\%$ indicates that the activity per Pd atom is reduced for the AgPd SAA foil.

While the activity measurements performed in this work are not a quantitative assessment of the activity of Pd atoms in the alloy, we discuss here why one would expect lower activity for such alloys. The dissociation of hydrogen is generally the rate-determining step in semi-hydrogenation reactions. The activation energy for the dissociation of H_2 is highly increased for the AgPd SAA compared to bulk Pd, which can be demonstrated by calculated activation energies for Pd(111) and Pd doped Ag(111) of 0.04 eV vs. 0.32 eV.[42] From the higher activation barrier it can already be expected that the reaction rate decreases for Pd in the alloy in comparison to the Pd foil (further discussion about the catalytic activity of AgPd SAAs is given in the main text (chapter 3.2.4.3)).

We shortly want to discuss here the challenges of obtaining correlations between the surface structure and the catalytic performance of SAAs, which is of fundamental importance towards rational catalyst design: To understand and to measure the surface structure of catalysts, e.g. by XPS, the complexity of the sample needs to be minimized, therefore a polycrystalline AgPd SAA foil was analyzed in this work. Instead, when investigating supported nanoparticles, which are due to the high surface area beneficial for measuring the catalytic performance, several layers of complexity are added to the system. For instance, nonreducible supports such as SiO_2 and Al_2O_3, are charging during XPS analysis, which makes it very challenging to analyze the electronic structure. Additionally, the low loadings of nanoparticles on the support significantly reduces the intensity of the XPS signals of the metals inside the nanoparticles, especially the single Pd sites in $Ag_{0.98}Pd_{0.02}$ could not be detected and analyzed anymore. Furthermore, additional complexity of the sample system complicates the fundamental understanding of process taken place at the sample surface, e.g. it is difficult to identify, whether metal-support-interactions or the single-atom sites are beneficial for the catalytic performance.

In this work, we tried to obtain the catalytic performance of 8×8 mm large foils (see experimental procedure above). In general, there are no appropriate reactors for foil materials, and the solution used here, was to analyze the catalytic performance within a XPS analysis chamber, where the gas phase was continuously pumped and analyzed by gas chromatography. With such setup it is not possible quantitatively analyze the catalytic activity (e.g. TOF). However, through the comparison of the catalytic performance of the Pd foil with the $Ag_{0.98}Pd_{0.02}$ foil, it could be obtained, that the conversion per Pd atom for the SAA is reduced by at least 5 times compared to the bulk Pd.

3.2.6.2.3 Pre-experiments to access the catalytic performance

In this section, more detailed information about the pre-experiments for the catalytic results presented above are given. To investigate the performance of the catalyst, three different quantities, the selectivity, product formation and conversion were calculated according to the following equations:[91]

$$selectivity = \frac{C_2H_4}{C_2H_4 + C_2H_6 + 2 \cdot C_4} \cdot 100 \tag{3-3}$$

$$product\ formation = \frac{C_2H_4 + C_2H_6 + 2 \cdot C_4}{C_2H_2 + (C_2H_4 + C_2H_6 + 2 \cdot C_4)} \cdot 100 \tag{3-4}$$

$$conversion = \frac{C_2H_2(feed) - C_2H_2}{C_2H_2(feed)} \cdot 100 \tag{3-5}$$

The desired product is C_2H_4, but also side products such as C_2H_6, butane and different kinds of butenes, which are summed together as C_4, can be formed. Since the C_4 products require two C_2H_2 molecules their intensity is doubled. The peak areas of the different products are calculated by subtracting the background peak areas, which were measured at room temperature without a sample and with the same gas feed as during the reaction. During the measurement it was sometimes observed that the peak area of the acetylene signal tends to increase with higher temperature. One possible explanation might be, that acetylene adsorbs on the sample or on the walls of the setup and desorbs at higher temperatures, which could lead to misleading results of the conversion. Hence the formation of all products (3-4), was calculated in addition to the conversion (3-5), since the product formation does not only depend on the detected C_2H_2.

First, the best catalytic parameters for the selective acetylene hydrogenation in NAP conditions for the polycrystalline Pd foil were investigated. The experiments were performed at the NAP-XPS end station at the BElChem beamline at BESSY II. After Ar^+ sputter cleaning the reaction mixture C_2H_2:H_2:N_2 1:10:1 was introduced with a total flow rate of 7.3 ml/min. The pressure in the analysis, regulated by a throttle valve, was set to 1 mbar. The temperature was increased in steps (50°C, 75°C and 100°C) at 100°C the highest product formation could be measured. In the following it was investigated how the flow rate and the pressure in the chamber influenced the product formation and the selectivity while the temperature was kept constant at 100°C. The halve of the flow rate results in an increase in product formation from 0.4% to 1.0% and a decrease in the selectivity (Figure S 3a). Increasing the pressure while maintaining the same total gas flow rate reveals also an increase in product formation from 1.0% to 2.5% and a slight decay in selectivity from 85% to 83% (Figure S 3a). From those results it can be concluded that the selectivity and product formation are inversely correlated, since a decrease in flow rate and an increase in pressure results in increasing product formation and decreasing selectivity. As the temperature is further increased at 2 mbar from 100°C to 125°C, the product formation decreases again (Figure S 3b). As a consequence, 100°C was chosen as the optimum temperature for the semi hydrogenation of acetylene in NAP conditions. The decrease in product formation above 100°C is caused by increasing polymerization of acetylene and ethylene, the resulting oligomers also known as green oil poison the catalyst and therefore reduce the product formation.

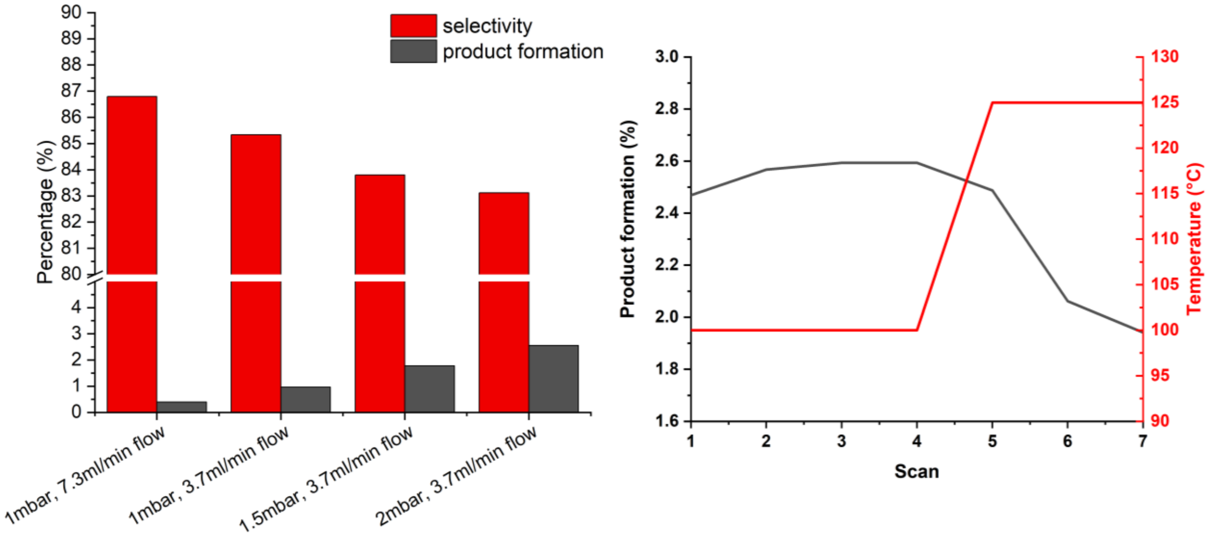

Figure S 3: a) Comparison of the selectivity and the product formation of the Pd foil at different pressures and flow rates at 100°C; b) Product formation of the Pd foil in 2 mbar at 100° and 125°C as a function of the scan number (each scan equals 15 min).

At the NAP-XPS test station (see previous section), the pressure was further increased to 100 mbar. Figure S 4 reveal that the pressure increase led to a remarkable increase in the product formation and conversion.

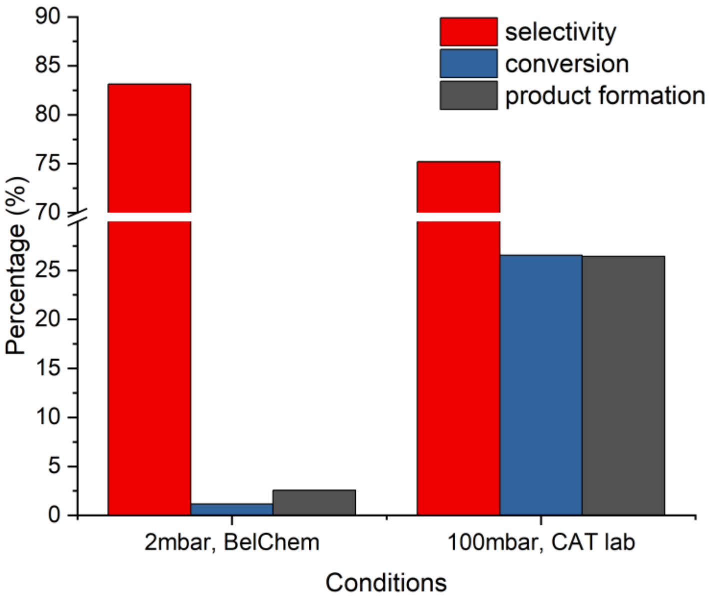

Figure S 4: Comparison of the selectivity, conversion and product formation of the Pd foil in acetylene hydrogenation at 2 mbar and 100 mbar at 100°C.

3.2.6.3 Changes in the Ag3d to Pd3d ratio upon heating and Ar^+ sputter cleaning

The first step of all XPS and catalytic experiments performed in this work with the AgPd SAA sample is Ar^+ sputter cleaning. The bombardment with the Ar^+ ions removes the top surface layers of a sample and with that also impurities such adventitious carbon, which adsorbs on the sample surface when it is exposed to air. Besides, morphology changes at the sample surface, e.g. due to phase segregation in NAP conditions, can be removed by Ar^+ sputtering, which enables equal starting conditions for every new experiment. Different materials exhibit different sputter profiles depending on their softness and brittleness. Hence, the surface composition of alloys might change due to the Ar^+ cleaning procedure.

After sputter cleaning the $Ag_{0.98}Pd_{0.02}$ sample had always a Pd to Ag ratio of 3 at% to 97 at%, which was measured from the XPS peak areas of the Ag3d and Pd3d signal. Upon heating the Pd to Ag ratio decreased. This change in ratio can be seen in Figure S 5a, where the AgPd sample was heated in vacuum with a heating rate of 3°C/min. During the heating ramp the surface concentration of Pd has reduced form 3 at% to 1.6 at%. When the temperature is kept constant at 450°C a steady state Pd concentration of 1.3 at% was reached. The reason for the Pd segregation into the Ag bulk upon heating is the lower surface energy of Ag compared to Pd (more details are given in chapter 3.3).

It was also investigated, whether H_2 induces Pd surface segregation. For this purpose, two different experiments were performed. First, the sample was heated in vacuum at 450°C until a steady state Pd concentration of 1.3 at% was reached, afterwards the sample was cooled down again followed by heating in 1 mbar H_2 with a heating rate of 2°C/min to 450°C. In Figure S 5b (solid line) it can be observed, that the Pd concentration stayed constant during this treatment, hence no surface segregation occurred. Second it was studied, how the surface concentrations changes when the sample is exposed to 1 mbar H_2 directly after sputtering. The dashed curve in Figure S 5b shows that the Pd concentration of 3.5 at% was constant until 180°C and afterwards decreased.

As for the acetylene hydrogenation reaction a high amount of active Pd atoms is required at the surface, Ar^+ sputter cleaning was the only pre-treatment, prior to exposing the sample to reaction conditions. At the reaction temperature of 100°C no bulk segregation of Pd is observed, hence the highest possible Pd concentration at the surface should be present under the applied acetylene hydrogenation conditions (see section 3.2.6.2).

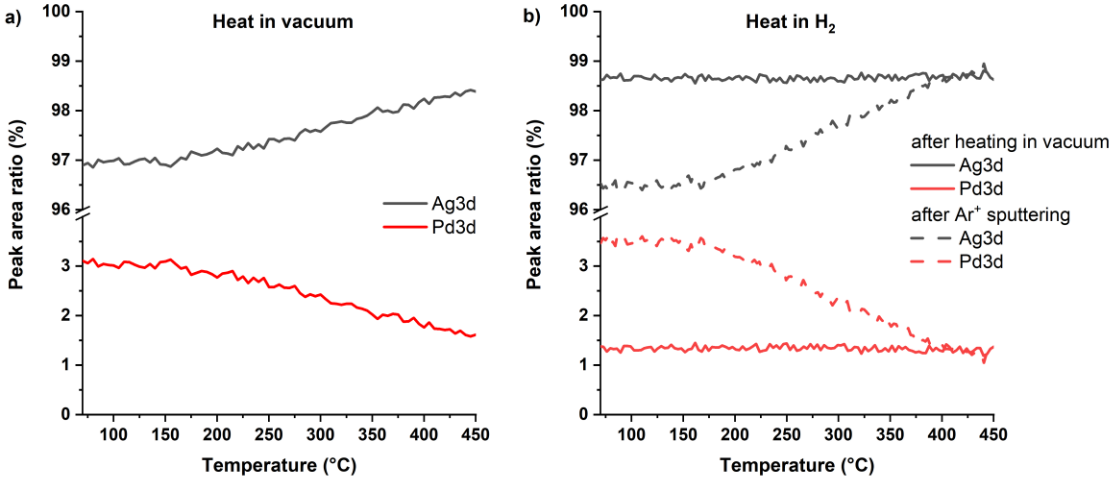

Figure S 5: Changes in the Ag3d to Pd3d ratio; a) when a freshly sputter cleaned $Ag_{0.98}Pd_{0.02}$ sample is heated in vacuum to 450°C with a heating ramp of 3°C/min; b) when the sample is heated (2°C/min) in 1 mbar H_2 after precious vacuum heating to 450°C (solid line) and when the sample is exposed to 1 mbar H_2 directly after sputter cleaning.

3.3 Surface composition of AgPd single-atom alloy catalyst in an oxidative environment

Caroline Hartwig[*], Kevin Schweinar[#], Rachel Nicholls[*], Sebastian Beeg[*], Robert Schlögl[*§], Mark Greiner[*]

[*] Max Planck Institute for Chemical Energy Conversion, Mülheim an der Ruhr, Germany.

[#] Max-Planck Institut für Eisenforschung GmbH, Düsseldorf, Germany.

[§] Fritz Haber Institute of the Max Planck Society, Berlin, Germany.

3.3.1 Abstract

Single-atom alloys (SAA) have recently gained considerable attention in the field of heterogeneous catalysis research, due to their potential for novel catalytic properties. While SAAs are often examined in reactions of reductive atmospheres, like hydrogenation reactions, in the present work, we change the focus to AgPd single-atom alloys in oxidative environments, since Pd has the highest catalytic activity of all metals for oxidative reactions. Here we examine how the chemical reactivity of AgPd SAAs differs from its constituent Pd in an oxidative atmosphere. For this purpose, electronic structure changes of an $Ag_{0.98}Pd_{0.02}$ SAA foil in 1 mbar of O_2 were studied by *in situ* X-ray photoemission spectroscopy (XPS), and compared with the electronic structure of a Pd foil under the same conditions. When heated in an oxidative atmosphere, Pd in $Ag_{0.98}Pd_{0.02}$ partly oxidizes and forms a meta-stable PdO_x surface oxide. By using a peak area modelling procedure, we conclude that PdO_x on $Ag_{0.98}Pd_{0.02}$ is present as thin, possibly monolayer thick, PdO_x islands on the surface. In comparison to the PdO formed on Pd foil, the PdO_x formed on AgPd is substantially less thermodynamically stable, decomposing at temperatures about 270°C lower than the native oxide on Pd. Such behavior is an interesting property of oxides formed on dilute alloys, which could potentially be utilized in catalytic oxidative reactions such as methane oxidation.

3.3.2 Introduction

During the last decade single-atom alloys (SAA) have gained attention in heterogeneous catalysis research, due to their unique structures, and potential for novel catalytic properties. A recently published review paper summarizes most of the work done so far in the field of single-atom alloy catalysis.[2] SAAs are intensively discussed in H_2 dissociation,[10,11,97] selective hydrogenation reactions[14,90–96] and C-H activation.[8] In most reported SAA cases, the dilute, active metal is Pd or

Pt substituted into a noble metal host of group 11 (Cu, Ag, Au).[1-11] This approach has the advantage that only a small amount of the expensive active metal is used.

Several promising properties of SAAs have been reported, such as the prevention of coking,[8] the spillover of adsorbates to different active sites,[10] and improved catalytic selectivity compared to the bulk active metal. These positive effects can be explained by the fact that alloying changes a metal's properties in terms of ensemble- and ligand effects. Ensemble effects refer to the change in coordination environment of atoms on the surface, while ligand effects refers to the change of the electronic structure of metals, which both occur upon alloying.[106]

Some ligand effects include the shifting of the metal's valence *d*-states relative to the Fermi level upon alloying, as described by the *d*-band model of Hammer and Nørskov.[15,21] These effects can be used to tune adsorbate bonding to optimize catalytic activity.[7,44,149,150] Other ligand effects include electronic state localization, whereby weak metal-metal interaction can give rise to very localized electronic states, as reported by Greiner *et al.* in $Ag_{0.995}Cu_{0.005}$.[3] It is expected that such localized electronic states might result in catalysts that resemble homogeneous catalyst active sites.[126,127]

While these features can be engineered into an alloy via chemical synthesis, when these catalysts are put into action, and exposed to reactive atmospheres, their initial structures may not be preserved. For instance, phase segregation via surface oxidation of the more oxophilic metal is known to occur when such alloys are exposed to oxidative atmospheres.[121,151,152] Interestingly, when oxides are formed on SAAs, the low chemical potential of the dilute solute, can result in unique surface-oxide monolayers. For instance, it was reported that a meta-stable 2-dimensional Cu oxide can form on dilute AgCu catalysts in oxidative conditions.[153] In cases where the chemical potential of the solute is high enough, bulk oxide phases form on the surface, such as Cu_2O and CuO, in the case of AgCu.[89] There is evidence that the 2-dimensional Cu oxide on dilute AgCu may be responsible for the improved selectivity in ethylene epoxidation compared to pure Ag.[153,154] Thus, oxides formed on SAAs can exhibit unique properties of their own, as a consequence of low solute concentration. It is important to see which ones are at play under operando conditions to identify structure-property relationships.

In the present work, we focus on AgPd single-atom alloys in oxidative conditions, using operando photoemission spectroscopy. Palladium has the highest catalytic activity of all metals for oxidative reactions,[155] such as the complete oxidation of hydrocarbons in automotive exhaust catalysts and the combustion of methane in gas-powered turbines. Methane is the main component in natural gas, which can be used as fuel. Since methane has a greenhouse gas potential approximately 33 times higher as CO_2,[120,156] efficient methane combustion at low temperatures is therefore crucial to avoid harmful methane emission. Usually temperatures above 300°C are used for Pd catalysts.[157,158]

Very important in this reaction is the oxidation state of Pd. Depending on the O_2 partial pressure and the temperature, Pd metal can be reversibly converted to PdO, e.g. at 1 atm O_2, PdO decomposes to Pd metal at 877°C.[159] Furthermore it was reported that a Pd_5O_4 surface oxide forms at room temperature, which is assumed to be the precursor to PdO formation.[65,67,160] Many research groups observed an activity hysteresis with Pd catalysts, i.e. differing methane combustion rates when heating or cooling the catalyst.[161–163] Such observations indicate that the Pd-O system is very dynamic, which is one reason why its catalytic mechanism is still under debate, and the focus of ongoing research. For instance, it is uncertain whether metallic Pd,[159,164] PdO,[63,165,166] a coexistence of both[167–169] or a surface Pd oxide[160] is the most active phase in methane combustion.

We begin this study examining the intrinsic oxidation behavior of Pd and AgPd by exposing them to a pure O_2 atmosphere. When AgPd is placed in an oxidizing environment, O_2-induced Pd surface segregation is expected, since Pd has a higher oxygen affinity compared to Ag. In a recent study van Spronsen *et al*. found surface segregation of Pd in Pd/Ag(111) in 1 Torr O_2 already at 400 K.[121] Kitchin *et al.*[170] investigated the surface segregation of an $Ag_3Pd(111)$ alloy in O_2 atmosphere using first-principal atomistic thermodynamics. Thereby they considered the interplay between surface segregation energies, oxygen binding energies and the gas phase chemical potential, as well as how these properties depend on the bulk alloy reservoir (Ag – or Pd rich alloy phase). Their results showed that Pd segregation is favored, as the oxygen chemical potential increases, and at higher temperatures a higher oxygen pressure is required to drive Pd surface segregation.[170,171] When Pd in the AgPd alloy is in its metallic state, Ag is preferred at the surface, due to its lower surface energy and lower cohesive energy.[35,36,148] From those studies, it follows that structure of an alloy's surface depends on many parameters, such as the catalyst pre-treatment, the temperature, the chemical potential of the reactive atmosphere and the composition of the alloy.

In the experiments exhibited here, $Ag_{0.98}Pd_{0.02}$ and bulk Pd are heated to temperatures ranging from 70°C to 400°C, in an atmosphere of 1 mbar O_2. We found that Pd in the AgPd alloy oxidizes at substantially lower temperatures compared to pure palladium, and also decomposes at lower temperatures. In-depth XPS analysis and a peak area modelling procedure suggests that a meta-stable PdO_x phase forms as thin, possibly monolayer thick, islands on the AgPd surface. From these observations, it is clear that the Pd-oxides formed on AgPd are considerably less stable than those formed on bulk Pd. The reason for this difference in stability is likely due to the high solubility of Pd in Ag, and the lower surface energy of Ag compared to Pd. This decrease in oxide stability is expected to influence how catalytically active the alloy's surface oxygen species are, and could potentially lead to, for example, methane combustion of the SAA at lower temperatures compared to pure palladium. We show that the meta-stable PdO_x surface oxide on AgPd is also present under methane oxidation conditions.

3.3.3 Experimental section

3.3.3.1 Synthesis of the $Ag_{0.98}Pd_{0.02}$ alloy

Quantitative amounts of the Ag (slugs 3×3mm, 99.99%) and Pd (granules <7mm, 99.95%) purchased from EvoChem were melted in a light oven, with a four times re-melting process for homogenization. Afterwards the alloy was cold-rolled to a 1.6 mm thick foil and then annealed for 6h at 800°C for grain size growth. The foil was cut into smaller pieces and polished, with incrementally finer grid, down to a 1 µm using diamond suspension. After additional Ar^+ sputtering and annealing (in O_2 and H_2 atmospheres) cycles, the grains of the polycrystalline $Ag_{0.98}Pd_{0.02}$ foil became visible under the scanning electron microscope. Through annealing in 0.5 mbar O_2 at 500°C, impurities such as Cu, K, S, Si, Cl came to the surface and could then be sputtered off by Ar^+ bombardment. This procedure was repeated several times to clean the sample. The last step was heating in UHV at 500°C for recrystallization.

3.3.3.2 Polycrystalline Pd foil

The 0.1 mm thick Pd foil from Alfa Aesar (99.9%) was cut into a 5×6mm piece and subsequently cleaned by several cycles of Ar^+ sputtering and annealing (in 0.5 mbar O_2 (see above)) at 700°C. The last step was heating in UHV at 700°C for recrystallization.

3.3.3.3 *In situ* XPS study

For the *in situ* XPS measurements, from which the working principal is explained elsewhere,[57] two different near ambient pressure (NAP) XPS setups were used; (i) a lab source (NAP) XPS using monochromatic Al Kα (1487 eV) radiation and a Phoibos NAP-150 hemispherical analyzer from SPECS GmbH, and (ii) the (NAP) XPS setup at the UE56-2_PGM1 beamline at Bessy II, which is also equipped with a hemispherical analyzer from SPECS. In both setups the samples were heated using an IR Laser from the rear, and the temperature was measured by a K-type thermocouple fastened between the sample and a mask, used to fix the specimen to the sample holder.

The heating and cooling ramp of the $Ag_{0.98}Pd_{0.02}$ alloy in 1 mbar of O_2 were performed with the lab source (NAP) XPS. After Ar^+ sputter cleaning, the sample was annealed in 0.5 mbar H_2 at 450°C for 30 min prior to oxidation in order to reach a steady state Pd surface concentration. The sample was than cooled to 70°C followed by taking reference spectra in vacuum. Afterwards 1 mbar O_2 was introduced and the position of the pressure regulating throttle valve was held at a fixed position. This should minimize gas expansion effects, which leads to increases in the XPS intensity at elevated temperatures, due to minimized inelastic scattering with the gas molecules[172]. As a consequence, the pressure in the XPS chamber slightly increases with increasing temperature. The sample was heated with a very low heating speed of 0.3°C/min from 70°C to 400°C (see Figure 3-13). After the heating ramp the sample was cooled in O_2 to 70°C using the same ramping conditions (see Figure 3-14).

To check the reproducibility of the observed behavior this whole process was performed twice, but with a faster heating speed of 1°C/min and also the pre-treatment was slightly different (0.5 mbar H_2, 400°C, for 2h) (see Figure 3-15).

Spectra were measured during the temperature ramps using ‘loops’, where each loop consists of a set of XPS spectra (Ag3d, Pd3d, O1s, $Pd3p_{3/2}$, S2p). Using this procedure, one obtains a high temperature resolution. All spectra measured in the same loop are labelled using the average temperature during that loop, but since they are not recorded at the same time the real temperature can differ by a few degrees Celsius.

The drawback of this loop-procedure is, that each spectrum is measured relatively quickly, and therefore the spectra are quite noisy, but the signal-to-noise ratio can be very much improved while retaining the time resolution, using principal component analysis (PCA). All XPS spectra shown in this publication are treated with the PCA noise reduction using CasaXPS 2.3.23.

To compare the oxidation behavior of AgPd with that of bulk Pd, a Pd foil was also oxidized using the laboratory source XPS. For this the Pd foil was pre-treated in the same way as the alloy sample and afterwards heated from 70°C to 750°C in 1 mbar O_2 with a temperature ramping speed of 0.4°C/min. Also in this case PCA noise reduction was applied.

Besides, the electronic structure of the Pd foil and $Ag_{0.98}Pd_{0.02}$ under methane oxidation conditions was studied. For this study a O_2 to CH_4 ratio of 5:1 was chosen, which is the same reactants ratio as it was previously reported for methane oxidation on Pd(111), studied by *in situ* XPS.[160]

Reference spectra were utilized for peak fitting. The reference spectra were measured in vacuum, a Tougaard background was applied. Additional components that arose during the oxidation process, for which reference spectra are not available (such as sub-oxide species), were fit using synthetic line shapes of a Voigt form. One difficulty when analyzing these spectra is that the O1s and Pd3p$_{3/2}$ spectra are overlapping. Additionally, O1s spectra are in general difficult to fit, due to the presence of different kinds of O1s species at the same time and small binding energy differences. Therefore, one needs to add constrains on the peak position and FWHM when fitting O1s species, but also after doing so, there is still a high uncertainty associated with the peak fit of O1s signals.

Table 3-1. Summary of experiments performed for this work, the experiment IDs will be used in the main text. The results of EX4 (SI) and EX5 (SI) are shown in the supplementary information.

Experiment ID	Sample	Instrument	Oxidation conditions	Pre-treatment
EX1	Pd foil	Lab-XPS; Al K_α radiation	Heating in 1 mbar O_2; 70°C-750°C 0.4°C/min	Ar^+ sputter cleaning; Reduction in 0.5 mbar H_2 at 450°C for 2h
EX2	$Ag_{0.98}Pd_{0.02}$	Lab-XPS; Al K_α radiation	Heating and cooling in 1 mbar O_2; 70-400°C; 0.3°C/min;	Ar^+ sputter cleaning; Reduction in 0.5 mbar H_2 at 450°C for 2h
EX3	$Ag_{0.98}Pd_{0.02}$	Lab-XPS; Al K_α radiation	Heating and cooling in 1 mbar O_2; 70-400°C; 1°C/min; several cycles	Ar^+ sputter cleaning; Reduction in 0.5 mbar H_2 for 2h
EX4 (SI)	$Ag_{0.98}Pd_{0.02}$	Synchrotron; excitation energy chose in a way that kinetic energy of photoelectrons is 150 eV	Heating in 1 mbar O_2; 100-326°C; 1°C/min	Ar^+ sputter cleaning
EX5 (SI)	$Ag_{0.98}Pd_{0.02}$	Lab-XPS; Al K_α radiation	Heating to 180°C, various O_2 pressures (0.1, 0.3, 0.5, 0.7, 1.0 mbar), stay at each pressure for 1 h	Ar^+ sputter cleaning
EX6	$Ag_{0.98}Pd_{0.02}$	Lab-XPS; Al K_α radiation	Heating in 1mbar O_2:CH_4:N_2 (5:1:2); 70°C-500°C; 1.0°C/min	Ar^+ sputter cleaning
EX7	Pd foil	Lab-XPS; Al K_α radiation	Heating in 1mbar O_2:CH_4:N_2 (5:1:2); 70°C-500°C; 1.5°C/min	Ar^+ sputter cleaning

Table 3-1 summarizes the experiments performed in this work, including the sample type, the instrument used to perform the experiment, the oxidation conditions and the pre-treatment. In order to avoid repeating the experiment specifications in the main text, each experiment is assigned to an experiment ID, which will be used to refer to a certain experiment. The results and experimental procedure of experiment EX4 and EX5 are discussed in more detail in the supplementary information.

3.3.4 Results and discussion

3.3.4.1 *In situ* oxidation of pure palladium

In this work the oxidation behavior of the AgPd single-atom alloy foil is compared with those of a polycrystalline Pd foil. Several *in situ* XPS investigations of palladium oxidation have been previously published. We summarize here the main findings from their analyses of the core-level spectra. In 2002, Lundgren *et al.* found, by a combination of STM, surface XRD, high resolution XPS and DFT calculations, a meta-stable two-dimensional Pd_5O_4 surface oxide species, where the corresponding $Pd3d_{5/2}$ emission line consists of two peaks at 335.5 eV and 336.2 eV with a ratio of 4:1 on a Pd(111) single crystal.[65] The corresponding two O1s lines have a ratio of 1:1 and are 3-fold and 4-fold coordinated to Pd. *In situ* XPS oxidation studies of Pd(111) reveal that this Pd_5O_4 surface oxide is the precursor species for the bulk PdO phase.[66,67] The XPS signals related to the Pd_5O_4 species were labeled Pd-ox(I), Pd-ox(II) (in the $Pd3d_{5/2}$ spectral region), as well as O(I) and O(II) (in the O1s spectral region). The same peak labels are used in this work. In that study the Pd-ox(II) signal was allowed to shift to become the bulk PdO species.[66] Ketteler *et al.* tried to experimentally determine, by *in situ* XPS, the phase diagram of Pd(111) as a function of the pressure and temperature. Thereby the high dynamic of the Pd/O system became evident, since they found chemisorbed oxide phases, surface oxides, possible sub-surface oxides and bulk PdO.[173]

Figure 3-11 shows the *in situ* XPS spectra of Pd oxidation from the present study. The plots show the Pd3d, $Pd3p_{3/2}$ and O1s spectra of the polycrystalline Pd foil during a heating ramp in 1 mbar of O_2 (EX1). The temperature starts at 160°C in this analysis, because below that temperature carbon contaminations, originating from hydrocarbons sticking to the side walls of the XPS chamber and which lead to additional signals[130,174,175] that are not relevant for this analysis, were present.

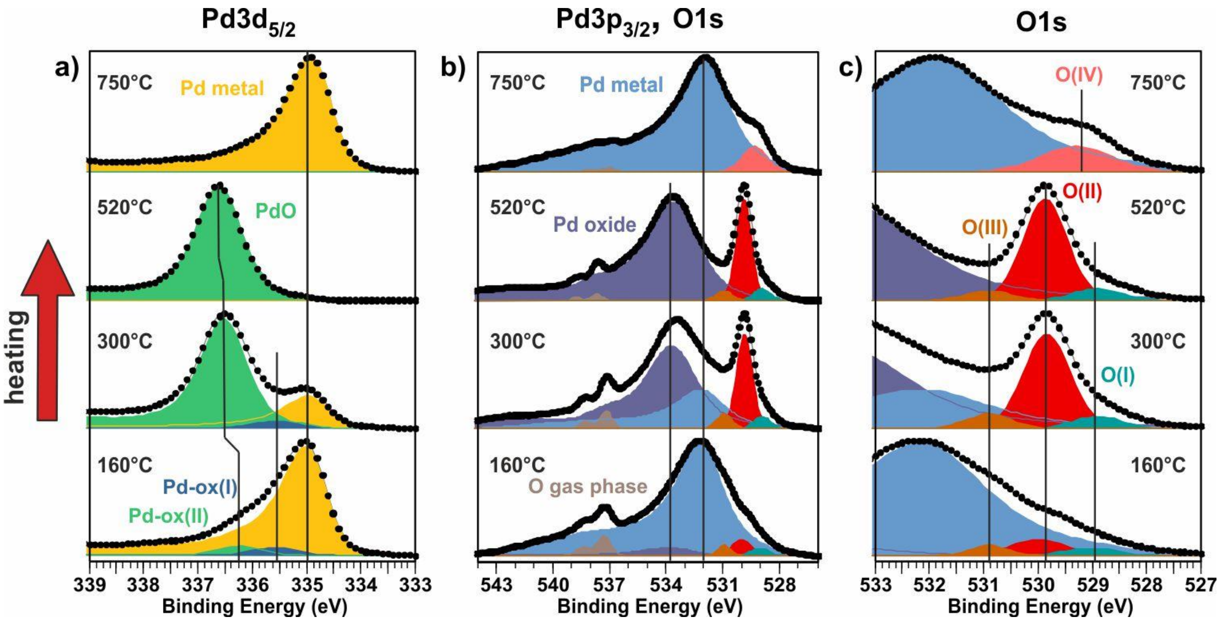

Figure 3-11: Pd3d$_{5/2}$ (a) and Pd3p$_{3/2}$, O1s (b) and (zoomed) O1s XPS spectra of the Pd foil during heating in 1 mbar O$_2$. The black circles represent the measured points after PCA noise reduction and background subtraction. Note, the ordinate axis in the spectra are normalized to maximum intensity.

In the Pd3d spectrum, three species could be differentiated: Pd metal, Pd-ox(I) and Pd-ox(II). Pd-ox(I) and Pd-ox(II) are assigned to a surface oxide precursor species, whereby, in the fitting procedure, the Pd-ox(II) peak is allowed to shift a bit as it transitions into the bulk PdO species. The binding energy for those core-level species is consistent with previous reports of Pd oxidation.[65,66,173]

The O1s signals overlap with the Pd3p$_{3/2}$ signal and the O1s gas phase signal (Figure 3-11b), which makes precise analysis of the oxygen species challenging. Using the Pd3p$_{3/2}$ signal from the reduced state of Pd, measured in vacuum as a reference spectrum, we can differentiate between the peaks of the metal and the oxide. With the help of previous O1s peak models from the published literature, we distinguish four O1s species: O(I), O(II), O(III) and O(IV).[66,176,177]

Before going into detail of the chemical characteristics of each species, we will have a closer look on how the peak areas change with temperature. Figure 3-12 shows line profiles, representing the XPS peak areas of each species documented here, as a function of time. The 'onset oxidation temperature' (OOT) we define here as the intercept between the baseline, and the line of the steepest slope of the line profile. In the same manner, the 'onset oxide decomposition temperature' (OODT) is defined. During heating, the OOT is at around 240°C. This is the point where PdO begins to grow on the surface. The PdO layer becomes at least 4.5 nm (3λ) thick, as is inferred from the fact that no more Pd metal signal could be detected at 440°C. At 590°C (OODT) PdO decomposes very rapidly to Pd metal.

Concurrent with the formation and decomposition of PdO, the O(II) signal increases and decreases, respectively (Figure 3-12b). This correlation between peak intensities is used to infer that the O(II) component represents the oxygen species of the PdO phase (i.e. lattice oxygen).

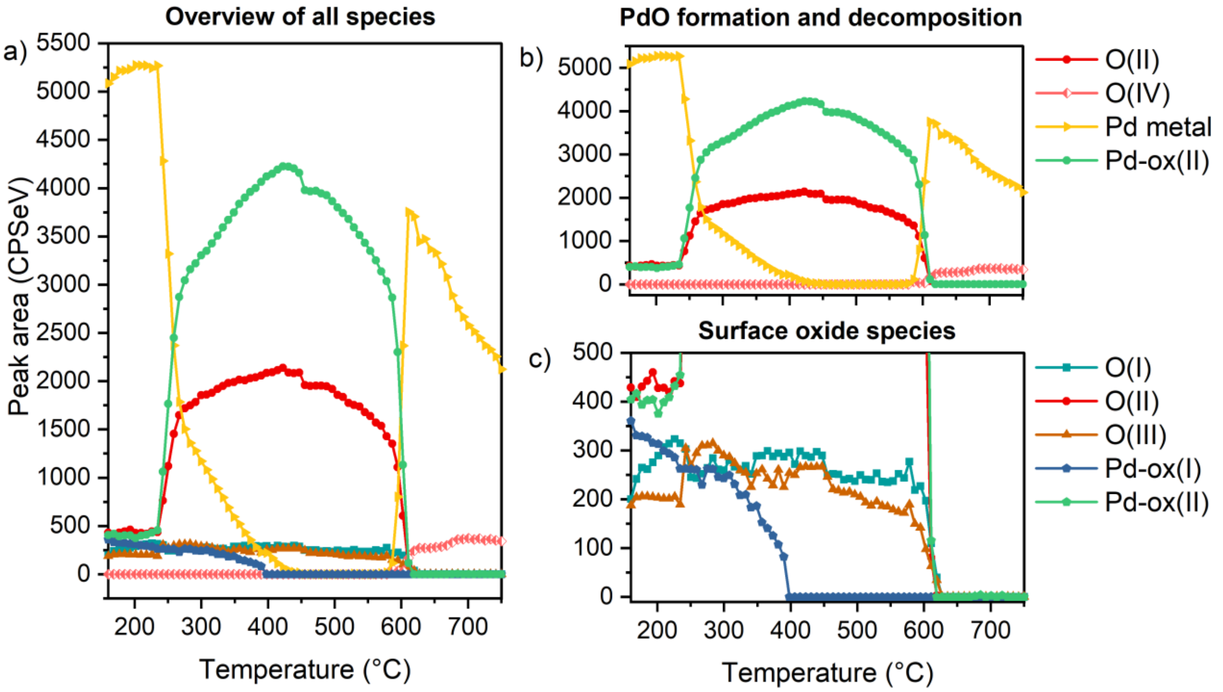

Figure 3-12: a) Peak area line profile of all relevant synthetic components as a function of temperature during heating of a polycrystalline Pd foil in 1 mbar O_2; b) Peak area line profile of Pd metal, Pd-ox(II), O(II) and O(IV), which shows the main trend of PdO formation and decomposition; c) Line profile of the less intensive synthetic components O(I), O(II), O(III), Pd-ox(I) and Pd-ox(II), which represent surface oxide species.

In the Pd-ox(II) and O(II) line profile of Figure 3-12b, one can observe a plateau below 240°C. This plateau in intensities of these features indicates that the O(I), O(III) and Pd-ox(I) species have already formed (Figure 3-12c). In agreement with previous literature, this observation would suggest that, under these conditions the oxide precursor species has already formed on the surface. The corresponding peak positions of Pd-ox(I) (335.55 eV), Pd-ox(II) (336.2 eV), O(I) (528.9 eV) and O(II) (529.8 eV) match well with the 2D Pd_5O_4 precursor species.[65,66] However, in the line profile (Figure 3-12c) one cans see that the area ratios of Pd-ox(I) to Pd-ox(II) (below 240°C) is substantially different from the previously reported 4:1 ratio.[65] In the present data-set, Pd-ox(II) has even a higher concentration than Pd-ox(I). We attribute this discrepancy to the fact that the sample investigated here is poly-crystalline, while the Pd_5O_4 surface oxide reported previously was from Pd(111).[65] It is expected that different metal surface orientations can form monolayer-oxides of differing stoichiometries, differing symmetries, and consequently, differing XPS peak ratios. Additionally, oxygen can also adsorb disorderly (e.g. on step edges), which influences the Pd3d$_{5/2}$ peak ratio.[66,173] Furthermore, a kinetic XPS study of Pd oxidation found that the PdO nucleation on Pd(110) proceeded at ∼100°C lower temperatures than on Pd(111).[176] XPS just provides an average electronic structure, therefore it might be possible that the Pd oxidation towards PdO may be more progressed on some grains than on others, which also affects the Pd-ox(I) to Pd-ox(II) ratio.

As the temperature increases further, the Pd-ox(II) signal shifts from 336.2 eV to 336.6 eV, and the intensities of the Pd-ox(I) and Pd metal species decrease. At 410°C, only the Pd-ox(II) signal is present, indicating that a thick film of bulk PdO has formed on the surface. The O1s spectrum of the PdO species exhibits two peaks: O(I) at 528.9 eV, and the more intense O(II) at 529.8 eV. Depth profiling indicates that O(I) originates from an oxygen-terminated PdO surface.[173] The line profile in Figure 2 shows that, from the beginning of the temperature ramp until the point that PdO decomposes, this O(I) species is present, and has a constant peak area. After PdO has completely decomposed, the O(I) species is no longer present. These observations are consistent with the interpretation that the O(I) species is due to an oxygen-terminated surface. The O(II) species, on the other hand, has the same binding energy as one of the precursor species; however, it strongly increases when PdO begins to form, which is consistent with the interpretation that O(II) is from lattice oxygen in PdO

In addition to these two oxide-related species, we observe an O1s species at 530.9 eV (O(III)). An oxygen species of this binding energy on Pd has also been previously reported,[176,177] and was attributed to hydroxyl groups.[177] Hydroxyl formation is also very likely in our case, since the sample was pretreated in H_2, which can lead to some PdH formation. The hydrides of PdH may then later bind to oxygen. The O(III) species also disappears as PdO decomposes, at around 600°C, and during this process another O1s species arises at 529.3 eV (O(IV)). A species of this binding energy has previously been suggested to be dissolved oxygen,[66] however, impurities bound to oxygen could also be a candidate for this species.

It should be noted that in the present work, we measured Pd oxidation with an Al K$_\alpha$ source (1487 eV), which is less surface sensitive than the photon energies used in the cited Pd oxidation studies, measured with synchrotron radiation. Therefore, we are less sensitive for surface oxide species, leading to very low signal intensities, and consequently to uncertainties and fluctuations in the peak fit.

3.3.4.2 *In situ* XPS oxidation of AgPd at 1 mbar

For comparison with the oxidation of bulk Pd, we performed an identical heating ramp, in O_2, on an AgPd single-atom alloy. The behavior of the chemical species on the surface is quite complex, as multiple chemical species are present simultaneously, and their relative concentrations change dynamically during the temperature ramp. We provide a detailed discussion in identifying the many peaks observed in the XPS spectra; however, the most clear and obvious take-away from this investigation is as follows: When the AgPd SAA is heated in O_2, the Pd becomes preferentially oxidized, and forms an oxide over-layer, similar to the case of bulk Pd oxidation, however, the oxide formed on the AgPd SAA does not form a thick layer, and it thermally decomposes at a much lower temperature (ca. 270°C lower) than does the oxide formed on Pd.

Before going into detail about the oxidative properties of $Ag_{0.98}Pd_{0.02}$, it is important to mention that we validated the homogeneous distribution of Pd in the Ag host by spectroscopic methods to ensure that the alloy is indeed a SAA.[74] Figure 3-13 shows the Pd3d, O1s / $Pd3p_{3/2}$ and Ag3d spectra measured during the heating ramp in 1 mbar O_2 (EX2).

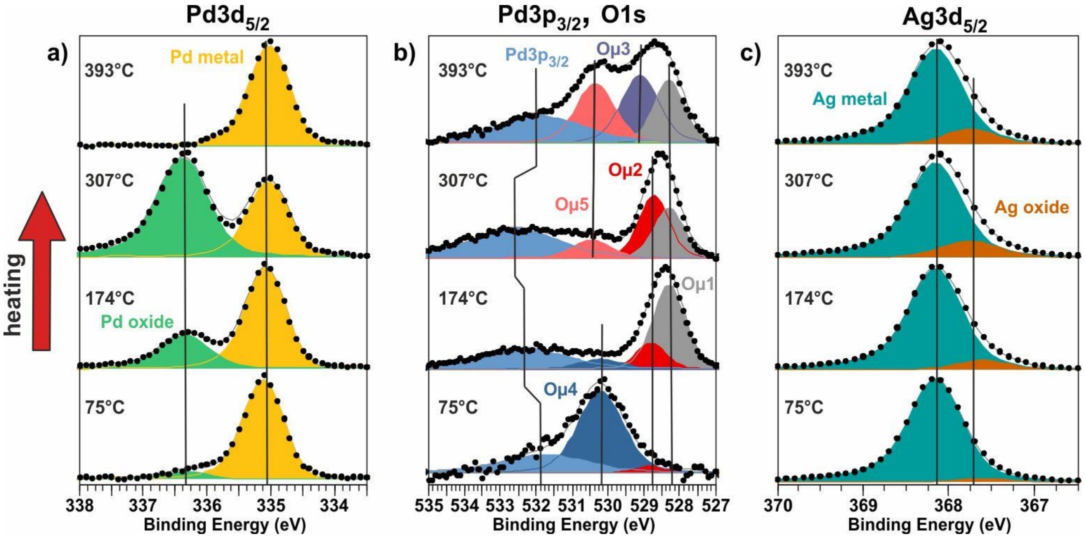

Figure 3-13: Comparison of XPS spectra of a) $Pd3d_{5/2}$, b) $Pd3p_{3/2}$ / O1s and c) $Ag3d_{5/2}$ during heating in 1 mbar O_2 from 70°C to 400°C. The black circles represent the measured points after PCA noise reduction and background subtraction; the gray envelope is the sum of the synthetic compounds. The ordinate axis in the spectra are normalized.

Figure 3-14 represents the same spectral regions during the cooling ramp. Noise reduction using PCA, was performed on these spectra in order to achieve both time resolution and signal quality.

After applying PCA noise reduction on the cooling data, some sulfur impurities could be detected that were not present during heating and because of the low signal-to-noise ratio of the S2p signal, there is a high uncertainty associated with its intensity and line shape. Note, that silicon, which is a very common impurity in Ag, could not be detected during heating and cooling in O_2.

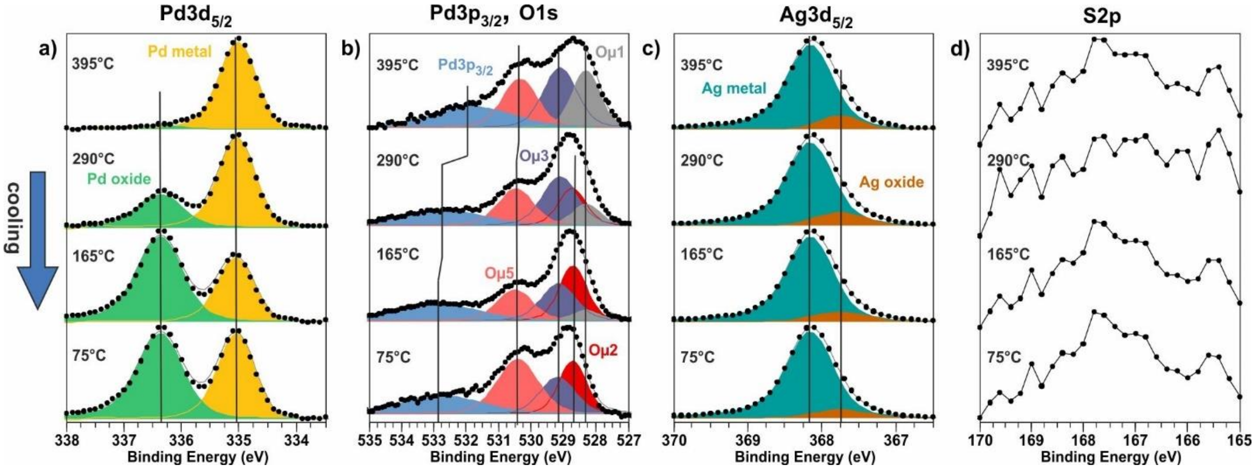

Figure 3-14: Comparison of spectra during cooling in 1 mbar O_2. a) $Pd3d_{5/2}$; b) O1s and $Pd3p_{3/2}$ spectra; c) $Ag3d_{5/2}$ spectra; d) S2p spectra. The black circles represent the measured points after PCA noise reduction and background subtraction; the gray envelope is the sum of the synthetic compounds. The ordinate values of the spectra are min-to-max normalized.

As the temperature increases beyond 100°C, an oxidized form of Pd becomes apparent in the Pd3d spectrum, with the appearance of a peak at 336.35 eV (i.e. shifted 1.3 eV to higher binding energy compared to the metallic Pd peak at 335.05 eV). As the temperature goes beyond 320°C, the Pd oxide thermally decomposes, leaving behind metallic Pd, as shown in Figure 3-13a. Note, this temperature is ca. 270°C lower than the temperature at which PdO decomposed on bulk Pd.

After decomposition of the oxidized Pd species, the sample was cooled to room temperature at a constant rate. During cooling, the Pd oxide re-forms, with a hysteresis in formation temperature, whereby the oxide begins to form at a lower temperature than the temperature at which it decomposed during the heating ramp. Additionally, the oxide persists after cooling to room temperature in oxygen (Figure 3-14a) and remains stable in vacuum.

The hysteresis in oxide stability temperature, during heating and cooling, can be clearly seen line profiles in Figure 3-15 (EX3), where the peak area of Pd metal and Pd oxide are plotted as a function of temperature. As seen here, Pd begins to oxidize at 70°C, reaches its maximum intensity at 295°C, and becomes fully decomposed by 375°C. During cooling, the oxide begins to re-form at an OOT of 335°C, reaching its maximum intensity at 220°C, after which its intensity remains constant. The Pd oxide signal intensity during cooling is observed to be higher than during heating.

When heating the sample for a second time, the Pd oxide OODT is at 285°C, that is, 15°C lower than during the first heating ramp. The complete decomposition, however, is reached at the same temperature in both cases (Figure 3-15a).

In Figure 3-15b) the same pre-treatment, heating and cooling ramp was repeated. During cooling the results are very reproducible, as can be seen from the overlap between the black and blue profiles in Figure 5b). During the second heating, a slightly higher Pd oxide intensity is measured (green solid line). The main outcome of the line profiles in Figure 3-15 is that the heating and cooling experiment in oxygen can be well reproduced.

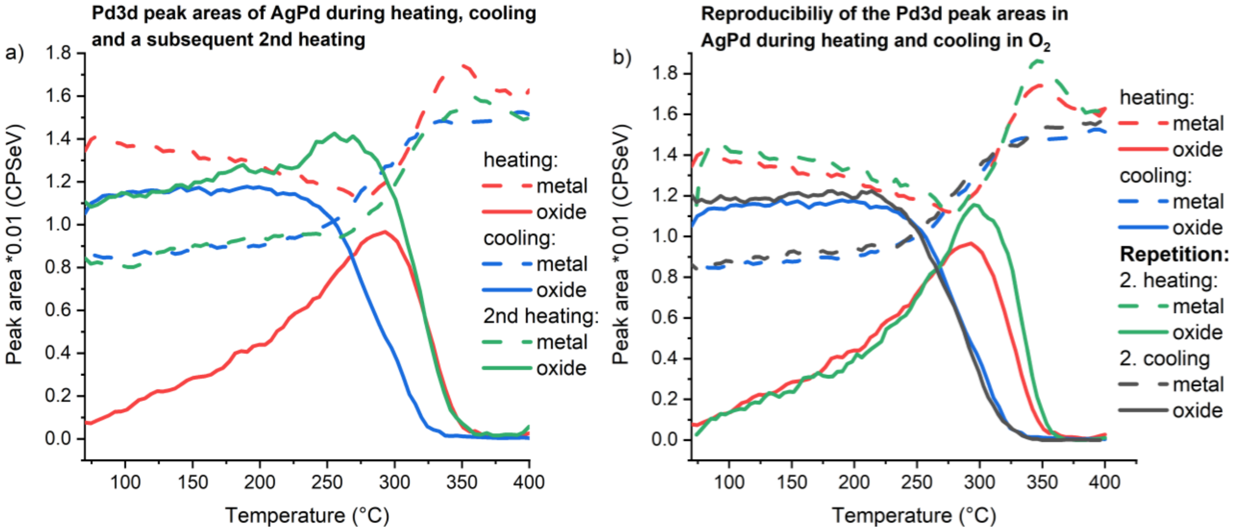

Figure 3-15: The graphs represent the intensity of the Pd oxide and the Pd metal Pd3d peak as a function of the temperature during heating and cooling of $Ag_{0.98}Pd_{0.02}$ in 1 mbar O_2; in a) a second heating was performed directly after the cooling. Whereas in figure b) the reproducibility was tested by performing the same heating and cooling experiment twice, the sample had the same sputter and reduction pre-treatment in each run.

After having discussed how the Pd3d species change with temperature, we will now have a closer look onto the O1s species to see how they correlate with Pd oxide formation. The investigation of the O1s species is the most complex of the analyses, because of the many oxygen species present on the surface. In Figure 3-13b one can see that we fitted the $Pd3p_{3/2}$ / O1s spectrum using 6 different species, which have only slight binding energy differences. The use of so many peaks is problematic, because it means that there is a high degree of uncertainty in the fitting model. Unfortunately, this is a fact one must live with in this case, because prior knowledge of Ag and Pd in oxygen tells us that at least 5 species of oxygen could form, e.g. oxygen from Ag_2O, PdO, Pd_5O_4, and from several O-adsorbate configurations on Ag and on Pd (as well as oxygen bound to impurities). Additionally, all the O1s peaks are overlaid on top of the Pd3p$_{3/2}$ peak, which complicates the analysis even further.

Depending on the degree of Pd oxide on the surface, the Pd3p$_{3/2}$ peak shifts between 531.8 eV (metallic) and 532.9 eV (mixture of Pd metal and oxide). A differentiation between Pd3p$_{3/2}$ metal and the Pd3p$_{3/2}$ oxide component was not possible due to the high FWHM of the peak and small chemical shift between the two states.

Based on a peak model that remains consistent for all data in the dataset, we arrive at five different O1s species (Oμ1, Oμ2, Oμ3, Oμ4, Oμ5). It is worth mentioning that in literature about Ag-O species one often distinguishes between 'electrophilic' (O$_{elec}$) and 'nucleophilic' (O$_{nuc}$) oxygen species.[178,179] The binding energy of the Oμ1, Oμ2 and Oμ3 species lay in the region of the nucleophilic O1s species and Oμ3 as well as Oμ4 have binding energies similar to the electrophilic oxygen species. It is important to note that there are even more possible oxygen species related to Pd,[45] Ag[42] or impurities,[48] which we possibly could not detect with certainty due to very little differences in the chemical shift, and a lower surface sensitivity compared measurements using synchrotron radiation.

Figure 3-16 shows the trends in peak area, for all species measured, as a function of time during the temperature ramp. The line profile in Figure 3-16b shows that the Oμ2 (528.7 eV) increases when the Pd oxide forms, and disappears after the Pd oxide decomposes. This correlation suggests that the Oμ2 species is from the Pd oxide. At lower binding energy, there is the Oμ1 signal (528.3 eV), which is still present after the Pd oxide has decomposed. Additionally, a Oμ3 signal at 529.1 eV arises as the Pd oxide decomposes. Furthermore, there is a relatively intense Oμ4 (530.2 eV) below 120°C during heating.

This Oμ4 (530.2 eV) species at low temperatures can be assigned to disordered atomically adsorbed oxygen on Ag, as previously reported.[182] The peak area at 530.2 eV is low at temperatures between 130°C and 280°C, then increases again at temperatures greater than 300°C. We assume that the peak that forms at temperatures greater than 300°C is actually a chemically distinct species from Oμ4. Thus, we introduce a species labelled Oμ5, which has a very similar binding energy to Oμ4, but represents a different chemical entity. This interpretation is reasonable, since atomically adsorbed oxygen on Ag is unstable at temperatures above 300°C; however, the actual transition temperature form Oμ4 to Oμ5 is uncertain, since these peaks are highly overlapped (Figure 3-16c).

From the broadening of the Ag3d$_{5/2}$ signals (Figure 3-13c), it is apparent that Ag oxide species are present on the surface.[180] To fit this line shape, a reference spectrum of Ag3d in the reduced state was chosen, and an oxide component was added to the low binding energy side, which was allowed to shift between 367.6 eV and 367.75 eV. The intensity of the Ag oxide increases until 300°C, and afterwards decreases slightly.

The position of Oµ1 of 528.3 eV is consistent with the reported binding energy of the common Ag-O reconstruction, called p(4×4)-O reconstruction on a Ag(111) surface (528.1 eV,[182] 528.3 eV,[180] 528.2-528.5 eV[88]). Consistent with this interpretation, we see that both Oµ1 and Ag oxide signals are correlated, and increase together at temperatures below 170°C (Figure 3-16c). At higher temperatures the Oµ5 and Oµ3 species formed. These species might also correlate with the Ag oxide intensity. Additionally, the number of Pd neighbors influences the broadening of the Ag.[121,177] The coordination number might change as Pd segregates to the surface to become oxidized. Consequently, a high uncertainty is associated with the intensity and chemical shift of the Ag oxide component. The Oµ3 species has a binding energy of 529.1 eV, this agrees with an oxide species on a Ag surface called Oα$_2$.[180] The origin of this species is still unknown. It is known that the signal increases with higher temperatures and is unstable in inert atmosphere or vacuum.

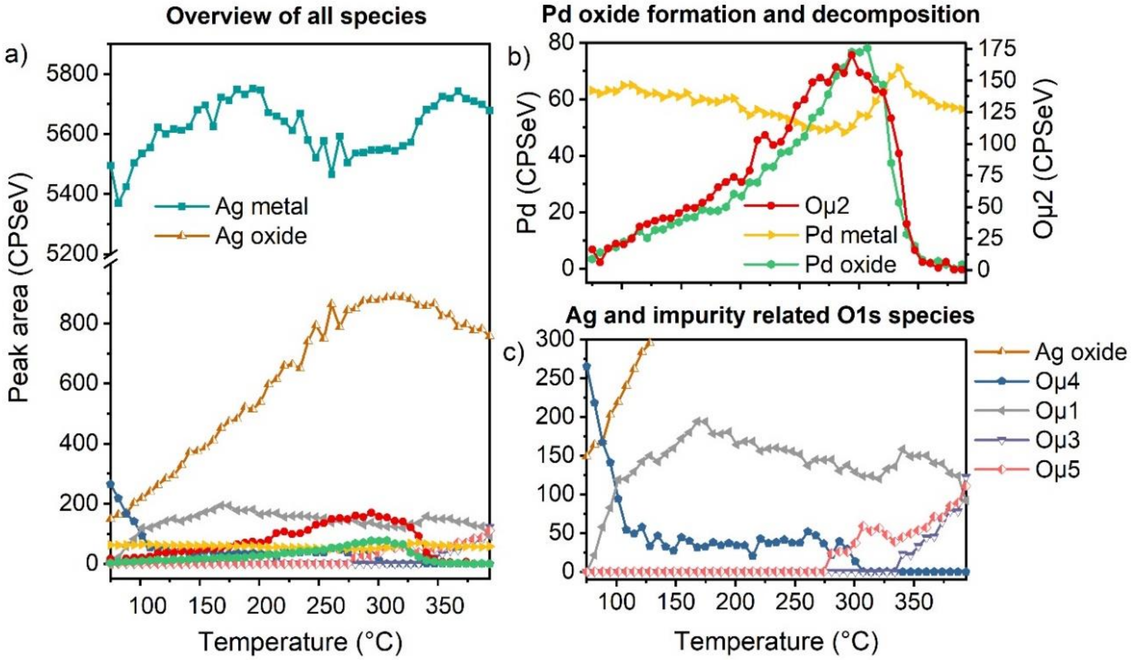

Figure 3-16: a) Peak area-line profile of all relevant synthetic components of Ag$_{0.98}$Pd$_{0.02}$ as a function of temperature during heating in 1 mbar O$_2$; b) Temperature-line profile showing the formation and decomposition of the surface Pd oxide. Oµ2 is plotted with its own y-scale to better see the correlation with Pd oxide; c) Profile of the O1s species, which are related to Ag or impurities.

At this point of analysis, no clear correlations between the Ag and Pd oxide and the Oµ5 species at 530.3 eV could be drawn, which leads to the assumption that it could be an impurity related oxide. Impurities and foreign atom such as Pd segregate to the surface of Ag in oxidative atmosphere, thereby they form nanostructures or even build layered structures when they wet the oxidized Ag surface. In this study it seems that the Pd oxide wet the Ag surface oxide. Besides Pd3d and O1s a very weak S2p signal was measured during cooling (see Figure 3-14d and the temperature-line profile in Figure S 6). On a Ag(111) surface, adsorbed SO_4 is supposed to have a binding energy of 530.2 eV and a SO_4 induced reconstruction, called ((7×√3)rect) a binding energy of 530.7 eV.[88] Hence, we assume that the Oµ5 species is correlated with the S2p signal. Since the lab XPS spectrometer with Al Kα radiation has a very low sulfur sensitivity, the S2p signal intensity highly fluctuates, and no clear temperature trend could be observed.

In order to verify the correlation between the Oµ5 species and SO_4 formation on the surface, similar measurements were performed using synchrotron radiation (EX4), which enables a much higher surface sensitivity compared to Al Kα radiation, since the photon energy can be tuned.

The main outcome of the oxidation of $Ag_{0.98}Pd_{0.02}$ using synchrotron radiation is that a pronounced S2p peak could be detected with increasing temperature, which is linearly correlated with the formation of the Oµ5 species. Additionally, the valence band was investigated showing corresponding S3p and O2p species. The binding energy of the S2p and Oµ5 species verify that indeed a SO_4 – induced reconstruction has formed (see SI Figure S 7 and Figure S 8).

3.3.4.3 Comparison of the $Ag_{0.98}Pd_{0.02}$ oxidation with pure palladium

The oxidation behavior of Pd in AgPd and bulk Pd are similar in the sense that, in both cases, Pd begins in a metallic state, then forms a Pd-oxide on the surface, followed by thermal decomposition at higher temperatures. The most striking difference between the two cases is that the thermal decomposition temperature differs by ca. 270°C. That is, the Pd-oxide formed on AgPd decomposes at a temperature 270°C lower than does the oxide formed on Pd. This difference will be emphasized here with a comparison of the Pd3d oxide and metal signals from the two samples (polycrystalline Pd foil and the AgPd SAA foil), as shown in (Figure 3-17). It was found that the Pd oxide on the AgPd alloy decomposes already around 320°C, whereas the PdO oxide formed on bulk Pd decomposes at 590°C.

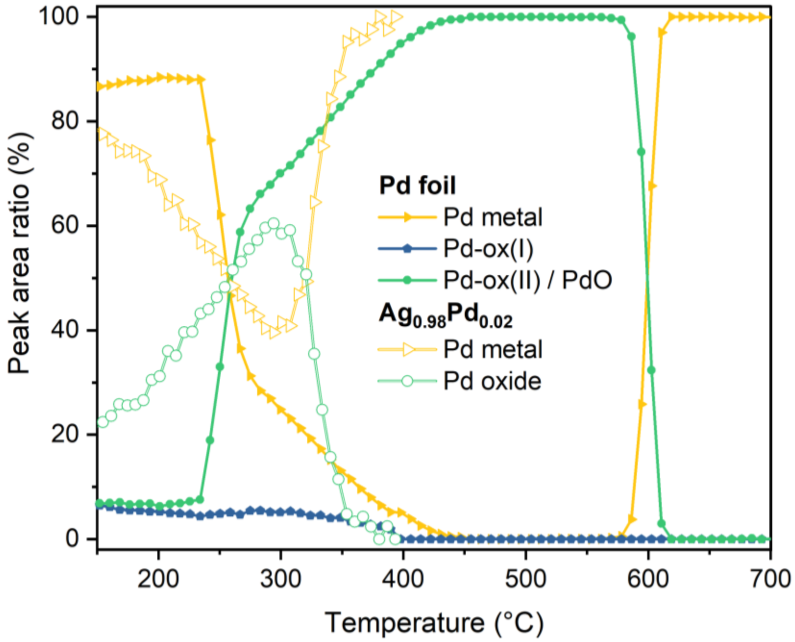

Figure 3-17: Comparison of the area ratio profile of the Pd3d metal and oxide peak of the $Ag_{0.98}Pd_{0.02}$ alloy with the polycrystalline Pd foil depending on the temperature during heating in 1 mbar O_2.

In addition, the onset of Pd oxidation exhibits differences between AgPd and Pd. On AgPd, the Pd oxide signal begins to form at a low temperature, and slowly but continuously increases with temperature, because this is a kinetic diffusion limited process. The diffusion is enhanced at higher temperature, as a consequence a fast slope of Pd oxide formation is expected, when the oxidation is performed at higher starting temperature (e.g. 300°C). In contrast, on Pd metal, the precursor species (Pd-ox(I), Pd-ox(II)) form at low temperature, remain stable and roughly constant in intensity, until at ~240°C, there is an abrupt phase transition from the PdO precursor species to PdO. It seems that at 240°C the reaction barrier for PdO seed formation is overcome, afterwards PdO grows gradually to thickness. The PdO decomposes rapidly around 590°C to Pd metal, without re-forming the intermediate oxide phase.[173] The Pd oxide decomposition on AgPd occur over a longer temperature range compared to PdO on Pd. The diffusion of Pd into the Ag bulk, when the Pd oxide decomposes is still diffusion limited, but enhanced compared to the oxide formation due to the higher temperature. Note that both samples are polycrystalline and therefore it might be possible, that the oxide formation and decomposition occurs on grains with different crystal orientation at different temperatures,[176] which lead to less sharp phase transitions than that on single crystals. Additionally, the exact transition temperatures, and their temperature range depend on the heating rate.

These observations reveal that the AgPd SAA exhibits substantially different behavior, both in terms of formation and thermodynamic stability, than does PdO formed on bulk Pd. One might therefore expect that it could also have different catalytic properties.

While the trends in oxide formation and decomposition temperature on PdO formed on Pd metal, versus the oxidized Pd formed on AgPd show clear differences in behavior, we more closely examined their respective XPS binding energies for further evidence of differences in electronic structure. Table 3-2 compares the measured binding energies of the different $Ag_{0.98}Pd_{0.02}$ XPS species with the characteristics of the polycrystalline Pd foil. Note, that the chemical species in the table are all intermediates, which are present in the O_2 atmosphere and might not be thermodynamic stable phases.

Table 3-2: XPS binding energies of Ag3d$_{5/2}$, Pd3d$_{5/2}$ and O1s of $Ag_{0.98}Pd_{0.02}$ and a Pd foil during oxidation, the peaks are assigned to their chemical origin by considering different references.

Sample	Conditions	Emission line	BE (eV)	Label	Interpretation	References
$Ag_{0.98}Pd_{0.02}$	Heating and cooling in 1 mbar O_2; 0.3°C/min; Lab-XPS (EX2)	**Ag3d$_{5/2}$**	368.18	Ag metal	Metal	88,177,180,182
			367.6-367.8	Ag oxide	Oxide	88,177,180,182
		Pd3d$_{5/2}$	335.05	Pd metal	Metal	30
			336.35	Pd oxide	Oxide	
		O1s	528.3	Oµ1	Ag-O reconst.	88,177,180,182
			528.7	Oµ2	Surface Pd oxide	
			529.1	Oµ3	Unknown Ag oxide related species	180
			530.2	Oµ4	Atomically adsorbed O	177,180
			530.3	Oµ5	Adsorbed SO_4, SO_4 induced reconst.	88
Pd foil	Heating and cooling in 1 mbar O_2: 0.4°C/min; Lab-XPS (EX1)	**Pd3d$_{5/2}$**	335.0	Pd metal	Metal	65–67,173
			335.55	Pd-ox(I)	PdO precursor	65–67,173
			336.2-336.6	Pd-ox(II)	PdO precursor and PdO	65–67,173
		O1s	528.9	O(I)	Precursor, surface oxides in PdO	67,173
			529.8	O(II)	Precursor, PdO	66,67,173
			530.9	O(III)	Hydroxyls	176,177
			529.3	O(IV)	unknown	66

From the peak positions listed in Table 2, we can see that the Pd3d$_{5/2}$ peak position from the metallic state of Pd in AgPd is very similar to that of the metallic state of bulk Pd. The oxidized form of Pd on AgPd also has a very similar binding energy to that of PdO formed on bulk Pd (336.35 eV vs. 336.2-6 eV, respectively). The O1s binding energy of the O-species in the oxide formed on AgPd; however, is very similar to the surface-terminated species from PdO (528.7 eV vs. 528.9 eV, respectively).

Thus, at first glance, the XPS data do not indicate any strong differences in electronic structure between the oxide on AgPd and PdO. However, when one considers core-hole screening effects, the interpretation changes. Consider that the oxide on AgPd is a very thin film. This means that when an electron hole is generated during photoemission, the hole is screened by the electron density of the surrounding material. In this case, the surrounding material is a metal, and screening is very efficient. When a hole is generated in a bulk oxide, the environment around the hole is an oxide. Oxides typically have lower free-electron density than metals. Thus, one would expect weaker core-hole screening in the bulk oxide.

Core-hole screening influences the XPS binding energy. A photoemission event that gives rise to a well-screened hole results in a peak with a lower binding energy than a photoemission event (from the same initial state) where the core-hole is poorly screened. Thus, even though Pd3d$_{5/2}$ binding energies from oxidized AgPd and PdO are very similar, it could be that the Pd centers have substantially different initial states (i.e. different ground state electronic structures).

If we assume that core-hole screening is more effective in the case of oxidized AgPd, and less effective in the case of PdO, then the observation of identical binding energies would imply that the Pd in oxidized AgPd possesses lower electron density that the Pd sites in PdO. Unfortunately, without *a priori* knowledge of the precise atomic structure of the oxidized AgPd surface, we cannot simulate the charge density on the atoms to confirm this assumption.

The screening effects from the underlying metal would give rise to the same effects in the O1s signals. When we compare O1s binding energies of oxidized AgPd, (the Oµ2 species) with the corresponding species for PdO on Pd (the O(II) species), we note that the O1s binding energy on AgPd is 0.9 eV lower in (528.7 eV vs. 529.6 eV, respectively). If we again, assume that the stronger core-hole screening in the case of oxide on AgPd shifts the O1s peak to lower binding energy, then one could infer that the initial states of the oxygen species are similar in both cases of oxidized AgPd and PdO.

In the next section we investigate in more detail the energetic effect leading to Pd oxide formation on the AgPd SAA, and why the Pd surface oxide decomposes at lower temperatures compared to PdO on a Pd foil.

3.3.4.4 Surface segregation of Pd in the AgPd SAA alloy

Based on the XPS peak intensities, we have until now assumed that the Pd oxide formed on AgPd is a very thin film, possibly mono-layer thick, and similar to oxide monolayers reported for previous dilute alloy systems.[153] To substantiate this belief, we present here a more detailed analysis of the XPS peak intensities. Through this analysis, we arrive at a model for the surface morphology that suggests the Pd oxide that formed on AgPd consists of 2-dimensional PdO_x islands on top of the Ag oxide, resulting in depletion of Pd from the sub-surface regions. Hence, the AgPd SAA is an excellent precursor for a meta-stable state which may not be possible to produce with other starting compositions, since the oxidation of conventional alloys would lead to immediate phase segregation and the formation of Pd nanoparticles.

Figure 3-18 shows how the total relative intensity of Pd changes through the oxidation and decomposition process (EX3).

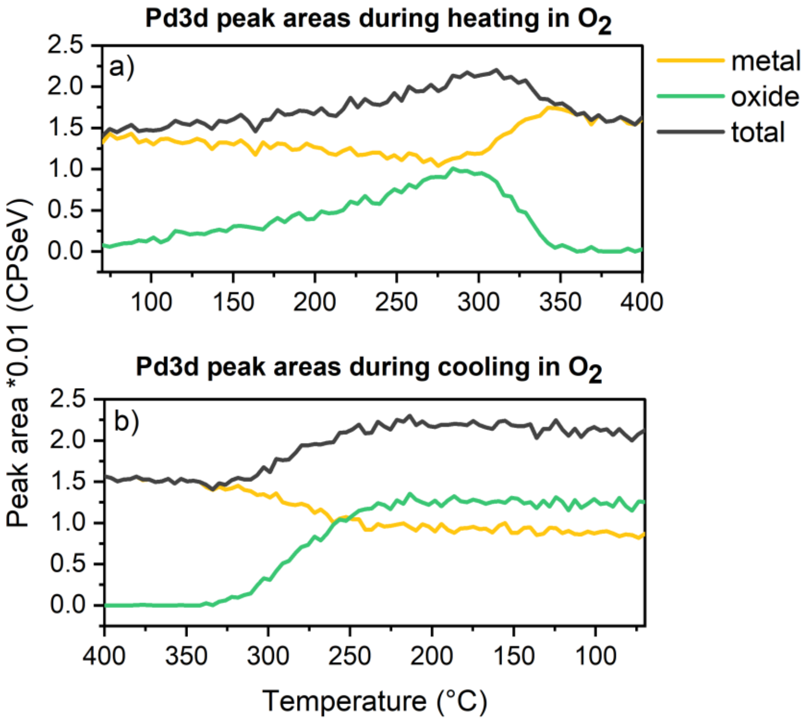

Figure 3-18: Pd3d peak areas of AgPd SAA (Pd3d metal, Pd3d oxide and the sum of both (total)) as a function of time; a) during heating; b) during cooling in 1 mbar O_2.

When oxidation starts, the metal peak decreases, and the oxide peak increases. Considering the total Pd signal, one can see that the Pd intensity raises as Pd becomes oxidized. This finding suggests that Pd surface segregation may be taking place. As the oxide decomposes again at higher temperatures, the total Pd intensity returns to approximately the same value as before oxidation. This observation proposes that the reduced Pd diffuses back into the Ag interior upon reduction. During cooling in oxygen, again Pd oxidation and surface segregation takes place.

The presumed surface segregation of Pd, as inferred from the increase in intensity, can be explained by the higher oxygen affinity of Pd compared to Ag, leading to adsorbate-induced surface segregation.[183] Whereas the migration of Pd into the Ag bulk after the Pd oxide decomposes, can be well explained by the more noble nature of Ag, and therefore, a lower surface energy.[35,36,148]

Kitchin *et al.*[170] found by their theoretical investigations of $Ag_3Pd(111)$ alloy in “reactive” O_2 atmosphere, that Pd segregation is favored with increasing oxygen chemical potential, which is achieved by increasing the oxygen partial pressure. This finding was experimentally verified in the present work (see Figure S 9 in SI). Note, that the oxygen chemical potential is inversely related to the temperature, which means that the chemical potential decreases as the temperature increases.[170,171] Hence, the PdO_x surface oxide formed on $Ag_{0.98}Pd_{0.02}$ as well as PdO formed on bulk Pd decomposes at a certain temperature, because the oxygen chemical potential is not sufficient anymore. The reason, why PdO_x on AgPd decomposes at 270°C lower temperatures compared to PdO on Pd, might be the lower stability of PdO_x, due to the high solubility of Pd in Ag as well as the lower surface energy of Ag compared to Pd.[184]

For better understanding how the Pd oxide layer on the $Ag_{0.98}Pd_{0.02}$ surface might look, XPS data was quantified, and a model for the Pd oxidation in the alloy was developed, thereby we assumed, that a monolayer thick PdO layer is formed on AgPd.

3.3.4.5 Peak area modeling procedure to estimate the morphology of the PdO_x surface oxide

Let us assume, that a homogeneous layer of PdO forms on the alloy surface during oxidation as visualized in Figure 3-19a.

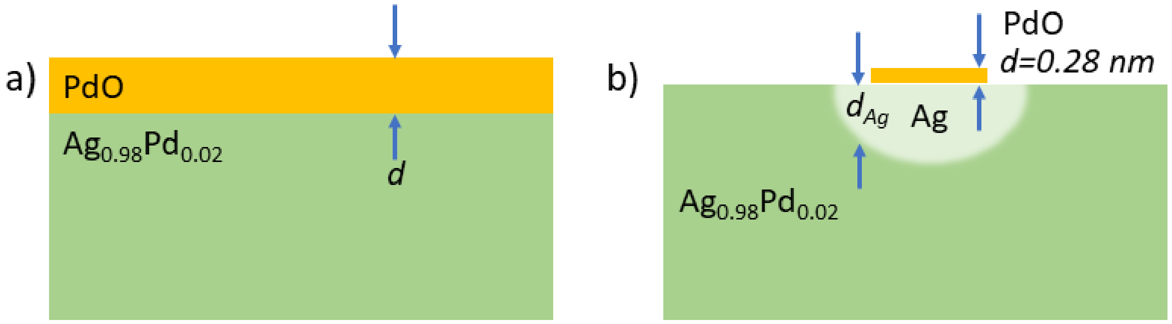

Figure 3-19: a) Scheme of a PdO layer on bulk $Ag_{0.98}Pd_{0.02}$. b) Scheme of fractional PdO monolayer coverage of the alloy, including a depletion area below the PdO monolayer, which consists only of Ag atoms.

If this were the case, then the intensity of Pd in the PdO layer can be obtained by integrating from the surface z=0 to d:[185,186]

$$I_{PdO}^{d} = I_{0,PdO}\left[1 - \exp\left(-\frac{d}{\lambda_{PdO,PdO} \times cos\alpha}\right)\right] \tag{3-6}$$

where $I_{0,PdO}$ is the hypothetical value for an infinitely thick PdO layer and $\lambda_{PdO,PdO}$ the effective attenuation length (EAL) of $Pd^{2+}3d_{5/2}$ electrons through PdO. All EAL values in this work were determined by the NIST database,[187] using an incident X-ray angle of 56°.

The formula for the intensity of $Pd3d_{5/2}$ signal from the Pd atoms buried below the oxide film is:[185,186]

$$I_{Pd,PdO} = I_{\infty,Pd} \exp\left(-\frac{d}{\lambda_{Pd,PdO}}\right) \tag{3-7}$$

Here, $I_{\infty,Pd}$ is the peak intensity of $Pd3d_{5/2}$ in a homogeneous $Ag_{0.98}Pd_{0.02}$ alloy. $\lambda_{Pd,PdO}$ is again the effective attenuation length (EAL) of buried $Pd^{0}3d_{5/2}$ electrons through PdO.

The different parameters used to apply equation (3-6) and (3-7) are discussed in the supplementary information, and listed in Table S 1.

If we assume a uniform coverage of PdO, as shown in Figure 10a, then the calculations from the equation (3-6) yield a PdO thickness of 0.022 nm. Given that this number is less than the atomic diameter of Pd, we infer that the assumption of uniform film thickness is not valid. A Pd atom has a diameter of 0.28 nm (covalent diameter). If we assume a layer thickness of 0.28 nm, and assume non-uniform coverage, then we arrive at a monolayer coverage of 7.7% (Table S 2).

If we now take this updated model, assuming a surface coverage of 7.7%, and use equation (3-7) to calculate the expected metallic Pd3d peak intensity (assuming a uniform Pd concentration of

2 at%), we find that the true Pd3d intensity is substantially lower than the calculated intensity. To explain this discrepancy, we need to add additional sophistication to the model.

The current model, does not consider the fact that the Pd incorporated into the PdO film came from diffusion from the underlying alloy. Thus, the underlying alloy should no longer have the full 2% Pd concentration that it started with. If we assume that the volume below the PdO film has been depleted of Pd, we arrive at the model depicted in Figure 3-19b. The Pd-depleted Ag region of such a model is of course not trivial to calculate, but was approached by implementing a finite element 3D model (see SI: Figure S 10, Table S 1 & S 2).

To summarize, with the peak intensity modelling procedure, we conclude that the oxidized surface of the AgPd alloy consists of thin, possibly monolayer thick, PdO_x islands, with Pd-depleted Ag below and around the islands. Additionally, while we cannot conclusively identify the electronic structure of the oxide, the similarity in binding energy, as well as the qualitative similarity in peak line shape to PdO, suggest that it could be a PdO (Pd^{2+})-like monolayer. An Ag_y-Pd_z-O_x oxide is unlikely, as no correlations between Pd $3d_{5/2}$ oxide and Ag $3d_{5/2}$ oxide were found.

3.3.4.6 $Ag_{0.98}Pd_{0.02}$ and Pd foil in methane oxidation conditions

After we have intensively discussed the electronic structure of Pd and $Ag_{0.98}Pd_{0.02}$ in oxidative atmospheres, it is of interest, to see whether such meta-stable Pd surface oxides are also present in a reaction mixture that would be used for a catalytic reaction. An oxidative reaction of great economical interest is the total combustion of methane, which is the main component in natural gas, and an attractive energy source.[158] Pd was found to be the most active metal of all elements in the complete oxidation of methane. To make the catalytic methane oxidation as energy efficient as possible low reaction temperatures are desired. So far Pd requires reaction temperatures above 300°C to catalyze the total methane oxidation.[157]

It has been shown in the past years of heterogeneous catalysis research, that mostly meta-stable surface species are the active catalytic phases. We therefore examined, whether the meta-stable Pd-oxide phase of $Ag_{0.98}Pd_{0.02}$ is also present in methane oxidation conditions, using a reaction mixture of O_2:CH_4:N_2 with a ratio of 5:1:2 (EX6). The measurements reveal that the meta-stable surface Pd-oxide does indeed form under methane oxidation conditions although the oxygen chemical potential has been reduced by mixing O_2 with CH_4. The surface oxide is most intense at 300°C. From this observation, we suggest that AgPd SAA catalysts might be candidates for low temperature methane combustion (≤300°C).

The electronic structure of $Ag_{0.98}Pd_{0.02}$ in methane oxidation at 300°C is compared with the polycrystalline Pd at the same conditions (Figure 3-20). At 300°C the Pd foil is in the transition state between surface oxide and bulk PdO, and when the temperature is further increased (430°C) bulk PdO has formed (EX7), similar as it was observed in pure O_2 environment.

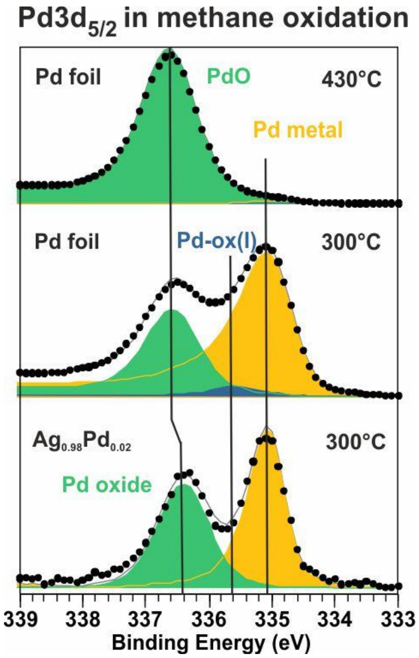

Figure 3-20: Electronic structure of the $Pd3d_{5/2}$ states of the Pd foil and the AgPd SAA under methane oxidation conditions.

The results shown here suggest to study the application of SAAs not only for reductive reactions (e.g. hydrogenation reactions) but also for oxidative reactions, since oxidative conditions facilitate the formation of meta-stable, active surface oxides, as it was for instance be shown for the AgCu SAA system in ethylene epoxidation.[153] During reactive studies, it is important to keep in mind, that the reaction atmosphere might change the geometric and electronic environment of the atoms, e.g. adsorbate-induced surface segregation might occur, which could lead to cluster or island formation on SAAs, and thus to a loss of the initial single-atom alloy character, as it is the case for the AgPd SAA system discussed here. Although in some cases, such catalyst transformation effects may not be desired, in other cases, such meta-stable surface species could participate in the catalytic performance of single-atoms alloys.

3.3.5 Conclusion

In this work, an AgPd SAA was studied under oxidative conditions, and compared with bulk Pd in similar conditions. We showed by *in situ* XPS spectroscopy, that in the case of $Ag_{0.98}Pd_{0.02}$ SAA, Pd segregates to the surface where it becomes partly oxidized. Through a peak area modeling procedure, we conclude that thin, possibly monolayer-thick, PdO_x islands form, with Pd-depleted Ag below and around the islands. This 2-dimensional surface oxide might be unique for AgPd SAAs, since the oxidation of conventional AgPd alloys would lead to phase segregation and nanoparticle formation. The meta-stable surface oxide on AgPd decomposes at relatively low temperatures (at 320°C in 1 mbar O_2), which is 270°C less than the temperature where bulk PdO was observed to decompose. This low decomposition temperature of the PdO_x oxide suggests that the contact with $Ag_{0.98}Pd_{0.02}$ influences the oxide's thermodynamic stability. Since meta-stable surface species are often the reactive phase of heterogeneous catalysts, and because Pd is highly active in the total methane oxidation reaction, we propose that the meta-stable PdO_x surface oxide on AgPd SAA could be active in methane oxidation at low temperatures ($\leq$300°C). We observed that the PdO_x surface oxide is indeed present under methane oxidation conditions.

Data Availability Statement

The data that support the findings of this study are openly available in Zenodo at https://doi.org/10.5281/zenodo.4482118, https://doi.org/10.5281/zenodo.4482214, and https://doi.org/10.5281/zenodo.4482000.

3.3.6 Supplementary information

3.3.6.1 *In* situ oxidation of $Ag_{0.98}Pd_{0.02}$

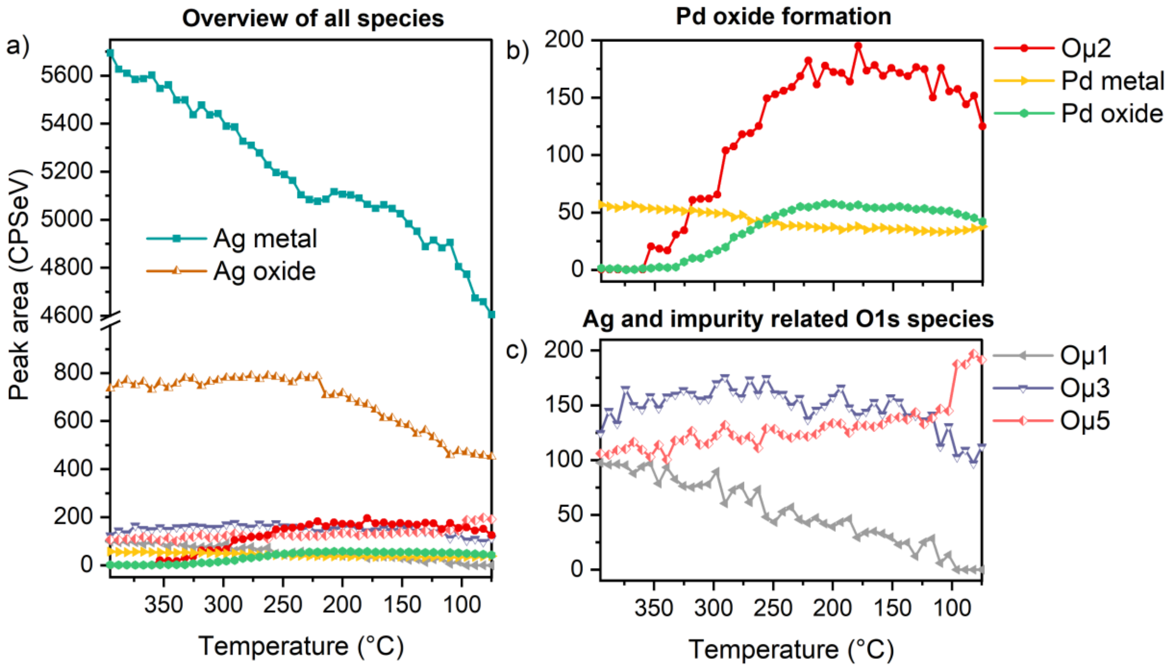

Figure S 6: a) Peak area-line profile of all relevant synthetic components of $Ag_{0.98}Pd_{0.02}$ (EX2) as a function of temperature during cooling in 1 mbar O_2; b) Temperature-line profile showing the formation of the surface Pd oxide; c) Profile of the O1s species, which are related to Ag or to impurities.

The main conclusion from the temperature-line profile in Figure S 6 is that that the formation of the Ag-O reconstruction (Oµ1) is independent from the Pd oxide (Oµ2) formation, since Oµ1 decreases as Oµ2 increases (Figure S 6b,-c). The onset oxidation temperature (OOT) of Pd oxide is 325°C and the oxide stays stable during cooling in O_2.

In order to verify the correlation between the Oµ5 species and SO_4 formation on the surface, similar measurements were performed using synchrotron radiation, which enables a much higher surface sensitivity compared to Al K_α radiation.

3.3.6.1.1 Additional information from Synchrotron measurements

In the main text, it was mentioned that the Oµ5 peak could correspond to a sulfur-induced reconstruction. This claim is supported by *in situ* XPS data from EX4 measured at the synchrotron (BESSY II), due to the tunable surface sensitivity using synchrotron radiation, as well as higher sensitivity towards sulfur detection. Figure S 7b shows the heavy increase of SO_4 formation during heating, at the same time the Oµ5 intensity increases (Figure S 7a). This correlation becomes even clearer in the normalized intensity line profile (Figure S 8), where it can be observed that the Oµ5 and S2p intensity, as well as Cl2p, increases rapidly starting at 250°C. The SO_4 formation can also be observed in the valence band spectra (Figure S 7c). With increasing SO_4 formation, an S3p and an O2p peak arise. To summarize, the four species S2p, Oµ5, O2p, and S3p have a remarkably similar temperature line profile (Figure S 8), from which it can be concluded that they all correspond to the same molecule SO_4, which forms on the surface at elevated temperatures. The binding energy of Oµ5 at 325°C is 530.7 eV, which is the same as measured for the SO_4 induced reconstruction ((7×√3)rect) on a Ag(111) surface.[88]

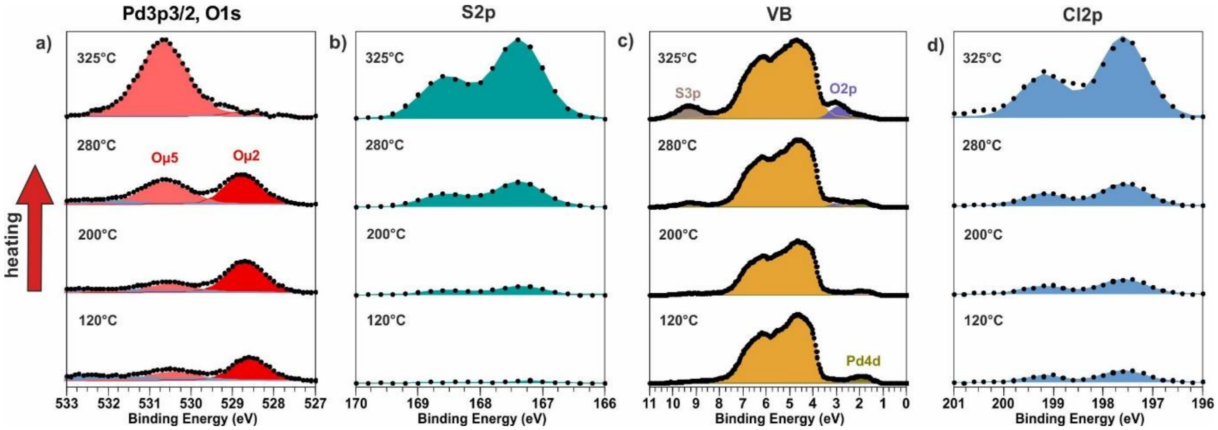

Figure S 7: Changes in the XPS spectra of $Ag_{0.98}Pd_{0.02}$ upon heating from 120 to 325°C using synchrotron radiation; a) $Pd3p_{3/2}$, O1s; b) S2p; c) valence band structure; d) Cl2p.

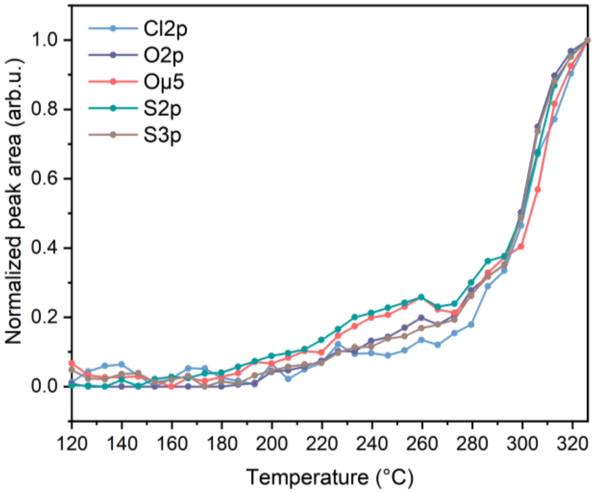

Figure S 8: Normalized peak area line profile of the impurity species Cl_2, and SO_4 on $Ag_{0.98}Pd_{0.02}$ as function of temperature.

3.3.6.1.2 Experimental procedure of the *in situ* oxidation of AgPd at BESSY II (EX4)

To examine the presence of impurities during oxidation, additional *in situ* oxidation experiments of $Ag_{0.98}Pd_{0.02}$ were performed at the UE56-2_PGM1 beamline at BESSY II. The ability to tune photon energy, and the high photon flux of synchrotrons provides a much higher sensitivity to typical impurity elements, such as sulfur, chlorine and silicon. At the synchrotron, excitation energies of 520 eV for Ag3d, 485 eV for Pd3d, 750 eV for O1s, 420 eV for C1s, Cl2p, S2p impurities and 200 eV for the valence band spectra were used. After Ar^+ sputter cleaning the sample was directly exposed to 1 mbar O_2 and 100°C (to avoid much carbon contamination) followed by starting the heating ramp using 1°C/min, the heating was stopped at 335°C. At this point 35 loops were measured.

3.3.6.2 Influence of the O_2 pressure on the surface segregation of Pd in $Ag_{0.98}Pd_{0.02}$

The calculated findings of Kitchin et al.[170], that Pd segregation is favored with increasing oxygen chemical potential, was experimentally verified in this work. For this experiment (EX5), the sputter cleaned sample was heated in 0.1 mbar O_2 at 180°C for 1 h, after which the pressure was increased in steps to 1 mbar, and kept constant for 1 h at each pressure. Figure S 9a shows that the oxidation of Pd increases with the oxygen pressure (oxygen chemical potential), whereas no change in the line shape of $Ag3d_{5/2}$ (Figure S 9b) occurred. This observation let us assume that the Ag oxide formation occurs independent of the Pd oxidation.

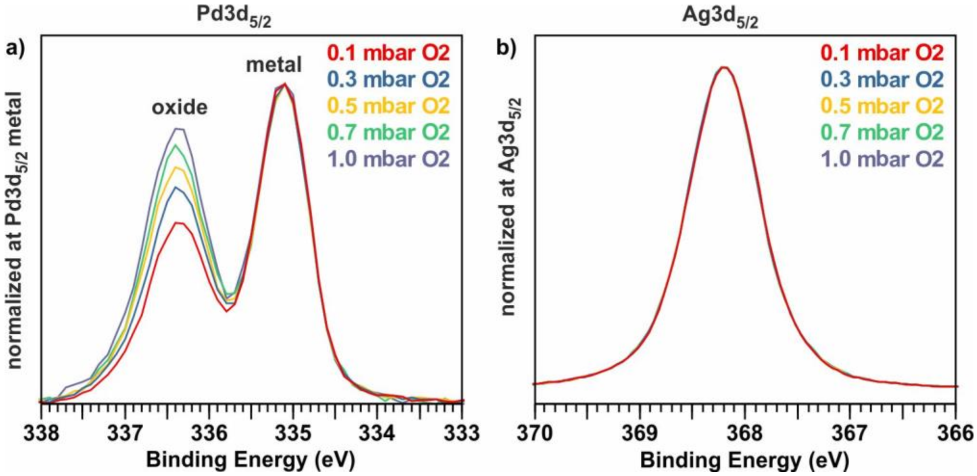

Figure S 9: a) Increasing oxidation of the $Pd3d_{5/2}$ signal of $Ag_{0.98}Pd_{0.02}$ at 180°C with increasing O_2 pressure, the spectra are normalized to the $Pd3d_{5/2}$ metal peak; b) At the same time the $Ag3d_{5/2}$ was measured and it can be seen that silver does not change its line shape with increasing O_2 pressure.

3.3.6.3 Peak area modeling procedure to estimate the morphology of the PdO_x surface oxide

To better understand the morphology of the Pd surface oxide (also named PdO_x) formed on AgPd (Figure S 10 bottom spectrum) we performed a peak area modeling procedure. A summary of the applied model and its outcome is given in the main text. Here, the underlaying calculations are explained in more detail.

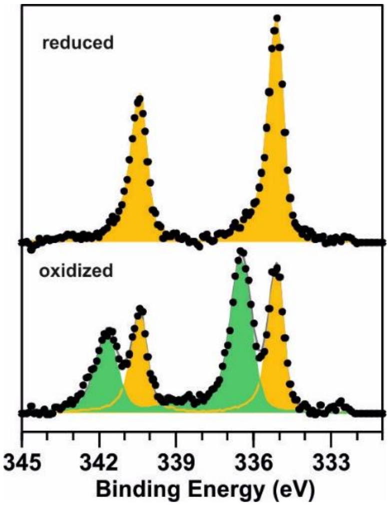

Figure S 10: $Pd3d_{5/2}$ spectra of the $Ag_{0.98}Pd_{0.02}$ alloy measured in 1 mbar O_2 at 70°C in the reduced state (top) and in the oxidized state, after cooling down again to 70°C in 1 mbar O_2 (bottom). The signal intensities of those two spectra are used to model the morphology of the PdO_x surface oxide.

To determine the average effective attenuation length (EAL) (note: for overlayer thickness calculation EAL instead of IMFP is used) values were taken from the NIST database[187] for equation (3-6) and (3-7) (main text). An initial approximation of a PdO thickness of 0.28 nm was chosen, which is close to the diameter of a Pd atom, since it is assumed that the surface oxide is not more than a monolayer thick.

The $I_{\infty,Pd}$ value (in (3-6)) was determined by the $Pd3d_{5/2}$ spectrum of $Ag_{0.98}Pd_{0.02}$ in the clean, reduced state (Figure S 10). The hypothetical value for $I_{0,PdO}$ is unknown, and has to be calculated. The XPS peak area can be calculated by the following simplified equation.[188]

$$I_A = RSF \times \lambda \times N_A \times T \tag{3-8}$$

Where RSF is the relative sensitivity factor taken from the Scofield cross sections corrected for a normal emission angle.[189] λ is in this case the IMFP, since in this case homogeneous samples and no overlayers are considered. The IMFP values were determined by the QUASES IMFP calculator software by the TPP2M formula.[190] N_A is the atomic density (number of atoms/nm³) and can be calculated by dividing the density of a material by its molar mass, multiplied by the Avogadro constant. The factor T is the transmission function, and implies all the spectrometer contributions to the intensity. The contributions to the XPS intensity are discussed in more detail elsewhere[186,191]. The transmission function T is unknown und was considered as a constant in this study because the kinetic energy difference of $Ag3d_{5/2}$ and $Pd3d_{5/2}$ is small. T was estimated from the intensity of the $Ag3d_{5/2}$ peak of the $Ag_{0.98}Pd_{0.02}$ alloy in the reduced state. The value was multiplied by 1.02 to consider pure Ag and not $Ag_{0.98}Pd_{0.02.}$ For identical spectrometer and pressure conditions, as it is the case for the measurements considered here, the factor T can be applied to calculate the density (N_A) of the Pd atoms in the AgPd SAA, as well as the hypothetical intensity of an infinitely thick PdO layer using equation (3-8). The different parameters used for the calculation are listed in Table S 1.

Table S 1: Parameter values of $Ag3d_{5/2}$, $Pd3d_{5/2}$ in Ag and PdO (hypothetical) to apply equation (3-8). The bold numbers are the calculated parameters, the other ones are given.

Species	RSF§	λ (IMFP)# [nm]	N_A [atoms/nm³]	$I_{\infty,A}$ [CPSeV]	T (transmission function)
$Ag3d_{5/2}$	10.66	1.602	58.56	170020*	**173.0**
$Pd3d_{5/2}$ in Ag	9.48	1.634	**0.808**	2171*	173.0
PdO_∞ (hypothetical)	9.48	1.78	40.82	**119448**	173.0

*Values are taken from measuring $Ag_{0.98}Pd_{0.02}$ in the clean reduced state (Figure S 10)

#Values from QUASES IMFP calculator software by the TPP2M formula.[190]

§ RSF (relative sensitivity factor) taken from CasaXPS (Scofield cross section[192]).

With the hypothetical $I_{0,PdO}$ value, and the intensity of Pd^{2+} from the $Ag_{0.98}Pd_{0.02}$ spectra (see Figure S 10) in the oxidized state, equation (3-6) can be applied to calculate the PdO thickness d_{PdO} revealing 0.022 nm.

Given that this number is less than the atomic diameter of Pd, we infer that the assumption of uniform film thickness is not valid. Consequently, a fractional monolayer coverage (islands) of a PdO layer on the AgPd alloy is expected. The coverage (C) is estimated by dividing the calculated thickness d_{PdO} by the Pd diameter. This results in a PdO monolayer coverage of 7.7% (Table S 2). The layer thickness *d* can also be calculated by applying equation (3-7) and using the intensity of the $Pd3d_{5/2}$ metal peak (Figure S 10). The result should, in principle, agree with the previously calculated 0.022 nm, but the calculation revealed a d_{PdO} value of 0.63 nm, which is 28 times higher, meaning that the measured $Pd3d_{5/2}$ metal intensity is less than expected for such a thin PdO layer.

This discrepancy can only partly be explained by the fractional coverage, mentioned above. The current model, does not consider that Pd trapped in the PdO film, came from diffusion from the underlying alloy. Thus, the underlying alloy should no longer have the full 2% Pd concentration that it started with. If we assume that the volumes below the PdO film have been depleted of Pd, we arrive at the model depicted in Figure 3-19b (main text). Such a model is of course not trivial to calculate, but can be approached by imagining a finite element 3D model, where the surface consists of 10000 cuboids with the volume of 1×1×$d_{\text{Ag atom}}$ nm, where $d_{\text{Ag atom}}$ is the diameter of one Ag atom (0.32 nm) (Figure S 11). Figure S 11 illustrates which variables are used to calculate the $Pd^0 3d_{5/2}$ intensity. The yellow cuboids are the fractional PdO monolayer, the white ones are pure Ag, and the green ones consist of $Ag_{0.98}Pd_{0.02}$.

Table S 2 shows the calculations of the different parameters, which were used to calculate a $Pd^0 3d_{5/2}$ intensity, which is close to the measured peak area.

Table S 2: Calculations of the different parameters, which needs to be considered to calculate the expected $Pd3d_{5/2}$ intensity from the model in Figure 11 (main text) bottom.

Parameter	Calculation	Result
$d_{\text{Pd atom}}$ (Height of PdO monolayer) [nm]	Diameter of Pd atom	0.28
$I_{Pd,PdO}$ (Intensity of Pd passing through the PdO monolayer)	$I_{Pd,PdO} = equation\ (3\text{-}7)$	1801
C (PdO coverage)	$C = \frac{d_{PdO}}{d_{Pd\ atom}}$	0.077
V_{PdO} (volume PdO monolayer) [nm³]	$V_{PdO} = 10000 \cdot d_{Pd\ atom} \cdot C$	216
$n_{Pd,\ PdO}$ (Pd atoms in PdO monolayer)	$n_{Pd,PdO} = V_{PdO} \cdot N_{Pd,PdO}$	8800
V_{Ag} (volume of depletion area) [nm³]	$V_{Ag} = \frac{n_{Pd,PdO}}{N_{Pd.AgPd}}$	10888
V_{cuboid} (volume of each cuboid in model) [nm³]	$V_{cuboid} = 1nm \cdot 1nm \cdot 0.32nm$	0.32
$n_{cuboids}$ (number of cuboids in depletion region)	$n_{cuboids} = \frac{V_{Ag}}{V_{cuboid}}$	34025

By having calculated a fractional monolayer coverage of 7.7% the volume of the PdO monolayer can be calculated, and hence the number of Pd atoms in the PdO monolayer ($n_{Pd,\ PdO}$). The density of Pd atoms in the AgPd alloy was calculated in Table S 1 and with this result, the volume of the depletion region can be calculated, which consist only of Ag atoms, since the Pd atoms segregated to the surface to form the PdO monolayer. Thereafter, the number of cuboids, the depletion region V_{Ag} consist of, can be calculated.

Having calculated all the relevant values (Table S 2) a python script (see appendix) was written to calculate layer by layer the Pd metal signal intensity of each colored box in the model of Figure S 11.

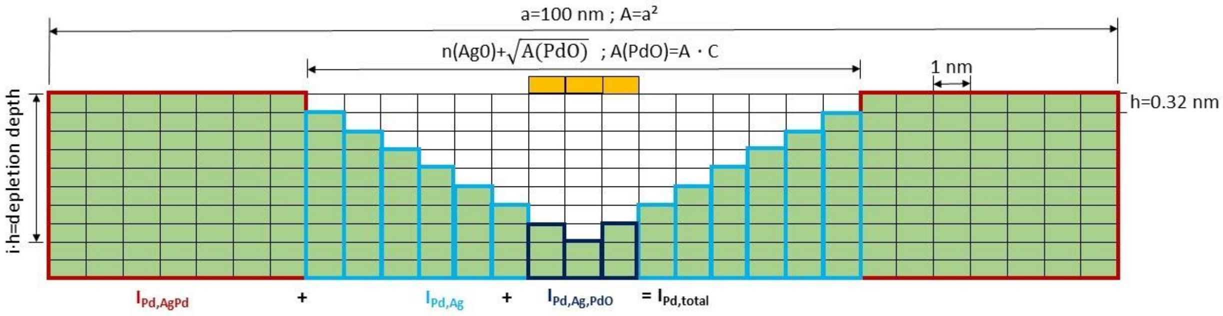

Figure S 11: 2D cross section model, to visualize, how the expected intensity of the Pd3d$_{5/2}$ metal peak is calculated.

The necessary input data for the calculation is n(Ag0), which determines the number of Ag cuboids in the top layer (i=0). The calculation was stopped, when either the number of cuboids, the Ag depletion layer consist of, were below 0, or when the area of a layer was below 0. Following equations (Table S 3) are used to determine the Pd intensity arising from the different colored squares in the model (Figure S 11), hereby P is the contribution (a_i/A) of each layer to the total Pd intensity.

Table S 3: Equations to calculate the different Pd intensities contributing to the total intensity of Figure S 11. Additionally the result for n(Ag0)=42 is given and compared with the measured value.

$I_{Pd,AgPd}$ (Pd Intensity from homogeneous AgPd region)	$\boldsymbol{I_{Pd,AgPd} = P \cdot I_{\infty Pd,AgPd}}$	
$I_{Pd,Ag}$ (Intensity of Pd passing the Ag depletion layer)	$I_{Pd,Ag} = I_{\infty Pd,AgPd} \exp\left(-\frac{i \cdot h}{\lambda_{Pd,Ag}}\right) \cdot P$	
$I_{Pd,Ag,PdO}$ (Intensity of Pd passing the Ag depletion layer and PdO monolayer)	$I_{Pd,Ag,PdO} = I_{Pd,PdO} \exp\left(-\frac{d_{Pd\ atom} + i \cdot h}{\lambda_{Pd,Ag}}\right) \cdot P$	
I_{Pd} (sum of all Pd intensities) [CPS]	$I_{Pd} = I_{Pd,AgPd} + I_{Pd,Ag} + I_{Pd,Ag,PdO}$	**I(n_{Ag0}=42)=1348**
$I_{Pd\ measured}$	measured	**1335**

The calculated intensity (1348 CPSeV) was closest to the measured intensity (1335 CPSeV) when n(Ag0), the number of Ag cuboids in the top layer equal to 42. Thereby the number of depletion layers (layers with white cuboids) is 9, which equals to a depth of 2.88 nm. It is worth mentioning that 83% of the Pd intensity is coming from the homogeneous, uncovered region $I_{Pd,Ag}$ (see Figure S 11).

3.3.7 Additional studies and information

After writing the above manuscript the performance of the AgPd SAA and the Pd foil in methane oxidation was investigated, which will be discussed in the next section.

Even better than simulating the PdO_x surface oxide, as done in the manuscript, would be to capture the morphology changes in oxidative atmosphere by ESEM. At the ETH in Zurich such ESEM measurements of the AgPd SAA sample and the Pd foil were performed, for more details see section 3.3.7.2.

3.3.7.1 Catalytic properties of Pd and AgPd SAA in methane oxidation

In order to study, whether the unique surface oxide forming on AgPd SAA is indeed a promising candidate for methane oxidation at low temperatures, catalytic measurements were performed using the GC analysis system of the FHI at BESSY II (for experimental details see 3.3.7.1.1).

First, it was tested if the GC is sensitive enough to detect methane combustion with the Pd foil, while simultaneously the electronic structure was measured at the NAP-XPS end station at the BElChem beamline. The methane to O_2 gas ratio was 1:5 in agreement with the literature.[160] Additionally, a small concentration of N_2 was added to the gas mixture as an internal standard. As an indication of the reaction performance the CO_2 formation was measured according to the following equation.

$$CO_2\, formation\, [\%] = \frac{CO_2}{CO_2 + CH_4} \cdot 100 \tag{3-9}$$

The Pd foil was pre-treated in O_2 at 300°C to burn off carbon from the sample surface. Afterwards the influence of the gas phase pressure and the flow rate was analyzed at 380°C, this temperature gave rise to a local maximum in CO_2 formation according to the reference.[160] Therefore the flow rate was kept constant, but the pressure in the analysis chamber was increased. Figure S 12a shows that by this procedure, the CO_2 formation could be increased from 0.45% at 1 mbar to 1.4% at 3 mbar. During those conditions PdO was present at the surface. To investigate, if the CO_2 formation can be further increased, at higher pressures, the same experiment was performed at the NAP-XPS test station in the CAT lab, where a maximum pressure of 100 mbar could be reached. Thereby only a small increase in CO_2 formation to 1.8% at 380°C could be achieved. It should be noted, that the two different setups had different MFCs and also a different TRACE GC, which lead to limited comparability of the results from the two devices.

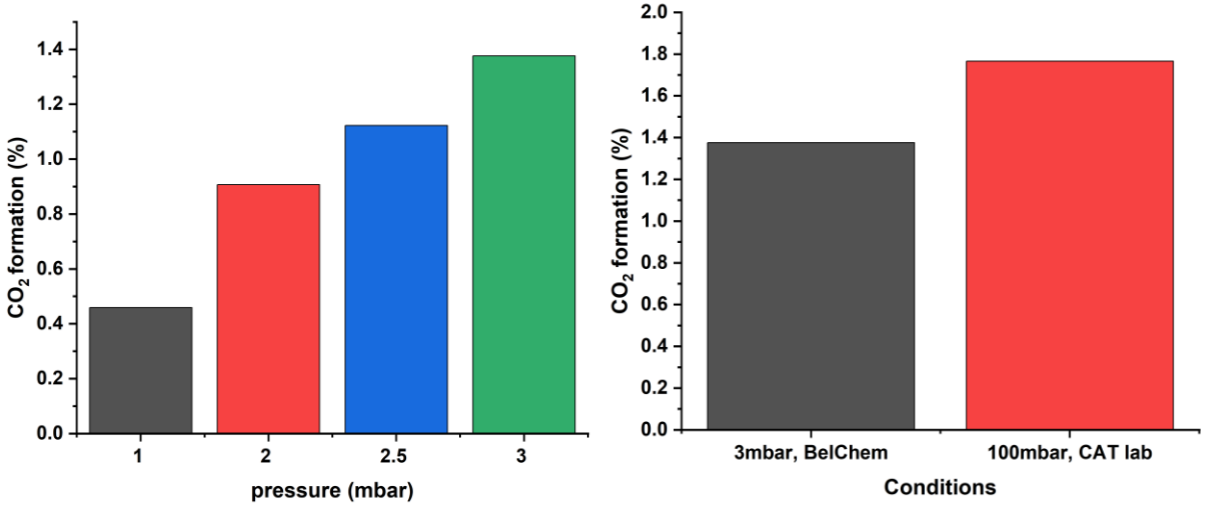

Figure S 12: CO_2 formation of Pd in methane oxidation conditions at 380°C; a) increase in CO_2 formation when the flow rate is kept constant (4.9ml/min) but the pressure is increased; b) comparison of the CO_2 formation at the BElChem beamline at 3 mbar and at the test station in the CAT lab at 100 mbar (35ml/min flow rate).

Additionally, the catalytic performance of the Pd foil as a function of the temperature was investigated (Figure S 13a). Afterwards the catalytic performance of AgPd SAA in methane combustion was investigated under the same conditions (Figure S 13b). Previous experiments of $Ag_{0.95}Pd_{0.05}$ at the BElChem beamline in methane oxidation atmosphere revealed that the Pd surface oxide decomposed above 300°C. The catalytic performance of the Pd foil shows a heavy increase in CO_2 formation from 0.2% to 1.8% as the temperature is increased from 300°C to 380°C (Figure S 13a). For the AgPd SAA no CO_2 formation could be measured until 300°C, afterwards the CO_2 formation increased from 0.005% at 300°C to 0.035% at 380°C. Hence, the conversion is for the Pd foil at 380°C 50 times higher as for the SAA sample. However, since the AgPd SAA contain only 5 at% of active Pd, a much lower conversion is expected. The main research question was, whether the unique PdO_x surface oxide leads to CO_2 formation at lower temperatures (≤300°C). Since below 300°C the CO_2 formation is 0%, and at 300°C only slightly above 0 and still around the detection limit of the instrument, it can be concluded that the surface PdO_x is not active in methane oxidation. Besides it is possible, that the weak CO_2 GC signal measured for the AgPd SAA is caused by the chamber or the stainless-steel sample holder and that the sample has no impact on the CO_2 formation. This could be investigated by a blank experiment (without sample), which was, due to time reasons, not performed. Note, that the experimental result might change for high surface area samples of supported AgPd nanoparticles.

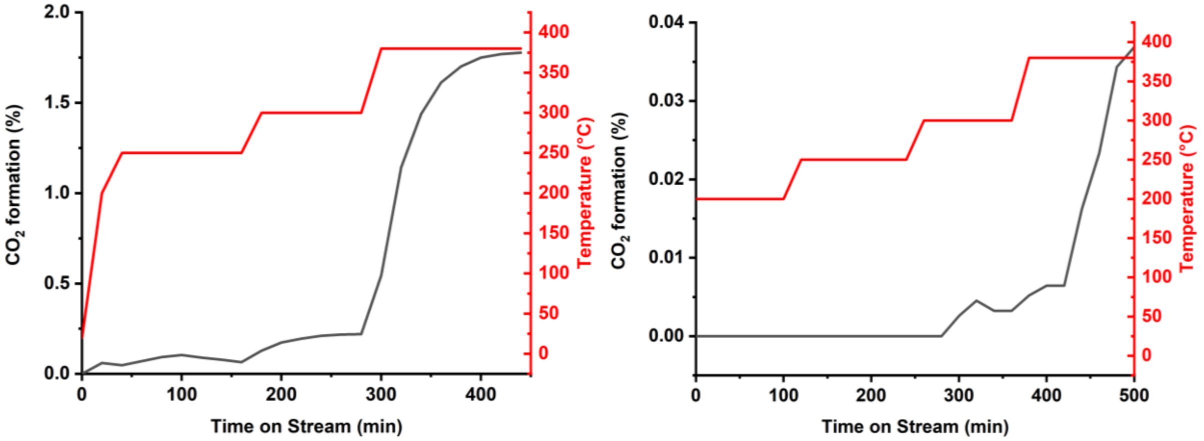

Figure S 13: Change in CO_2 formation as a function of temperature and time on stream at 100 mbar; a) of the Pd foil; b) of $Ag_{0.95}Pd_{0.05}$.

3.3.7.1.1 Experimental procedure to investigate the catalytic performance of Pd and AgPd SAA in methane oxidation

The catalytic testing was performed to compare the catalytic properties of the Pd foil and $Ag_{0.95}Pd_{0.05}$ in methane combustion towards CO_2. The tests were carried out at two different setups. The NAP-XPS end station (BElChem, UE56-2_PGM1 beamline) with operating gas phase pressures between 1 and 3 mbar, and in a NAP-XPS test station (in the CAT lab at BESSY II), i.e. the same setup used to perform NAP-XPS experiments using synchrotron radiation, but without the attachment of the electron energy analyzer. This configuration enabled higher gas pressures to be reached, up to 100 mbar. In both cases the reaction chamber, which has a volume of 4 L, was pumped continuously, and the gas phase was detected with a gas chromatograph (GC) (TRACE 1310, thermo scientific). Both setups had their own GC of the same instrument type. The samples (of the size 8×8 mm) were cleaned by means of Ar^+ sputtering before loading into the reaction chamber. Prior to the treatment in methane oxidation conditions, the samples were heated to 200-300°C in O_2 to burn off carbon contaminants. The flow rate of the MFCs for the specific gases was adjusted using the conversion factors (of the MFC manual) to achieve a gas mixture of CH_4:O_2:N_2 1:5:0.5. Whereby N_2 was introduced as internal standard. First, the reaction conditions were optimized for the Pd foil at the BElChem beamline. At a temperature of 380°C and a total flow rate of 4.9 ml/min, the pressure, which is automatically regulated by a throttle valve, was increased from 1 mbar to 3 mbar in steps of 0.5 mbar. At each pressure the gas phase changes were measured until steady-state conditions are reached. Simultaneously XPS spectra were recorded.

Afterwards the catalytic performance of the Pd foil at the NAP-XPS test station at 100 mbar was investigated. After the oxidation pre-treatment, CO_2 formation as a function of the reaction temperature was investigated. For this the temperature was increased in steps (200°C, 250°C, 300°C, 380°C) and the gas phase composition was measured for 2h at each temperature. The total flow rate was hereby 35 ml/min. The same experimental procedure was repeated for the $Ag_{0.95}Pd_{0.05}$ sample.

For all experiments the background gas flow was measured using the same gas flow at room temperature without any sample, the background was later subtracted from the measured GC peak areas.

3.3.7.2 ESEM

From XPS data alone, one can often not conclude how the morphological structure of a surface looks like. To obtain better insights into the Pd oxide structure, we performed ESEM measurements. ESEM was chosen because an *in situ* method is necessary to examine the structures that form at elevated temperatures in oxygen, as these structures will immediately change when removed from their formation environment.

Environmental SEM of the oxidation of a Pd foil and the $Ag_{0.98}Pd_{0.02}$ alloy, using very similar conditions as for the *in situ* XPS, were performed at the ETH (see chapter 2.3.1.1 for more information of the instrument). A polycrystalline Pd foil was treated at 800°C in H_2 in the ESEM prior to oxidation, to remove all adsorbed impurities from the surface. The oxidation at 1 mbar was performed with a ramping speed of 20°C/min. At 400°C dark spots appear all over the sample. It is expected that these features are the seeds of PdO formation (Figure S 14a). With increasing temperature, the seeds continue to grow (Figure S 14b). At 550°C the thickest oxide layer is detected. It is worth noting that there are still gaps between these oxide islands, where apparently no oxide has yet formed (Figure S 14c). Furthermore, different grains exhibit different oxidation kinetics. Similar observation have been reported by comparing *in situ* oxidation on Pd(111) and Pd(110).[176] Further heating to 600°C leads to a contrast and morphology change (Figure S 14d). From the knowledge gained from the NAP-XPS experiments, this process likely corresponds to the decomposition of the Pd oxide. The surface after PdO decomposition exhibits holes at the places where the oxide crystals were previously located, and exhibits a much different morphology compared to the initial surface.

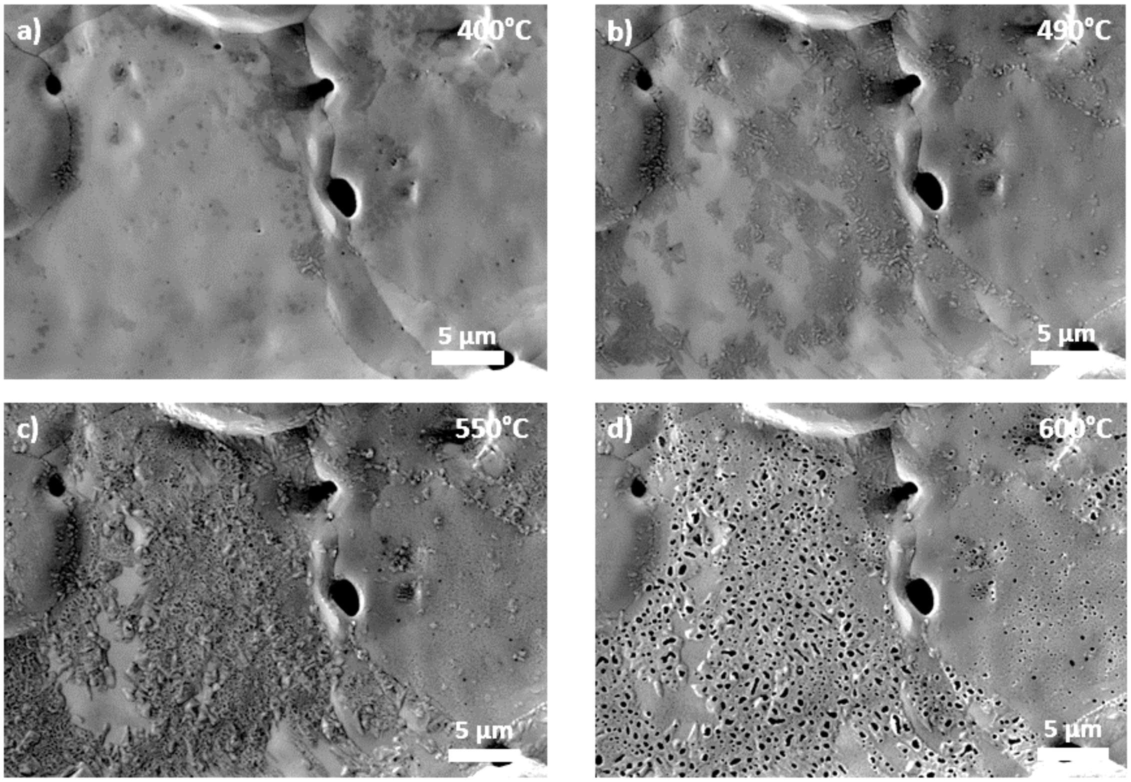

Figure S 14: SEM micrograph with 15000x magnification during oxidation of a Pd foil with 20 K/min in 1 mbar of O_2; a) PdO seed formation at 400°C; b) growth of the PdO seeds at 490°C; c) Pd oxidation at its most intense state at 550°C; d) contrast change, which can be referred to PdO decomposition at 600°C.

The main conclusions which can be made from this *in situ* ESEM experiment is, that the oxidation process occurs in no means homogenously over the sample surface and that the grain orientation plays a role for the oxidation process. It is rather impossible to detect the two-dimensional PdO precursor species by this ESEM, but from the differences in the PdO seed formation it is expected that there might be different surface oxides on different grains. Finally, the surface structure after PdO has decomposed is very interesting. Due to the H_2 pretreatment PdH forms, the H atoms might react with oxygen to form water, which might change the morphology of the sample. The rough Pd surface structure after PdO decomposition might include some oxygen, which gives rise to the O(IV) signal. For better understanding of the surface processes seen with the ESEM during Pd oxidation, more research has to be done. However, this exceeds the scope of the thesis, since it is focused on AgPd SAAs.

The oxidation of the same $Ag_{0.98}Pd_{0.02}$ sample as used for the XPS measurement was also investigated by *in situ* SEM, after reduction in H_2 at 300°C. For the oxidation, the sample was heated with 3°C/min from 70°C to 230°C in 1 mbar of O_2. The SEM micrograph in Figure S 15 demonstrates that no change can be observed during heating in O_2.

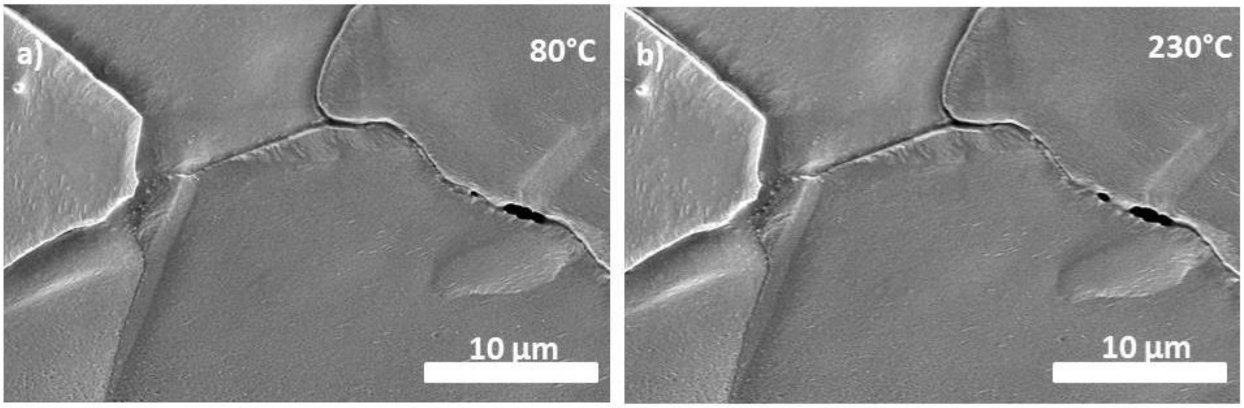

Figure S 15: Micrograph of the $Ag_{0.98}Pd_{0.02}$ during treatment in 1 mbar of O_2 with a heating ramp of 3K/min and 10000x magnification at a) 80°C and b) 230°C, no morphological or contrast changes could be observed.

There might be two different reasons for this: (i) no Pd surface oxide has formed or (ii) the estimated 7.7% surface coverage of monolayer thick PdO_x islands (see section 3.3.6.3 and the main text), does not give rise to contrast changes resolvable with ESEM. Note, that Ag is also expected to reconstruct in O_2 atmosphere, which also could not be observed by the ESEM experiment.

A main difference between sample preparation for NAP-XPS and ESEM is that the NAP-XPS samples were cleaned by Ar^+ sputtering prior to the H_2 treatment and the subsequent oxidation. The attempt to oxidize $Ag_{0.98}Pd_{0.02}$ without the Ar^+ sputter step failed in the XPS, also it seems that the Pd surface oxide is highly sensitive to any carbon impurities inside the analysis chamber, which led to faster degradation of the Pd oxide. As a consequence, it is assumed that no Pd oxide has formed during the ESEM experiment. Another possible way to see the Pd surface oxide and the Ag oxidation, or Ag reconstruction is to perform the oxidation in the NAP-XPS, afterwards cool the sample down to room temperature in O_2 and subsequent investigation of the surface by electron microscopy. For this procedure an inert transfer or in O_2 might be necessary between XPS and SEM, but the available instruments were not designed to make this possible, and in air the Pd surface oxide decomposes and the surface structure might change.

3.4 Data analysis methods for time series *in situ* XPS data

3.4.1 Introduction

The capability of some modern XPS instruments to perform *in situ* studies, enabled researchers to perform kinetic (time dependent) and temperature dependent investigations in reactive atmospheres. As a consequence, dynamic electronic structure changes, which depend on the applied conditions, can be observed. To get a fundamental understanding of the processes taken place at the surface e.g. of catalysts in reactive atmospheres, it is crucial to identify correlations between for instance chemical shifts of the metal species and the O1s species, or between oxide species and impurities. To study such correlations, a good time or temperature resolution of all chemical species is required, since their electronic structure might constantly change, due to changes in the environmental conditions. A sufficient temperature, time and energy resolution can be achieved by measuring all relevant high-resolution XPS spectra repeatedly in rapid successions, whereby the temperature is increased in a slow, constant rate. Such repeating measurements can be easily performed by using the 'loop' function in SpecsLab Prodigy, which is the standard software for *in situ* XPS measurements. By this procedure large, challenging datasets, where each spectrum has a poor signal-to-noise ratio, are obtained. Alternatively, each spectrum could be measured until a sufficient signal-to-noise ratio is obtained. However, since structure changes might occur within those 'long' acquisition times, the electronic structure can't be correlated to another chemical species, which makes this alternative fail to study structure correlations. Hence, methods need to be developed by which the large and challenging datasets, where the peak fitting model need to be internally consistent across hundreds or thousands of spectra, can be analyzed in appropriate time and with high reliability of the peak fitting model.

In this chapter of the thesis, different data analysis methods are presented, applied and critically evaluated to improve the analysis and understanding of large time/temperature series *in situ* XPS datasets. The data analysis methods imply different statistical visualization tools for example correlograms (scatter matrix) and Pearson correlation-based heat maps. However, the main focus lays on principal component analysis (PCA), which is applied two times within the data analysis procedure. First, to reduce the noise in the raw data, and second, on the peak areas of the different XPS species, received from the peak fitting process. In the existing literature there are two examples, where PCA was applied on XPS peak areas to find patterns in the electronic structure of different samples.[193,194] However, PCA on peak areas of time/temperature series *in situ* XPS data has to the best of my knowledge never been published before. All the here utilized data analysis methods have in common that they can be easily applied to large datasets of dynamic processes (e.g. by a few lines of code in a python script).

Finding the right peak fitting model of XPS data is not straight forward, which starts already with uncertainties in the binding energy calibration and the background choice (see XPS method section 2.1) and it becomes even more challenging when there are many overlying signals as it is very often the case for O1s and C1s spectra.[50,64] When chemically and physically interpreting O1s or C1s signals care needs to be taken to not overinterpreted the data. Besides, the addition of more peaks to a signal leads typically to improved fitting, although it can be chemically meaningless.[64] The reliability improves when additional spectra are shown, e.g. a metal oxide species can be referred to an O1s species. However, scientists could still just show those selected spectra which matches to their explanation.

In contrast to latter, the data analysis methods described and applied herein consider all measured spectra over the entire time or temperature range. Such large time or temperature resolved datasets deliver good statistics and hence when correlations extending over the whole measurement range are present, it gives evidence for a correct and reliable peak fitting model. On the other hand, when no correlations between the different species can be found over time, it indicates that the peak fitting needs to be improved, e.g. by adding additional chemical meaningful constraints. Thus, the here applied data analysis methods support the finding of correlations in temperature series *in situ* XPS datasets, as well as the iteratively adaption of the peak-fitting model in appropriate time, and with a high reliability.

The here introduced data analysis methods, were applied on many datasets collected during this PhD project, and are presented in this chapter using the example of a Pd foil in oxidative environment.

3.4.2 Experimental section

3.4.2.1 Experimental workflow

The routine experimental workflow for many *in situ* XPS datasets collected during this PhD project was already explained in chapter 2.1.3 and was also applied for the study in this chapter. After noise reduction by PCA, and peak fitting, the peak fitting model is evaluated by a line profile.

Thereby the peak areas of the chemical species are plotted as a function of temperature (or time). With such line profiles (see chapter 3.3 for examples) it can, for instance, be obtained at which time certain chemical species are forming and which species are correlated with each other, e.g. a metal oxide peak and its corresponding O1s signal. The line profile guides the peak fitting procedure and helps to identify errors within this process.

In the following additional statistical data analysis tools are described, which help to process large temperature series *in* situ XPS datasets in appropriate time and with a high reliability of the peak fitting model.

3.4.2.2 Description of the different statistical data analysis methods

3.4.2.2.1 PCA on XPS peak areas

During this PhD project XPS data was intensively analyzed by principal component analysis (PCA). Thereby PCA was not only applied on the raw data (see method section 2.1.3.1), to perform noise reduction and to get an indication of how many linearly independent chemical species could be present in a collection of spectra,[60,63] but also on the peak areas of the different synthetic chemical species after peak fitting.

The first PCA (noise reduction) is already applied in the XPS community, especially for X-ray photoelectron spectromicroscopy data, where each image pixel contains a noisy XPS spectrum.[62,195] Hence, PCA on spectra is already implemented into the XPS data analysis software CasaXPS. The second application of PCA on peak areas for time series XPS data is a new approach.

To perform PCA the singular value decomposition (SVD) function in Python was used (see appendix for the code).[61,63]

$$X_{m\times n} = U_{m\times n} \times S_{n\times n} \times V_{n\times n}^{T} \tag{3-10}$$

m is hereby the number of collected spectra, each at a different temperature and n the number of synthetic chemical species found in the peak fitting procedure.

Before processing SVD, the variables n (peak areas) are autoscaled, through which each chemical species gains equal magnitude, and hence, equal importance in the analysis. Autoscaling is done by subtracting the mean of each variable (peak area of chemical species) and division by the standard deviation.

SVD returns the loading matrix V, where each row contains the contribution of each chemical species (peak area) to the PC. The rows are also called eigenvectors and contain as many data points as there are chemical species. The loadings are expressed by bar plots in this work. PC1 has the highest variance and explains the data matrix X in the best possible way. Thus, PC1 is associated with the highest singular value in the diagonal matrix S. PC2 is perpendicular to PC1 and has the second largest singular value, and so on. The singular value is the square root of the eigenvalue and describes, how much of the dataset's variation (spread of the data) is described by the PC/eigenvector. By multiplying the score matrix U with S, a line profile is obtained, where the score/contribution of each PC as a function of the temperature is plotted. As closer the line of a PC is fluctuating around 0, it can be associated to noise. Another way to see how many dimensions/PCs are needed to explain the variability in the original dataset is the histogram of the cumulative variation explained. Here, it can be seen how many PCs are needed to explain e.g. 98% variability.

For a more detailed explanation of PCA, the reader is referred to chapter 2.1.3.1 and other literature.[58,59,63]

3.4.2.2.2 Pearson correlation heat map

The Pearson correlation coefficient ρ, which is intensively applied in statistics, measures the linear correlations of two variables (x and y), meaning to which extent the two variables vary together. Thereby the covariance (3-11) of x and y, which measures to which extend the elements of two variables move in the same direction ($\bar{x}$ = mean value), is divided by the product of the standard deviation of variable x and y (3-12).[196]

$$cov\,(x,y) = \frac{\sum(x_i-\bar{x})(y_i-\bar{y})}{(N-1)} \tag{3-11}$$

$$\rho(x,y) = \frac{cov(x,y)}{std(x)\cdot std\,(y)} \tag{3-12}$$

The Pearson correlation coefficient can have values between -1 and 1. A value of 1 means a fully positive linear correlation and -1 a fully negative or anti correlation. Values around 0 can be assigned to no correlation. To get an overview, which species are correlated with each other, the design of a Pearson correlation heat map is a very fast and easy interpretable tool (see appendix for the Python code). Nonetheless, it has so far not been used to study correlations in XPS datasets.

3.4.2.2.3 Correlogram, scatter matrix

The correlation heat map gives an excellent overview of the correlations. However, if one is interested in more details, especially for the interpretation of data of intermediate correlation coefficients (-0.8 → +0.8), a scatter matrix or correlogram might be helpful. Thereby the peak areas of each chemical species are plotted against the peak areas of all other species in a scatter plot. From this matrix it can be obtained, if the correlation is positive or negative, or if there are regions, where there is some correlation and in others not, giving rise to intermediate correlation coefficients. This data analysis method becomes even more conclusive if a third dimension is added to the data like the time or temperature. The third dimension can be added by giving the scatter points colors depending on their value. One drawback of the correlogram is that it might become very space demanding and more time consuming to interpret as more variables (chemical species) are included.

3.4.2.2.4 Rolling Pearson correlations

In the correlation heat map the Pearson correlation coefficient of the entire dataset is presented, which gives a good overview, but it is insensitive for correlations in a small temperature or time range. To be able to obtain even such small linear correlations, rolling (or moving) correlation calculations can be performed. Thereby a window size is specified, which is the number of data points used to calculate the correlation. This window is then “rolling” throughout the dataset from low to high temperature (or times).[196] The smaller the window the better is the temperature resolution, however it will also be more sensitive to noise in the data. It is important to consider that changes in the data are required in order to see linear correlations. If two species are present at the same time without changing, no linear correlation can be observed with the rolling correlation method. Additionally, no correlation coefficient can be calculated, if one or both of the peak areas in the considered window are 0. Furthermore, the rolling correlation leads to a shift of the data towards higher temperatures or times, since e.g. with a window of 30, the Pearson correlation can first be calculated for the 30est value. However, by using the center function (in Python, see appendix), the correlation can be shifted back to the center of the window. A good way to graphically represent the rolling correlation results is to plot the peak areas of one of the two species considered in the correlation as a function of the temperature or time (scatter line profile) and then colorize the scatter points according to the rolling Pearson correlation value.

3.4.2.3 NAP-XPS study of Pd in oxidative environment

For the *in situ* XPS measurements, a lab source NAP-XPS using monochromatic Al Kα (1486.6 eV) radiation and a Phoibos NAP-150 hemispherical analyzer from SPECS GmbH, was used. The samples were heated using an IR laser from the rear, and the temperature was measured by a chromel-alumel thermocouple.

Prior to the experiment, the 0.1 mm thick Pd foil (Alfa Aesar, 99,9% purity) was cut into a 8×8 mm piece and afterwards cleaned by several Ar^+ sputtering and annealing cycles (in 0.5 mbar O_2) at 700°C to soak out impurities.

For the oxidation experiment, the Pd foil was pretreated, after Ar^+ sputter cleaning, in 0.5 mbar air (accidently, because there was a leak in the hydrogen line) at 400°C for 90 min. Afterwards the Pd foil was heated in 1 mbar O_2 with a temperature ramping speed of 1.5°C/min from 180-800°C. The spectra were recorded during the temperature ramp using 'loops', where each loop consist of a set of XPS spectra (Pd3d, $Pd3p_{3/2}$ / O1s, the valence band and an impurity survey spectrum (between 300-80 eV)). In total 153 loops were recorded. Using this procedure, a temperature resolution of 5°C per loop is obtained. All spectra measured in the same loop are labelled using the average temperature during that loop, but since they are not recorded at the same time the real temperature can differ by $\pm$ 2.5°C. The drawback of this loop-procedure is that each spectrum is measured relatively quickly, and therefore the spectra are quite noisy. Fortunately, the signal-to-noise ratio can be very much improved, while retaining the time resolution, by using the already described PCA noise reduction. All XPS spectra shown in this chapter are treated with the PCA noise reduction using CasaXPS 2.3.23. Reference spectra were utilized for peak fitting. The reference spectra were measured in vacuum, and a Tougaard background was applied. Additional components that arose during the oxidation process, for which reference spectra are not available (such as sub-oxide species), were fit using synthetic line shapes of a Voigt form. For more details about the XPS analysis procedure, see chapter 2.1.3.

3.4.3 Results and discussion

When the polycrystalline Pd foil is exposed to 1 mbar oxygen, PdO is formed above 300°C. In the $Pd3d_{5/2}$ spectrum (Figure 3-21a) it can be observed that the PdO peak shifts towards higher binding energies from 336.6-336.8 eV as the temperature further increases. At even higher temperatures (see 800°C spectrum, Figure 3-21a) the oxide decomposes again to Pd metal. The O1s signal overlays with the $Pd3p_{3/2}$ peak and the O1s gas phase signal (Figure 3-21b). Using the $Pd3p_{3/2}$ signal measured in vacuum in the reduced state as reference spectra, it was possible to differentiate between the $Pd3p_{3/2}$ metal and the oxide. Additionally, two O1s species O(I), O(II) were identified (Figure 3-21c).

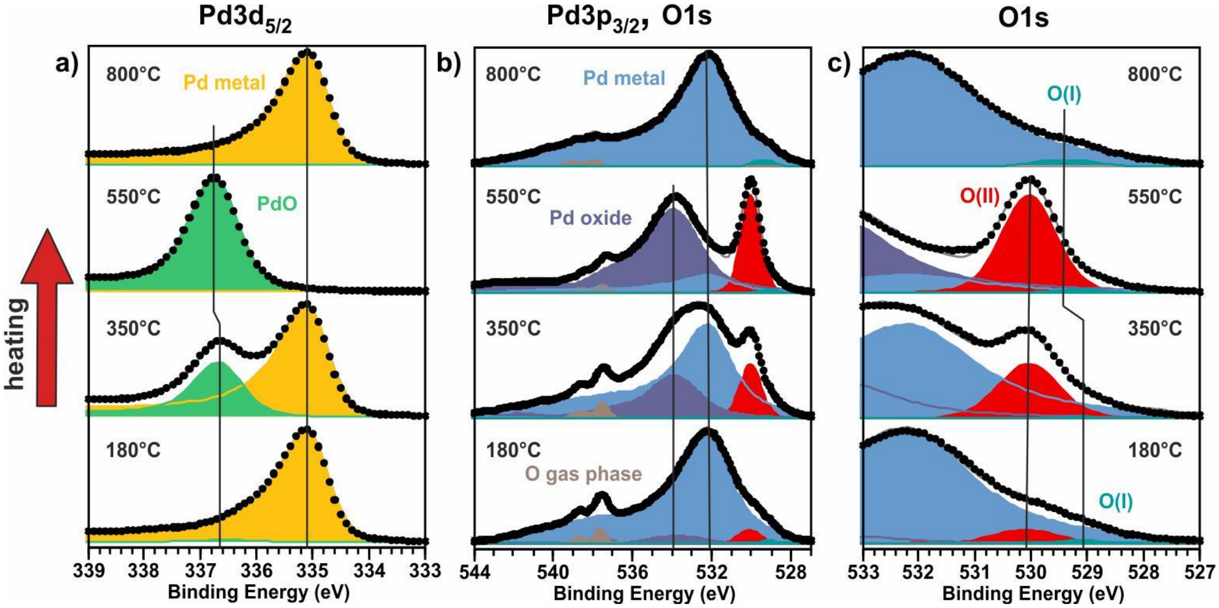

Figure 3-21: $Pd3d_{5/2}$ (a) and $Pd3p_{3/2}$, O1s (b) and (zoomed) O1s (c) XPS spectra of the Pd foil during heating in 1 mbar O_2. The black circles represent the measured points after PCA noise reduction and background subtraction. The spectra are min to max normalized.

To get an overview of how the concentration of the different species are changing with time, their relative peak areas are plotted in a temperature-line profile (Figure 3-22a). The $Pd3p_{3/2}$ and oxygen gas phase signals are not considered here, since the focus was to investigate the correlations between the $Pd3d_{5/2}$ and O1s signals. The 'onset oxidation temperature' (OOT) in Figure 3-22a is defined as the intercept between the baseline and the line of the steepest slope,[197] the onset oxide decomposition temperature (OODT) is defined in the same manner. The OOT is at approximately 325°C, this is the point where PdO begins to grow on the surface. The PdO grows to at least 4.5 nm (3λ) thick, as is inferred from the fact that no more Pd metal signal could be detected at 440°C. At 630°C (OODT) PdO decomposes very rapidly to Pd metal. Already in the temperature line profile the correlation of PdO and O(II) can be clearly observed.

3.4.3.1 Principal component analysis

In the next step the peak areas of the synthetic components are analyzed by PCA over the entire temperature range (description see 3.4.2.2.1). The results of the PCA for the Pd foil are shown in

Figure 3-22. After the peak fitting, all peak areas (synthetic chemical species) will be auto-scaled in order to give each species equal importance in the PCA. From the histogram of cumulated variation explained (Figure 3-22b) it can be obtained that two principal components explain 99.8% of the variability in the original dataset, PC1 explains already 84%. Thus, two PCs are sufficient to explain the variability of the dataset, and the dimension could be reduced from 4 chemical species to 2 linearly independent components. In general, the sign of the loadings and scores can be exchanged by multiplying with -1, therefore the absolute values are decisive. O(II) and PdO have with -0.54 equal and the highest contribution to PC1, followed by Pd metal (0.52) and O(I) (0.37) (Figure 3-22d). The corresponding score plot (line profile, Figure 3-22c) shows a positive contribution below 330°C, it then is negative until 650°C and afterwards again highly positive. This can be interpreted as representing the oxidation of Pd, whereby Pd metal is anticorrelated with PdO and O(II) since the Pd metal peak disappears as it oxidizes to PdO.

PC2 explains 16% variation of the dataset, from the loadings (Figure 3-22e) it can be observed that O(I) has the highest contribution to PC2, whereas O(II), PdO and Pd metal have only little contribution and hence are not correlated with O(I). The score plot shows, that PC2 has positive intensity until 350°C and then gradually decreases, with fluctuations at the oxide formation and decomposition temperature. This pathway reflects the inverted temperature line profile of O(I), which is present before the OOT (<325°C) at 529.1 eV and appears again at 529.4 eV as the temperature increases and it is still present above the OODT (>620°C). According to the literature O(I) is linked to a low binding energy Pdox(I) species, which is a part of a 2D oxide Pd_5O_4 precursor species, present prior to PdO.[65–67,176] This Pd_5O_4 species consist of two peaks at 335.5 eV (Pdox(I)) and 336.2 eV (Pdox(II)) with a ratio of 4:1 on a Pd(111) single crystal. The corresponding oxygen species have binding energies of 528.9 and 529.6 eV.[65,66] In the pathway of PC1 a plateau is observed below 325°C, where there is already a weak PdO and O(II) signal present. It might be that in this temperature range the reported Pd_5O_4 precursor species is present. It should be noted that in the present work, the Pd oxidation was measured with an Al Kα source (1486.6 eV), which is less surface sensitive than the photon energies used in previous Pd oxidation studies measured at synchrotron facilities.[65–67,176] Therefore, these measurements are less sensitive for the Pd_5O_4 2D oxide. The O(I) species is also present as the PdO signal decomposes (>620°C) at a binding energy of 529.4 eV, and has been previously suggested to be dissolved oxygen,[66] however, impurities bound to oxygen could also be a candidate for this species.

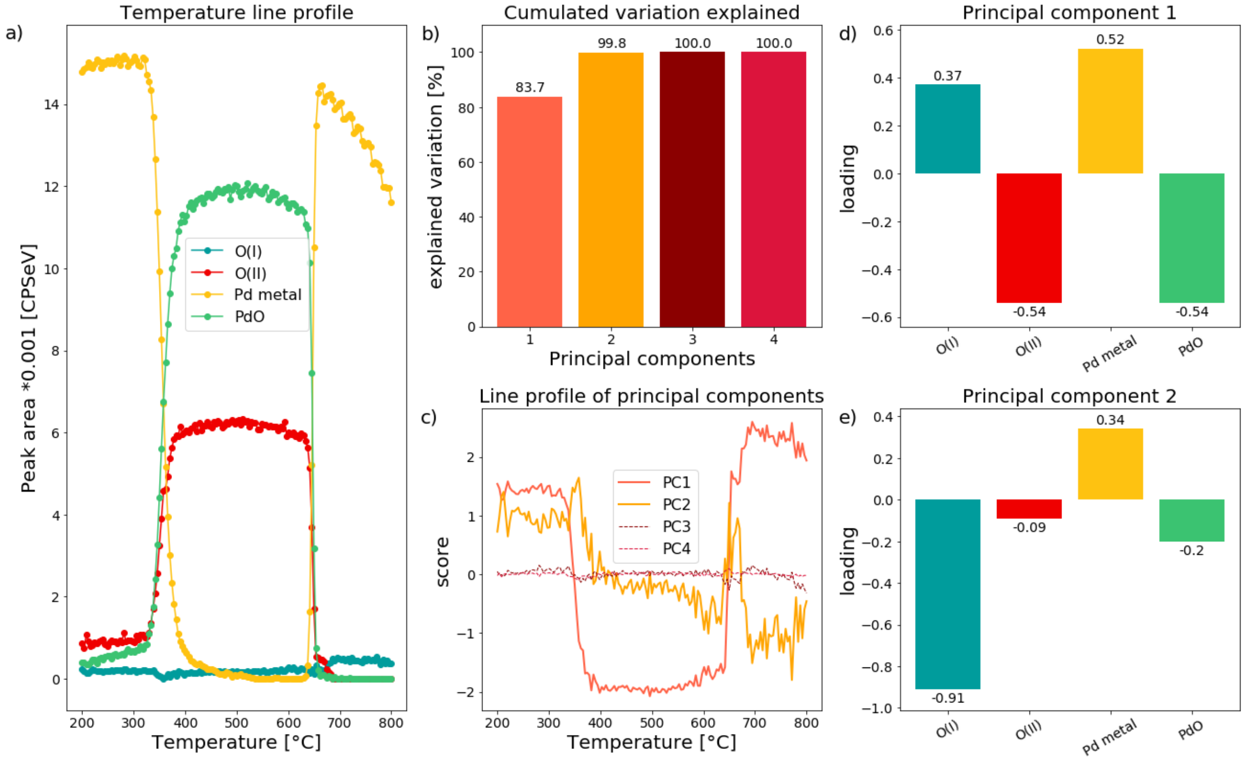

Figure 3-22: a) Peak area line profile of the synthetic components as a function of temperature during heating; b) Explained variation after performing PCA on the peak areas of the different species; c) Pathway of the principal components; d, e) Contribution of each chemical species to the principal component 1 and 2 (graphic representation of the eigenvectors).

With the information gained from the PCA and the help of the available literature on Pd oxidation using NAP-XPS, the peak fit was improved by adding Pdox(I), Pdox(II) as well as a O(IV) (high temperature O1s species) and a O(PdO) species. The binding energies of those species were set to the values reported in literature, and only very small peak shifts (0.2 eV) were allowed. The new peak fit is visualized in Figure 3-23. The ratio of the newly added Pdox(I) and Pdox(II) species is always very close to 4:1, this ratio is characteristic for the Pd_5O_4 precursor species and verifies its presence.[65]

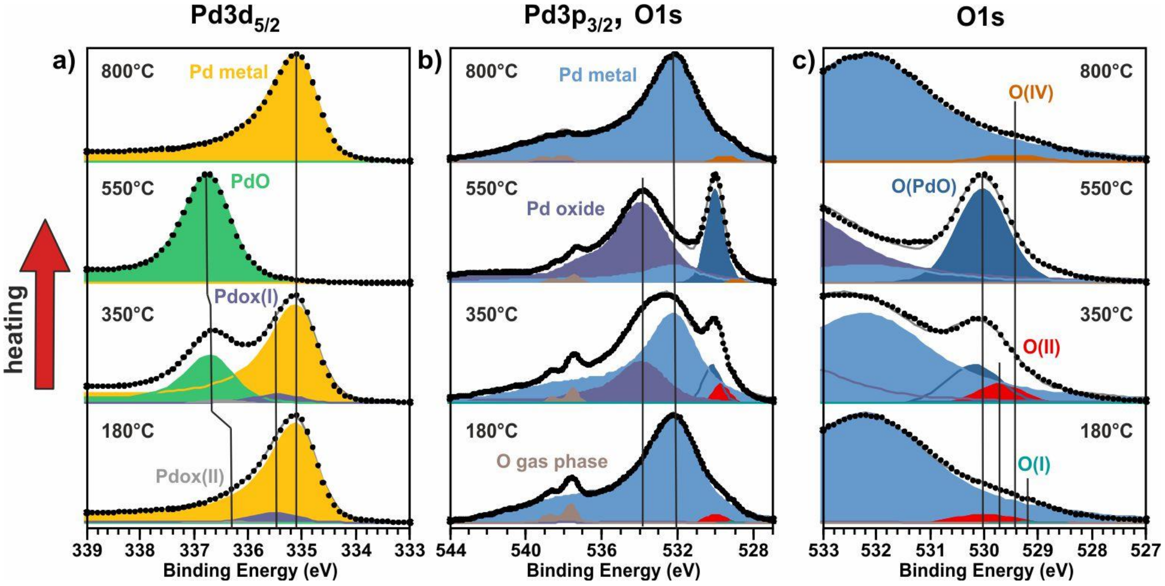

Figure 3-23: Improved peak fitting model of Pd3d$_{5/2}$ (a) and Pd3p$_{3/2}$, O1s (b) and (zoomed) O1s (c) XPS spectra of the Pd foil during heating in 1 mbar O_2. The black circles represent the measured points after PCA noise reduction and background subtraction. The spectra are min to max normalized.

Figure 3-24 represents the temperature-line profile and the result of the PCA analysis of the improved peak fitting model. In the new fitting model, the first two PCs explain 97% of the variation (Figure 3-24b), which is 3% less than in the previous simplified peak fit (Figure 3-22). The reason for this is, that the addition of more species reduces the certainty of the peak areas especially of the O1s species, which are located very close to each other and additionally also overlap with the Pd3p$_{3/2}$ species. The higher uncertainty of the peak areas can be observed by the fluctuations of PC3 below 325°C in the PC line profile plot (Figure 3-24c). As the noisy PC3 does not contain any valuable chemical information, the dimensions could be reduced from 8 chemical species to 2 linearly independent principal components. PC1 explains 70% of the variation in the dataset. The Pd_5O_4 precursor species, Pdox(I), Pdox(II), O(I), O(II) have the highest loadings associated with PC1 (-0.4 each) followed by Pd metal (-0.34) and PdO as well as O(PdO) with 0.33 respectively. The score plot has a highly negative intensity below the OOT (>325°C), becomes then positive and reduces to almost 0 above the OODT (>640°C). The fact that Pdox(I), Pdox(II), O(I) and O(II) have the same loadings to PC1, verifies a good peak fitting and gives evidence that the Pd_5O_4 precursor species is indeed present prior to PdO formation. The Pd metal species is also positively correlated with the precursor species, since they all together disappear as PdO forms. However, the contribution of Pd metal is less than of the Pd_5O_4 species, since Pd metal appears again above the OODT. PdO and O(PdO) are negatively correlated to the Pd_5O_4 and the

Pd metal species, since they are present, as the other chemical species are not. Thus, PC1 describes the oxidation of the Pd_5O_4 precursor species to PdO and to some extend also the decomposition of PdO.

PC2 explains 27% variation. O(IV) has the largest contribution to this component (-0.58), The loading of Pd metal is -0.41 and has almost the same magnitude as the anticorrelated PdO and O(PdO) with 0.42 each (Figure 3-24e). The four precursor species have little contribution to PC2. The temperature line profile of PC2 is relatively constant below the OODT and then decreases significantly. Consequently, PC2 describes the decomposition of PdO and the formation of the high temperature O(IV) species.

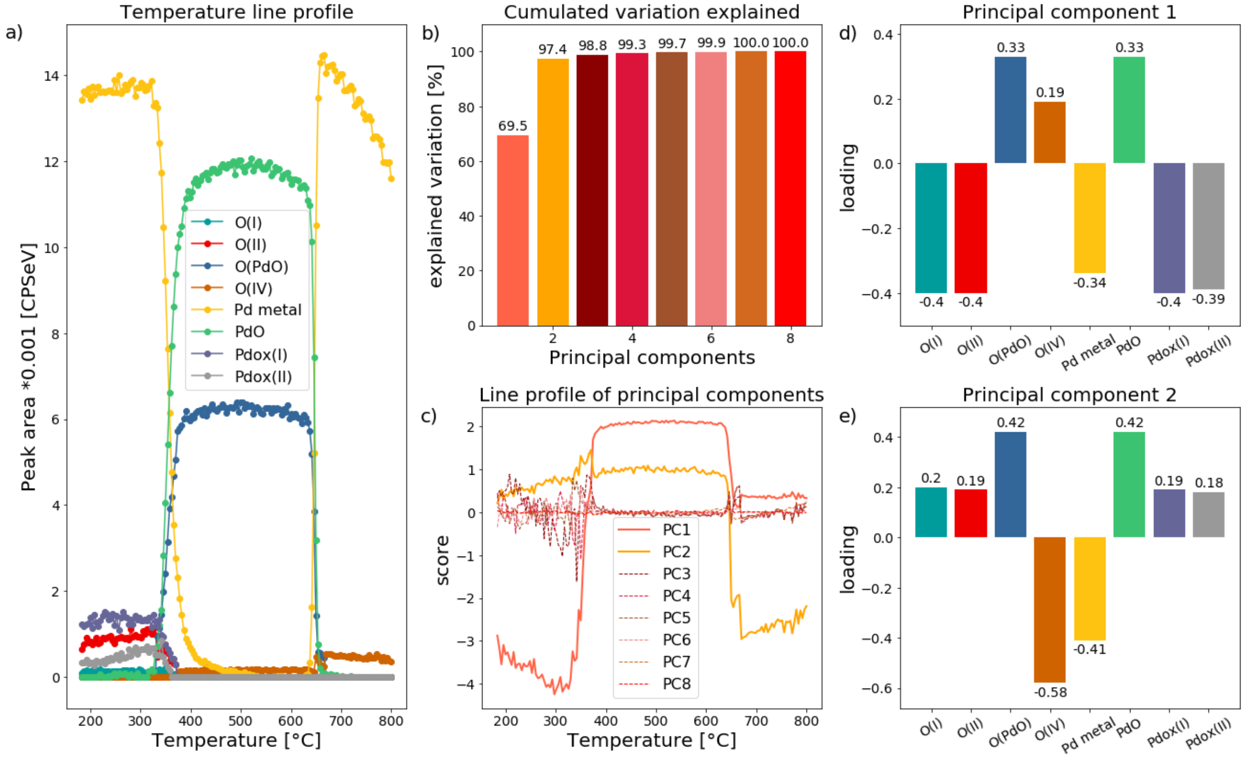

Figure 3-24: Improved peak fit; a) Peak area line profile of the synthetic components as a function of temperature during heating; b) Explained variation after performing PCA on the peak areas of the different chemical species; c) Pathway of the principal components; d, e) Contribution of each synthetic component to the principal component 1 and 2.

In summary, the temperature-line profile and the PCA analysis procedure helped to identify the Pd_5O_4 precursor species and clearly identified the positive correlations between Pdox(I), Pdox(II), O(I) and O(II), as well as between PdO and O(PdO). Through the trends and fluctuations in the temperature-line profile of the chemical species as well as of the PCs (Figure 3-24a and c) it is possible to evaluate the reliability of the peak fitting model.

Through the consideration of all spectra and peak areas, the here applied analysis procedure offers much more insight into the correctness of the peak model, than if just a few selected XPS spectra are shown.

3.4.3.2 Pearson correlation heat map

The same dataset was investigated by a Pearson correlation heat map, which is a matrix, showing the Pearson correlation coefficient of the peak areas of the different synthetic components over the entire temperature range (180-800°C). The correlation coefficients are symbolized by colors ranging from dark brown (-1) for negative correlations to dark green (+1) for positive correlations (see color bar in Figure 3-25).

By a quick view on the correlation heat map (Figure 3-25) one can see that Pdox(I), Pdox(II), O(I) and O(II) are positively (>0.8) correlated to each other, this is reasonable since they all belong to the Pd_5O_4 precursor species. Furthermore, PdO and the corresponding O1s species O(PdO) are clearly positively correlated and Pd metal is negatively correlated with the formed PdO.

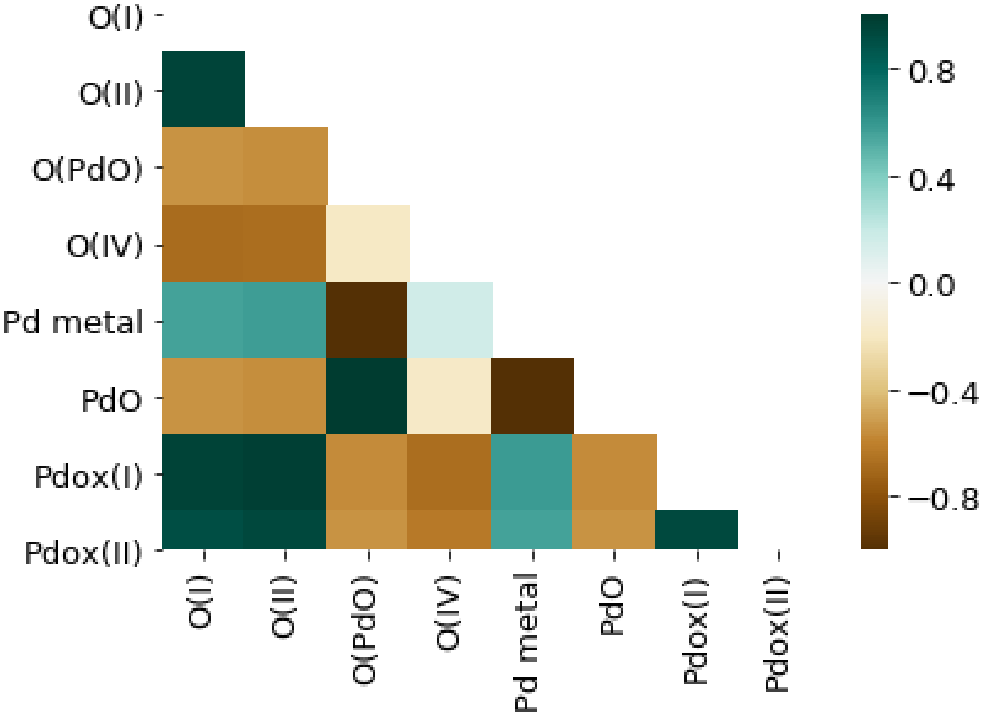

Figure 3-25: Correlation heat map for the oxidation of Pd.

The Person correlation heat map is very helpful to quickly identify patterns in the dataset, but to understand what is going on in the case of all intermediate correlations, the correlogram (scatter matrix) will provide deeper information.

3.4.3.3 Correlogram, scatter matrix

In the correlogram the peak areas of all synthetic components are plotted against each other in a matrix (Figure 3-26), thereby each correlation is present twice, in a way that the data can be mirrored by the diagonal. The measurement points are colored according to their temperature (rounded to the nearest 100°C), the colors reach from dark blue (200°C) to dark red (800°C).

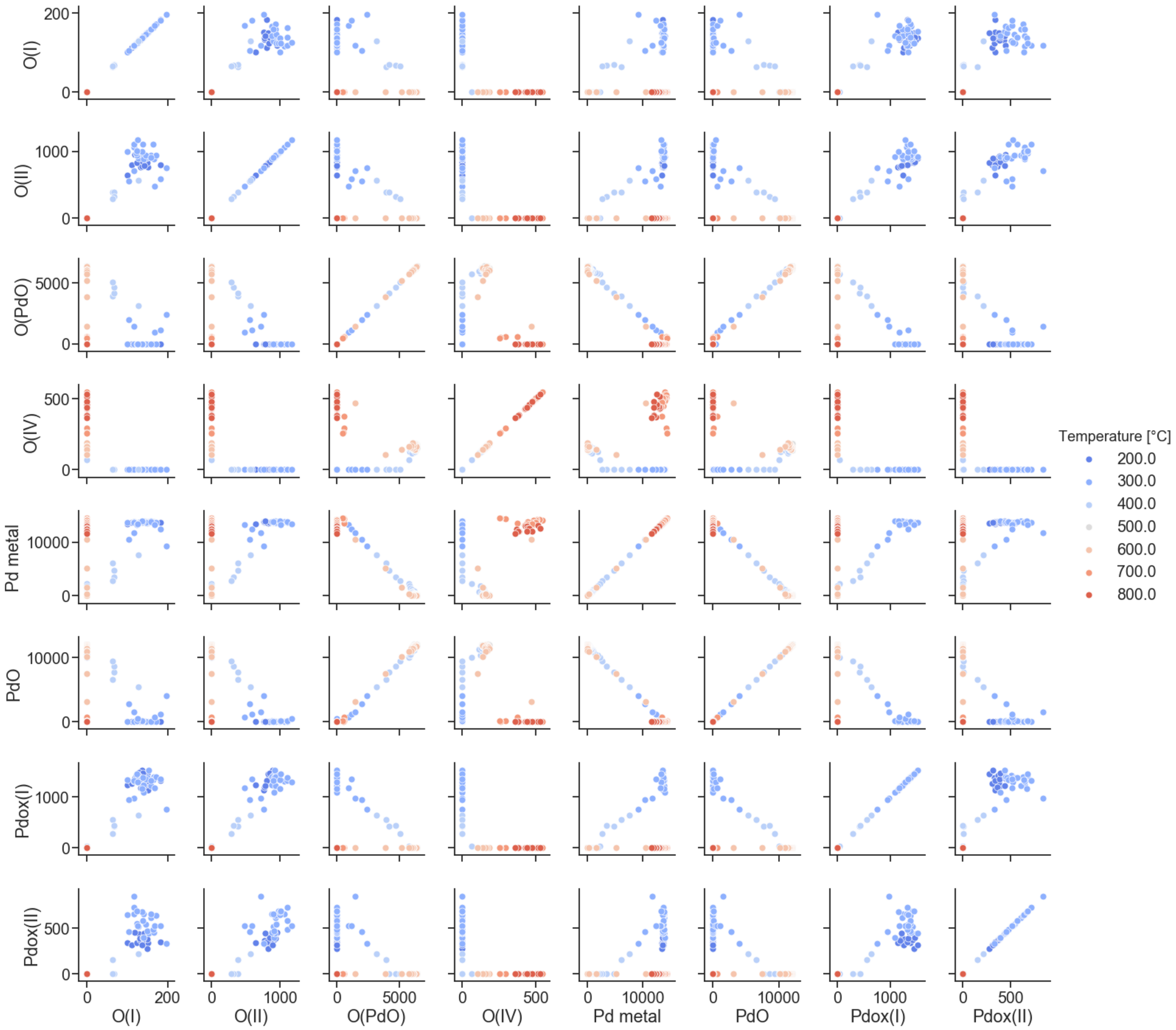

Figure 3-26: Correlogram of all species present during the oxygen treatment of Pd. The measurement points are colored according to their temperature (rounded to the nearest 100°C), the legend for this in the right-hand side of the graph.

From the diagonal of the matrix it can be obtained how the peak intensities of each species are distributed with temperature, all Pd_5O_4 species are for instance only present below 400°C. It can be seen that this scatter matrix becomes very large. Here, eight different synthetic components are shown, revealing 64 scatter plots, this makes a correlogram quite overwhelming and difficult to interpret. Selected scatter plots will be investigated in more detail in the next section.

3.4.3.4 Scatter plots and rolling Pearson correlation

In the following a closer look is taken on the correlations between Pdox(I), which represents the Pd_5O_4 precursor species with PdO and between PdO and O(IV). For this purpose, the corresponding scatter plot, which are already shown (in small) in Figure 3-26 and additionally their rolling Pearson correlation (Figure 3-27) will be discussed.

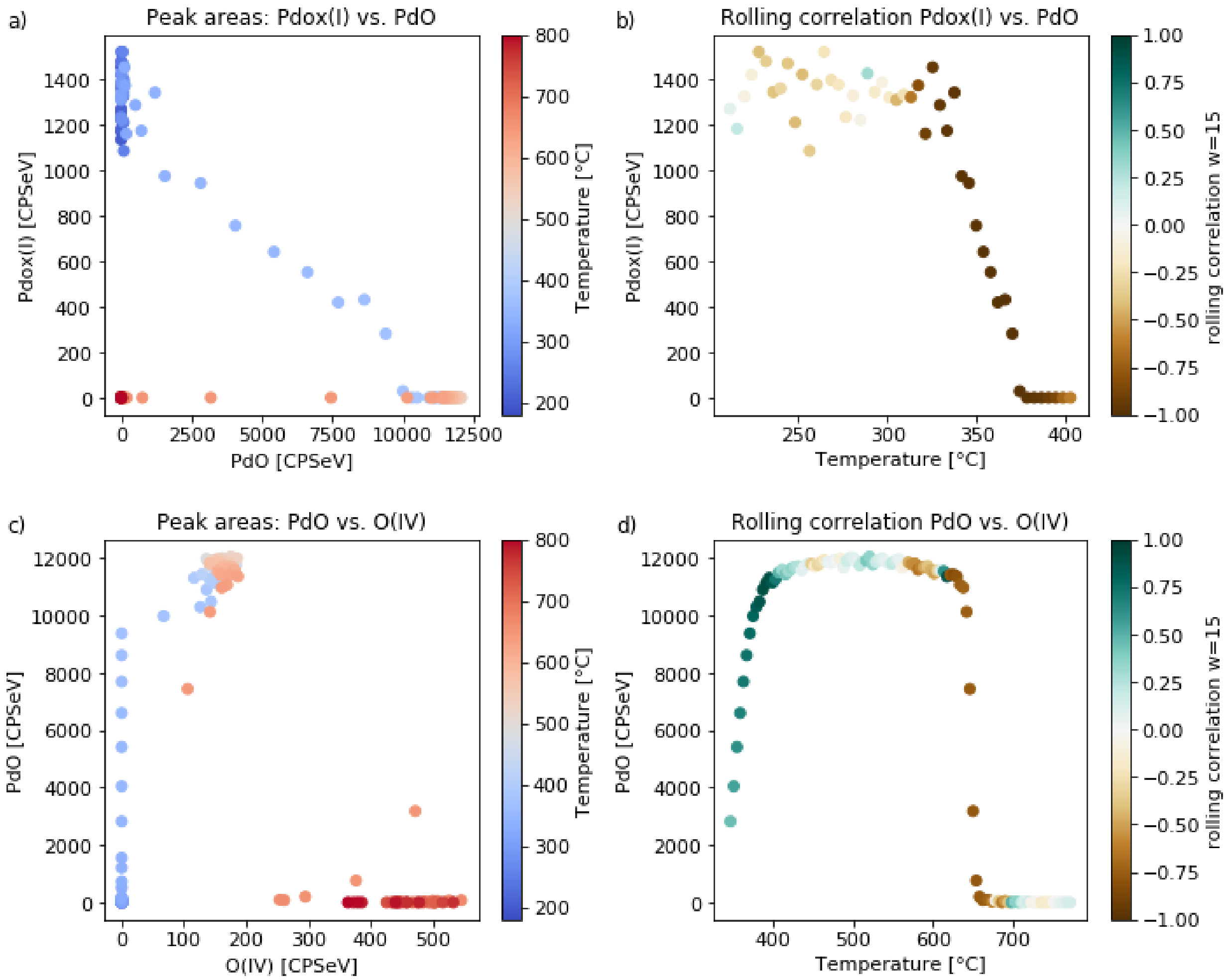

Figure 3-27: a) Scatter plot of Pdox(I) peak areas vs. PdO; b) Corresponding rolling correlation plot with a window size of 15. Thereby the peak area of Pdox(I) vs. the temperature is plotted and the Pearson correlation with PdO is symbolized by the color; c) Scatter plot of PdO vs. O(IV); d) Rolling correlation plot with a window size of 15. Thereby the peak area of PdO vs. the temperature is plotted and the Pearson correlation with O(IV) is symbolized by the color.

From the rolling correlations in Figure 3-27 it can be observed that positive or negative correlation can only be detected, when the data is changing (two species are increasing or decreasing at the same time). At constant peak areas, for example on the plateaus of PdO and Pdox(I), there is no correlation (correlation coefficients between -0.5 and 0.5). Additionally, when one of the peak areas are 0, no correlation can be calculated, which is why the temperature scale in Figure 3-27b does not exceed 400°C.

When looking at the scatter plot of Pdox(I) and PdO (Figure 3-27a) it can be recognized, that below 325°C only Pdox(I) is present, then the Pdox(I) is decreasing, whereas in the same time PdO is forming, this give rise to the linear decay in the scatter plot and accordingly to a highly negative correlation during the decrease of the Pdox(I) (see also Figure 3-27b). O(IV) has a pathway, where a small amount is formed as PdO starts to form, revealing a positive correlation below 400°C (Figure 3-27d). Above 600°C PdO then decomposes, whereas O(IV) further increases leading to a negative correlation (Figure 3-27c,d). From the analysis it can be concluded, that rolling correlations are a powerful method to identify and interpret correlations in a small temperature or time ranges. Additionally, the scatter matrix and rolling correlations facilitate in depth analysis of electronic structure changes at the surface of catalysts.

3.4.4 Conclusion

In this chapter the application of different statistical data analysis tools, which were used during this PhD project to find correlations in large and challenging temperature series *in situ* XPS datasets, were discussed. A polycrystalline Pd foil in oxidative environment was studied as an example system. The statistical data analysis methods represented here (PCA on peak areas, Pearson correlation heat map, correlogram and rolling correlations) all have in common that they can be easily applied to large data sets of dynamic processes (e.g. by a python script with few lines of code), thereby each of those methods has their own advantages and disadvantages. The PCA on peak areas together with the peak area-temperature line profile reveal that a PdO precursor species might be present prior to the PdO formation and hence helped to guide and to iteratively adapt the peak fitting procedure. Additionally, correlations between PdO and the corresponding O(PdO) species as well as between Pdox(I), Pdox(II), O(I) and O(II), which all correspond to the Pd_5O_4 precursor species, were found. An even faster way to identify correlations and patterns in the dataset, is the Pearson correlation heat map, but it is less appropriate to identify and understand intermediate correlations. For such cases scatter matrixes (correlograms) and rolling correlations are better suited, since the can identify correlations in short time or temperature ranges, but are as a consequence more challenging to interpret. In addition, those methods facilitate high reliable peak fitting models, since they cover the entire time or temperature range and not just a few selected spectra.

Since the fundamental understanding of correlations taken place at the surface of catalyst are essential for the way towards rational catalyst design, it would be beneficial, if the here discussed data analysis methods would be applied more often in the *in situ* surface science community. Thereby they are not only applicable to *in situ* XPS datasets, but can be applied to find correlations and patterns in all challenging, dynamic datasets.

4. Overall discussion and conclusion

The aim of this work was to study structure-function correlations of AgX (X=Cu, Pd) single-atom alloys, where the active Cu or Pd atoms are present as single isolated sites in an Ag matrix. Previous work from Greiner *et al.* showed, that $Ag_{0.997}Cu_{0.003}$ SAAs exhibit a unique free-atom-like electronic structure, where the Cu3d valence states are electronically and spatially separated from the Ag4d valence states.[3] As a consequence, the Cu3d states are so narrow, that the electronic state is more similar to an isolated Cu atom in gas phase than to bulk Cu.

In this work it was shown by comparing the Pd4d valence states (measured by XPS) with the calculated photoemission signal of a free Pd atom in gas phase, that $Ag_{0.98}Pd_{0.02}$ SAA exhibit a similar free-atom-like electronic structure than AgCu SAAs (see chapter 3.2). Consequently, the aim was to study, what effect the unique electronic structure of AgPd and AgCu SAAs has on adsorbate bonding and catalysis. Such structure-function correlation studies are essential towards rational catalyst design and are based on *operando* investigations. *Operando* in the case of NAP-XPS studies means, that the catalytic performance will be simultaneously measured with the XPS signal, which provides information about the electronic structure of the catalyst. The catalytic performance can thereby be monitored by detecting the gas phase, either by GC or QMS. There exist many requirements for a SAA catalyst to be analyzed by *operando* XPS, which is first of all a sufficient high specific surface area to detect product formation. Furthermore non-conductive support materials such as Al_2O_3 or SiO_2 should be avoided, since they charge during the photoemission process, which leads to shifts of broadening of the XPS signal and hence an infeasible electronic structure analysis. Additionally, supports add an additional complexity to the sample system, which should be held as simple as possible to study fundamentally the impact of the isolated atoms in the SAA system on the catalytic performance. Therefore, the sample also needs to have a very high purity.

Within this work it was tried to fulfil those requirements by depositing AgCu SAA nanoparticles on an Ag support. It was expected that the Ag support will not alter the chemical behavior of the sample much, since it is anyway the main constituent of the AgCu SAA. The sample preparation was performed in cooperation with CENIDE (Chemical engineering group of Prof. Stephan Barcikowski, University Duisburg Essen). Thereby the AgCu nanoparticles were created by pulsed laser ablation in liquids and afterwards deposited on an Ag support by electrophoretic deposition. The Ag support was made by creating a disc out of Ag powder and subsequent sintering. After developing the “Sniffer QMS” system to detect the gas phase inside the analysis chamber of the laboratory NAP-XPS, the AgCu high surface area samples were investigated under epoxidation conditions. Thereby the total oxidation product CO_2 could be detected, which was a highly positive result because it revealed that the in-house designed “Sniffer QMS” was sensitive enough to detect product formation. Unfortunately, it was not possible to draw conclusions about the structure-function correlation due to the following reasons. Firstly, a reference sample consisting only of the Ag support showed similar activity. Secondly, the reaction conditions highly affected the surface structure of the sample, as it could be shown by SEM images before and after the reaction. During the reaction the AgCu nanoparticles sinter together and unite with the Ag support, as a consequence the surface area decreased and the Cu, which had an initial concentration of 2at% in the AgCu nanoparticles, became more and more dilute in Ag. At some point no Cu signal could be detected by the XPS anymore. Those drastic structure changes made it impossible to study structure-function correlations. Another approach, where the surface area of a silver foil was increased by laser induced surface roughening (in cooperation with TU Clausthal) also failed, since the surface area was still too low to detect product formation with the “Sniffer QMS”.

The here discussed studies highlight the challenges towards rational catalyst design, especially to overcome the “material gap”. The samples have to be chosen and prepared to fulfil the requirements of the analysis methods, at the same time a high surface area is required to measure the catalytic properties and to investigate sample systems close to real industrial catalysts. Additionally, to draw real structure-property correlations, fundamental processes need to be understood, which requires simple sample systems (model catalysts). Finally, the huge parameter space during *operando* conditions causes structure dynamics, whereby the scientist loses the control over the surface structure and the processes taken place at the surface of the sample.

In this thesis the above-mentioned challenges were approached by investigating polycrystalline AgPd SAA foil model catalysts in detail. Thereby the properties of the isolated Pd atoms in the Ag host were compared with a bulk Pd sample in shape of a polycrystalline foil. Pd has the highest catalytic activity of all metals for oxidative reactions.[155] Therefore, it was examined how the electronic structure of the $Ag_{0.98}Pd_{0.02}$ SAA differs from bulk Pd in oxidative atmosphere (see chapter 3.3). For this study the samples were heated inside the NAP-XPS in 1 mbar oxygen with a slow, constant rate. It was found that Pd in $Ag_{0.98}Pd_{0.02}$ partially oxidizes, forming a meta-stable PdO_x surface oxide. This PdO_x is in comparison to PdO formed on the Pd foil substantially less thermodynamically stable, and decomposes at temperatures about 270°C lower than the native oxide on Pd. Through a peak area modelling procedure, it was concluded that the PdO_x on the AgPd SAA is present as thin, possibly monolayer, PdO_x islands. The results of the modelling procedure could not be verified by *in situ* SEM. The reason for this behavior might be, that the Ar^+ sputter pre-treatment, which is a common cleaning step for XPS investigations, could not be performed in the ESEM. This observation emphasizes the uniqueness of the PdO_x formed on the AgPd SAA in NAP-XPS conditions. On conventional AgPd alloys, the oxidative atmosphere, would instead lead to phase segregation and nanoparticle formation, which could not be observed for the AgPd SAA. Since meta-stable surface species are often the reactive phase of heterogeneous catalysts, and because Pd is highly active in the total methane oxidation reaction, it was investigated whether the meta-stable PdO_x surface oxide on AgPd SAA could be active in methane oxidation at low temperatures (≤300°C). The investigation was performed at BESSY II, where a highly sensitive GC was attached to the XPS analysis chamber. The results revealed that although the PdO_x surface oxide is present at a reaction temperature of 300°C under methane combustion conditions, no product (CO_2) could be detected, whereas CO_2 formation could indeed be detected for the polycrystalline Pd foil (see chapter 3.3).

AgPd alloys are known for their superior performance in the selective hydrogenation of acetylene towards ethylene, where those alloys have a higher selectivity compared to pure Pd.[103–105] Hence, the question arose whether it is beneficial to drive the dilution of Pd to the single-atom level. To study this question catalytic tests were performed using the same setup as for the methane oxidation. It was found that in contrast to the pure Pd foil and $AgPd/SiO_2$ SAA[91] (from Pei *et al.*) the AgPd SAA foil exhibits no measurable activity in the semi-hydrogenation of acetylene. From this result and by discussion appropriate literature it was concluded that the electronic and geometric Pd-site-isolation in the inert Ag host deactivates the catalyst. The main issue hereby is, that the Ag host is fully inert, therefore the educts H_2 and acetylene, which can only be activated on the isolated Pd sites, are too far away from each other for the adsorbates to react. Instead, when the host metal participates in the reaction, as it is the case for e.g. CuPd SAA, where H_2 is dissociated on the Pd sites followed by spillover to the Cu host,[29] than SAAs are able to show reactivity with a high selectivity. Additionally, defect sites in the support are able to activate H_2

and hence increase the H_2 uptake and the catalytic performance.[91,142,144] Consequently, it was fond out in this work, that the active isolated sites in SAAs need their surrounding atoms (from the host or support) to participate in the reaction for overall catalytic activity of the catalyst.

Note, that this conclusion does not explain, why no activity of the AgPd SAA in methane oxidation could be observed, since due to the oxidation the alloy might lose its SAA character by forming PdO_x islands and within those islands the Pd atoms will only have short distances between each other. It is still possible that catalytic activity could be measured, if the AgPd SAA sample would have a higher surface area (e.g. supported nanoparticles). As a consequence, this catalytic study highlights again the challenges of rational catalyst design, since with a model catalyst (low surface area) sample catalytic tests are difficult, but with a complex, high surface area sample it becomes almost impossible to draw structure-function correlations.

In the following common issues of surface science and XPS studies, which are highly related to catalysis research, and which could be observed within this thesis are discussed. The alert reader might have noticed that there are differences in the Pd3d peak fitting model for the *in situ* oxidation of the polycrystalline Pd foil in chapter 3.3 and 3.4. Those differences include the precursor species present prior to PdO oxidation, the transition phase between the precursor and PdO formation and the appearance of an additional O(III) species, which was so far assigned to surface hydroxide formation in chapter 3.3 according to the literature.[177] The *in situ* analysis of Pd oxidation to PdO and the subsequent decomposition to Pd metal disclose that even the understanding of the oxidation mechanisms of simple, pure metals is highly complex. Therefore, the differences in the Pd oxidation process highlight very well the challenges of surface science, especially under *in situ* conditions, and reveal the impact of minor parameter changes. For instance, the Pd foil in chapter 3.3 was pretreated in 0.5 mbar H_2 at 450°C for 2h, which is the same pretreatment as used for the AgPd SAA alloy, with the purpose of comparability between the two sample systems. This reduction treatment can lead to the formation of Pd hydrides, which might then form hydroxides in the subsequent O_2 treatment and might give rise to the O(III) signal. On the other hand, no H_2 pretreatment was performed for the Pd sample discussed in chapter 3.4. Furthermore, the ramping speed was different in both cases (0.4°C/min in chapter 3.3 and 1.5°C/min in chapter 3.4), this difference might have an influence on the kinetics of the precursor and PdO formation. In addition, there is the complicating factor, that the Pd samples are polycrystalline and that different (precursor) surface oxides might form on the different crystal grains, which might lead to different

Pd-ox(I) and Pd-ox(II) peak positions and area ratios. For instance the formation of the Pd_5O_4 precursor was so far only reported for a Pd(111) sample system.[65] Nevertheless, the PdO nucleation process might on different grains occur at different temperatures and rates, as the ESEM investigation in chapter 3.3 proves. Finally, the laboratory XPS with an Al Kα excitation energy of 1486.6 eV is not very sensitive for the topmost surface layers, for O1s species, and for impurities (e.g. S, Si, Fe, Ni)[198], which could form additional oxides on the sample surface, thus, there is some uncertainty in the correct peak assignment.

In addition to the above mentioned catalytic and electronic structure observations, measurement and data analysis procedures were developed within this thesis to understand the dynamic process taking place at the sample's surface in reactive atmospheres. For such studies a sufficient temperature, time and energy resolution as well as signal quality was required, which was achieved by measuring all relevant high-resolution XPS spectra repeatedly in rapid succession, whereby the temperature was increased at a slow, constant rate. Thereby large datasets with good temperature resolution were generated, which was beneficial to identify correlations between e.g. metal oxide species and the corresponding O1s species. The peak fitting models needed to be internally consistent across all measured spectra. Therefore, the developed data analysis procedures can process the large and challenging datasets in appropriate time and with high reliability of the peak fitting model. For the data analysis PCA, Pearson correlation and correlograms were applied to find correlations in temperature series *in situ* XPS datasets, and to iteratively adapt the peak-fitting model. The different data analysis methods were discussed in detail in this thesis using the example of Pd in oxidative atmosphere (see chapter 3.4). By the applied data analysis methods and measurement procedure fundamental understanding of correlations taken place at the surface of catalysts could be gained, hence they are highly relevant for the way towards rational catalyst design.

References

1. Giannakakis, G., Flytzani-Stephanopoulos, M. & Sykes, E. C. H. Single-Atom Alloys as a Reductionist Approach to the Rational Design of Heterogeneous Catalysts. *Acc. Chem. Res.* **52**, 237–247 (2019).
2. Hannagan, R. T., Giannakakis, G., Flytzani-Stephanopoulos, M. & Sykes, E. C. H. Single-Atom Alloy Catalysis. *Chem. Rev.* **120**, 12044–12088 (2020).
3. Greiner, M. T. *et al.* Free-atom-like d states in single-atom alloy catalysts. *Nat. Chem.* **10**, 1008–1015 (2018).
4. Frenken, J. & Groot, I. *Operando Research in Heterogeneous Catalysis*. (Springer, 2017).
5. Evans, M. G. & Polanyi, M. Inertia and Driving Force of Chemical Reactions. *Trans. Faraday Soc.* **34**, 11–24 (1938).
6. Kilpatrick, M. & Kilpatrick, M. L. Acid and basic catalysis. *Chem. Rev.* **10**, 213–227 (1932).
7. Medford, A. J. *et al.* From the Sabatier principle to a predictive theory of transition-metal heterogeneous catalysis. *J. Catal.* **328**, 36–42 (2015).
8. Marcinkowski, M. D. *et al.* Pt/Cu single-atom alloys as coke-resistant catalysts for efficient C–H activation. *Nat. Chem.* **10**, 325–332 (2018).
9. Christensen, A. *et al.* Phase diagrams for surface alloys. *Phys. Rev. B - Condens. Matter Mater. Phys.* **56**, 5822–5834 (1997).
10. Lucci, F. R. *et al.* Controlling Hydrogen Activation, Spillover, and Desorption with Pd-Au Single-Atom Alloys. *J. Phys. Chem. Lett.* **7**, 480–485 (2016).
11. Tierney, H. L., Baber, A. E., Kitchin, J. R. & Sykes, E. C. H. Hydrogen dissociation and spillover on individual isolated palladium atoms. *Phys. Rev. Lett.* **103**, 246102 (2009).
12. Baber, A. E., Tierney, H. L., Lawton, T. J. & Sykes, E. C. H. An atomic-scale view of palladium alloys and their ability to dissociate molecular hydrogen. *ChemCatChem* **3**, 607–614 (2011).
13. Fan, J. *et al.* Recent Progress on Rational Design of Bimetallic Pd Based Catalysts and Their Advanced Catalysis. *ACS Catal.* **10**, 13560–13583 (2020).
14. Thirumalai, H. & Kitchin, J. R. Investigating the Reactivity of Single Atom Alloys Using Density Functional Theory. *Top. Catal.* **61**, 462–474 (2018).

15. Hammer, B. & Nørskov, J. K. Why gold is the noblest of all the metals. *Nature* vol. 376 238–240 (1995).

16. Niemantsverdriet, J. W. *Spectroscopy in Catalysis; An Introduction*. *Catalysis Today* vol. 3 (Wiley-VCH, 2007).

17. Chorkendorff, I. & Niemantsverdriet, J. W. *Concepts of Modern Catalysis and Kinetics*. *Adsorption Journal Of The International Adsorption Society* (WILEY-VCH Verlag, 2003). doi:10.1002/3527602658.

18. Libuda, J. & Freund, H. J. Molecular beam experiments on model catalysts. *Surf. Sci. Rep.* **57**, 157–298 (2005).

19. Bligaard, T. *et al.* The Brønsted-Evans-Polanyi relation and the volcano curve in heterogeneous catalysis. *J. Catal.* **224**, 206–217 (2004).

20. Abild-Pedersen, F. *et al.* Scaling properties of adsorption energies for hydrogen-containing molecules on transition-metal surfaces. *Phys. Rev. Lett.* **99**, 4–7 (2007).

21. Hammer, B. & Nørskov, J. K. Theoretical Surface Science and Catalysis — Calculations and Concepts. *Adv. Catal.* **45**, 71–129 (2000).

22. Nørskov, J. K., Abild-Pedersen, F., Studt, F. & Bligaard, T. Density functional theory in surface chemistry and catalysis. *Proc. Natl. Acad. Sci.* **108**, 937–943 (2011).

23. Hammer, B. & Nørskov, J. K. Electronic factors determining the reactivity of metal surfaces. *Surf. Sci.* **343**, 211–220 (1995).

24. Sabatier, P. *La catalyse en chimie organique*, *Librairie Polytechnique*. (1920).

25. Darby, M. T., Stamatakis, M., Michaelides, A. & Sykes, E. C. H. Lonely Atoms with Special Gifts: Breaking Linear Scaling Relationships in Heterogeneous Catalysis with Single-Atom Alloys. *J. Phys. Chem. Lett.* **9**, 5636–5646 (2018).

26. Knop-Gericke, A. ; et al. X-Ray Photoelectron Spectroscopy for Investigation of Heterogeneous Catalytic Processes. in *Advances in Catalysis* 213–272 (Elsevier Inc., 2009).

27. Liu, P. & Nørskov, J. K. Ligand and ensemble effects in adsorption on alloy surfaces. *Phys. Chem. Chem. Phys.* **3**, 3814–3818 (2001).

28. Ponec, V. Alloy catalysts: The concepts. *Appl. Catal. A Gen.* **222**, 31–45 (2001).

29. Kyriakou, G. *et al.* Isolated Metal Atom Geometries as a Strategy for Selective Heterogeneous Hydrogenations. *Science (80-.).* **335**, 1209–1212 (2012).

30. Hüfner, S., Wertheim, G. K. & Wernick, J. H. Virtual Bound States of Pd in Cu, Ag and Au

and of Pt in Ag. *Solid State Commun.* **17**, 1585 (1975).

31. van der Marel, D., Jullianus, J. A. & Sawatzky, G. A. Pd and Pt impurity-induced changes in noble-metal density of states: Photoelectron spectroscopy and theory. *Phys. Rev. B* **32**, 6331 (1985).
32. Myers, H. P., Walldén, L. & Karlsson. Some optical properties of CuPd, AgPd, AuPd and CuMn, AgMn alloys. *Philos. Mag.* **18**, 725–744 (1968).
33. Armbrüster, M. *et al.* Pd-Ga intermetallic compounds as highly selective semihydrogenation catalysts. *J. Am. Chem. Soc.* **132**, 14745–14747 (2010).
34. Luo, Y. *et al.* Addressing electronic effects in the semi-hydrogenation of ethyne by InPd2 and intermetallic Ga-Pd compounds. *J. Catal.* **338**, 265–272 (2016).
35. Wang, L. L. & Johnson, D. D. Predicted trends of core-shell preferences for 132 late transition-metal binary-alloy nanoparticles. *J. Am. Chem. Soc.* **131**, 14023–14029 (2009).
36. Ruban, A. V., Skriver, H. L. & Nørskov, J. K. Surface segregation energies in transition-metal alloys. *Phys. Rev. B - Condens. Matter Mater. Phys.* **59**, 15990–16000 (1999).
37. Papanikolaou, K. G., Darby, M. T. & Stamatakis, M. CO-Induced Aggregation and Segregation of Highly Dilute Alloys: A Density Functional Theory Study. *J. Phys. Chem. C* **123**, 9128–9138 (2019).
38. Norris, C. & Myers, H. P. Photoemission study of the electronic structure of silver palladium alloys. *J. Phys. F Met. Phys* **1**, 62–77 (1971).
39. McLachlan, A. D., Jenkin, J. G., Leckey, R. C. G. & Liesegang, J. A valence band study of Ag-Pd alloys using ultraviolet photoelectron spectroscopy. *J. Phys. F Met. Phys* **5**, 2415–2424 (1975).
40. Friedel, J. Metallic alloys. *Nuovo Cim.* **7**, 287–311 (1958).
41. Anderson, P. W. Localized Magnetic States in Metals. *Phys. Rev.* **124**, 41–53 (1961).
42. Darby, M. T., Réocreux, R., Sykes, E. C. H., Michaelides, A. & Stamatakis, M. Elucidating the Stability and Reactivity of Surface Intermediates on Single-Atom Alloy Catalysts. *ACS Catal.* **8**, 5038–5050 (2018).
43. Liu, J. *et al.* Tackling CO Poisoning with Single-Atom Alloy Catalysts. *J. Am. Chem. Soc.* **138**, 6396–6399 (2016).
44. Vojvodic, A. & Nørskov, J. K. New design paradigm for heterogeneous catalysts. *Natl. Sci. Rev.* **2**, 140–143 (2015).

45. Marcinkowski, M. D. *et al.* Controlling a spillover pathway with the molecular cork effect. *Nat. Mater.* **12**, 523–528 (2013).

46. Marcinkowski, M. D. *et al.* Pt/Cu single-atom alloys as coke-resistant catalysts for efficient C–H activation. *Nat. Chem.* **10**, 325–332 (2018).

47. Gago, A. S., Ansar, A. S., Wagner, N., Arnold, J. & Friedrich, K. A. A0703 Titanium coatings deposited by thermal spraying for bipolar plates of PEM electrolysers. *4th Eur. PEFC H2 Forum* 11–18 (2013).

48. Greiner, M. T. Transition Metal Oxides in Organic Electronics. *Thesis* (University of Toronto, 2012).

49. Seah, M. P.; Dench, W. A. Quantitative Electron Spectroscopy of Surfaces : *Surf. Interface Anal.* **1**, (1979).

50. Greczynski, G. & Hultman, L. X-ray photoelectron spectroscopy: Towards reliable binding energy referencing. *Prog. Mater. Sci.* **107**, 100591 (2020).

51. Yeh, J. J. & Lindau, I. Atomic Subshell Photoionization Cross Sections and Asymmetry Parameters. *At. Data Nucl. Data Tables* **32**, 1–155 (1985).

52. Shirley, D. A. High-resolution x-ray photoemission spectrum of the valence bands of gold. *Phys. Rev. B* **5**, 4709–4714 (1972).

53. Tougaard, S. Inelastic background correction and quantitative surface analysis. *J. Electron Spectros. Relat. Phenomena* **52**, 243–271 (1990).

54. Tougaard, S. Energy loss in XPS: Fundamental processes and applications for quantification, non-destructive depth profiling and 3D imaging. *J. Electron Spectros. Relat. Phenomena* **178**–**179**, 128–153 (2010).

55. Siegbahn, H. & Siegbahn, K. ESCA applied to liquids. *J. Electron Spectros. Relat. Phenomena* **2**, 319–325 (1973).

56. Sezen, H., Al-Hada, M., Amati, M. & Gregoratti, L. In situ chemical and morphological characterization of copper under near ambient reduction and oxidation conditions. *Surf. Interface Anal.* **50**, 921–926 (2018).

57. Salmeron, M. & Schlögl, R. Ambient pressure photoelectron spectroscopy: A new tool for surface science and nanotechnology. *Surf. Sci. Rep.* **63**, 169–199 (2008).

58. Härdle, W. K. & Simar, L. *Applied Multivariate Statistical analysis*. *Journal of Chemical Information and Modeling* vol. 53 (Springer Berlin Heidelberg, 2012).

59. Mc Evoy, K. M., Genet, M. J. & Dupont-Gillain, C. C. Principal component analysis: A versatile method for processing and investigation of XPS spectra. *Anal. Chem.* **80**, 7226–7238 (2008).

60. Zhou, J., Varazo, K., Reddic, J. E., Myrick, M. L. & Chen, D. A. Decomposition of dimethyl methylphosphonate on TiO2(1 1 0): Principal component analysis applied to X-ray photoelectron spectroscopy. *Anal. Chim. Acta* **496**, 289–300 (2003).

61. Bro, R. & Smilde, A. K. Principal component analysis. *Anal. Methods* **6**, 2812–2831 (2014).

62. Walton, J. & Fairley, N. Noise reduction in X-ray photoelectron spectromicroscopy by a singular value decomposition sorting procedure. *J. Electron Spectros. Relat. Phenomena* **148**, 29–40 (2005).

63. Artyushkova, K. & Fulghum, J. E. Identification of chemical components in XPS spectra and images using multivariate statistical analysis methods. *J. Electron Spectros. Relat. Phenomena* **121**, 33–55 (2001).

64. Major, G. H. *et al.* Practical guide for curve fitting in x-ray photoelectron spectroscopy. *J. Vac. Sci. Technol. A* **38**, 061203 (2020).

65. Lundgren, E. *et al.* Two-dimensional oxide on Pd(111). *Phys. Rev. Lett.* **88**, 2461031–2461034 (2002).

66. Gabasch, H. *et al.* In situ XPS study of Pd(1 1 1) oxidation at elevated pressure, Part 2: Palladium oxidation in the 10-1 mbar range. *Surf. Sci.* **600**, 2980–2989 (2006).

67. Zemlyanov, D. *et al.* In situ XPS study of Pd(1 1 1) oxidation. Part 1: 2D oxide formation in 10-3 mbar O2. *Surf. Sci.* **600**, 983–994 (2006).

68. Briggs, D. & Grant, J. T. *Surface Analysis by Auger and X-Ray Photoelectron Spectroscopy*. (2003).

69. Lavagnini, I., Magno, F., Seraglia, R. & Traldi, P. *Quantitative Applications of Mass Spectrometry*. (John Wiley & Sons Ltd, 2006).

70. Brown, K. L. & Tautfest, G. W. Faraday-cup monitors for high-energy electron beams. *Rev. Sci. Instrum.* **27**, 696–702 (1956).

71. Barroo, C., Wang, Z. J., Schlögl, R. & Willinger, M. G. Imaging the dynamics of catalysed surface reactions by in situ scanning electron microscopy. *Nat. Catal.* **3**, 30–39 (2020).

72. Anderson, J. R. & Boudart, M. *Catalysis: Science and Technology*. (Springer Berlin Heidelberg, 1996).

73. Hartwig, C. *et al.* Surface composition of AgPd single-atom alloy catalyst in an oxidative environment. *J. Chem. Phys.* **154**, (2021).
74. Hartwig, C. *et al.* Isolated Pd atoms in a silver matrix : Spectroscopic and chemical properties. *J. Chem. Phys.* **154**, (2021).
75. Barcikowski, S. & Compagnini, G. Advanced nanoparticle generation and excitation by lasers in liquids. *Phys. Chem. Chem. Phys.* **15**, 3022–3026 (2013).
76. Rehbock, C. *et al.* Current state of laser synthesis of metal and alloy nanoparticles as ligand-free reference materials for nano-toxicological assays. *Beilstein J. Nanotechnol.* **5**, 1523–1541 (2014).
77. Zhang, D., Gökce, B. & Barcikowski, S. Laser Synthesis and Processing of Colloids: Fundamentals and Applications. *Chem. Rev.* **117**, 3990–4103 (2017).
78. Lopez-Sanchez, J. A. *et al.* Facile removal of stabilizer-ligands from supported gold nanoparticles. *Nat. Chem.* **3**, 551–556 (2011).
79. Zhang, D., Gökce, B. & Barcikowski, S. Laser Synthesis and Processing of Colloids: Fundamentals and Applications. *Chem. Rev.* **117**, 3990–4103 (2017).
80. Amendola, V. & Meneghetti, M. Laser ablation synthesis in solution and size manipulation of noble metal nanoparticles. *Phys. Chem. Chem. Phys.* **11**, 3805–3821 (2009).
81. Wagener, P., Schwenke, A. & Barcikowski, S. How citrate ligands affect nanoparticle adsorption to microparticle supports. *Langmuir* **28**, 6132–6140 (2012).
82. Marzun, G. *et al.* Role of Dissolved and Molecular Oxygen on Cu and PtCu Alloy Particle Structure during Laser Ablation Synthesis in Liquids. *ChemPhysChem* **18**, 1175–1184 (2017).
83. Ferrari, A. C. Raman spectroscopy of graphene and graphite: Disorder, electron-phonon coupling, doping and nonadiabatic effects. *Solid State Commun.* **143**, 47–57 (2007).
84. Neirinck, B., Van Der Biest, O. & Vleugels, J. A current opinion on electrophoretic deposition in pulsed and alternating fields. *J. Phys. Chem. B* **117**, 1516–1526 (2013).
85. Gabler, A. *et al.* Ultrashort-pulse laser structured titanium surfaces with sputter-coated platinum catalyst as hydrogen evolution electrodes for alkaline water electrolysis. *Int. J. Hydrogen Energy* **43**, 7216–7226 (2018).
86. Ozbek, M. O., Onal, I. & Van Santen, R. A. Why silver is the unique catalyst for ethylene epoxidation. *J. Catal.* **284**, 230–235 (2011).

87. Wyrwich, R. *et al.* LEED - I (V) Structure Analysis of the (7 × √ 3)rect SO 4 Phase on Ag(111): Precursor to the Active Species of the Ag-Catalyzed Ethylene Epoxidation. *J. Phys. Chem. C* **122**, 26998–27004 (2018).
88. Jones, T. E. *et al.* The Selective Species in Ethylene Epoxidation on Silver. *ACS Catal.* **8**, (2018).
89. Greiner, M. T. *et al.* Phase Coexistence of Multiple Copper Oxides on AgCu Catalysts during Ethylene Epoxidation. *ACS Catal.* **8**, 2286–2295 (2018).
90. Boucher, M. B. *et al.* Single atom alloy surface analogs in Pd0.18Cu15 nanoparticles for selective hydrogenation reactions. *Phys. Chem. Chem. Phys.* **15**, 12187 (2013).
91. Pei, G. X. *et al.* Ag alloyed Pd single-atom catalysts for efficient selective hydrogenation of acetylene to ethylene in excess ethylene. *ACS Catal.* **5**, 3717–3725 (2015).
92. Lucci, F. R. *et al.* Selective hydrogenation of 1,3-butadiene on platinum-copper alloys at the single-atom limit. *Nat. Commun.* **6**, 8550 (2015).
93. Pei, G. X. *et al.* Performance of Cu-Alloyed Pd Single-Atom Catalyst for Semihydrogenation of Acetylene under Simulated Front-End Conditions. *ACS Catal.* **7**, 1491–1500 (2017).
94. Kruppe, C. M., Krooswyk, J. D. & Trenary, M. Selective Hydrogenation of Acetylene to Ethylene in the Presence of a Carbonaceous Surface Layer on a Pd/Cu(111) Single-Atom Alloy. *ACS Catal.* **7**, 8042–8049 (2017).
95. Aich, P. *et al.* Single-Atom Alloy Pd-Ag Catalyst for Selective Hydrogenation of Acrolein. *J. Phys. Chem. C* **119**, 18140–18148 (2015).
96. Jørgensen, M. & Grönbeck, H. Selective Acetylene Hydrogenation over Single-Atom Alloy Nanoparticles by Kinetic Monte Carlo. *J. Am. Chem. Soc.* **141**, 8541–8549 (2019).
97. Fu, Q. & Luo, Y. Active sites of Pd-doped flat and stepped Cu(111) surfaces for H 2 dissociation in heterogeneous catalytic hydrogenation. *ACS Catal.* **3**, 1245–1252 (2013).
98. Baber, A. E., Tierney, H. L., Lawton, T. J. & Sykes, E. C. H. An atomic-scale view of palladium alloys and their ability to dissociate molecular hydrogen. *ChemCatChem* **3**, 607–614 (2011).
99. Borodziński, A. & Bond, G. C. Selective hydrogenation of ethyne in ethene-rich streams on palladium catalysts. Part 1. Effect of changes to the catalyst during reaction. *Catal. Rev. - Sci. Eng.* **48**, 91–144 (2006).

100. Johnsson, M. M., Walker, D. W. & Nowack, G. P. US Patent. (1983).
101. Johnsson, M. M. & Cheung, T. P. US Patent. (1996).
102. Thanh, C. N., Didillon, B., Sarrazin, P. & Cameron, C. US Patent. (2000).
103. Huang, D. C. *et al.* Effect of Ag-promotion on Pd catalysts by XANES. **53**, 155–159 (1998).
104. Khan, N. A., Shaikhutdinov, S. & Freund, H. J. Acetylene and ethylene hydrogenation on alumina supported Pd-Ag model catalysts. *Catal. Letters* **108**, 159–164 (2006).
105. Zhang, Q., Li, J., Liu, X. & Zhu, Q. Synergetic effect of Pd and Ag dispersed on Al2O3 in the selective hydrogenation of acetylene. *Appl. Catal. A Gen.* **197**, 221–228 (2000).
106. Bligaard, T. & Nørskov, J. K. Ligand effects in heterogeneous catalysis and electrochemistry. *Electrochim. Acta* **52**, 5512–5516 (2007).
107. Cole, R. J., Brooks, N. J. & Weightman, P. Madelung potentials and disorder broadening of core photoemission spectra in random alloys. *Phys. Rev. Lett.* **78**, 3777–3780 (1997).
108. Rodriguez, J. A. & Goodman, D. W. The nature of the metal-metal bond in bimetallic surfaces. *Science (80-.).* **257**, 897–903 (1992).
109. Abrikosov, I. A., Olovsson, W. & Johansson, B. Valence-Band Hybridization and Core Level Shifts in Random Ag-Pd Alloys. *Phys. Rev. Lett.* **87**, 176403 (2001).
110. Bagus, P. S., Ilton, E. S. & Nelin, C. J. The interpretation of XPS spectra: Insights into materials properties. *Surf. Sci. Rep.* **68**, 273–304 (2013).
111. Weinert, M. & Watson, R. E. Core-level shifts in bulk alloys and surface adlayers. *Phys. Rev. B* **51**, 17168–17180 (1995).
112. Haverkort, M. W., Zwierzycki, M. & Andersen, O. K. Multiplet ligand-field theory using Wannier orbitals. *Phys. Rev. B - Condens. Matter Mater. Phys.* **85**, 165113 (2012).
113. Giannozzi, P. *et al.* QUANTUM ESPRESSO : a modular and open-source software project for quantum simulations of materials. *J. Phys. Condens. Matter* **21**, 395502 (2009).
114. Dal Corso, A. Pseudopotentials periodic table: From H to Pu. *Comput. Mater. Sci.* **95**, 337–350 (2014).
115. Allison, E. G. & Bond, G. C. The Structure and Catalytic Properties of Palladium-Silver and Palladium-Gold Alloys. *Catal. Rev.* **7**, 233–289 (1972).
116. Wouda, P. T., Schmid, M., Nieuwenhuys, B. E. & Varga, P. STM study of the (111) and (100) surfaces of PdAg. *Surf. Sci.* **417**, 292–300 (1998).
117. Lim, J. S. *et al.* Evolution of Metastable Structures at Bimetallic Surfaces from Microscopy

and Machine-Learning Molecular Dynamics. *J. Am. Chem. Soc.* **142**, 15907–15916 (2020).

118. Doniach, S. & Sunjic, M. Many-electron singularity in X-ray photoemission and X-ray line spectra from metals. *J. Phys. C Solid State Phys.* **3**, 285–291 (1970).
119. Bayer, A., Flechtner, K., Denecke, R. & Steinru, H. Electronic properties of thin Zn layers on Pd (1 1 1) during growth and alloying. *Surf. Sci.* **600**, 78–94 (2006).
120. McGuirk, G. M., Ledieu, J., Gaudry, É. & de Weerd, M.-C. Surface structures of In-Pd intermetallic compounds . I . Experimental study of In thin films on Pd (111) and alloy formation. *J. Chem. Phys.* **141**, 084702 (2014).
121. Van Spronsen, M. A. *et al.* Dynamics of Surface Alloys: Rearrangement of Pd/Ag(111) Induced by CO and O2. *J. Phys. Chem. C* **123**, 8312–8323 (2019).
122. Grönbeck, H. *et al.* Mechanism for reversed photoemission core-level shifts of oxidized Ag. *Phys. Rev. B* **85**, 115445 (2012).
123. Steiner, P. & Hüfner, S. Thermochemical Data of Allaoy from Photoelectron Spectroscopy. *Acta Met.* **29**, 1885 (1981).
124. Sigalas, M., Papaconstantopoulos, D. A. & Bacalis, N. C. Total energy and band structure of the 3d, 4d, and 5d metals. *Phys. Rev. B* **45**, 5777–5783 (1992).
125. Zhang, L., Zhou, M., Wang, A. & Zhang, T. Selective Hydrogenation over Supported Metal Catalysts: From Nanoparticles to Single Atoms. *Chem. Rev.* **120**, 683–733 (2020).
126. Taccardi, N. *et al.* Gallium-rich Pd–Ga phases as supported liquid metal catalysts. *Nat. Chem.* **9**, 862–867 (2017).
127. Rupprechter, G. Popping up to the surface. *Nat. Chem.* **9**, 833–834 (2017).
128. Wang, Y., Wang, B., Ling, L., Zhang, R. & Fan, M. Probe into the effects of surface composition and ensemble effect of active sites on the catalytic performance of C2H2 semi-hydrogenation over the Pd-Ag bimetallic catalysts. *Chem. Eng. Sci.* **218**, 115549 (2020).
129. González, S., Neyman, K. M., Shaikhutdinov, S., Freund, H. J. & Illas, F. On the promoting role of Ag in selective hydrogenation reactions over Pd-Ag bimetallic catalysts: A theoretical study. *J. Phys. Chem. C* **111**, 6852–6856 (2007).
130. Teschner, D. *et al.* The roles of subsurface carbon and hydrogen in palladium-catalyzed alkyne hydrogenation. *Science (80-.).* **320**, 86–89 (2008).
131. Studt, F. *et al.* Identification of Non-Precious Metal Alloy Catalysts for Selective Hydrogenation of Acetylene. *Science (80-.).* **320**, 1320–1322 (2008).

132. Mei, D., Neurock, M. & Smith, C. M. Hydrogenation of acetylene-ethylene mixtures over Pd and Pd-Ag alloys: First-principles-based kinetic Monte Carlo simulations. *J. Catal.* **268**, 181–195 (2009).

133. Qin, R., Liu, K., Wu, Q. & Zheng, N. Surface Coordination Chemistry of Atomically Dispersed Metal Catalysts. *Chem. Rev.* **120**, 11810 (2020).

134. Coulthard, I. & Sham, T. K. Charge redistribution in Pd-Ag alloys from a local perspective. *Phys. Rev. Lett.* **77**, 4824–4827 (1996).

135. Meitzner, G. & Sinfelt, J. H. X-ray absorption studies of the electronic structures of Pd-Ag and Pd-Au alloys. *Catal. Letters* **30**, 1–10 (1994).

136. Vignola, E. *et al.* Evaluating the Risk of C-C Bond Formation during Selective Hydrogenation of Acetylene on Palladium. *ACS Catal.* **8**, 1662–1671 (2018).

137. Vignola, E., Steinmann, S. N., Vandegehuchte, B. D., Curulla, D. & Sautet, P. C2H2-Induced Surface Restructuring of Pd-Ag Catalysts: Insights from Theoretical Modeling. *J. Phys. Chem. C* **120**, 26320–26327 (2016).

138. Vignola, E. *et al.* Acetylene Adsorption on Pd-Ag Alloys: Evidence for Limited Island Formation and Strong Reverse Segregation from Monte Carlo Simulations. *J. Phys. Chem. C* **122**, 15456–15463 (2018).

139. Zhukov, V., Rendulic, K. D. & Winkler, A. Coadsorption of hydrogen and potassium on silver single crystal surfaces. *Vacuum* **47**, 5–11 (1996).

140. Armbrüster, M. *et al.* How to Control the Selectivity of Palladium-based Catalysts in Hydrogenation Reactions: The Role of Subsurface Chemistry. *ChemCatChem* **4**, 1048–1063 (2012).

141. Bron, M. *et al.* Silver as acrolein hydrogenation catalyst: Intricate effects of catalyst nature and reactant partial pressures. *Phys. Chem. Chem. Phys.* **9**, 3559–3569 (2007).

142. Hohmeyer, J. *et al.* Activation of dihydrogen on supported and unsupported silver catalysts. *J. Catal.* **269**, 5–14 (2010).

143. Delmon, B. & Froment, G. F. Remote control of catalytic sites by spillover species: A chemical reaction engineering approach. *Catal. Rev. - Sci. Eng.* **38**, 69–100 (1996).

144. Prins, R. Hydrogen spillover. Facts and fiction. *Chem. Rev.* **112**, 2714–2738 (2012).

145. Frey, G. D., Lavallo, V., Donnadieu, B., Schoeller, W. W. & Bertrand, G. Facile Splitting of Hydrogen and Ammonia by Nucleophilic Activation at a Single Carbon Center. *Science*

(80-.). **316**, 439–441 (2007).

146. Baumgarten, E. & Denecke, E. Hydrogen spillover in the System Pt/Al2O3. *J. Catal.* **95**, 296–299 (1985).
147. Jia, J., Haraki, K., Kondo, J. N., Domen, K. & Tamaru, K. Selective Hydrogenation of Acetylene over Au/Al2O3 Catalyst. *J. Phys. Chem. B* **104**, 11153–11156 (2000).
148. Ruban, A. V. & Skriver, H. L. Calculated surface segregation in transition metal alloys. *Comput. Mater. Sci.* **15**, 119–143 (2003).
149. Abild-Pedersen, F. *et al.* Scaling properties of adsorption energies for hydrogen-containing molecules on transition-metal surfaces. *Phys. Rev. Lett.* **99**, 4–7 (2007).
150. Jacobsen, C. J. H. *et al.* Catalyst design by interpolation in the periodic table: Bimetallic ammonia synthesis catalysts [2]. *J. Am. Chem. Soc.* **123**, 8404–8405 (2001).
151. Zafeiratos, S., Piccinin, S. & Teschner, D. Alloys in catalysis: phase separation and surface segregation phenomena in response to the reactive environment. *Catal. Sci. Technol.* **2**, 1787 (2012).
152. Tao, F., Zhang, S., Nguyen, L. & Zhang, X. Action of bimetallic nanocatalysts under reaction conditions and during catalysis: Evolution of chemistry from high vacuum conditions to reaction conditions. *Chem. Soc. Rev.* **41**, 7980–7993 (2012).
153. Schweinar, K. *et al.* Formation of a 2D Meta-stable Oxide by Differential Oxidation of AgCu Alloys. *ACS Appl. Mater. Interfaces* **12**, 23595–23605 (2020).
154. Piccinin, S., Stampfl, C. & Scheffler, M. Ag-Cu alloy surfaces in an oxidizing environment: A first-principles study. *Surf. Sci.* **603**, 1467–1475 (2009).
155. Anderson, R. B., Stein, K. C., Feenan, J. J. & Hofer, L. J. E. Catalytic Oxidation of Methane. *Ind. Eng. Chem.* **53**, 809–812 (1961).
156. Shindell, D. T. *et al.* Forcing to Emissions. *Science (80-.).* **326**, 716–718 (2009).
157. Li, Z. & Hoflund, G. B. A Review on Complete Oxidation of Methane at Low Temperatures. *J. Nat. Gas Chem.* **12**, 153–160 (2003).
158. He, L., Bellettre, J., Yue, J. & Luo, L. A review on catalytic methane combustion at low temperatures : Catalysts , mechanisms , reaction conditions and reactor designs. *Renew. Sustain. Energy Rev.* **119**, (2020).
159. Lyubovsky, M. & Pfefferle, L. Complete methane oxidation over Pd catalyst supported on α-alumina. Influence of temperature and oxygen pressure on the catalyst activity. *Catal.*

Today **47**, 29–44 (1999).

160. Gabasch, H. *et al.* Methane oxidation on Pd(111): In situ XPS identification of active phase. *J. Phys. Chem. C* **111**, 7957–7962 (2007).
161. Monteiro, R. S., Zemlyanov, D., Storey, J. M. & Ribeiro, F. H. Surface area increase on Pd foils after oxidation in excess methane. *J. Catal.* **201**, 37–45 (2001).
162. Burch, R., Urbano, F. J. & Loader, P. K. Methane combustion over palladium catalysts: The effect of carbon dioxide and water on activity. *Appl. Catal. A, Gen.* **123**, 173–184 (1995).
163. Carstens, J. N., Su, S. C. & Bell, A. T. Factors affecting the catalytic activity of Pd/ZrO2 for the combustion of methane. *J. Catal.* **176**, 136–142 (1998).
164. Xiong, H. *et al.* Design considerations for low-temperature hydrocarbon oxidation reactions on Pd based catalysts. *Appl. Catal. B Environ.* **236**, 436–444 (2018).
165. Willis, J. J. *et al.* Systematic Structure-Property Relationship Studies in Palladium-Catalyzed Methane Complete Combustion. *ACS Catal.* **7**, 7810–7821 (2017).
166. Persson, K., Jansson, K. & Järås, S. G. Characterisation and microstructure of Pd and bimetallic Pd-Pt catalysts during methane oxidation. *J. Catal.* **245**, 401–414 (2007).
167. Kinnunen, N. M., Hirvi, J. T., Venäläinen, T., Suvanto, M. & Pakkanen, T. A. Procedure to tailor activity of methane combustion catalyst: Relation between Pd/PdOx active sites and methane oxidation activity. *Appl. Catal. A Gen.* **397**, 54–61 (2011).
168. Hellman, A. *et al.* The active phase of palladium during methane oxidation. *J. Phys. Chem. Lett.* **3**, 678–682 (2012).
169. Nilsson, J. *et al.* Chemistry of Supported Palladium Nanoparticles during Methane Oxidation. *ACS Catal.* **5**, 2481–2489 (2015).
170. Kitchin, J. R., Reuter, K. & Scheffler, M. Alloy surface segregation in reactive environments: First-principles atomistic thermodynamics study of Ag3 Pd(111) in oxygen atmospheres. *Phys. Rev. B - Condens. Matter Mater. Phys.* **77**, 1–12 (2008).
171. Reuter, K. & Scheffler, M. Composition, structure, and stability of (formula presented) as a function of oxygen pressure. *Phys. Rev. B - Condens. Matter Mater. Phys.* **65**, 1–11 (2002).
172. Tao, F. & Nguyen, L. Interactions of gaseous molecules with X-ray photons and photoelectrons in AP-XPS study of solid surface in gas phase. *Phys. Chem. Chem. Phys.* **20**, 9812–9823 (2018).
173. Ketteler, G. *et al.* In situ spectroscopic study of the oxidation and reduction of Pd(111). *J.*

Am. Chem. Soc. **127**, 18269–18273 (2005).

174. Gabasch, H. *et al.* Carbon incorporation during ethene oxidation on Pd(111) studied by in situ X-ray photoelectron spectroscopy at 2 × 10-3 mbar. *J. Catal.* **242**, 340–348 (2006).

175. Velasco-Vélez, J. J. *et al.* The Role of Adsorbed and Subsurface Carbon Species for the Selective Alkyne Hydrogenation Over a Pd-Black Catalyst: An Operando Study of Bulk and Surface. *Top. Catal.* **61**, 2052–2061 (2018).

176. Zemlyanov, D. *et al.* Kinetics of palladium oxidation in the mbar pressure range: Ambient pressure XPS study. *Top. Catal.* **56**, 885–895 (2013).

177. O’Connor, C. R. *et al.* Hydrogen migration at restructuring palladium–silver oxide boundaries dramatically enhances reduction rate of silver oxide. *Nat. Commun.* **11**, 1–6 (2020).

178. Carbonio, E. A. *et al.* Are multiple oxygen species selective in ethylene epoxidation on silver? *Chem. Sci.* **9**, 990–998 (2018).

179. Jones, T. E. *et al.* Insights into the Electronic Structure of the Oxygen Species Active in Alkene Epoxidation on Silver. *ACS Catal.* **5**, 5846–5850 (2015).

180. Rocha, T. C. R. *et al.* The silver – oxygen system in catalysis : new insights by near ambient pressure X-ray photoelectron spectroscopy. *Phys. Chem. Chem. Phys.* **14**, 4554–4564 (2012).

181. Reichelt, R., Günther, S. & Wintterlin, J. Strongly-bound oxygen on silver surfaces: A molybdenum oxide contamination? *J. Phys. Chem. C* **115**, 17417–17428 (2011).

182. Heine, C., Eren, B., Lechner, B. A. J. & Salmeron, M. A study of the O/Ag(111) system with scanning tunneling microscopy and x-ray photoelectron spectroscopy at ambient pressures. *Surf. Sci.* **652**, 51–57 (2016).

183. Todorova, M. *et al.* Role of Subsurface Oxygen in Oxide Formation at Transition Metal Surfaces. *Phys. Rev. Lett.* **89**, 1–4 (2002).

184. Karakaya, I. & Thompson, W. T. The Ag-Pd (silver-palladium) system. *Bull. Alloy Phase Diagrams* **9**, 237–243 (1988).

185. Seah, M. P. *Practical Surface Analysis*. (John Wiley, 1983).

186. Powell, C. J. & Jablonski, A. Progress in quantitative surface analysis by X-ray photoelectron spectroscopy: Current status and perspectives. *J. Electron Spectros. Relat. Phenomena* **178–179**, 331–346 (2010).

187. Powell, C. J. & Jabloski, A. *NIST Effective-Attenuation-Length Database*. (2011).

188. Hesse, R., Streubel, P. & Szargan, R. Improved accuracy of quantitative XPS analysis using predetermined spectrometer transmission functions with UNIFIT 2004. *Surf. Interface Anal.* **37**, 589–607 (2005).

189. Tougaard, S. Surface nanostructure determination by x-ray photoemission spectroscopy peak shape analysis. *J. Vac. Sci. Technol. A Vacuum, Surfaces, Film.* **14**, 1415–1423 (1996).

190. Tanuma, S. & Powell, C. J. Electron Inelastic Mean Free Paths. 5. Data for 14 organic-compunds over the 50-2000 eV range. *Surf. Interface Anal.* **21**, 165–176 (1994).

191. Seah, M. P. *Surface Analysis by Auger and X-Ray Photoelectron Spectroscopy*. (IM Puplications LLP and SurfaceSpectra Limited, 2003).

192. Scofield, J. H. Hartree-Slater subshell photoionization cross-sections at 1254 and 1487 eV. *J. Electron Spectros. Relat. Phenomena* **8**, 129–137 (1976).

193. Artyushkova, K., Pylypenko, S., Olson, T. S., Fulghum, J. E. & Atanassov, P. Predictive modeling of electrocatalyst structure based on structure-to-property correlations of X-ray photoelectron spectroscopic and electrochemical measurements. *Langmuir* **24**, 9082–9088 (2008).

194. Artyushkova, K., Lvendosky, S., Atanassov, P. & Fulghum, J. XPS Structural Studies of Nano-composite Non-platinum Electrocatalysts for Polymer Electrolyte Fuel Cells. *Top. Catal.* **46**, 263–275 (2007).

195. Hajati, S., Tougaard, S., Walton, J. & Fairley, N. Noise reduction procedures applied to XPS imaging of depth distribution of atoms on the nanoscale. *Surf. Sci.* **602**, 3064–3070 (2008).

196. Votano, J., Parham, M. & Hall, L. *Applied Chemometrics for Scientists*. *Chemistry & ...* (2004).

197. Volponi, J. E., Helena, L., Mei, I. & Rosa, S. Use of Oxidation Onset Temperature Measurements for Evaluating the Oxidative Degradation of Isotatic Polypropylene. *J. Polym. Environ.* **12**, (2004).

198. Alarcón Villaseca, S., Levchenko, S. V. & Armbrüster, M. CO adsorption on the GaPd(111) surface: A comparative DFT study using different functionals. *Phys. Chem. Chem. Phys.* **18**, 14390–14400 (2016).

Appendix

Python scripts for data analysis

i. Peak area modelling procedure

```
import numpy as np
#%% determining the known variables
I_Ag = 170020 #From spectrum in reduced state
RSF_Ag = 10.66
IMFP_Ag = 1.602
N_Ag = 58.56
I_PdAg=2171 #From spectrum in reduced state
RSF_PdAg=9.48
IMFP_PdAg=1.634 #homogeneous alloy
EAL_PdAg=1.296
RSF_PdO=9.48
IMFP_PdO=1.78
EAL_PdO=1.50
N_PdO=40.82
d_Pd=0.28 # (height of PdO monolayer in nm)
I_Pd2=1705 # PdO intensity from spectrum
I_Pdmetal=1335
#%% determining T(Tranmission function), N_PdAg, I_PdO
T = I_Ag*1.02/(RSF_Ag*IMFP_Ag*N_Ag)
N_PdAg = I_PdAg/(RSF_PdAg*IMFP_PdAg*T)
I_PdO= RSF_PdO*IMFP_PdO*N_PdO*T
# expected IPd,PdO (Intensity of Pd passing through the PdO monolayer)
I_Pd_PdO = I_PdAg*np.exp(-d_Pd/EAL_PdO)
#%% PdO thickness calculation
```

```
d = -EAL_PdO*np.log(1-I_Pd2/I_PdO)
d_hypo=-EAL_PdAg*np.log(I_Pdmetal/I_PdAg)

C= d/d_Pd
#surface area A
a = 100
A= a*a
#Volume PdO monolayer
V_PdO=A*C*d_Pd
# Pd atoms in PdO monolayer
n_Pd=V_PdO*N_PdO
# volume of depletion layer
V_Ag=n_Pd/N_PdAg
#cube volume, h=height
h=0.32 #hight
b=1#Breite
t=1#Tiefe
cube=h*b*t
#number of cubes for depeltion layer (pure Ag)
n_cube=V_Ag/cube
# goal calculated I_Pd should be as close as possible to the measured I_Pdmetal
#n_Ag0 = input("n_Ag0: ")
def func(Ag0):
    """gives the total calculated Intensity of Pd metal (see power point drawing)
    the while loop stops when there are no more cuboids n_cubes
    (represents the volume of the depletion layer) to distribut. or when v
    the legths of the depletion layer in a layer i (index) is negative (since this
    value will be suared area a is always positive) first if statement i==0 is for
    the homogeneous AgPd part; elif: for the Pd metal signal which has to pass through the
    Ag depletion layers (signal depends on the depth of the depletion layer); else for the case
    where the electrons have to pass through the Ag depletion layer and the surface Pd0
```

```
oxide; at the endo of each while loop the area is made smalller by subtracting 2 from the
Ag0 value. last if is fore the case that the full depletion volume n_cube is used already,
and it should measure the intensity comming from below the depletion area + the part from
below depletion layer and PdO monolayer.
The result is a dictionary revealing the number of layers, the number of left over n_cubes
and the total Pd intensity
"""
results=[]
a=1 # area of depletion layer
R=1 # outer circle of a layer which is used to calculate I_Pd
P=1 # % contribution of a layer to total Pd intensity
n_cube=V_Ag/cube
i=0 # index was the number of depletion layers
v=0 #
while n_cube >=0 and i>=0 and v >= 0:
    a=np.square(np.sqrt(A*C)+(Ag0*b))
    if i==0:
        P=(A-(a))/A
        I_Pd_AgPd=P*I_PdAg
        results.append(I_Pd_AgPd)
        start_Ag0=Ag0
    elif Ag0>=0:
        R=np.square(np.sqrt(A*C)+(Ag0+2)*b)-a
        P=R/A
        I_Pd_Ag=I_PdAg*np.exp(-i*h/EAL_PdAg)*P
        results.append(I_Pd_Ag)
    else:
        R=np.square(np.sqrt(A*C)+(Ag0+2)*b)-a
        P=R/A
        I_Pd_Ag_PdO=I_Pd_PdO*np.exp(-(i*h+d_Pd)/EAL_PdAg)*P
        results.append(I_Pd_Ag_PdO)
```

```
        n_cube=n_cube-a
        Ag0-=2
        v=np.sqrt(A*C)+(Ag0*b)
        i=i+1
        #print("n_cube" + str(i)+ "=" + str(n_cube))
    if n_cube <= 0:
        P=(a-A*C)/A
        I_Pd_end= I_PdAg*np.exp(-i*h/EAL_PdAg)*P + I_Pd_PdO*np.exp(-(i*h+d_Pd)/EAL_PdAg)*C
        #print('I_Pd_end'+ str(i) + ':'+ str(I_Pd_end))
        results.append(I_Pd_end)
    total_I = sum(results)
    return { 'Ag0' : start_Ag0,  'layers': i, 'I_Pd_total' : total_I, 'n_cube_end': n_cube}

Ag0=40
print('start_Ag0' + '=' + str(Ag0))
dict=func(Ag0)
I_Pd=dict['I_Pd_total']
print(dict)
I_Pd_measured=I_Pdmetal
I_Pd_calc = I_Pd_measured*1.01
I_Pd_calc2 = I_Pd_measured*0.99

""" for any AgO starting value it finds the most suited AgO value by
adding or subtracting 2 from the starting Ag0 value
to get with the result as close possible (2% deviation is allowed)
to the calculated Pd intensity. It return the dictionry of func()
returns the best fitting Ag0 value """
while I_Pd >= I_Pd_calc:
    Ag0+=2
    #print('new AgO' + '=' + str(Ag0))
```

```
    dict=func(Ag0)
    I_Pd=dict['I_Pd_total']
    #print('I_Pd_total' + '=' + str(I_Pd))
    print(dict)
while I_Pd <= I_Pd_calc2:
    Ag0-=2
    #print('new AgO' + '=' + str(Ag0))

    dict=func(Ag0)
    I_Pd=dict['I_Pd_total']
    #print('I_Pd_total' + '=' + str(I_Pd))
    print(dict)
else:
    print ('Ag0=' + str(Ag0) + ' is the best fitting Ag0 value')
```

ii. Line profile + PCA visualization

```
import numpy as np
from sklearn import preprocessing
import scipy.linalg
import matplotlib.pyplot as plt
from mpl_toolkits.mplot3d import Axes3D
plt.rcParams.update({'font.size': 12})
#Importing data
# Note: this assumes that the first two lines contain header info and that the first column contains temperature information
# USER INPUT: define filepath to data:
#datafile = r'C:\Users\hartwig\ownCloud2\PCA manuscript\Python analysis\ASCII data files\Ex367 up Pd5O4.dat'
# USER INPUT: define number of different types of peak areas (i.e. number of
#           columns excluding temperature)
num_cols = 8
```

```
# import data:
data = np.genfromtxt(datafile, delimiter='\t', skip_header=2)
# temperature scale
temp = data[:,0].copy()
# areas of peaks
areas = data[:,1:num_cols+1].copy()

# gets header names (assumes first column is temperature)
with open(datafile, 'r') as file:
    header = file.readline().split('\t')
    header[7]='Pdox(I)'
    header[8]='Pdox(II)'
    header[4]='O(IV)'
labels = header[1:num_cols+1]
labels[-1]=labels[-1][:-1]
labels[7]='Pdox(II)'
# Scale data (subtract mean and divide by standard deviation)
areas_scaled = preprocessing.scale(areas)
# PCA by SVD
U, s, V = scipy.linalg.svd(areas_scaled, full_matrices=False)
# Explanation:
# V: a matrix where the rows contains the principle components (i.e. the contribution of
#    each peak area to a component)
# U: a matrix where the columns contain the columns contain the contribution
#    of each component to a spectra taken (at a given temperature)
# s: an array containing the eigenvalues of each component (used to calculate
#    the explained variance of each component)

#grid for fig
fig3 = plt.figure(constrained_layout=True)
gs = fig3.add_gridspec(2, 3)
```

```
f3_ax1 = fig3.add_subplot(gs[:, 0])
f3_ax1.set_title('Temperature line profile', fontsize=20)
f3_ax1.annotate('a)', (-0.18, 0.98), xycoords='axes fraction', fontsize=20)
f3_ax2 = fig3.add_subplot(gs[0, 1])
f3_ax2.set_title('Cumulated variation explained', fontsize=20)
f3_ax2.annotate('b)', (-0.18, 0.95), xycoords='axes fraction', fontsize=20)
f3_ax3 = fig3.add_subplot(gs[1, 1])
f3_ax3.set_title('Line profile of principal components', fontsize=20)
f3_ax3.annotate('c)', (-0.18, 0.95), xycoords='axes fraction', fontsize=20)
f3_ax4 = fig3.add_subplot(gs[0, 2])
f3_ax4.annotate('d)', (-0.18, 0.95), xycoords='axes fraction', fontsize=20)
f3_ax5 = fig3.add_subplot(gs[1, 2])
f3_ax5.annotate('e)', (-0.18, 0.95), xycoords='axes fraction', fontsize=20)

variance = []
for value in range(0,len(s)):
    variance.append((s**2)[0:value+1].sum() / (s**2).sum()*100)
variance =  [round(x,1) for x in variance]
 color_list=['tomato','orange','darkred','crimson','sienna','lightcoral','chocolate', 'red']
rect=f3_ax2.bar(range(1, areas.shape[1]+1), variance, color=color_list)
f3_ax2.set_ylabel('explained variation [%]', fontsize=20)
f3_ax2.set_xlabel('Principal components', fontsize=20)
f3_ax2.set_ylim(0, 110)

def autolabel(rects, ax):
    """Attach a text label above each bar in *rects*, displaying its height."""
    for rect in rects:
        height = rect.get_height()
        va='bottom'
        space= 2
        if height < 0:
```

```
            va='top'
            space*=-1.5
        ax.annotate('{}'.format(height),
                    xy=(rect.get_x() + rect.get_width() / 2, height),
                    xytext=(0, space),  # 2 points vertical offset
                    textcoords="offset points",
                    ha='center', va=va, size=14)
autolabel(rect, f3_ax2)

#ax3 Components line profile
comp=U*s
styl_list=['-', '-', '--', '--', '--', '--', '--', '--', '--', '--', '--']
linewidth_list=[2, 2, 1, 1, 1,1, 1, 1, 1, 1 ]
for indx, t in enumerate(range(0, num_cols)):
    f3_ax3.plot(temp,   comp[:,t],   ls=styl_list[t],   linewidth=linewidth_list[t],   color=color_list[t], label=('PC'+str(t+1)))
    f3_ax3.set_xlabel('Temperature [°C]', fontsize=20)
    f3_ax3.set_ylabel('score', fontsize=20)
    f3_ax3.legend(loc='upper center', bbox_to_anchor=(0.51, 0.82 )) #legend_list, loc='best')
    f3_ax3.set_xlim(f3_ax3.get_xlim()[::-1])

#ax4-6 weigths of each species to a components
label_colours = {'Ag metal':  (102/255, 153/255, 204/255, 1),
                'Ag oxide': (153/255, 153/255, 153/255, 1),
                'Oµ1' : (0/255, 156/255, 156/255, 1),
                'Oµ2': (239/255, 0.0, 0.0, 1),
                'Oµ3' : (206/255,99/255, 0.0, 1),
                'Oµ4':(51/255, 102/255, 153/255, 1) ,
                'Pd metal':(254/255, 194/255, 17/255, 1),
                'Pd3d metal':(254/255, 194/255, 17/255, 1),
                'Pd oxide': (59/255, 195/255, 113/255, 1),
```

```
            'PdO': (59/255, 195/255, 113/255, 1),
            'O(I)':(0/255, 156/255, 156/255, 1),
            'O(II)':(239/255, 0.0, 0.0, 1),
            'Pdox(II)': (153/255, 153/255, 153/255, 1),
            'Pdox(I)': (102/255, 102/255, 153/255),
            'O(IV)': (206/255,99/255, 0.0, 1),
            'O(PdO)':(51/255, 102/255, 153/255, 1),

#round the values for the bar plot
V= np.around(V , decimals=2)
factor = 1     # plots the first factor
rect1=f3_ax4.bar(labels, V[factor-1, :], color=[label_colours[label] for label in labels])
f3_ax4.set_title('Principal component ' + str(factor), fontsize=20)
f3_ax4.set_xticklabels(labels, rotation=30)
f3_ax4.set_ylabel('loading', fontsize=20)
f3_ax4.set_ylim(min(V[factor-1, :])-0.1, max(V[factor-1, :])+0.1)
autolabel(rect1, f3_ax4)
factor = 2     # plots the second factor
rect2=f3_ax5.bar(labels, V[factor-1, :], color=[label_colours[label] for label in labels])
f3_ax5.set_title('Principal component ' + str(factor), fontsize=20)
f3_ax5.set_xticklabels(labels, rotation=30)
f3_ax5.set_ylabel('loading', fontsize=20)
f3_ax5.set_ylim(min(V[factor-1, :])-0.1, max(V[factor-1, :])+0.1)
autolabel(rect2, f3_ax5)

#ax1 peak areas line profile
for indx, t in enumerate(range(0, num_cols)):
   f3_ax1.plot(temp, areas[:,t]/1000, marker="o", color=[label_colours[label] for label in labels][t])
f3_ax1.set_xlabel('Temperature [°C]', fontsize=20)
f3_ax1.set_ylabel('Peak area *0.001 [CPSeV]', fontsize=20)
```

```
f3_ax1.legend(labels, loc='upper center', bbox_to_anchor=(0.53, 0.70 ))
# other figure specifications
fig3.set_size_inches(w=18,h=11)
```

iii. Pearson correlation heatmap

```
import pandas as pd
import matplotlib.pyplot as plt
import seaborn as sns
import numpy as np
from scipy.stats import pearsonr

plt.rcParams.update({'font.size': 13})
filepath=r'C:\Users\hartwig\ownCloud2\PCA manuscript\Python analysis\ASCII data files\Ex367 up Pd5O4.dat'
d=pd.read_csv(filepath, delimiter='\t',header=1, index_col=0, encoding= 'unicode_escape') #, header=1 for some files
d.columns=d.columns.str[:-6]
d.rename(columns={list(d)[4]:'Pd metal'}, inplace=True)
d.rename(columns={list(d)[3]:'O(IV)'}, inplace=True)
corr=d.corr()
mask = np.triu(np.ones_like(corr, dtype=np.bool))
#optional color map
cmap = sns.diverging_palette(220, 10, as_cmap=True)
figa= sns.heatmap(corr, cmap='BrBG', mask=mask)
figa= plt.gcf()
```

iv. Scatter matrix (correlogram) with rounded temperature

```
import pandas as pd
import matplotlib.pyplot as plt
import seaborn as sns
import numpy as np
```

```
from scipy.stats import pearsonr

filepath=r'C:\Users\hartwig\ownCloud2\PCA manuscript\Python analysis\ASCII data files\Ex367 up Pd5O4.dat'
df= pd.read_csv(filepath, delimiter='\t', header=1, encoding= 'unicode_escape')
sns.set(style='ticks')
sns.set_context('talk', font_scale=1.3)
# delete CPSeV from the column names
df.columns=df.columns.str[:-6]
df.rename(columns={list(df)[5]:'Pd metal'}, inplace=True)
df.rename(columns={list(df)[4]:'O(IV)'}, inplace=True)
# rename first column
df.rename(columns={list(df)[0]:'Temperature [°C]'}, inplace=True)
# round the temperature. -2 means round to the next 100
df.iloc[:,0]=df.iloc[:,0].round(-2)
# in this case the temperature is also plotted
fig=sns.pairplot(df, vars=['O(I)', 'O(II)', 'O(PdO)', 'O(IV)', 'Pd metal', 'PdO', 'Pdox(I)', 'Pdox(II)'], hue='Temperature [°C]', palette='coolwarm', diag_kind=None) # change the range here according to the data
plt.show()
```

v. Scatter plot and rolling correlations figures

```
import pandas as pd
import matplotlib.pyplot as plt
import numpy as np
import seaborn as sns
filepath=r'C:\Users\hartwig\ownCloud2\PCA manuscript\Python analysis\ASCII data files\Ex367 up Pd5O4.dat'
df= pd.read_csv(filepath, delimiter='\t', header=1, encoding= 'unicode_escape')
# remove CPSeV from the coolumn names
df.columns=df.columns.str[:-6]
```

```
# rename columns
df.rename(columns={list(df)[0]:'Temperature'}, inplace=True)
df.rename(columns={list(df)[5]:'Pd metal'}, inplace=True)
df.rename(columns={list(df)[4]:'O(IV)'}, inplace=True)
temp=df['Temperature']
#%% Two plots plotting
plt.rcParams.update({'font.size': 11})
def rolling_plot(x,  y, w):
    fig, axs=plt.subplots(1,2, tight_layout=True)
    fig.set_size_inches(w=10,h=4)
    a=axs[0].scatter(df[x], df[y], c=temp, cmap='coolwarm', vmin=180, vmax=800)
    cbar=fig.colorbar(a, ax=axs[0])
    cbar.set_label('Temperature [°C]')
    axs[0].set_title('Peak areas: '+str(y)+ ' vs. '+str(x), fontsize=12)
    axs[0].set_xlabel(str(x) +' [CPSeV]')
    axs[0].set_ylabel(str(y) +' [CPSeV]')
    axs[0].annotate('a)', (-0.26, 1.02), xycoords='axes fraction', fontsize=12)
    corr=df[y].rolling(w, center=True).corr(df[x])
    b=axs[1].scatter(temp, df[y], c=corr, cmap='BrBG', vmin=-1, vmax=1)
    axs[1].set_xlabel('Temperature [°C]')
    axs[1].set_ylabel(y +' [CPSeV]')
    axs[1].set_title('Rolling correlation '+str(y)+ ' vs. '+str(x), fontsize=12)
    axs[1].annotate('b)', (-0.26, 1.02), xycoords='axes fraction', fontsize=12)
    cbar2=fig.colorbar(b, ax=axs[1])
    cbar2.set_label('rolling correlation'+' w='+str(w))
    return a
    return b
rolling_plot('PdO','Pdox(I)' , 15)
```

List of publications and conference contributions

First-author:

1. C. Hartwig, K. Schweinar, T. E. Jones, S. Beeg, F. Schmidt, R. Schlögl, M. Greiner. Isolated Pd toms in a silver matrix: Spectroscopic and chemical properties. *J. Chem. Phys.* **2021**, *154*, 184703.
2. C. Hartwig, K. Schweinar, R. Nicholls, S. Beeg, R. Schlögl, M. Greiner. Surface composition of AgPd single-atom catalyst in oxidative environment. *J. Chem. Phys.* **2021**, *154*, 174708.

Co-author:

1. K. Schweinar, S. Beeg, C. Hartwig, C. R. Rajamathi, O. Kasian, S. Piccinin, M. J. Prieto, L.C. Tanase, D. M. Gottlob, T. Schmidt, D. Raabe, R. Schlögl, B. Gault, T. E. Jones, and M. T. Greiner. Formation of a 2D Meta-stable Oxide by Differential Oxidation of AgCu Alloys. *ACS Applied Materials & Interfaces*. **2020**, *12*, 23595-23605.
2. L. Pielsticker, R. Nicholls, S. Beeg, C. Hartwig, G. Klihm, R. Schlögl, S. Tougaard, M. Greiner. Inelastic electron scattering by the gas phase in near ambient pressure XPS measurements. *Surf Inter Anal.* **2021**, 1-13.

Oral-presentation

1. "NAP-XPS study of AgPd single-atom alloy catalysts" E-MRS 2019 Fall Meeting, Symposium: "New frontiers for the in-situ and operando spectroscopic investigation of interfaces applied to catalysis and electrochemistry", Warsaw, Poland, September 2019.

Poster presentation

1. "Electronic structure of AgCu and AgPd single-atom alloy catalysts" 2nd IMPRES-RECHARGE Symposium "Catalysis Towards Greener Chemistry", Mülheim a. d. Ruhr, Germany, May 2019.

Research scholarship

DAAD scholarship from the German-Russian interdisciplinary Science Center (G-RISC), for a research stay at the Boreskov Institute of Catalysis, Novosibirsk, Russia (not conducted due to the Corona virus).

Lebenslauf (Curriculum Vitae)

Der Lebenslauf ist in der Online-Version aus Gründen des Datenschutzes nicht enthalten

Eigenständigkeitserklärung (statement)

Hiermit versichere ich, dass ich die vorliegende Arbeit mit dem Titel

„ AgCu and AgPd Single-atom Alloys:
Electronic Structure, Surface Dynamics and Chemical Properties”

selbst verfasst und keine außer den angegebenen Hilfsmitteln und Quellen benutzt habe, und dass die Arbeit in dieser oder ähnlicher Form noch bei keiner anderen Universität eingereicht wurde.

Essen, Juni 2021